THEORETICAL MODELING WITH VALIDATION OF A COMBINED HQ-LINER SYSTEM FOR TURBOFAN ENGINE NOISE CONTROL

By

José Santiago Alonso-Miralles

Dissertation submitted to the Faculty of the
Virginia Polytechnic Institute and State University
in partial fulfillment of the requirements for the degree of

Doctor of Philosophy
in
Mechanical Engineering

Ricardo A. Burdisso, Chair
Hwa W. Kwan
Marty Johnson
Wing Ng
Don J. Leo
Muhammad Hajj

September 15th, 2004
Blacksburg, Virginia

Keywords: Turbofan noise, Aeroacoustics, Herschel-Quincke tube, Acoustic Liners

THEORETICAL INVESTIGATION WITH VALIDATION OF A COMBINED HQ-LINER SYSTEM FOR TURBOFAN ENGINE NOISE CONTROL

By

José Santiago Alonso-Miralles

Committee chairman: Ricardo A. Burdisso, Mechanical Engineering

(ABSTRACT)

The combination of traditional passive acoustic liners with Herschel-Quincke (HQ) waveguides is proposed in this work as a device for Turbofan Engine Noise Control. The approach consists of installing circumferential arrays of HQ tubes on the lined sector of the inlet of a turbofan engine. A theoretical model is developed to predict the performance of this system assuming that the engine inlet is a circular lined duct with uniform mean flow. The tube-duct interfaces are modeled as finite piston sources that couple the sound field inside the duct with the dynamics of the HQ tubes. The finite piston source radiation is modeled in terms of a ***new closed form*** Green's function, which is found as the solution of the non-homogeneous convected acoustic wave equation with soft wall boundary conditions. The Green's function is extended from a point source to a finite piston by using the Divergence Theorem in the appropriate form. The dynamics of the HQ tube are both modeled as plane waves inside a straight tube and experimentally determined. The experimental determination of the HQ-dynamics is undertaken using impedance tubes with a 4-microphone technique. The newly developed theoretical model was used to predict the performance of a combined HQ-Liner system, which was tested on a scale simulated turbofan rig. The model is validated for broadband noise with the experimental data obtained from this test rig. The analytical predictions are shown to correlate well with experimental data. The results of the application of a HQ-Liner on a turbofan engine show a great potential in order to improve the performance of traditional passive acoustic liners.

Acknowledgments

In the first place, I would like to thank my advisor, Prof. Ricardo Burdisso, for his valuable guidance over all the challenging research projects that I had the opportunity to be part of. His advice has helped me not only to learn the technical material but also to understand the physics of acoustics and communicate it to researchers of different backgrounds. Also, I would like to thank Dr. Kwan for his technical support and Goodrich Corporation for giving me the chance of working as a part of the acoustics team in the effort of reducing turbofan engine noise. I am also expressing my gratitude to Prof. Marty Johnson, Prof. Wing Ng, Prof. Don Leo, and Prof. M. Hajj for serving in my committee.

Secondly, I give many thanks to the Vibrations and Acoustics Laboratories personnel, especially Linda King for supplying her help in every way available. It was a great experience to share the technical knowledge with the graduate students in the VAL team. I want to particularly show my gratitude for Kenji Homma and Yu Du with who it was very comfortable to work with. Also, I would like to thank Leonardo Molisani for taking with me this long journey of studying the high fundamentals of linear operators and most importantly offering me his friendship. The color plots presented in this dissertation were generated with a code developed by him. Thanks Leo!

This period as a graduate student at Virginia Tech has also left me a lot of friends, Carlos, Pedro, Dieguin, Cemil, Marcos, Valerio, Mauricio, Baris, José Fernando, Marco, Sergio and many more. I want to express my gratitude to them for all those the great moments.

My parents deserve the best of my gratitude for giving all they had in hand to help me find my way. It is very hard to be far away from them but it is also very encouraging to know that they were present in the moments I needed them most. Finally, I would like to thank my fiancée, Andrea, for accepting my decision to come to study in the United States and waiting for me until I finished. Her support and love were a great motivation to keep me going and work hard to reach my objectives.

Contents

List of Figures

List of Tables

Chapter 1 Introduction

Global economic growth has led to demand for air transportation to a level that twenty years ago could hardly have been imagined. This growth made possible the high increase in commercial freight transportation both nationally and worldwide, and also in the movement of passengers. Air transportation reduces distances and saves time considerably, resulting in a very effective service which became a necessity for most trade operations. Nevertheless, due to this increasing demand, aviation industry is facing the environmental barrier that could limit or even lead to a reduction in air transport activity: noise. The concern about aircraft noise has even started to take part into the decision process and strategies of airline companies. Furthermore, the regulations on aircraft noise requirements have become more stringent as residents around airports have become more concerned about noise pollution.

As a consequence of this important obstacle, various attempts have been made to reduce aircraft noise or even improve the effectiveness of current noise control techniques. This dissertation is concerned about the reduction of the noise of one of the main aircraft sources: turbofan engine noise. One of the most successful techniques to reduce fan noise is the implementation of acoustic liners. Although the application of liners is mostly effective for the attenuation of broadband noise, the shorter inlet ducts of modern ultra high bypass turbofan engines and the lower blade passage frequencies (BPF) for these engines, opened the door for investigation on parallel techniques to make the traditional passive liner technology more efficient. The present study proposes the integration of acoustic liners with the Herschel-Quincke (HQ) tube concept (HQ-Liner). The HQ concept applied to turbofan engines has been previously investigated in hard

wall inlets and showed promising results. Therefore, this research will concentrate on combining the HQ device with acoustic liners.

This Chapter presents an introduction to turbofan engine noise and the current techniques for its reduction. A brief introduction to the use of liners and HQ tubes will be presented in order to identify the systems that will be later combined. Since this work includes the mathematical modeling of the HQ-Liner, a literature review of propagation of sound in lined ducts was undertaken and is presented in this Chapter. Finally, the organization of this dissertation is explained in the last section.

1.1 Introduction to Aircraft Noise

Concern about aircraft noise is one of the reasons why the aviation industry is currently not able to expand further. For instance, the construction of new airports has been delayed or even canceled because of the problem of noise. And this issue is not only limited to people living on the airport surroundings but also from neighborhoods that are 15 miles away. As a result, from being just a concern, noise has become a matter of economic importance for airlines. Even the passengers would be affected because of the inability of the aviation companies to satisfy the increasing demand. Consequently, the International Civil Aviation Organization (ICAO) has decided to adopt a new set of regulation standards. These new noise standards are intended to produce a noise relief from the communities, and at the same time create a new certification procedure for new aircrafts. In this way, the aviation industry would be able to move forward and correctly take care of noise pollution.[†]

To be able to satisfy the regulations, aircraft manufacturers and engine companies have started cooperative research projects for noise abatement. These investigations include to propose new noise control techniques as well as to improve the present ones. In order to understand the possible solutions to this problem, the first step is to identify the noise sources from an aircraft. As shown in Figure 1.1, aircraft noise is due to two main sources: airframe and engine noise. The airframe noise is produced by the

[†] Information obtained from the article "*Aircraft Noise: Addressing a Potential Barrier to Global Growth*", by Gerald L. Baliles, former Governor of Virginia, member of Transportation Infrastructure Practice Group

aerodynamic turbulence created by the different parts of the airplane structure, such as landing gear, lifting devices, and so forth. This source becomes of great importance during the approach condition previous to final landing, i.e. with reduced power and fully extended airframe. In addition, the engine noise is produced by the rotating turbofan parts and dominates at the take-off and cutback conditions.

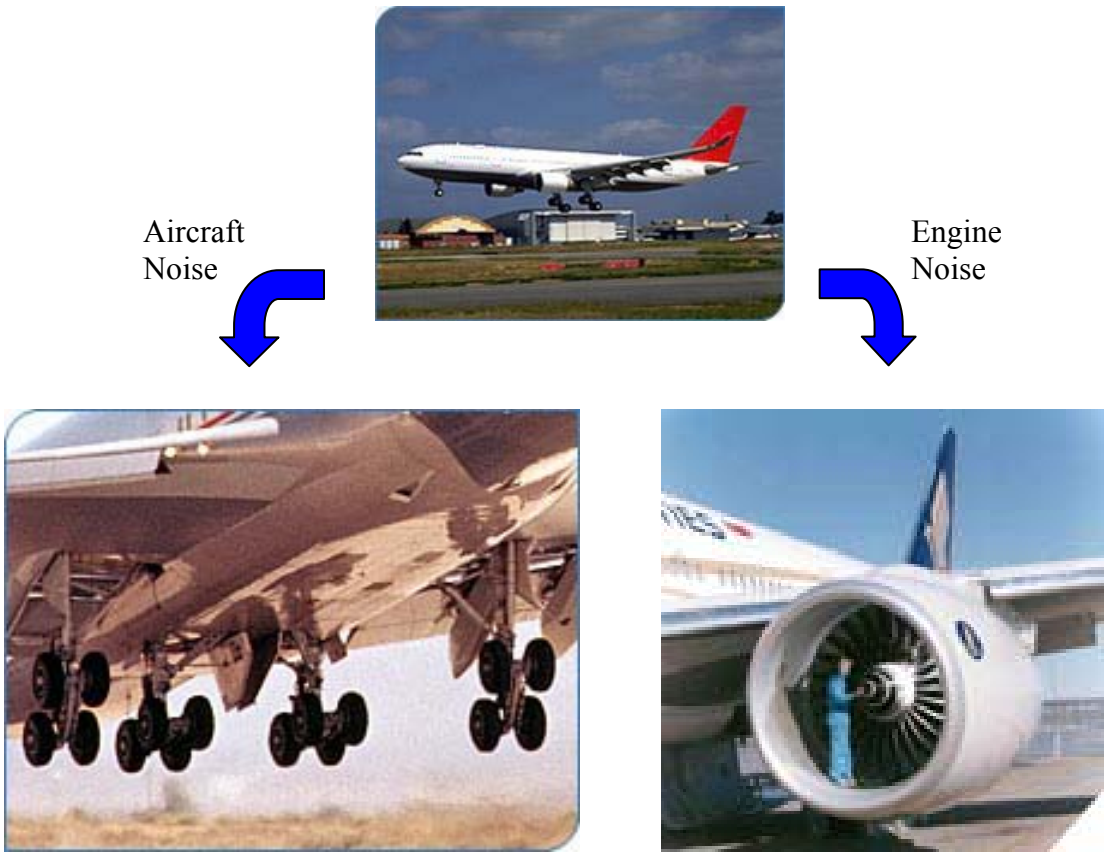

Figure 1.1: Aircraft Noise – Sources.

Certainly, regulations for aircraft certification are concerned about the noise produced at the stages of airport transit, i.e. landing and take-off. They require manufacturers to develop aircrafts that stay within well-defined noise limits. Therefore, the FAA certification [58] involves measuring the noise produced by the airplane at three locations during the flight conditions illustrated in Figure 1.2. As shown in the figure, these conditions are approach (during the final landing), sideline and cutback (during the take-off). The approach condition consists on measuring the sound produced by the

aircraft during the descending path previous to final landing. The aircraft has to descend on a 3^{o} slope and the noise has to be measured at 2000 meters from the landing track. In addition, it is required to set the noisiest configuration which requires having the landing gear and flaps fully extended.

The take-off (TO) path is divided in sideline and cutback conditions. The sideline condition consists on performing a normal take-off at full engine power and maximum TO weight. For this case, the noise has to be measured when the aircraft is about 1000 ft off the ground, and 450 m to the side of the landing track axis. The cutback condition is produced when the power is cut from maximum speed to normal climbing rate. The next measuring location is with this power setting at the end of the landing track (Flyover).

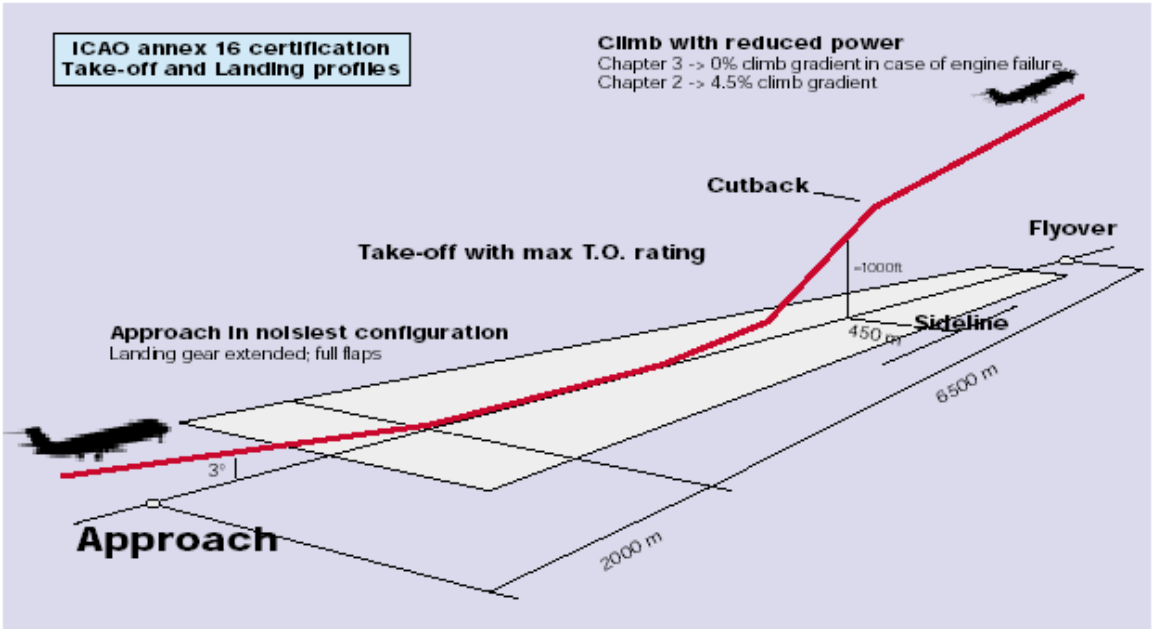

Figure 1.2: Certification Take-off and Landing Profiles according to ICAO regulations[†].

As mentioned before, the regulations consider these conditions and require keeping the noise levels below a certain specified limit according the size of the aircraft. This limit has recently become more rigorous due to the concern of the communities living around airport areas. Figure 1.3 presents the certification noise level of different aircrafts over the last 50 years. This picture shows that the noise levels have been gradually reduced over the past decades, reflecting the concern of the regulations on the noise

[†] Picture taken from Airport Business magazine, December 2000 – January 2001, ACI Europe

problem. Note that a significant noise reduction has been achieved during the 70's by the change from turbojet to turbofan engines. In addition, acoustic liners have been able to obtain lower certification noise levels for the turbofan engines over the years since their implementation started in the middle 60's.

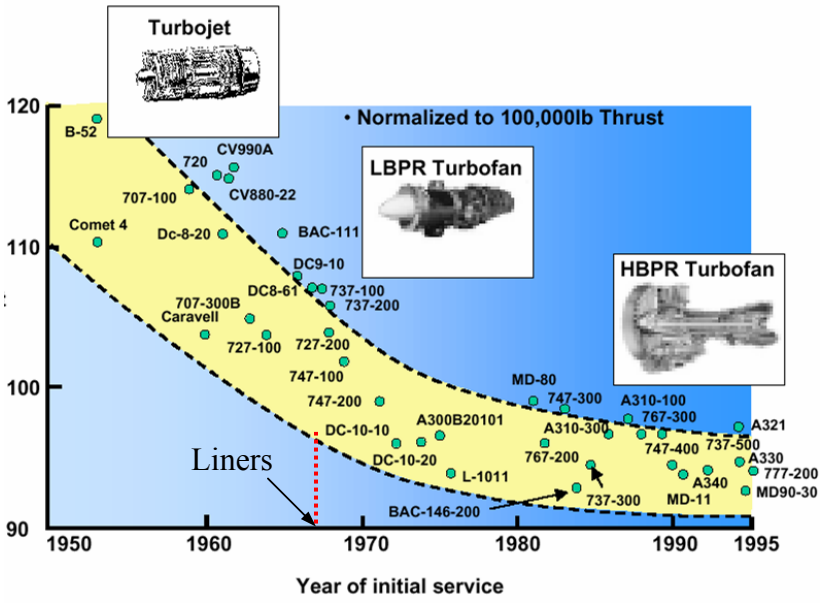

Figure 1.3: Certification Noise Levels over the past 50 years[†].

During the take-off path, the noise component that will affect the regulations is dominated by the engine noise. The engine regimes for this condition are set to the maximum available power, which is in fact the noisiest case. The next section gives an introduction to the noise produced by the turbofan engines.

1.2 Turbofan Engine Noise

Turbofan noise is produced from different rotating parts of the engine as well as from the turbulence due the air flow. Each noise component produced by the different parts of the engine has an impact on the overall generated noise depending on the type of turbofan considered. The noise pattern has changed considerably over the past years from the old low bypass ratio engines to the new generation high bypass (HBP) ratio turbofans. As

[†] Picture available at www.larc.nasa.gov

shown in Figure 1.4, the high speed exhaust gases from the old low bypass ratio engines caused the jet and shock wave noise to be dominant over the rest of the components. But the need of more economic engines led manufacturers to increase the fan diameter in order to gain more thrust with less fuel consumption. The consequence was the creation of new high bypass ratio engines with significantly lower speed exhaust gases. The jet noise for these engines was significantly reduced but, on the other hand, the fan noise became a major problem.

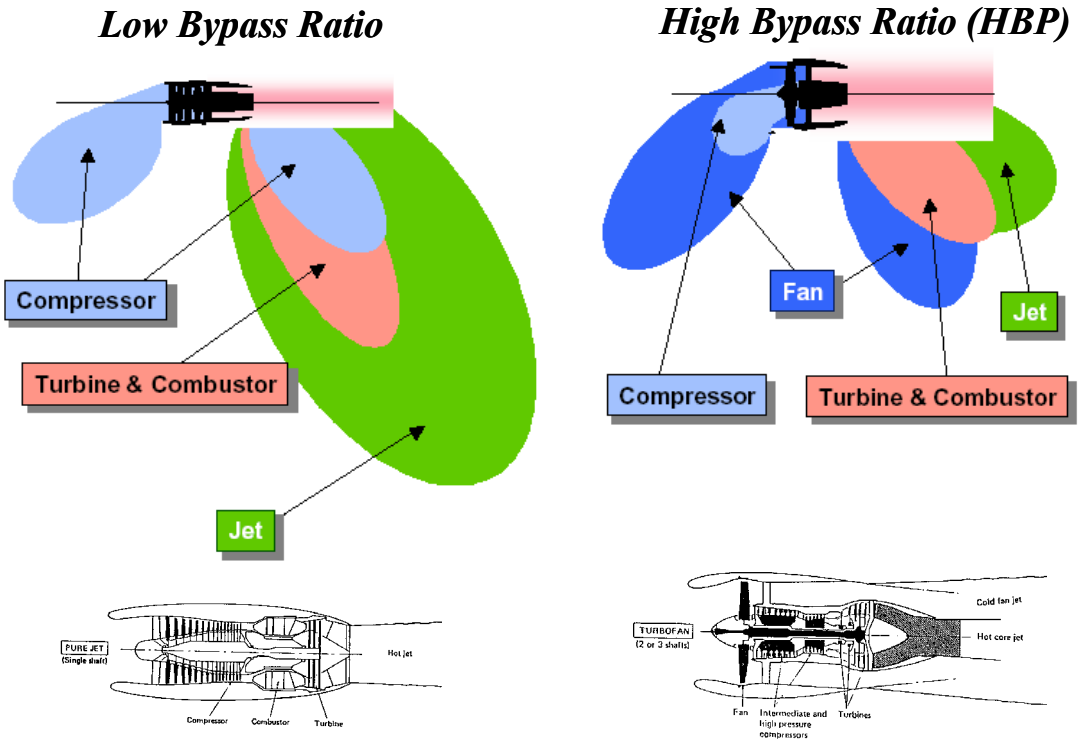

Figure 1.4: Noise Components of low and high bypass ratio turbofan engines.

The high bypass turbofan engine noise is divided in several components, as shown in Figure 1.5. The main contribution is given by the fan noise, which is radiated to the front (inlet radiation) and the back (aft radiation) of the engine. The rotation of the fan produces very strong tones at the BPF due to the wakes generated by the blades and the interaction of these wakes with the stator vanes. The BPF tone magnitudes are further increased at the high power regimes by the presence of shock waves at the blade tips, i.e. supersonic fan condition at take-off and cutback. The large fan diameter and the high rotational speed of

the fan result in a blade tip speed on the transonic range and consequent generation of shock waves.

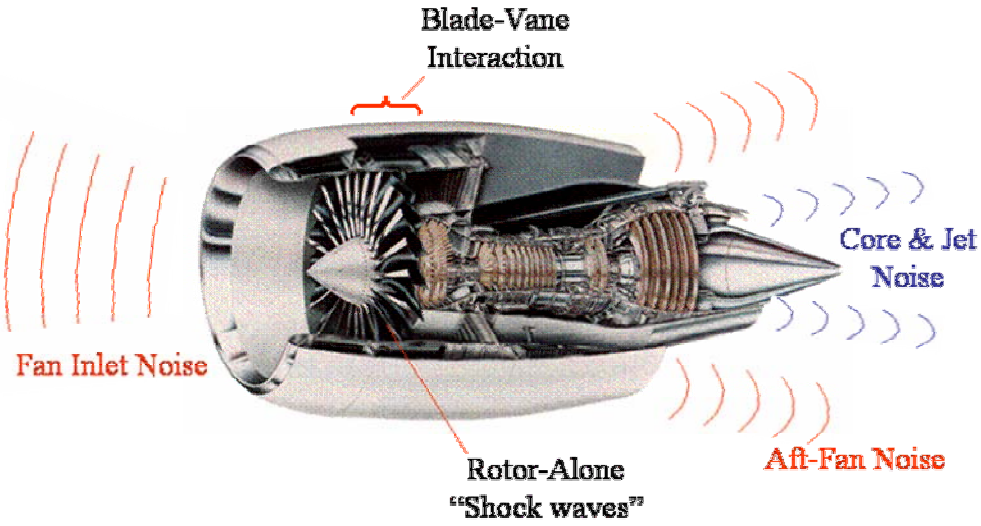

Figure 1.5: Noise Components of high bypass turbofan engines.

The typical noise spectrum produced by a turbofan engine for different conditions is presented in Figure 1.6. The low engine speed noise spectrum in Figure 1.6(a) is characterized by a broadband component (produced by the turbulence in the engine) and the BPF and harmonics tones. The figure shows that the BPF tone levels can be at levels 8 dB higher than the broadband level. In contrast, the high engine speed noise spectrum in Figure 1.6(b) is dominated by a set of combination tones, which appear as a consequence of the generation of shock waves at the blade tips. This component is known as the "buzz saw" noise, and it behaves as a set of pure tones rather than a broadband noise. These tones are generated as a consequence of the non-uniform generation of the shock waves in each rotor blade. Although the "buzz saw" noise is not important for airport noise, it represents a real problem for passenger comfort. At the high power setting of take-off, this shock-wave dominated noise is directed towards the front of the aircraft and affects the interior of the passenger cabins. In fact, the first and business class cabins are located at this front sector of the aircraft where it is most imperative to maintain a quiet and comfortable ambient.

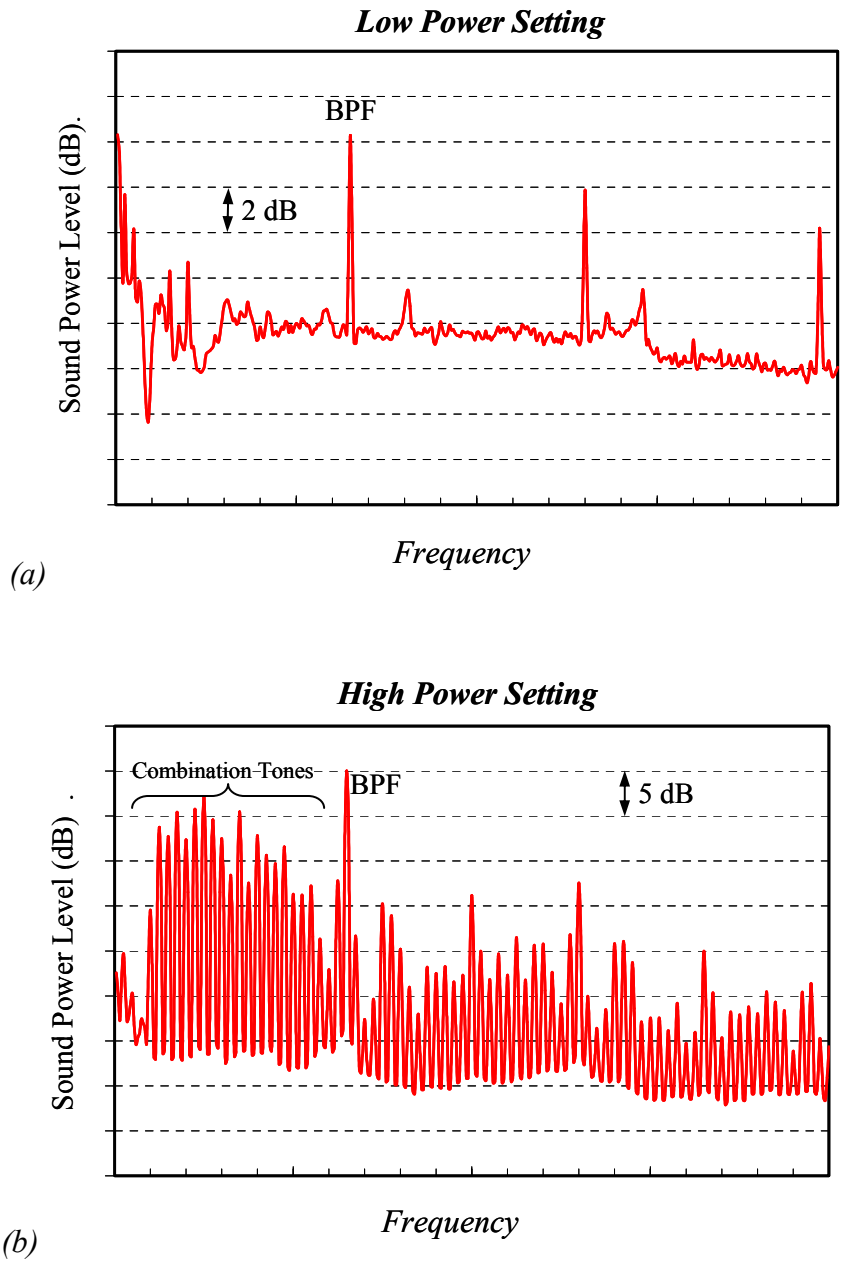

Figure 1.6: Typical Noise Spectrum of high bypass turbofan engines at (a) low power settings and (b) high power settings.

1.3 Noise Control of Turbofan Engines

In the last few decades, various attempts have been made to reduce the noise from turbofan engines. A common approach to reduce the fan noise has been to directly change the design of the fan. For example, the geometry of the fan blades and the rotor vanes can

be modified to reduce the generated noise due to rotor-stator aerodynamic interactions [1-3]. Systems with increased spacing between the rotor and stator, as well as fans with leaned blades were investigated. Although these systems achieve significant noise reduction, these advanced rotor-vane systems also resulted in unwanted stress concentration in the structure of the blades. Another technique consists in the use of **acoustic liners**, which has been extensively used to reduce fan noise [4] and has been the most successful method in the past years. Their characteristics and applications are discussed in this section.

Acoustic liners are porous materials that are typically placed on the wetted internal surfaces of the engine's nacelle. Their efficiency is proportional to the effective length or area of the applied treatment. These liner systems generally consist of a combination of absorptive materials and resonating cavities. The structure of a single degree of freedom (SDOF) liner is sketched in Figure 1.7. A thin sheet of perforated facing material and a solid backing surface are separated by a cavity divided into compartments by a honeycomb core. This forms an array of resonators which effectively attenuate a predominantly narrow frequency band of noise.

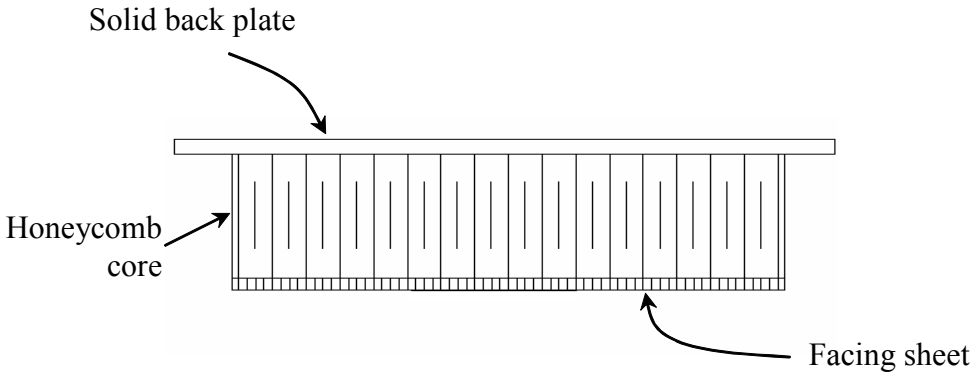

Figure 1.7: SDOF Liner Structure.

In order to obtain a better attenuation over a broader frequency band, the perforated plate is often covered by a thin porous absorptive facing layer with high acoustic resistance. The presence of this high resistance implies adding a considerable amount of damping into the resonances of the liner cavities. As a result, the narrow band attenuation of the array of resonators is reduced, but at the same time, extended over a wide range of frequencies.

However, this range of frequencies is limited and has to be determined based on a design condition for every particular engine, e.g. to target a frequency range around the BPF or one of its harmonics. As a consequence, once the target frequencies are identified, it will be difficult to control other frequency ranges that might also be of concern.

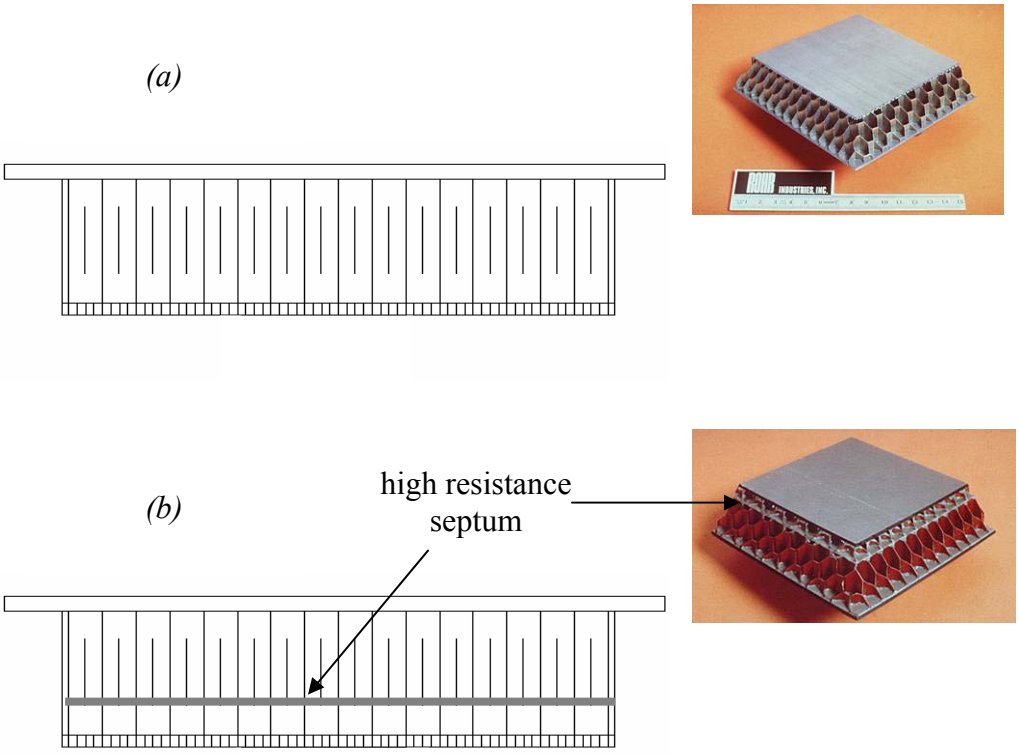

Figure 1.8: (a) SDOF and (b) DDOF liners[†].

An improved performance of the liner can be obtained by placing a second, high resistance, perforate screen inside the resonant cavities. This structure is known as the double degree of freedom (DDOF) liner, which is shown in Figure 1.8(b). The high resistance septum divides the resonant cavities into two cells that resonate at two different frequencies. As a consequence, this technology allows tuning the liner to more than one frequency and obtaining reduction over an even broader range. Nevertheless, DDOF liners can improve the attenuation mostly for higher frequencies without being able to control the

[†] Pictures are courtesy of Goodrich Corp.

lower frequency components that are present in ultra high bypass ratio engines. A comparison of the SDOF and the DDOF liner is presented in Figure 1.8. As seen in the pictures, the assembly of the DDOF liners involves a more complex technology, which results in a higher cost of fabrication. Furthermore, the additional material required by the DDOF liner contributes to increase the weight of the aircraft, which is a critical parameter.

The use of liners started during the 60's and, since then, they have controlled noise from turbofans effectively (*see Figure 1.3*). They have been able to obtain lower certification noise levels for the turbofan engines over the years since their implementation started. They can even control the noise for the case of the high bypass engines with large fans producing shock waves at the take off conditions. Although the applications of liners are effective, the shorter inlet ducts of modern ultra high bypass turbofan engines and the lower BPF for these engines made the traditional passive liner technology less efficient in attenuating the fan noise. Because of these difficulties, active noise control techniques were assumed to provide the potential of producing an effective noise control solution for fans [5-9]. However, despite the recent advances in active noise control methods for controlling the BPF tone and harmonics, the complexity of these systems implied that the implementation of a practical system for production may be still many years away. Furthermore, it has been reported that simply reducing the BPF tone and harmonics, i.e., without any reduction in the broadband levels, may result in little or no reduction in the EPNLdB, which is the metric used to quantify aircraft flyover noise [10, 11]. Thus, it was determined that an active noise control system would need to be combined with a broadband noise control to produce an effective noise control solution for turbofan engines.

As a result, the trends on recent research show that liner technology will continue to be used over the next years. Therefore, the challenge was opened to investigate parallel techniques that can be implemented in conjunction with liners and improve their performance. ***This dissertation is an investigation of the integration of acoustic liners with the Herschel-Quincke* (*HQ) tube technology applied to turbofan engine noise***. Thus, a brief review of the HQ concept for control of engine noise is presented in the next section.

1.4 HQ Tube Concept

This section describes the HQ tube from its initial conception to the eventual application to control turbofan engine noise. The HQ tube consists of a side-waveguide that is connected to the wall of a duct by its two open ends. The simple case of a single HQ tube for the control of plane waves in a two-dimensional duct is presented in Figure 1.9. The acoustic energy traveling in the main duct enters the HQ tube on one of the tube openings and then recombines with the noise that propagated in the main duct at the next tube-duct interface.

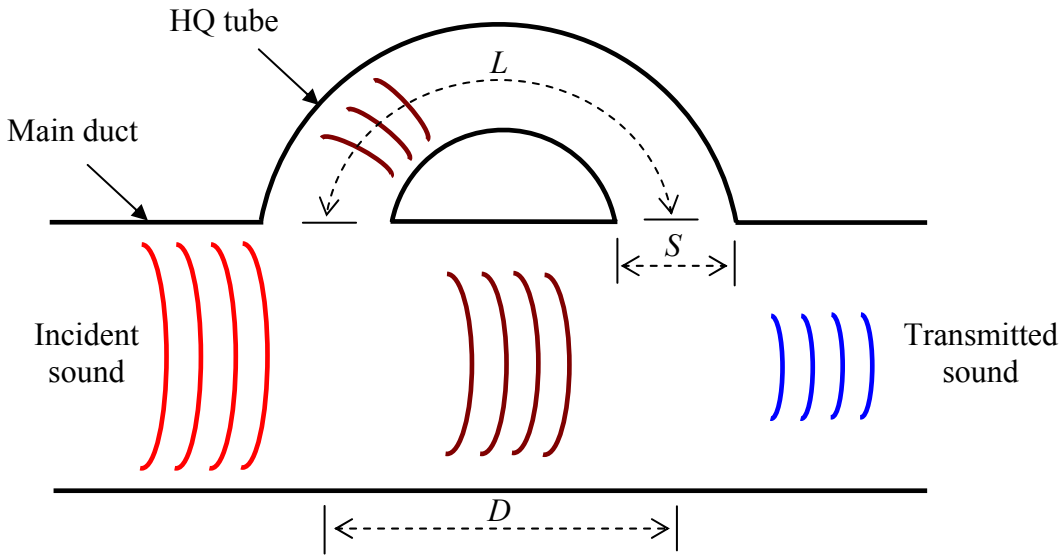

Figure 1.9: Schematic of Herschel-Quincke (HQ) tube for the control of plane wave.

The initial application of the HQ concept was restricted to the control of only simple plane waves in ducts. In 1833, Herschel [12] was the first to investigate the acoustic interference of musical tones with this type of waveguides. He predicted that the system would produce cancellation of tones when the path length difference between the recombined signals was $(2m+1)(\lambda/2)$, where λ is the wavelength of the acoustic wave and m is any integer. Later, in 1866, Quincke [13] experimentally confirmed that this system is in fact able to cancel sound as predicted by Herschel. In the 20th century, Steward [14] refined the HQ concept theory and verified that cancellation occurs when the path length

difference is $(2m+1)(\lambda/2)$, but also when the path length difference is $m\lambda$, with limited attenuation at other transitional frequencies. However, Stewart assumed that the cross-sectional areas of the parallel duct sections were equal. More recently, Selamet *et al.* [15] extended Stewart's work by deriving an analytical model without the limitations on duct cross-sectional geometry.

As mentioned before, the noise cancellation observed with the HQ tube can be explained as acoustic energy traveling in the main duct and entering the HQ tube on one of the tube openings. Then, the noise that travels through the HQ tube recombines with the noise that propagated in the main duct at the next tube-duct interface. At some particular frequencies, the recombining noise is out-of-phase given the fact that the sound propagating along the duct traveled a different distance than the sound in the tube. As a consequence, there will be noise cancellation at these frequencies, which are dictated by the geometrical parameters of the HQ tubes such L, D or S. This explanation is oversimplified since the actual dynamics are much more complex, as sound waves can propagate in both directions within the main duct and the tubes. In addition, the presence of higher order modes in the duct also contributes to the complexity of the propagation phenomena.

Only recently, the potential use of HQ waveguides for attenuating higher-order modes in two-dimensional ducts has been analytically investigated by Brady *et al.* [16] recently. This study proposed a model to predict the effect of a HQ tube in the presence of higher-order modes and showed that the noise attenuation mechanisms involved reflection of incident energy as well as scattering and recombination of energy between radial modes. Later, the approach was extended to the implementation of circumferential arrays of HQ waveguides for attenuating higher-order modes in three-dimensional hard wall circular ducts by Hallez [17]. This work was applied to noise attenuation on turbofan engine inlets as illustrated in Figure 1.10, where a single array of HQ tubes is used. For this system the three-dimensional pressure fields that exist in circular ducts in the presence of higher-order modes makes the problem more complicated to analyze. In the case of turbofan engine inlets in particular, the sound field at the BPF tone is made up of propagating spinning modes with multiple circumferential and radial orders. This results in a complex pressure field in the cross-sectional plane of the inlet with non-uniform

circumferential variation in the acoustic pressure. In addition, an HQ system will always lead to reflection back towards the fan and scattering of the acoustic energy among both circumferential and radial propagating modes inside the engine inlet.

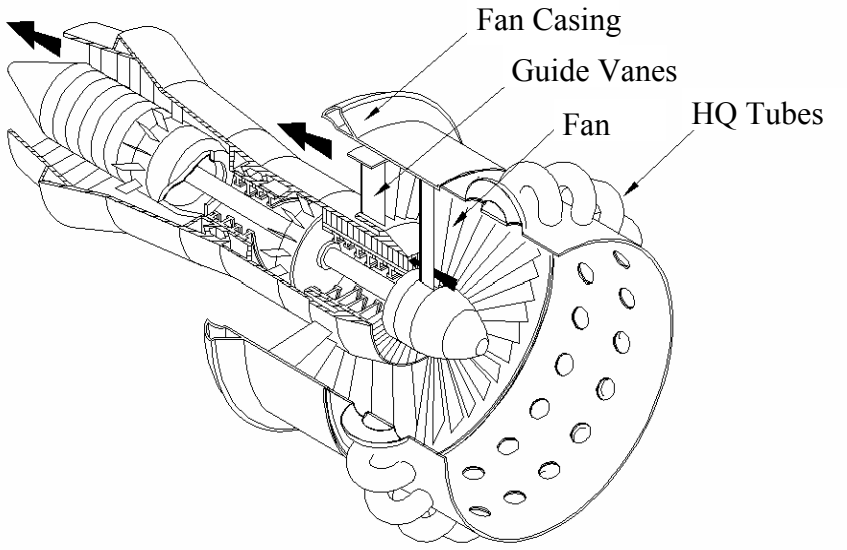

Figure 1.10: Schematic of the HQ tube concept applied to the inlet of a turbofan engine.

The implementation of HQ tubes to reduce noise from real turbofan engines was initially investigated by Burdisso *et al.* [18], on a running Pratt & Whitney JT15D turbofan engine. The results showed a very good reduction of tonal noise at discrete frequencies as well as broadband noise. Figure 1.11 presents a picture of a HQ-system tested on the P&W JT15D engine. Further experiments were performed on a production Honeywell TFE731-60 turbofan engine which again showed promising results [19]. A picture of the two-arrays HQ-system mounted on the Honeywell TFE731-60 engine is presented in Figure 1.12. These engine experiments demonstrated the remarkable potential of the HQ concept for reducing noise from turbofan engines.

In both engine experiments, the HQ system was implemented on a hard walled duct. But as mentioned before, since the performance of liners is proved to be very robust, the practical implementation the HQ system is in conjunction with currently used acoustic liners. Since the HQ system has been shown to be effective at controlling tonal while

liners are designed as broadband noise attenuators, a strategic design of a HQ-liner could be a very effective noise treatment for turbofan engines.

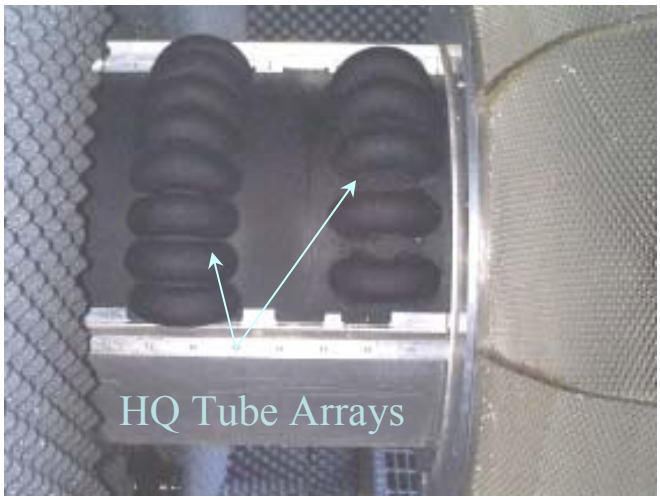

Figure 1.11: HQ-system mounted on the Pratt & Whitney JT15D engine.

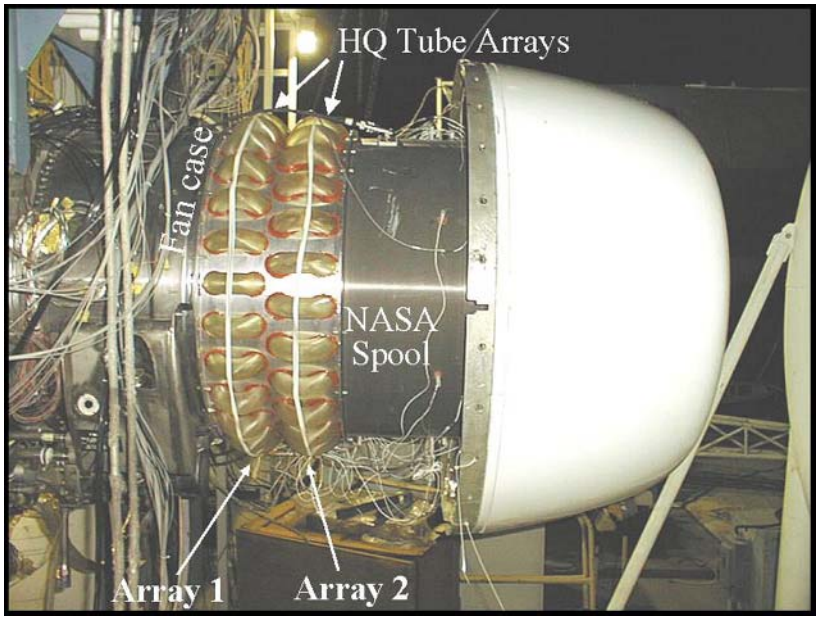

Figure 1.12: HQ-system mounted on the Honeywell TFE731-60 engine.

This dissertation describes the development of an analytical tool to model and design the combined HQ-liner system as well as a comparison to experimental results to validate the model. To this end, a new mathematical model will be derived in order to simulate the performance of the HQ tubes in conjunction with the liner. The analytical formulation of this problem requires a high mathematical background of sound propagation in lined ducts with flow. For this purpose, a literature review of this subject is presented in the next section.

1.5 Literature Review of Sound Propagation in Lined Ducts

The propagation of sound in lined ducts has been extensively studied over the past years, especially because its direct application to turbofan engine noise. The investigation of turbofan engine noise from a theoretical point of view was a valuable contribution to start solving this environmental problem. Although a lot of advances and discoveries were made in analytical treatment of sound propagation in ducts, the acoustic phenomena in a turbofan inlet were still unknown to a number of engineers. But since Tyler and Sofrin [1] presented in 1961 a clear mathematical and physical explanation of this matter, a great progress has been achieved in understanding the generation and propagation of fan noise. A later paper by Syed et al. [20] also showed that the predictions obtained using circular lined duct acoustics well match the experimental data obtained from real engine intakes.

The first studies consisted in finding solutions to the equations of acoustic motion derived by Morse [21], in a rectangular cross-section lined duct with fluid at rest relative to the duct walls. These equations were later modified to take into account the effect of a uniform, subsonic, axial, mean flow [22] that takes place in the inlets of turbofan engines. Also, Pridmore-Brown [23] extended the analysis to include the effect of an axial fluid velocity which does vary across the duct cross-section (shear flows).

The solutions to the formulations stated above are usually investigated by imposing certain restrictions that allow posing a solvable problem, e.g. constant cross section, uniform impedance, etc. Nevertheless, there have been theoretical studies where these restrictions were removed in order to analyze different effects on the solution. These

studies include solving the propagation in ducts with non-uniform [24, 25] and non-locally reacting [26] impedance boundary condition as well as in lined ducts of variable cross section [27, 28]. The present work is constrained to solving the propagation and radiation of sound in an infinite circular lined duct (with constant cross section) and uniform locally reacting impedance.

In order to find the correct solution for this convected wave equation with uniform mean flow [22] the appropriate soft wall boundary condition was derived. For the case of a rectangular [29, 30] and a circular [31] duct with lined walls, the boundary condition was developed using continuity of pressure and particle displacement. In a more general analysis, the same boundary condition was formally derived by Myers [51] for a duct of an arbitrary shape and flow field. Although this formulation can be considered as the most general, the expressions collapse being the same as stated by Ko [29, 31] and Tester [30] for constant cross-sections with uniform flow parallel to the duct axis.

The solution to the wave equation in a moving media with the appropriate boundary condition was then investigated. For ducts of constant cross section, the solution of the propagation of sound was found in terms of acoustic modes [29, 30, 31, 32]. According to the duct geometry, a different characteristic equation has to be obtained in terms of the wall impedance in order to find the eigenvalues that correspond to every acoustic mode. Since this characteristic equation depends on the wall impedance, the eigenvalues are found to be complex and dependent upon frequency. In other words, the set of eigenvalues have a certain location in the complex plane for every frequency of calculation. This location of the eigenvalues contains the information about the attenuation of every single mode at a particular frequency. Results on these investigations have shown that the fundamental mode is not necessarily the least attenuated mode in a lined duct [29]. Also, since the eigenvalues are located in the complex plane, it has been found to be difficult to order them according to their magnitude. In order to solve this problem, Eversman [32] proposed to determine the order of the eigenvalues according to the magnitude of their real part, but it will be shown in this dissertation that this procedure may lead to incorrect results.

Tester [30] showed another interesting result regarding the behavior of certain “strange” modes. These modes are defined as having a phase speed in the opposite

direction of attenuation. In his work, these modes are used to represent instabilities that can be produced by the presence of a source in the lined duct. According to several references [33, 34, 35, 36, 37] these unstable effects are accepted to exist and are treated in detail. On the other hand, there is no spatial amplification observed in real systems and the theoretical existence of these instabilities may be an inadequacy of the model. Furthermore, some investigators solving the mode propagation in finite length liners even do not talk about any unstable mode [38, 39, 40]. A study presented by Koch and Möhring [41] remarks that the presence of instabilities has to be compensated by other nonlinearities which are in fact not modeled. Therefore, these instabilities have to be set to zero as a first approximation with a linear solution.

The effect of the presence of shear flow on the acoustic propagation was also extensively investigated [31, 42, 43, 44, 45, 46, 47, 48]. The main concern of this effect on a uniform flow model is the application of the correct boundary condition to account for the presence of boundary layers. Nevertheless, Tester [42] verified that if the boundary layer is small enough, the displacement boundary condition is correct, and therefore the effect of the boundary layer can be accounted in a model for the impedance of the wall. The derivations in this thesis will assume a uniform flow model of this kind.

Finally, the last study included in this review of lined duct acoustic models concerns the sound radiation from a point source. Expressions for the sound radiation have been extensively investigated in terms of the Green's functions for the case of a **hard wall** duct with mean uniform flow [49, 50]. These Green's functions have been found as a linear combination of the acoustic modes inside the hard wall duct. Also, the solution was also found in a similar fashion for the case of lined duct **without flow** [22]. However, the extension of the formulation to the case of a lined wall duct with mean flow is still open for further research. Although the same hard wall approaches may be extended to the lined wall case, some questions arise in the process of finding the solution. The main problem is the fact that the acoustic modes in the lined duct with flow may not form a complete set of eigenfunctions. As a consequence, many investigators consider inappropriate the use of modal expansions to find the corresponding Green's functions. On the other hand, since it is accepted that sound propagates in ducts as acoustic modes, it is valid to assume that all the radiated sound from the point source will

be transmitted into modes. Therefore, a modal expansion method will lead to correct formulations. Previous work by Zorumski [38] extends a method developed by Drischler [49] which finds the Green's functions for a point source as a linear combination of inverse Fourier transforms. Although the solution is at the end found in terms of modes, this method has the disadvantage of not being able to impose the continuity of the Green's function at the plane of the location of the source. Also, Tester [30] derived the Green's functions for a two-dimensional lined duct using a Lorentz transformation that allows posing the problem as if the fluid was at rest relative to the duct walls. But unfortunately, since there were some difficulties to apply the boundary conditions, this model led to have limitations on the solution. The Green's functions presented in this thesis are found as a linear combination of modes satisfying the continuity and first derivative jump conditions. They are a new contribution to science and will be able to address some of the difficulties often encountered.

1.6 Objectives and Contribution

This dissertation is concentrated in studying the combination of traditional acoustic liners with HQ waveguides. Therefore, the **first objective** of this work is to develop an analytical formulation to model the effect of the HQ tubes on the lined inlets of turbofan engines. In order to develop this model it is necessary to derive the mathematical tools that simulate the sound propagation and radiation inside circular lined ducts with mean flow. Then, these mathematical tools have to be applied to the case of the presence of the HQ tubes. A computer (FORTRAN) code is developed to run preliminary predictions that can be used as an important part of the HQ-Liner design procedure.

The **second objective** is in fact to develop a design procedure that can lead to obtain a first combined HQ-Liner configuration that meets the engine manufacturer requirements. The HQ-Liner design will consist in designing first the liner and HQ tubes separately and then integrating them. The integration process will provide the information to identify the influence of one system on the other and lead to a future configuration optimization.

The **third objective** of this work is concentrated on validating the developed mathematical model. The validation will be undertaken by comparing predictions with experimental results on the inlet of a fan with a HQ-Liner. The result of this comparison will give valuable information in order to readjust the design tools.

As mentioned before, the model of the HQ tubes in a lined duct requires deriving the mathematical formulation to simulate the propagation and radiation of sound in the duct. This investigation led to undertake a number of tasks that are an original contribution to science. These contributions can be listed as follows

- A new numerical method to solve the eigenvalue problem of the convected acoustic wave equation in a lined duct with flow was developed. This method allows keeping track of the location in the complex plane of the eigenvalues from the low frequency assumptions to higher frequencies.
- A new, closed form Green function is found as the solution of the non-homogenous solution of the convected acoustic wave equation with mean flow. This solution represents the sound radiation from a point source inside the duct.
- The validity of the new Green's function is also investigated by comparison with a numerical solution obtained by using the traditional wavenumber transform method.
- The sound radiation from a simple source is extended to the case of finite piston radiation using the Divergence Theorem. The solution is also found in closed form.
- The newly developed model for sound radiation has recently contributed to simulate the effect of liner splices in turbofan engine inlets [59].
- The sound radiation model is used on a direct application, i.e. the HQ-Liner system. The model is used to predict the performance of real system. The

results are validated using experimental results obtained on an engine manufacturer testing facility.

- An experimental technique to measure the dynamics of a single HQ cell of arbitrary cross section is developed.

1.7 Organization

This section summarizes the organization of this dissertation, which consists of four main Chapters. The analytical formulation of the liner in conjunction with the HQ tubes is developed in two parts. First, the mathematical tools for sound propagation and radiation in a lined duct with flow are derived in Chapter 2. This formulation is based in solving the convected acoustic wave equation in a lined duct with flow and the presence of point sources. This theory is then applied to the modeling of arrays of HQ tubes in a lined circular duct in Chapter 3. The modeling approach consists in developing formulations for the sound inside the duct and the HQ tubes separately, and then coupling both systems at the interfaces. The sound radiation of the HQ tubes is modeled using Green's functions.

The experimental validation of the model is presented in Chapter 4. As part of the research project, an HQ-Liner system was designed and tested on a scale engine rig at the Rolls Royce Ansty facility. The experiments were funded and performed by **Goodrich Corporation**. The rig configuration consisted of a 1/3 scale of the Rolls Royce Trent 500 turbofan engine. The main goal of these experiments was to demonstrate the potential of the HQ-Liner technology in a realistic environment. The experimental results were then provided by Goodrich in order to perform the model validation in Chapter 4. The HQ-Liner model was used to predict the noise attenuation of the broadband and BPF tone components for a few subsonic fan conditions. Then, the validation was performed by comparing the predictions with the experimental data.

Finally, Chapter 5 presents the conclusions of this investigation and future work to improve the model and design tools for HQ-Liner systems. The organization of this dissertation is presented in the chart of Figure 1.13.

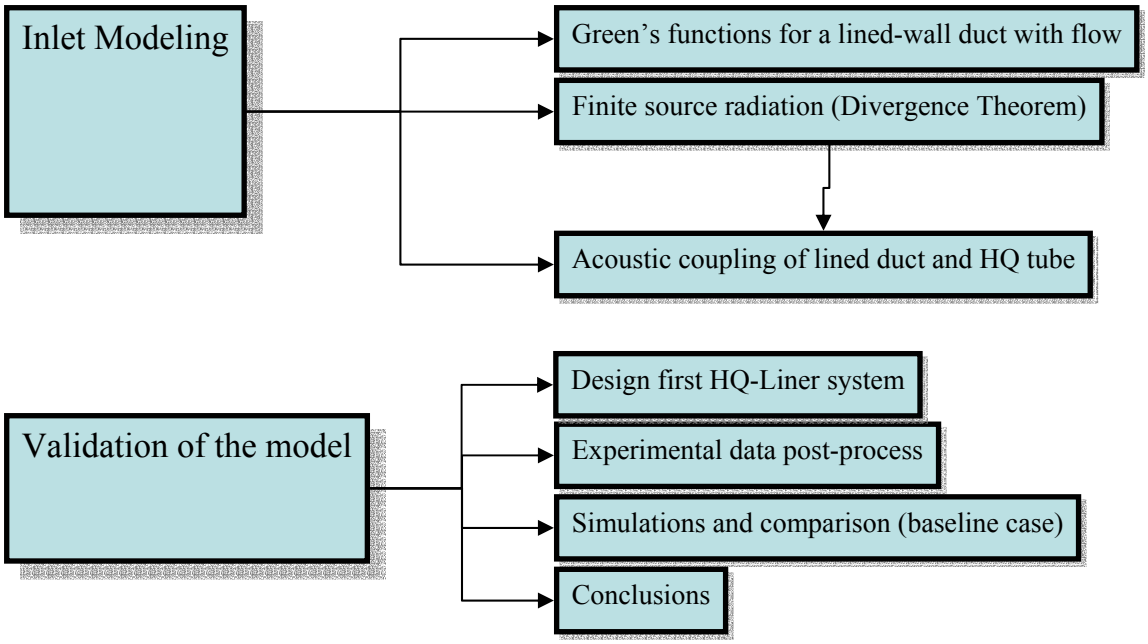

Figure 1.13: Organization of the dissertation.

Chapter 2 Sound Radiation in Lined Circular Ducts with Mean Flow

In this chapter, the theoretical formulation of sound radiation in a lined circular duct with mean flow is presented. This formulation is the mathematical foundation for the development of a model to simulate the effect of the HQ-Liner system on the propagation of sound in the lined duct. As illustrated in Figure 2.1, the HQ tubes work as resonators radiating sound into the duct; and the vibration of the fluid at the open ends of these resonators can be represented by a sector of the duct wall as a moving boundary. Therefore, the problem consists of finding the sound field in the lined duct generated by the motion of a finite boundary.

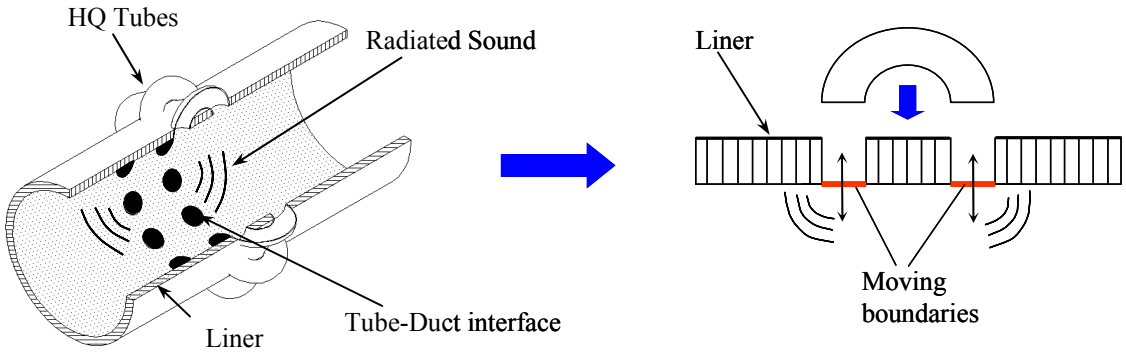

Figure 2.1: Schematic of HQ-Liner analytical formulation.

The radiated sound from these moving boundaries can be expressed in terms of the Green's function for the convected acoustic wave equation inside the lined duct. This function was previously investigated using the wavenumber transform (WT) approach [38], but only an **approximate** closed form solution was found. Although a numerical

solution can also be found by using the WT method, it would be impractical for the case of HQ tube modeling. Therefore, this Chapter is concentrated on developing **an exact closed form expression for the Green's function, which is an original contribution of this dissertation.** In addition, the model of the HQ-Liner will be presented in Chapter 3.

The approach to find the closed form Green's function is based on the modal expansion method. This approach is illustrated in Figure 2.2. The first step consists in formulating the homogenous problem and solve for the lined duct propagating modes (eigenfunctions). This process involves the derivation of the soft wall boundary condition equation as well as an efficient scheme to compute the eigenvalues. To this end, the eigenvalue problem is presented first in Section 2.1.

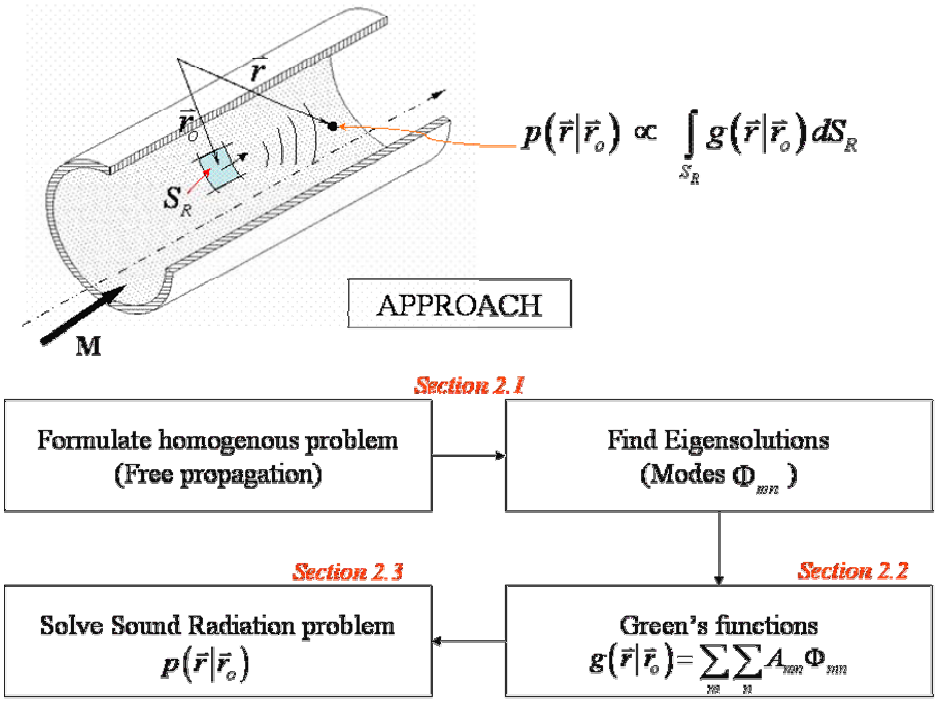

Figure 2.2: Schematic of sound radiation formulation approach.

Since the problem is linear, the Green's function can be expressed as a superposition of the propagating modes inside the duct. Therefore, **the exact closed form solution is derived in terms of a series expansion of the obtained eigenfunctions**, as presented in Section 2.2. Later, the solution will be extended to the radiation of sound from a finite portion of moving boundary by using the Divergence Theorem. This integration is correctly derived to account for the effect of the flow and it is presented in

Section 2.3. Finally, the power computation formula for the radiated sound from the moving boundaries is derived in Section 2.4.

2.1 The eigenvalue problem

In this section, the expression that describes the propagation of sound inside a lined circular duct as a linear expansion of the acoustic modes is presented. To this end, the eigenvalue problem is formulated in order to find these acoustic modes that represent the sound field propagating in the duct. Figure 2.3 presents a schematic of the lined circular duct to be investigated. The duct is assumed to be embedded in a liner with locally reactive impedance and infinite in the axial z-direction. The flow inside the duct is considered to be perfectly uniform, i.e. no radial variation. Also, it is assumed that the boundary layer does not affect the propagation of sound inside the duct and is therefore disregarded.

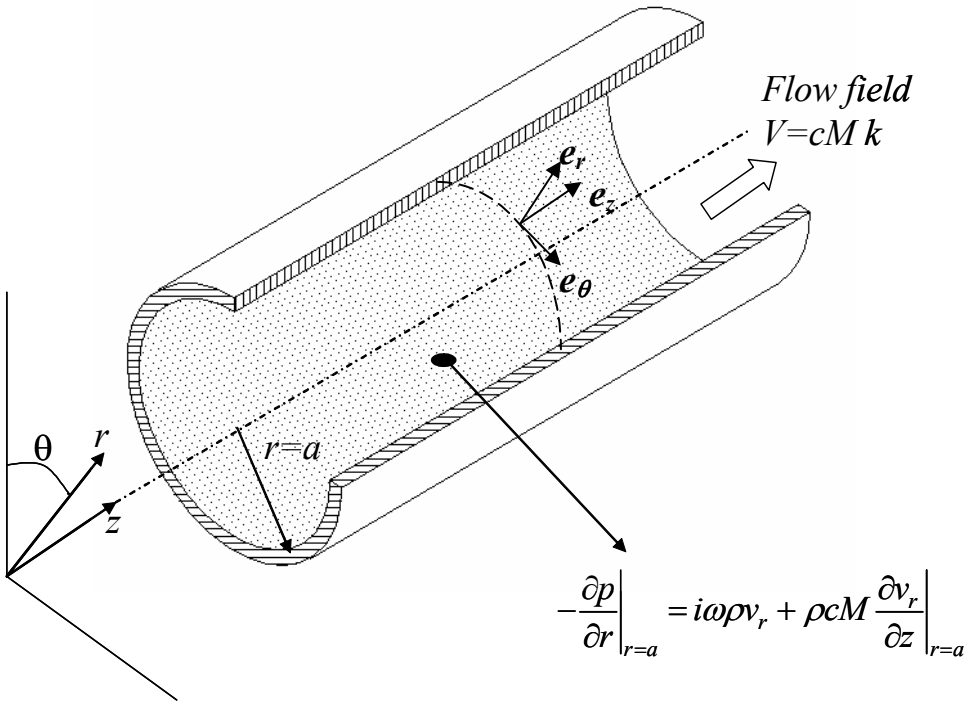

Figure 2.3: Infinite circular duct with soft walls and uniform flow. Definition of coordinate system.

The sound field that propagates inside the duct is obtained by solving the homogeneous acoustic wave equation in a moving media [22]:

$$\nabla^2 p = \frac{1}{c^2}\left(\frac{\partial}{\partial t} + \vec{V}\cdot\nabla\right)^2 p \tag{2.1}$$

where $\nabla^2(.)$ is the Laplacian operator in cylindrical coordinates, $p(r,\theta,z)$ is the acoustic pressure, c is the speed of sound, and $\vec{V}$ is the flow velocity vector. In order to derive the boundary condition at the wall of the lined duct, the equilibrium equation will also be considered as [22]

$$-\nabla p = \rho\left(\frac{\partial}{\partial t} + \vec{V}\cdot\nabla\right)\vec{v} \tag{2.2}$$

where $\nabla(.)$ is the gradient operator in cylindrical coordinates, ρ is the fluid density, and $\vec{v}$ is the acoustic particle velocity vector, i.e. $\vec{v} = (v_r, v_\theta, v_z)$. Assuming the uniform flow field in the positive z-direction, i.e. $\vec{V} = cM\,\vec{e}_z$, and considering harmonic motion of the form $e^{i\omega t}$, equation (2.1) and (2.2) in cylindrical coordinates become (*see Figure 2.3*)

$$\frac{\partial^2 p}{\partial r^2} + \frac{1}{r}\frac{\partial p}{\partial r} + \frac{1}{r^2}\frac{\partial^2 p}{\partial \theta^2} + \frac{\partial^2 p}{\partial z^2} = -k_o^2 p + 2iMk_0\frac{\partial p}{\partial z} + M^2\frac{\partial^2 p}{\partial z^2} \tag{2.3}$$

where k_o is the acoustic free wavenumber, and

$$\begin{aligned} -\frac{\partial p}{\partial r} &= i\omega\rho v_r + \rho cM\frac{\partial v_r}{\partial z} \\ -\frac{1}{r}\frac{\partial p}{\partial \theta} &= i\omega\rho v_\theta + \rho cM\frac{\partial v_\theta}{\partial z} \\ -\frac{\partial p}{\partial z} &= i\omega\rho v_z + \rho cM\frac{\partial v_z}{\partial z} \end{aligned} \tag{2.4}$$

respectively. The solution to the partial differential equation (2.3) is assumed to be separable and propagating in the infinite z-direction as

$$p(r,\theta,z,t) = \Phi(r,\theta)e^{-ik_z z}\;e^{i\omega t} \tag{2.5}$$

where k_z is the propagating constant, i.e. axial wavenumber. Note that the time dependant term $e^{i\omega t}$ will not be shown in the remaining derivations. Replacing (2.5) into (2.3) gives

$$-k_z\Phi+\frac{\partial^2\Phi}{\partial r^2}+\frac{1}{r}\frac{\partial\Phi}{\partial r}+\frac{1}{r^2}\frac{\partial^2\Phi}{\partial\theta^2}=-k_o^2\Phi+2Mk_0k_z\Phi+M^2k_z^2\Phi \tag{2.6}$$

where the term e^{-ik_zz} cancels out. Reordering equation (2.6) gives

$$\frac{\partial^2\Phi}{\partial r^2}+\frac{1}{r}\frac{\partial\Phi}{\partial r}+\frac{1}{r^2}\frac{\partial^2\Phi}{\partial\theta^2}+\left\{k_o^2-k_z^2\left(1-M^2\right)-2k_0k_zM\right\}\Phi=0 \tag{2.7}$$

To find $\Phi(r,\theta)$, it is required to satisfy (2.7) and the duct wall boundary condition. This boundary condition can be derived by imposing the equilibrium equation (2.4) at the wall in the radial direction as follows (*see Figure 2.3*)

$$-\left.\frac{\partial p}{\partial r}\right|_{r=a}=i\omega\rho v_r(a,\theta)+\rho cM\left.\frac{\partial v_r}{\partial z}\right|_{r=a} \tag{2.8}$$

where $v_r(r,\theta,z)$ is the acoustic particle velocity in the *r*-direction and assumed to also take the form $v_r(r,\theta,z)=v_r(r,\theta)e^{-ik_zz}$. Assuming the solution as in equation (2.5), the equilibrium condition in terms of $\Phi(r,\theta)$ becomes

$$-\left.\frac{\partial\Phi}{\partial r}\right|_{r=a}=i\rho c\left(k_0-Mk_z\right)v_r(a,\theta) \tag{2.9}$$

The particle velocity at the wall $v_r(a,\theta)$ is obtained by matching the particle displacement in the *r*-direction inside the liner and in the duct at *r* = *a* as described by Ko [29]. As illustrated in Figure 2.4, the fluid inside the liner is separated from the duct by a moving shear layer produced by the flow. In the liner side, the air particles move perpendicular to the liner surface while, in the duct side, they are also convected by the flow. Consequently, the particle velocity will present a discontinuity at the location of this shear layer and the correct matching condition is obtained using the particle displacement. That is, matching the radial displacement across the shear layer leads to

$$\frac{v^{\ell}}{i\omega} = \frac{v_r}{i\omega\left(1 - M\frac{k_z}{k_o}\right)} = \frac{v_r}{i\omega(k_o - Mk_z)/k_o} \tag{2.10}$$

where v^{ℓ} is the particle velocity in the liner.

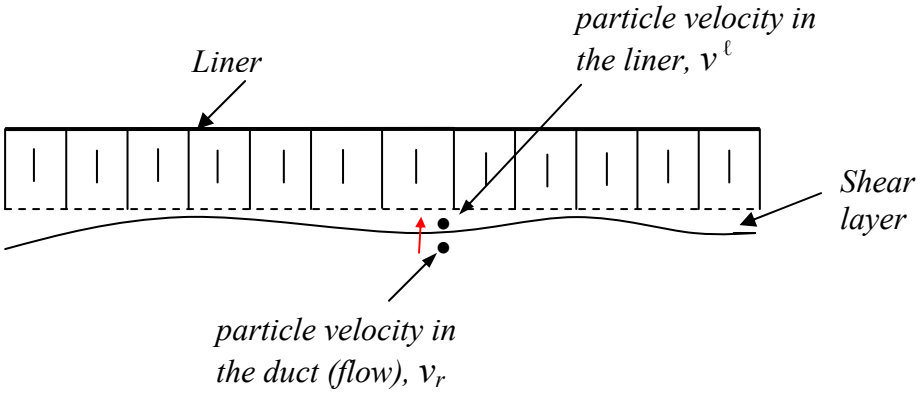

Figure 2.4: Particle velocities inside and outside the shear layer.

The soft wall properties of a locally reactive liner are characterized by the impedance Z_w. The impedance is commonly written in terms of the specific admittance β_w as

$$Z_w = \frac{\rho c}{\beta_w} \tag{2.11}$$

The particle velocity and the pressure in the liner surface are related through the "locally reacting" liner specific admittance as

$$v^{\ell} = \frac{p^{\ell}}{Z_w} = \beta_w \frac{p^{\ell}}{\rho c} \tag{2.12}$$

where p^{ℓ} is the pressure in the liner. Then, combining eqs. (2.10) with (2.12) and setting $p = p^{\ell}$, i.e. matching pressure, the particle velocity is given by

$$v_r(a,\theta) = \frac{\beta_w}{\rho c}\frac{(k_o - k_z M)}{k_o}\Phi(a,\theta) \tag{2.13}$$

Then, replacing (2.13) into (2.9) yields the boundary condition for $\Phi(r,\theta)$ as [32, 38]

$$\left.\frac{\partial \Phi}{\partial r}\right|_{r=a} = -i\beta_w \frac{\left(k_0 - k_z M\right)^2}{k_0} \Phi\big|_{r=a} \tag{2.14}$$

The same equation for the boundary condition can be derived using the formulation of Myers [51] and considering that the flow is inviscid. Thus, the solution $\Phi(r,\theta)$ needs to satisfy (2.7) and the boundary condition (2.14). To this end, assume it is separable as the product of two functions as follows

$$\Phi(r,\theta) = \Theta(\theta) \cdot R(r) \tag{2.15}$$

where $\Theta(\theta)$ satisfies the periodic condition

$$\Theta(\theta) = \Theta(\theta + 2m\pi) \qquad m = 0,1,2,..... \tag{2.16}$$

Replacing (2.15) into (2.7) and multiplying by $r^2 / R(r)\Theta(\theta)$ gives

$$\frac{r^2}{R}\left(\frac{d^2R}{dr^2} + \frac{1}{r}\frac{dR}{dr}\right) + \frac{1}{\Theta}\frac{d^2\Theta}{d\theta^2} + r^2 k_{mn}^2 = 0 \tag{2.17}$$

where

$$k_{mn}^2 = k_o^2 - k_z^2(1 - M^2) - 2k_o k_z M \tag{2.18}$$

Replacing (2.15) into the boundary condition in (2.14) leads to

$$\left.\frac{\partial R}{\partial r}\right|_{r=a} = -i\beta_w \frac{\left(k_0 - k_z M\right)^2}{k_0} R\big|_{r=a} \tag{2.19}$$

The solution to (2.17) implies that

$$\frac{1}{\Theta}\frac{d^2\Theta}{d\theta^2} = -m^2 \tag{2.20}$$

and

$$\frac{r^2}{R}\left(\frac{d^2R}{dr^2} + \frac{1}{r}\frac{dR}{dr}\right) - m^2 + r^2 k_{mn}^2 = 0 \tag{2.21}$$

where m^2 is a constant and equation (2.21) is the well known Bessel's equation of m^{th} order.

The differential equation in (2.20) with the periodic condition in (2.16) results in a solution of the form

$$\Theta(\theta) = A\cos(m\theta) + B\sin(m\theta) \qquad m = 1, 2, 3, ... \tag{2.22}$$

which it can also be written in the form of spinning modes as

$$\Theta(\theta) = Ae^{im\theta} + Be^{-im\theta} \qquad m = 1, 2, 3, ... \tag{2.23}$$

On the other hand, the solutions to equation (2.21) are the m^{th} order Bessel functions as

$$R(r) = CJ_m(k_{mn}r) + DY_m(k_{mn}r) \tag{2.24}$$

where $J_m(.)$ is the first kind $Y_m(.)$ is the second kind or Neumann's function and C and D are unknown constants. Because Y_m has a singularity at the origin, D is set to zero, i.e. the solution must be bounded in the domain. Thus, equation (2.24) can be written as

$$R(r) = CJ_m(k_{mn}r) \tag{2.25}$$

The replacement of (2.25) into (2.19) yields the characteristic equation to solve for the eigenvalues k_{mn} that give a possible solution to the problem. That is

$$i\beta_w \frac{(k_o - Mk_z)^2}{k_o} J_m(k_{mn}a) = -k_{mn}J'_m(k_{mn}a) \tag{2.26}$$

In the presence of flow, i.e. $M \neq 0$, this characteristic equation depends on the value of k_z, which is obtained from (2.18). That is, from

$$k_{mn}^2 = k_o^2 - k_z^2(1 - M^2) - 2k_o k_z M \tag{2.18}$$

the two values for k_z are

$$k_z^{(+)} = \frac{-k_0 M + \sqrt{k_0^2 - (1 - M^2)k_{mn}^2}}{(1 - M^2)} \tag{2.27a}$$

$$k_z^{(-)} = \frac{-k_0 M - \sqrt{k_0^2 - (1 - M^2)k_{mn}^2}}{(1 - M^2)} \tag{2.27b}$$

where $k_z^{(+)}$ and $k_z^{(-)}$ correspond to positive and negative *z*-direction propagating waves. This implies that the value of k_{mn} and $J_m(.)$ will also depend on the direction of wave propagation. Thus, the equation (2.26) has to be solved for both positive and negative propagation directions as

$$i\beta_w \frac{\left(k_o - Mk_z^{(+)}\right)^2}{k_o} J_m\left(k_{mn}^{(+)}a\right) = -k_{mn}^{(+)} J'_m\left(k_{mn}^{(+)}a\right) \tag{2.28a}$$

where $k_z^{(+)}$ is obtained by replacing $k_{mn}^{(+)}$ into (2.18), and

$$i\beta_w \frac{\left(k_o - Mk_z^{(-)}\right)^2}{k_o} J_m\left(k_{mn}^{(-)}a\right) = -k_{mn}^{(-)} J'_m\left(k_{mn}^{(-)}a\right) \tag{2.28b}$$

where $k_z^{(-)}$ is obtained by replacing $k_{mn}^{(-)}$ into (2.18).

Finally, the solution for the acoustic modes is

$$\Phi_{mn}^{(+)}(r,\theta) = A_{mn}^{(+)}\Theta(\theta) J_m\left(k_{mn}^{(+)}r\right) \tag{2.29a}$$

$$\Phi_{mn}^{(-)}(r,\theta) = A_{mn}^{(-)}\Theta(\theta) J_m\left(k_{mn}^{(-)}r\right) \tag{2.29b}$$

for positive and negative *z*-direction propagation, respectively. The constants $A_{mn}^{(+)}$ and $A_{mn}^{(-)}$ are unknown modal amplitudes while the function $\Theta(\theta)$ will take either the form in (2.22) or (2.23). The values $k_{mn}^{(+)}$ and $k_{mn}^{(-)}$ are the mode wavenumber for the positive and negative propagating modes, respectively. For the case of the lined duct with flow, the wavenumbers $k_{mn}^{(+)}$ and $k_{mn}^{(-)}$ are complex and depend upon frequency.

In general, the sound field in the lined circular duct with flow is expressed as a linear combination of the acoustic modes present in the duct as follows

$$p\left(\vec{r}\right) = \sum_m \sum_n A_{mn}^{(+)}\Phi_{mn}^{(+)}(r,\theta) e^{-ik_z^{(+)}z} e^{i\omega t} + \sum_m \sum_n A_{mn}^{(-)}\Phi_{mn}^{(-)}(r,\theta) e^{-ik_z^{(-)}z} e^{i\omega t} \tag{2.30}$$

where the superscripts (+) and (-) indicate variables associated to positive and negative z-direction propagation, respectively. The subscripts m and n refer to the circumferential and radial mode order, respectively.

2.1.1 Solution of the eigenvalue problem

This section describes the technique for the solution of the eigenvalue problem in equations (2.27) and (2.28). The procedure to find a numerical solution to this problem is certainly not an easy task because of the nature of the transcendental equation (2.28). As presented in the previous section, this equation is complex valued and it depends on the complex axial wavenumber k_z, which is also a non-linear function of k_{mn}. Consequently, the proper technique to be chosen requires having good numerical stability as well as computational efficiency. Then, the objective of this section is to find the mode eigenvalues $k_{mn}^{(+)}$ and $k_{mn}^{(-)}$ that define the solutions in (2.29) and, thus, the mode propagation inside the lined duct. The propagation of each mode in the duct depends directly on the mode eigenvalues $k_{mn}^{(+)}$ and $k_{mn}^{(-)}$. Indeed, the mode axial wavenumber is given by

$$k_z^{(+)} = \frac{-k_0 M + \sqrt{k_0^2 - \left(1-M^2\right)k_{mn}^2}}{\left(1-M^2\right)} \tag{2.27a}$$

$$k_z^{(-)} = \frac{-k_0 M - \sqrt{k_0^2 - \left(1-M^2\right)k_{mn}^2}}{\left(1-M^2\right)} \tag{2.27b}$$

It is important to note that for the hard wall case the mode eigenvalues $k_{mn}^{(+)}$ and $k_{mn}^{(-)}$ are the same and furthermore real. Thus, the square root terms in (2.27) are either real or imaginary indicating that the mode is either propagating (cut-on) or decaying (cut-off), respectively [17]. The mode cut-on frequency is the boundary between these two conditions, i.e. obtained from setting the square root term to zero. Also, the sign of the square root assigned to either direction of propagation is easily determined from considering that the mode amplitudes must be bounded.

As mentioned in the previous section, the lined wall case characteristic equation with flow needs to be solved for each direction of propagation. The reason of this requirement is that the characteristic equations (2.28) depend on both the mode eigenvalues and the mode axial wavenumbers. Moreover, the fact that the equations (2.28) are complex valued always leads to having complex valued eigenvalues. Thus, the square root term in equations (2.27) is also always complex. In this case, the cut-on frequency is not defined. The approach to select the sign of the complex square root terms is obtained so as to have decaying propagating modes. The decay rate of each mode will be given by the exponential term $e^{-i(k_z)z}$ in equation (2.30). If the wavenumber k_z is complex, the exponential term can be factored as

$$e^{-i(k_z)z} = e^{-i(\mathrm{Re}[k_z])z} \cdot e^{(\mathrm{Im}[k_z])z}$$

where the complex factor determines the propagation, and the real factor determines the decay rate of the mode. Figure 2.5 presents a schematic of a typical decaying mode inside a lined duct. Decaying waves will take place only if the exponent $\{\mathrm{Im}[k_z]\cdot z\}$ is negative. This condition will be satisfied when $\mathrm{Im}[k_z]$ is negative for positive propagating modes and $\mathrm{Im}[k_z]$ is positive for negative propagating modes, respectively.

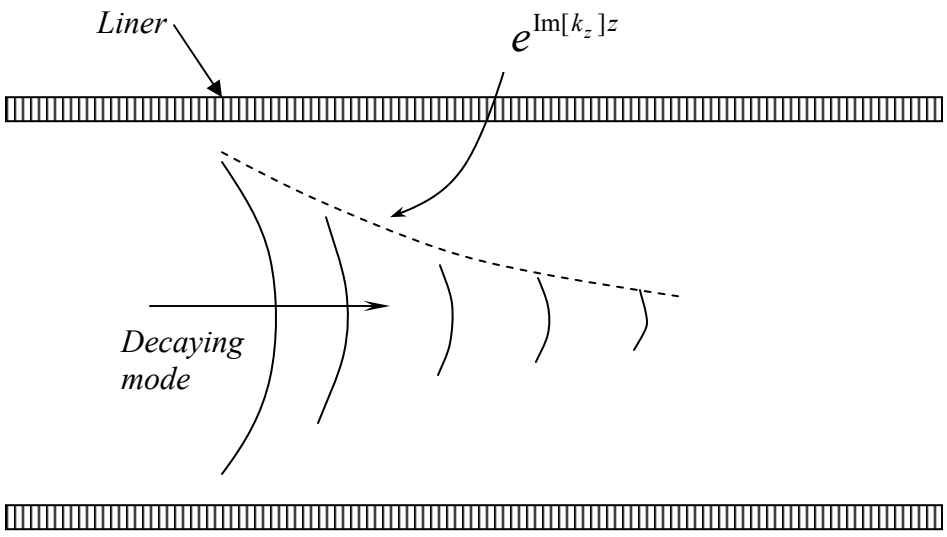

Figure 2.5: Schematic of a decaying mode inside a lined-wall duct.

The sign of the imaginary part of the wavenumbers k_z depends directly on the sign preceding the square root as well as the sign of the imaginary part of the square root itself. In addition to this, as this square root term can take two values, i.e. one is the negative of the other one, only one must be considered. As a convention, the root with negative $\mathrm{Im}\left[\sqrt{k_0^2-\left(1-M^2\right)k_{mn}^2}\right]$ is always chosen. In this way, the positive and negative sign is conveniently assigned according to the direction of propagation as

$$k_z^{(+)}=\frac{-k_0M+\sqrt{k_0^2-\left(1-M^2\right)k_{mn}^{(+)2}}}{\left(1-M^2\right)} \qquad \textit{Positive propagating}$$

$$k_z^{(-)}=\frac{-k_0M-\sqrt{k_0^2-\left(1-M^2\right)k_{mn}^{(-)2}}}{\left(1-M^2\right)} \qquad \textit{Negative propagating}$$

In summary, the positive sign is assigned to the positive traveling mn^{th} mode, i.e. $k_z^{(+)}$; and the negative sign corresponds to the negative traveling mn^{th} mode, i.e. $k_z^{(-)}$. Note that this analysis is also valid for the no flow case with the simplification that the mode eigenvalues $k_{mn}^{(+)}$ and $k_{mn}^{(-)}$ are the same.

Once the axial wavenumbers have been correctly identified, equations (2.28) can be solved separately for each direction of propagation. As the eigenvalues $k_{mn}^{(+)}$ and $k_{mn}^{(-)}$ cannot be obtained explicitly from these equations, a numerical technique was implemented, i.e. the simplex method. This technique allows to find the minimum of a multivariable real function based on an approximate initial guess and without the need for derivatives. Thus, in order to apply this method to the eigenvalue problem, equations (2.28) need to be rearranged in the form of a positive real valued equation as follows

$$\left|k_{mn}^{(+)}J_m'\left(k_{mn}^{(+)}a\right)+i\beta_w\frac{\left(k_0-k_z^{(+)}M\right)^2}{k_0}J_m\left(k_{mn}^{(+)}a\right)\right|=0 \qquad (2.31)\text{a}$$

$$\left|k_{mn}^{(-)}J_m'\left(k_{mn}^{(-)}a\right)+i\beta_w\frac{\left(k_0-k_z^{(-)}M\right)^2}{k_0}J_m\left(k_{mn}^{(-)}a\right)\right|=0 \qquad (2.31)\text{b}$$

In this way, the zeros of the characteristic equation are found by minimizing the absolute value of the equations in (2.31). It is important to note that each one of the complex unknowns $k_{mn}^{(+)}$ and $k_{mn}^{(-)}$ are also separated in their real and imaginary components as

$$k_{mn}^{(+)} = \mathrm{Re}\left[k_{mn}^{(+)}\right] + i\,\mathrm{Im}\left[k_{mn}^{(+)}\right] = X^{(+)} + i\,Y^{(+)} \tag{2.32a}$$

$$k_{mn}^{(-)} = \mathrm{Re}\left[k_{mn}^{(-)}\right] + i\,\mathrm{Im}\left[k_{mn}^{(-)}\right] = X^{(-)} + i\,Y^{(-)} \tag{2.32b}$$

Thus, the real valued equations (2.31) are solved for the two independent unknowns, i.e. X and Y, which will finally lead to the mode eigenvalues and axial wavenumbers.

As mentioned above, the numerical technique, i.e. the simplex method, needs an approximate initial guess to find the zeros of the real valued equation. The approach taken to find this approximate initial guess is to solve the equation continuously from very low frequencies and up to the desired frequency of calculation. The initial guess for every mode at the first point of calculation, i.e. at very low frequency, is the hard wall eigenvalue. This approximation can be done due to the fact that the liner impedance at very low frequency is very large and thus very close to a hard wall condition. Then, the eigenvalues for this very low frequency must also be close to the hard wall case which is trivial to compute. Once the eigenvalues are computed, they will be considered as initial guess for the next point of calculation. Figure 2.6 presents the typical solution of k_{mn} obtained for a fixed m order. As shown in this figure, the eigenvalues approach the real axis for low frequencies, i.e. hard wall solutions, and describe a pattern in the complex plane as a function of frequency. The arrows inside every "lobe" show the increasing direction of the frequency parameter. A common problem associated with this solution is that the mode shapes become complex-valued functions which are difficult to identify as physical modes. Nevertheless, the advantage of computing the zeros of the characteristic equations (2.28) with this proposed technique is that the location as a function of frequency of a single eigenvalue in the complex plane can be identified and tracked. Then, it is very easy to associate the mode order to all the eigenvalues based on the order of the hard wall eigenvalues. Another problem of main concern can arise when two eigenvalue solutions get very close to each other and the solutions "jumps" from one mode to the other. This situation is indicated in Figure 2.6 and it is a critical problem. It

was determined that using a very small frequency step in these regions can overcome this problem.

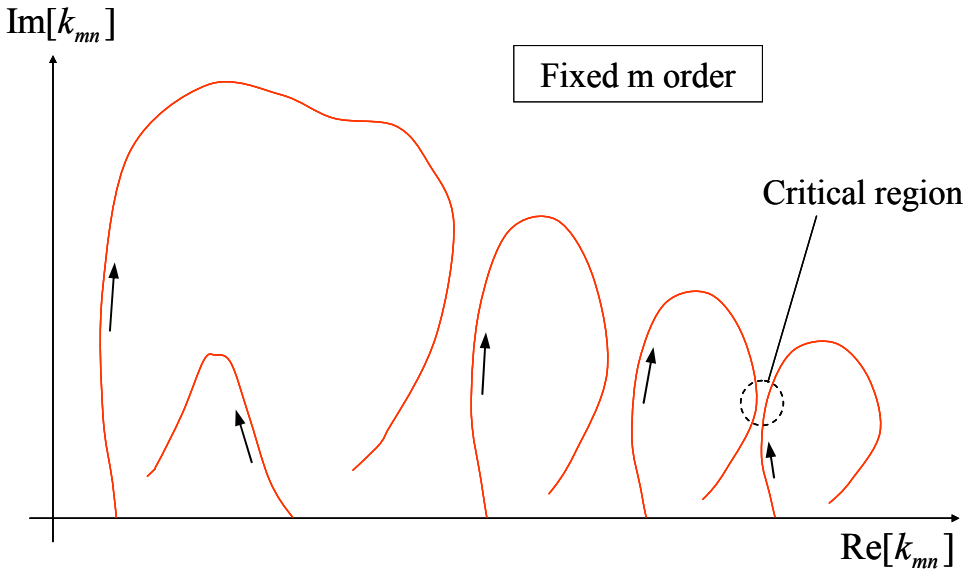

Figure 2.6: Schematic of typical eigenvalue solution for a soft wall circular duct.

2.2 Green's Functions

The solution of the non-homogenous convected wave equation is presented in this section in terms of the Green's functions. Indeed, the Green's function represents the radiated sound field due to the presence of a point source inside the duct. The method to find the Green's function is based in assuming the solution to be a linear combination of the propagating modes inside the ducts, i.e. **modal expansion approach**. The application of this method to solve this problem is **a novel contribution of this dissertation**. This new solution is then compared to the one obtained with the wavenumber transform method [38, 49]. The main advantages and drawbacks of both methods are discussed.

The Green's function is derived in closed form for the case of a source located on the wall of the lined circular duct with flow, $\vec{r}_o = (a, \theta_o, z_o)$. Then, the solution can be extended to a finite region applying the Divergence Theorem. In this process, the solution of the adjoint problem is needed. Thus, the derivation of the adjoint Green's functions is also presented in this section.

2.2.1 Modal Expansion Approach

The Green's functions are the solution to the Laplace transformed non-homogeneous wave equation in cylindrical coordinates under the soft wall boundary condition and uniform flow. That is

$$\frac{\partial^2 g}{\partial r^2}+\frac{1}{r}\frac{\partial g}{\partial r}+\frac{1}{r^2}\frac{\partial^2 g}{\partial \theta^2}+\frac{\partial^2 g}{\partial z^2}\left(1-M^2\right)-2iMk_0\frac{\partial g}{\partial z}+k_0^2 g=\frac{1}{r}\delta(\vec{r}\,|\vec{r}_o) \tag{2.33}$$

under the soft wall boundary condition [38]:

$$\left.\frac{\partial g}{\partial r}\right|_{r=a}=-i\beta_w\frac{\left(k_0-k_z M\right)^2}{k_0}g \tag{2.34}$$

where g is the sought Green's function, $\vec{r}_o=(r_0,\theta_0,z_0)$ is the location of the simple source, and $\delta(\vec{r}\,|\vec{r}_o)=\delta(r-r_0)\delta(\theta-\theta_0)\delta(z-z_0)$ is the delta Dirac function. The solution to equations (2.33) and (2.34) was previously investigated by Zorumski [38] using approximations with series of circumferential inverse Fourier transforms denoted as wavenumber transform (WT) technique. The approach taken here is based on the modal (eigenfunctions) expansion method similar to the hard wall case [17]. One of the main advantages of this method is that it is possible to explicitly satisfy that the Green's function is continuous at the source location plane. Another benefit is that the formulation is simpler and provides a closed form solution. A comparison of the modal expansion and WT methods will be presented in section 2.2.2.

The solution to equations (2.33) and (2.34) is assumed as a linear combination of the acoustic modes inside the duct. In the case of the hard wall duct, the mode shapes are independent of the direction of propagation which results in a straight forward formulation that leads to a well-known solution [17]. On the contrary, according to Section 2.1, the acoustic modes in the soft wall duct with flow have different expressions depending on the direction of propagation (*see equation (2.29)*). Figure 2.7 illustrates the approach that requires expressing the solution as two functions depending on the propagation field, i.e. $g^{(+)}$ and $g^{(-)}$. Therefore, depending on the relative location

between the observer and the point source at z_0 , the Green's function is expressed as follows

$$g^{(+)}\left(\vec{r}\,|\vec{r}_o\right)=\sum_{m=0}^{M}\sum_{n=0}^{N}A_{mn}^{(+)}\Phi_{mn}^{(+)}e^{-ik_z^{(+)}(z-z_0)} \qquad z>z_0$$
$$g^{(-)}\left(\vec{r}\,|\vec{r}_o\right)=\sum_{m=0}^{M}\sum_{n=0}^{N}A_{mn}^{(-)}\Phi_{mn}^{(-)}e^{-ik_z^{(-)}(z-z_0)} \qquad z<z_0 \tag{2.35}$$

where M and N are the maximum number of terms to be included in the expansion, i.. number of acoustic modes to use in the expansion.

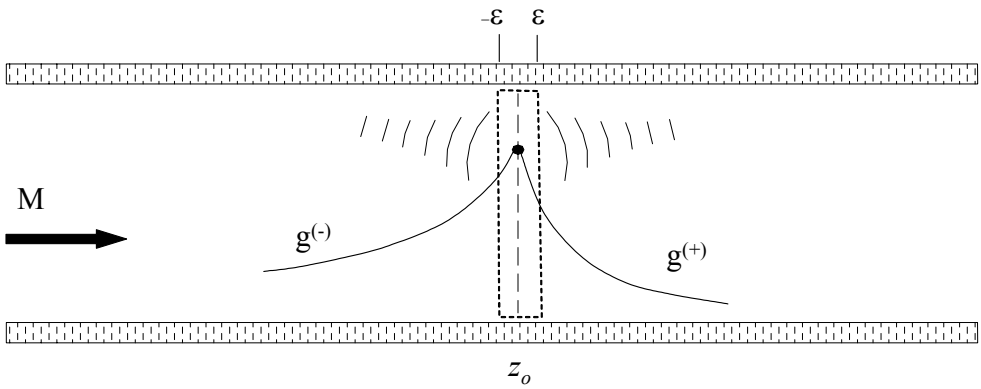

Figure 2.7: Solution of Green's function in the positive and negative propagating fields – Condition of continuity in a small volume near the source at z_o.

A critical step in the derivation is to define the sought solution as a single continuous function in the spatial domain. To this end, the Green's functions is expressed with the help of the Heaviside function $H\left(z-z_0\right)$ (i.e. $H\left(z\right)=1\ (z>0)$; $H\left(z\right)=0\ (z<0)$ and $H\left(0\right)=1/2$) as follows

$$g\left(\vec{r}\,|\vec{r}_0\right)=g^{(+)}\left(\vec{r}\,|\vec{r}_o\right)H\left(z-z_0\right)+g^{(-)}\left(\vec{r}\,|\vec{r}_o\right)\left[1-H\left(z-z_0\right)\ \right] \tag{2.36}$$

For the Green's functions, the mode shapes are selected to have the form

$$\Phi_{mn}^{(+)}\left(r,\theta\right)=\cos\left[m\left(\theta-\theta_o\right)\right]J_m\left(k_{mn}^{(+)}r\right) \tag{2.37a}$$

$$\Phi_{mn}^{(-)}\left(r,\theta\right)=\cos\left[m\left(\theta-\theta_o\right)\right]J_m\left(k_{mn}^{(-)}r\right) \tag{2.37b}$$

The problem is now reduced to find the modal amplitudes $A_{mn}^{(+)}$ and $A_{mn}^{(-)}$ that define the Green's functions in (2.35). This task involves the use of two required conditions:

- Discontinuity in the slope of the Green's function
- Continuity of the Green's function.

at the source location $z = z_o$.

Condition 1: ***Discontinuity in the slope of the Green's function.***

The first condition is to impose the discontinuity in the slope at the point source location. For the sake of clarity, a compact notation is used for the linear operator $L(.) = \frac{\partial^2(.)}{\partial r^2} + \frac{1}{r}\frac{\partial(.)}{\partial r} + \frac{1}{r^2}\frac{\partial^2(.)}{\partial \theta^2}$, which does not depend on the z coordinate. Then equation (2.33) can be rewritten as:

$$k_0^2 g + L(g) + \frac{\partial^2 g}{\partial z^2}\left(1-M^2\right) - 2iMk_0\frac{\partial g}{\partial z} = \delta(r-r_0)\frac{\delta(\theta-\theta_0)}{r}\delta(z-z_0) \qquad (2.38)$$

Replacing equation (2.36) into (2.38) yields:

$$\begin{aligned}
&\left(k_0^2 + L\right)\left[g^{(+)}H\left(z-z_0\right) + g^{(-)}\left[1-H\left(z-z_0\right)\right]\right] \\
&+\left(1-M^2\right)\frac{\partial^2}{\partial z^2}\left[g^{(+)}H\left(z-z_0\right) + g^{(-)}\left[1-H\left(z-z_0\right)\right]\right] \\
&-2iMk_0\frac{\partial}{\partial z}\left[g^{(+)}H\left(z-z_0\right) + g^{(-)}\left[1-H\left(z-z_0\right)\right]\right] = \frac{1}{r}\delta(\vec{r}|\vec{r}_0)
\end{aligned} \qquad (2.39)$$

Considering that the derivative of the Heaviside function is $H'(z-z_0) = \delta(z-z_0)$, equation (2.39) can be rearranged as follows

$$\begin{aligned}
&\left(k_0^2 + L\right)\left[g^{(+)}H\left(z-z_0\right) + g^{(-)}\left[1-H\left(z-z_0\right)\right]\right] + \left(1-M^2\right)\left[\frac{\partial^2 g^{(+)}}{\partial z^2}H\left(z-z_0\right) + \frac{\partial^2 g^{(-)}}{\partial z^2}\left[1-H\left(z-z_0\right)\right] + \right. \\
&\left. + 2\left(\frac{\partial g^{(+)}}{\partial z} - \frac{\partial g^{(-)}}{\partial z}\right)\delta\left(z-z_0\right) + \left(g^{(+)} - g^{(-)}\right)\delta'\left(z-z_0\right)\right] - \\
&-2iMk_0\left[\frac{\partial g^{(+)}}{\partial z}H\left(z-z_0\right) + \frac{\partial g^{(-)}}{\partial z}\left[1-H\left(z-z_0\right)\right] + \left(g^{(+)} - g^{(-)}\right)\delta\left(z-z_0\right)\right] = \frac{1}{r}\delta(\vec{r}|\vec{r}_0)
\end{aligned} \qquad (2.40)$$

In order to find the modal amplitudes for the expressions in (2.35), equation (2.40) needs to be pre-multiplied by the acoustic modes defined in the complete domain as follows

$$\Phi_{er} = \Phi_{er}^{(+)} H\left(z - z_o\right) + \Phi_{er}^{(-)} \left[1 - H\left(z - z_o\right)\right]$$

and integrated over the small volume as shown in Figure 2.7. The axial dimension of this volume is defined as 2ε, where $\varepsilon \to 0$. After imposing continuity (*Condition 2*), solving the integral in the z coordinate, and taking the limit $\varepsilon \to 0$, it can be shown that most terms in equation (2.40) vanish. This procedure leads to

$$\int_0^a \int_0^{2\pi} \lim_{\varepsilon \to 0} \int_{z_o-\varepsilon}^{z_o+\varepsilon} \left(1 - M^2\right) \left\{ \left(\frac{\partial g^{(+)}}{\partial z} - \frac{\partial g^{(-)}}{\partial z} \right) \left(\Phi_{er}^{(+)} H(z - z_o) + \Phi_{er}^{(-)} \left[1 - H(z - z_o)\right] \right) \delta\left(z - z_0\right) \right\} dz \, r \, d\theta \, dr =$$

$$= \int_0^a \int_0^{2\pi} \lim_{\varepsilon \to 0} \int_{z_o-\varepsilon}^{z_o+\varepsilon} \left\{ \delta(r - r_o) \frac{\delta(\theta - \theta_o)}{r} \delta(z - z_o) \left(\Phi_{er}^{(+)} H(z - z_o) + \Phi_{er}^{(-)} \left[1 - H(z - z_o)\right] \right) \right\} dz \, r \, d\theta \, dr \tag{2.41}$$

Finally, replacing the expanded solution (2.35) into (2.41) and solving the integrals yields:

$$\sum_{n=0}^{N} \left\{ k_z^{(+)} A_{mn}^{(+)} \int_0^{2\pi} \int_0^a \left(\frac{\Phi_{mr}^{(+)} + \Phi_{mr}^{(-)}}{2} \right) \Phi_{mn}^{(+)} \, r \, d\theta \, dr - k_z^{(-)} A_{mn}^{(-)} \int_0^{2\pi} \int_0^a \left(\frac{\Phi_{mr}^{(+)} + \Phi_{mr}^{(-)}}{2} \right) \Phi_{mn}^{(-)} \, r \, d\theta \, dr \right\} =$$

$$= i \frac{\Phi_{mr}^{(+)}\left(r_0, \theta_0\right) + \Phi_{mr}^{(-)}\left(r_0, \theta_0\right)}{2\left(1 - M^2\right)} \qquad m = 0, 1, 2, 3, \ldots\ldots \tag{2.42}$$

where the factor 2 in the denominator of the right hand side appears as a consequence of solving the Dirac delta integral on the axial location of the source. Note that the orthogonality of the modes in the circumferential direction has been used in (2.42). However, the system of equations is fully coupled because the modes are not orthogonal in the radial direction.

The mathematical steps to arrive at equation (2.42) are very extensive and complex but the critical part of the derivations is presented here. For the sake of completeness, the detailed development of equation (2.42) is presented in Appendix F.

Condition 2: C*ontinuity of the Green's function.*

Equation (2.42) is a system of $m \times n$ equations with $2(m \times n)$ unknowns, i.e. the modal amplitudes $A_{mn}^{(+)}$ and $A_{mn}^{(-)}$. This is again because the positive traveling modal amplitudes are different from the negative traveling ones. The remaining set of $m \times n$ equations is obtained by explicitly imposing the continuity of the Green's function at $z = z_0$ as follows [52]:

$$g^{(+)}\Big|_{z=z_0} = g^{(-)}\Big|_{z=z_0} \tag{2.43}$$

It is important to remark that the formulation by Zorumski [38] does not explicitly impose the continuity condition as the formulation here in (2.43).

For this case, equation (2.43) is simply pre-multiplied by $(\Phi_{er}^{(+)} + \Phi_{er}^{(-)})/2$ and integrated over the duct cross section to yield

$$\sum_{n=0}^{N}\left\{ A_{mn}^{(+)} \int_0^{2\pi}\int_0^{a}\left(\frac{\Phi_{mr}^{(+)} + \Phi_{mr}^{(-)}}{2}\right)\Phi_{mn}^{(+)}\, r\, d\theta\, dr - A_{mn}^{(-)} \int_0^{2\pi}\int_0^{a}\left(\frac{\Phi_{mr}^{(+)} + \Phi_{mr}^{(-)}}{2}\right)\Phi_{mn}^{(-)}\, r\, d\theta\, dr \right\} = 0$$

$$m = 0,1,2,3,.....$$

(2.44)

Like the system in (2.42), this system of equations is fully coupled because the modes are not orthogonal in the radial coordinate.

The system of equations for the modal amplitudes $A_{mn}^{(\ell)}$ $\ell = +,-$ in (2.42) and (2.44) can be written in matrix form as

$$\left[\begin{array}{c|c} \left[\Lambda_{m,nr}^{(+)}\right]\left[k_z^{(+)}\right] & -\left[\Lambda_{m,nr}^{(-)}\right]\left[k_z^{(-)}\right] \\ \hline \left[\Lambda_{m,nr}^{(+)}\right] & -\left[\Lambda_{m,nr}^{(-)}\right] \end{array}\right] \left\{\begin{array}{c} A_{mn}^{(+)} \\ \hline A_{mn}^{(-)} \end{array}\right\} = \left\{\begin{array}{c} \psi_r \\ \hline \underline{0} \end{array}\right\} \tag{2.45}$$

$$m = 0,1,2,3,.....$$

where

$$\{\Psi_r\} = i\frac{\left(\Phi_{mr}^{(+)}(r_0,\theta_0) + \Phi_{mr}^{(-)}(r_0,\theta_0)\right)}{2\pi a^2\left(1-M^2\right)} \tag{2.46}$$

The matrices $\left[\Lambda^{(+)}_{m,nr}\right]$ and $\left[\Lambda^{(-)}_{m,nr}\right]$ are fully populated because the modes are not orthogonal in a lined duct with flow, and their components are defined by

$$\Lambda^{(+)}_{m,nr} = \frac{1}{\pi a^2}\int_0^{2\pi}\int_0^{a}\left(\frac{\Phi^{(+)}_{mr}+\Phi^{(-)}_{mr}}{2}\right)\Phi^{(+)}_{mn}\, r\, d\theta\, dr \tag{2.47a}$$

$$\Lambda^{(-)}_{m,nr} = \frac{1}{\pi a^2}\int_0^{2\pi}\int_0^{a}\left(\frac{\Phi^{(+)}_{mr}+\Phi^{(-)}_{mr}}{2}\right)\Phi^{(-)}_{mn}\, r\, d\theta\, dr \tag{2.47b}$$

On the other hand, matrices $\left[k_z^{(+)}\right]$ and $\left[k_z^{(-)}\right]$ are diagonal and contain the axial wavenumber for each mode. Note that equation (2.42) was divided by πa^2 and thus this term appears in the denominator of equations (2.46) and (2.47).

In the particular case of the hard wall duct, the formulation simplifies because the modes are orthogonal to each other and do not depend on the direction of propagation. For this reason, the normalization factors in (2.47) collapse in the same expression, which also vanish for $r \neq n$. Consequently, the system of equations in (2.45) becomes diagonal, leading to a direct formula for the Green's function modal amplitudes.

2.2.2 Validation of Green's functions using the Wavenumber Transform

The modal expansion approach for the Green's functions presented in the previous section is a new an unique contribution to the body of knowledge. In this section, the derived Green's function using the modal expansion approach is compared to the solution obtained using the classical wavenumber transform (WT) technique. This comparison is motivated by the need of verifying the validity of certain aspects of the newly developed formulation. In particular, the main concern that arises in the derivation using the modal expansion approach is related to the completeness of the solution. Given the nature of the characteristic equation (2.28), the homogeneous solutions (eigenfunctions) used to find the Green's function are not guaranteed to be complete. Therefore, there is a concern that the modal expansion method may not provide all the necessary information to reproduce the sound field originated by a point source. On the other hand, although its use will not be practical for the HQ modeling, the WT method guarantees the functional completeness of the homogenous solution in the wavenumber domain. Nevertheless, in the process of

recovering the spatial axial coordinate by the commonly used Theory of Residues, the solution requires the same eigenproperties as in the modal expansion approach. To avoid this problem, a numerical (not practical) integration will be used to find the WT solution in the spatial domain.

The application of the WT approach to find the Green's functions was previously investigated by Drischler [49] for the hard wall case and then extended to the lined wall case by Zorumski [38]. The WT method consists of a completely different approach to find the solution to the problem. One of the main differences from the modal expansion method is that the continuity of the Green's function at the source plane is not explicitly imposed. In addition, the eigenvalue problem for the WT method has to be formulated in the wavenumber domain and has to be solved independently for every value of the wavenumber variable $\hat{k}_z$. However, since the two different methods are used to solve the same problem it is expected to arrive to a similar solution.

As in the previous section, the Green's function is obtained as the solution of the non-homogeneous convected wave equation in cylindrical coordinates given in equation (2.33). The application of the WT method to find the solution is presented in detail in Appendix D. In summary, the Green's function is obtained as the solution of the following integral equation as

$$g(r,\theta,z|r_o,\theta_o,z_o;k_o)=\frac{1}{2\pi}\sum_{m=0}^{M}\sum_{n=0}^{N}\cos\left(m\left(\theta-\theta_o\right)\right)\int_{-\infty}^{\infty}\frac{J_m\left(K_{mn}(k_o,\hat{k}_z)r_o\right)J_m\left(K_{mn}(k_o,\hat{k}_z)r\right)}{\Lambda_{mn}(k_o,\hat{k}_z)\left[K^2(k_o,\hat{k}_z)-K_{mn}^2(k_o,\hat{k}_z)\right]}e^{-i\hat{k}_z(z-z_o)}d\hat{k}_z \tag{2.48}$$

This integral expression is the Inverse Fourier Transform of the Green's function solved in the wavenumber domain as described in Appendix D. The expression in eq. (2.48) suggests that although the continuity condition is never imposed by the WT approach, it must be naturally satisfied. The reason for this is that the exponential term $e^{-i\hat{k}_z(z-z_o)}$ converges to 1 for $z\to z_o$.

The integral in eq. (2.48) is commonly evaluated in closed form by applying the Theory of Residues [38,49] which results in a robust formulation for the case of the hard wall duct. However, this theory is not convenient for the soft wall case in order to find the correct closed form Green's function. The application of this method requires

introducing a branch cut for every pole in the $\hat{k}_z$-complex plane to avoid the presence of multi-valued functions. Therefore, the evaluation of the integrals in eq. (2.48) across these branch cuts adds a non-zero component to each modal term obtained by the conventional theory of residues. Numerical results have been evaluated during the course of this investigation [60] in which these additional terms were disregarded. The results showed that the Green's functions did not satisfy the condition of continuity at the source plane, i.e. they did not have the information to reproduce the near fields. This suggests that the integral terms due to the presence of the branch cut cannot be ignored. Since it is not possible to find a closed form for these non-zero components, the method will not lead to a practical solution and will not be included in this work.

In addition, the solution obtained by the theory of residues depends on the same eigenproperties as in the modal expansion approach and thus on the direction of propagation. As a result, this formulation would lead to face the same concern about the eigenfunction completeness and it will be avoided. In order to address these problems, a numerical technique was developed to perform the Fourier inverse integral and presented in Appendix D.

The formulations presented in this chapter can be used to evaluate and compare the Green's function for several cases. The Green's function was used to model the presence of a point source at the wall of a circular duct as shown in Figure 2.8. As shown in this figure, the cross section plane at the source location defines a propagation interface between the positive and negative propagating sound fields. This interface is a sector of main interest for the computation of the Green's functions since the condition of continuity has to be satisfied. In addition to the computation in this plane, the solution was also evaluated along the coordinate z for a fixed radial location r. The duct of radius is $a = 0.43$ m was assumed to have a uniform flow of M=-0.44, i.e. opposite to the positive direction of propagation. The source is located at the upper point in the section as indicated in the figure. The wall properties were considered for a liner of a resistance level of $3\rho c$ and a core depth of 0.5 inches. The number of modes used for both formulations is 1600, i.e. 40 circumferential by 40 radial orders.

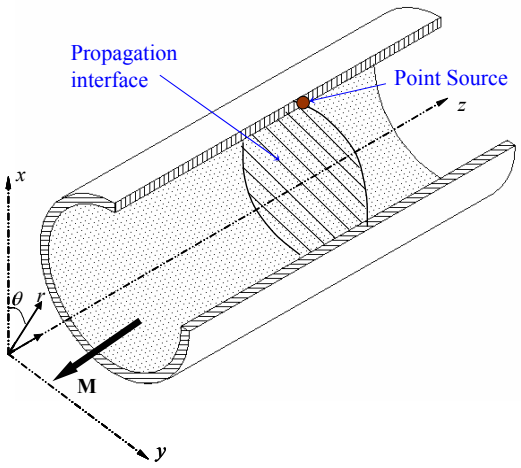

Figure 2.8: Schematics of the propagating interface and source position.

Results for 1000 Hz

The first numerical case presented in this section is for 1000 Hz and a wall normalized admittance of $\beta_w = 0.121 + i0.155$. The solution is found by the two considered approaches: the Modal Expansion and the WT method. In addition, the improper integral required by WT method was solved by using the direct numerical integration technique developed in Appendix D. Figures 2.9 and 2.10 present the results for the Green's function obtained at the source plane in terms of magnitude and phase. The Modal Expansion approach is illustrated in Figure 2.9. The magnitude and phase of the Green's function for the positive propagating waves are shown in part (a) and for the negative propagating waves in part (b). It is observed that the Green's function obtained by the modal expansion method is continuous in magnitude and has also maintained the relative phase at the propagating interface (compare Figs. 2.9(a) and 2.9(b)). Figure 2.10 illustrates the WT method (numerical integration). Unlike the closed form solution, it is not necessary to make a distinction between positive and negative propagation in this numerical case. Also, as observed in expression (2.48), the continuity condition is naturally satisfied. The results confirm that the magnitude and phase of Green's function for the WT method (numerical integration) present similar trends as the Modal Expansion approach. However, there is a difference of a constant factor between the plots of the magnitude obtained by both methods.

The comparison of the Modal and WT methods (numerical integration) is also undertaken by evaluating the solution of the Green's function in the axial direction of the duct for a fixed radial coordinate $r=0.2159$ m and azimuth coordinate $\theta=0$. This comparison is presented in Figure 2.11 for both magnitude and phase. Similar to the results at the source plane, both approaches show good agreement in terms of the phase. However, the magnitude shows the same shape but the modal expansion solution differs from the WT method by a constant factor.

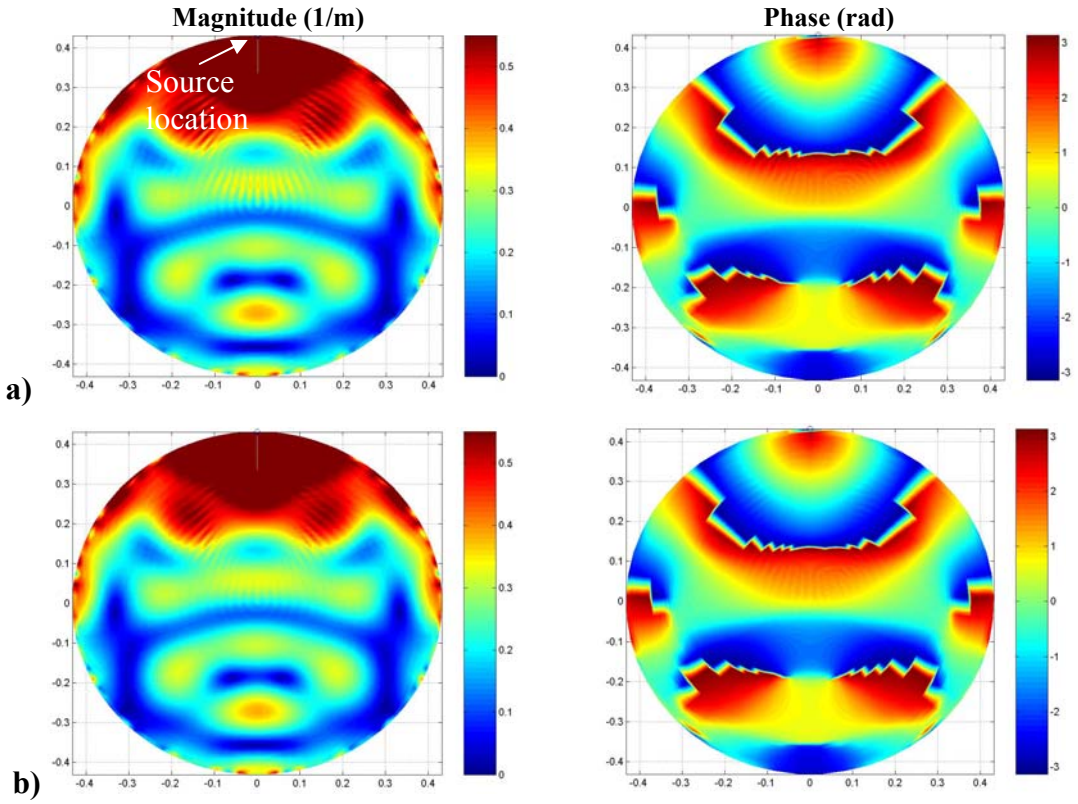

Figure 2.9: Magnitude and Phase of the soft wall Green's function at the propagating interface at 1000 Hz for the Spectral Expansion Method a) positive propagating, and b) negative propagating.

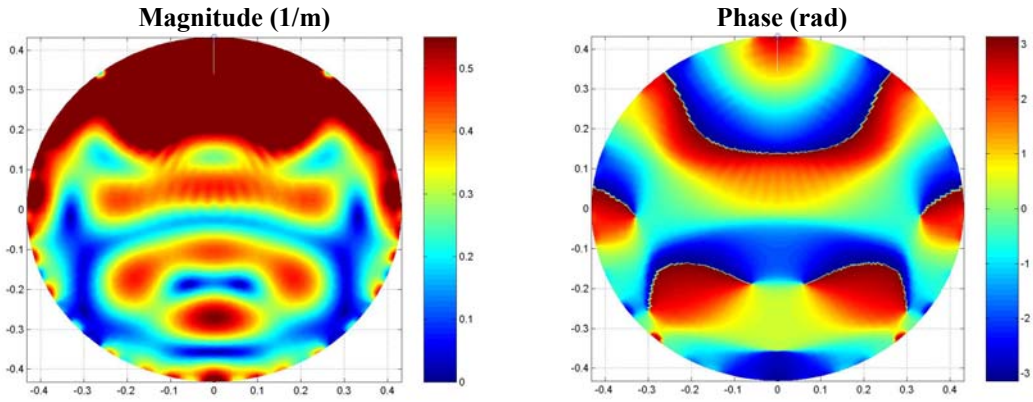

Figure 2.10: Magnitude and Phase of the soft wall Green's function at the propagating interface at 1000 Hz for the WT Method using a numerical integration.

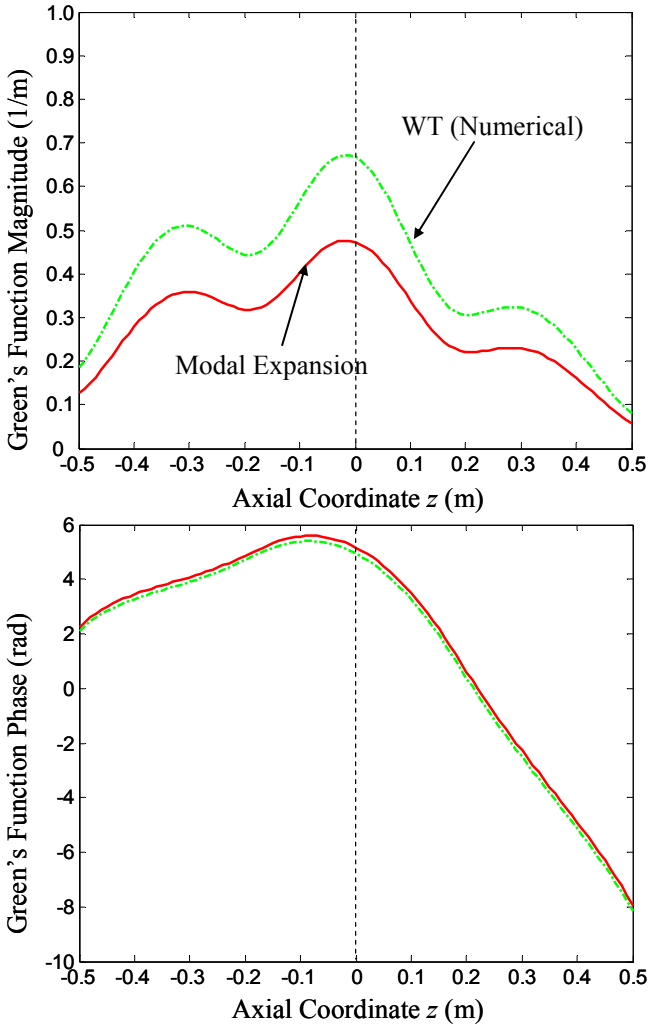

Figure 2.11: Magnitude and Phase of the Green's function in the axial direction at 1000 Hz.

Results for 3000 Hz

This section presents the numerical results for a higher frequency of 3000 Hz, and a corresponding wall normalized admittance of $\beta_w = 0.30 + i0.065$. This case was selected in order to investigate the Green's function for an extreme condition of high frequency and flow Mach number. The comparison in magnitude and phase of the Green's functions given by the two approaches at the propagating interface is presented in the same fashion as the previous section. The Modal Expansion approach is illustrated in Figure 2.12. The magnitude and phase of the Green's function for the positive propagating waves are shown in part (a) and for the negative propagating waves in part (b). Similar to the previous results, the Green's function obtained by the modal expansion method is continuous in magnitude and has also maintained the relative phase at the propagating interface (compare Figs. 2.12(a) and 2.12(b)). The results using the WT method (numerical integration) are presented in Figure 2.13, where the continuity condition is naturally satisfied as in the previous case. This figure confirms that the magnitude and phase of Green's function for the WT method (numerical integration) present similar trends as the Modal Expansion approach. Moreover, for this case, the magnitude level obtained by the WT method (numerical integration) shows a very close similarity with respect to the Modal Expansion approach.

Figure 2.14 presents the comparison of the methods by evaluating the solution of the Green's function in the axial direction of the duct for a fixed radial coordinate $r=0.2159$ m and azimuth coordinate $\theta=0$. Similar to the results at the source plane, the WT solution obtained by the numerical integration shows a very close agreement with the Modal Expansion approach.

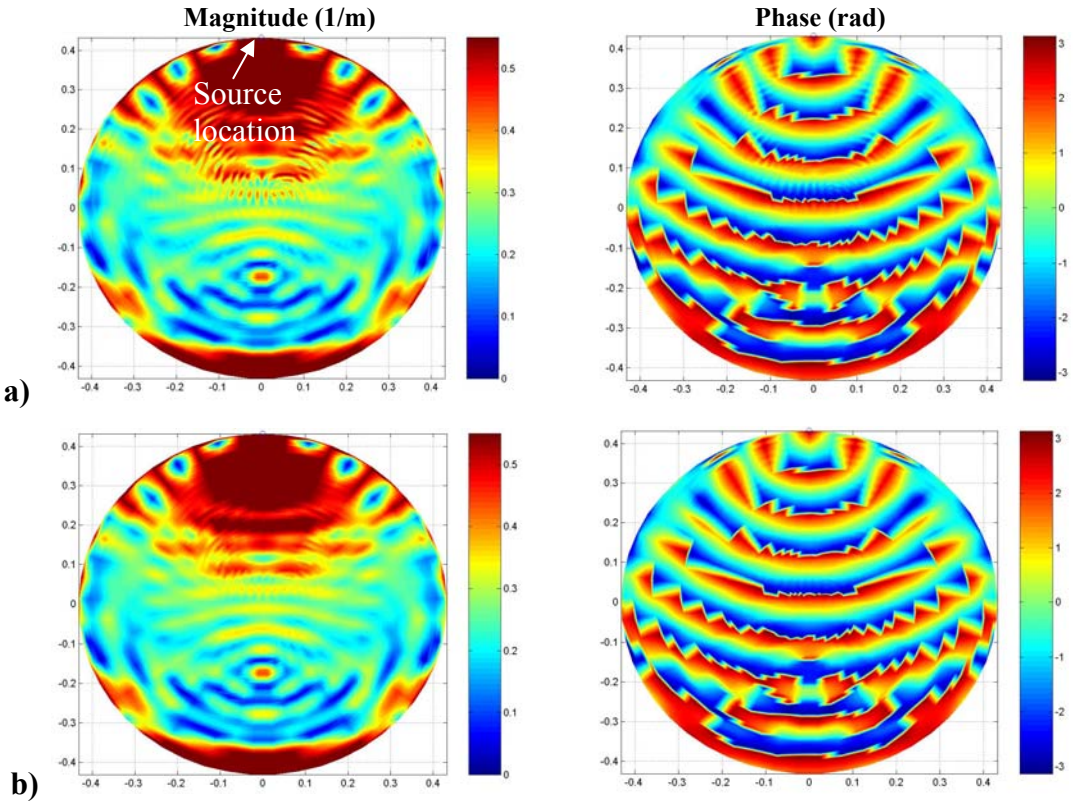

Figure 2.12: Magnitude and Phase of the soft wall Green's function at the propagating interface at 3000 Hz for the Spectral Expansion Method a) positive propagating, and b) negative propagating.

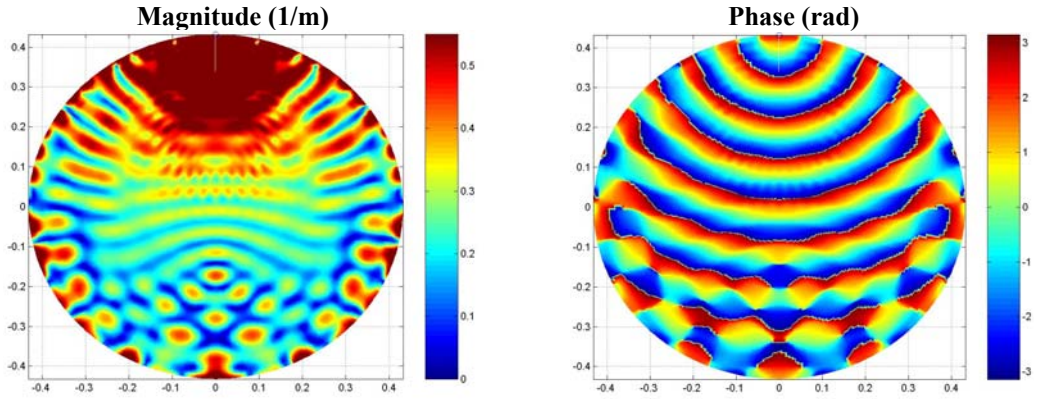

Figure 2.13: Magnitude and Phase of the soft wall Green's function at the propagating interface at 3000 Hz for the WT Method using a numerical integration.

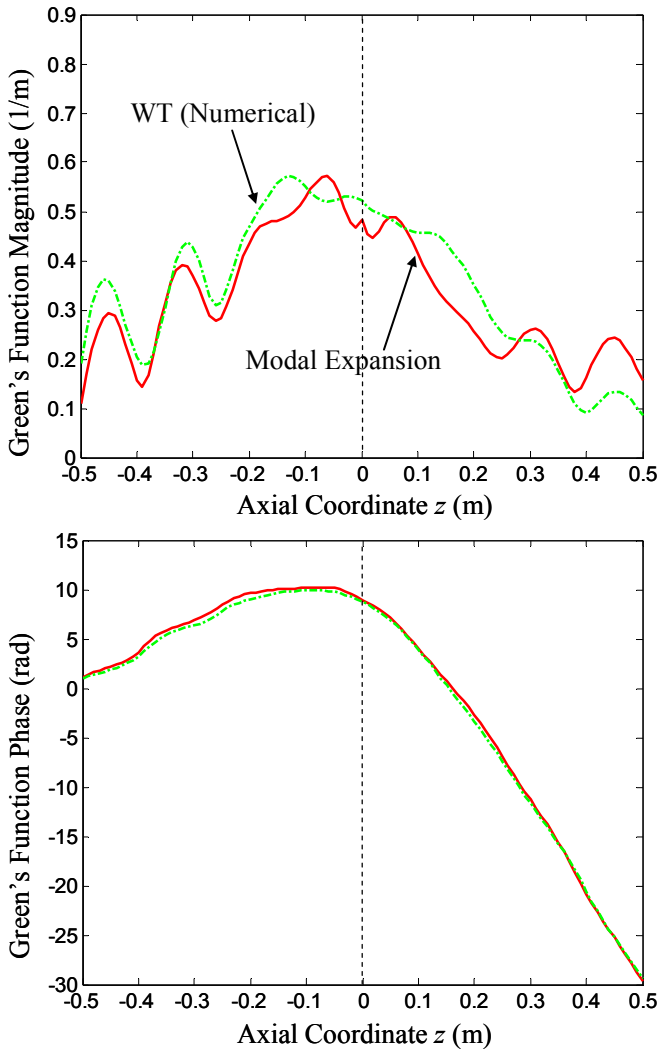

Figure 2.14: Magnitude and Phase of the Green's function in the axial direction at 3000 Hz.

In conclusion, the comparison between both methods, i.e. Modal Expansion and WT (numerical integration), confirms that the modal expansion solution gives a safe formulation to obtain the radiation of sound from a point source in the lined duct. In addition, the results obtained by the WT method require performing a numerical integration that is computationally expensive. For this reason, the method was only developed in order to compare the formulations but it not practical for the HQ modeling. On the other hand, **the modal expansion approach not only provides a reliable solution but it is also computationally efficient.**

As observed in the results, the continuity condition at the source plane is perfectly achieved by using both methods. Note that this condition is explicitly imposed in the modal expansion approach and naturally satisfied in the WT method (numerical integration). However, an attempt to find a closed form solution with the WT method by using the Theory of Residues will lead to discontinuous expressions [60]. As a consequence, a practical application of this method to the sound radiation in lined ducts with flow is not possible. Appendix D presents numerical results for other cases with different liners and flow conditions showing similar trends as in this section.

2.2.3 Solution of the Adjoint Green's Functions

The Green's function found in Section 2.2.1 can now be used to find the radiated sound due to a finite piston source acting on the duct wall. This process involves using the Divergence Theorem as well as the Maxwell Reciprocity principle [53, 54]. However, the differential operator defining the convected acoustic wave equation in a circular lined duct defined by equations (2.33) and (2.34) is not self-adjoint. The reason for this is due to the presence of the flow and the non-homogeneous boundary condition given by $\beta_w \neq 0$. Therefore, the Green's function found in Section 2.2.1 does not satisfy the Maxwell Reciprocity principle, i.e. $g\left(\vec{r}\middle|\vec{r}_o\right) \not\asymp g\left(\vec{r}_o\middle|\vec{r}\right)$. In this case, the Maxwell Reciprocity is defined in terms of the adjoint Green's function which is the solution of the associated adjoint acoustic problem. This section presents this adjoint Green's function to be used later in Section 2.3.

Considering that the Green's function, g, is in a Hilbert space with inner product defined as in Appendix A, the associated adjoint problem of the convected acoustic wave equation in a lined duct is given as follows [22, 38, 53]

$$\frac{\partial^2 g^*}{\partial r^2}+\frac{1}{r}\frac{\partial g^*}{\partial r}+\frac{1}{r^2}\frac{\partial^2 g^*}{\partial \theta^2}+\frac{\partial^2 g^*}{\partial z^2}\left(1-M^2\right)-2iMk_0\frac{\partial g^*}{\partial z}+k_0^2 g^* = \frac{1}{r}\delta(\vec{r}\,|\vec{r}_o) \qquad (2.49)$$

under the soft wall boundary condition [32, 38]:

$$\left.\overline{\frac{\partial g^*}{\partial r}}\right|_{r=a} = -i\beta_w \frac{\left(k_0-k_z M\right)^2}{k_0}\overline{g^*} \qquad (2.50)$$

where g^* is the adjoint Green's function and the bar over a variable, e.g. $\overline{f}$, indicates the complex conjugate. Equations (2.49) and (2.50) show that the difference between the direct and the adjoint problem of the convected wave equation is given by the boundary condition, i.e. the boundary condition on the adjoint problem is given in terms of the complex conjugate of the solution.

The problem defined by equations (2.49) and (2.50) has a similar analytical solution as the direct problem defined by (2.33) and (2.34). However, the difference from the direct solution lays on the eigenvalues corresponding to the new boundary condition defined in (2.50). Then, the solution to equations (2.49) and (2.50) can be assumed as a linear combination of the adjoint eigenfunctions as follows

$$g^{*(+)}\left(\vec{r}\,|\vec{r}_o\right)=\sum_{m=0}^{M}\sum_{n=0}^{N}A_{mn}^{*(+)}\,\Phi_{mn}^{*(+)}e^{-ik_z^{*(+)}(z-z_0)} \tag{2.51}$$

$$g^{*(-)}\left(\vec{r}\,|\vec{r}_o\right)=\sum_{m=0}^{M}\sum_{n=0}^{N}A_{mn}^{*(-)}\,\Phi_{mn}^{*(-)}e^{-ik_z^{*(-)}(z-z_0)}$$

where *M* and *N* are the maximum number of terms to be included in the expansion. Note that the direction of propagation of each solution is not yet given.

The eigenfunctions can be found following the same steps as from equation (2.5) to (2.29). Finally, they are selected to have the form

$$\Phi_{mn}^{*(+)}\left(r,\theta\right)=\cos\left[m\left(\theta-\theta_o\right)\right]J_m\left(k_{mn}^{*(+)}r\right) \tag{2.52a}$$

$$\Phi_{mn}^{*(-)}\left(r,\theta\right)=\cos\left[m\left(\theta-\theta_o\right)\right]J_m\left(k_{mn}^{*(-)}r\right) \tag{2.52b}$$

The eigenvalues $k_{mn}^{*(+)}$ and $k_{mn}^{*(-)}$ are obtained from replacing the eigenfunctions (2.52) into the boundary condition as follows

$$-i\beta_w\frac{\left(k_o-Mk_z^{*(+)}\right)^2}{k_o}\overline{J_m\left(k_{mn}^{*(+)}a\right)}=\overline{k_{mn}^{*(+)}J_m'\left(k_{mn}^{*(+)}a\right)} \tag{2.53a}$$

$$-i\beta_w\frac{\left(k_o-Mk_z^{*(-)}\right)^2}{k_o}\overline{J_m\left(k_{mn}^{*(-)}a\right)}=\overline{k_{mn}^{*(-)}J_m'\left(k_{mn}^{*(-)}a\right)} \tag{2.53b}$$

where the relation between k_{mn}^* and k_z^* is given by

$$k_{mn}^{*2} = k_o^2 - k_z^{*2}(1-M^2) - 2k_o k_z^* M \tag{2.54}$$

At this point, it is clear that solving the characteristic equation (2.53) with (2.54) yields the complex conjugate of the eigenvalues of the direct problem (*see equations (2.28)*). Then, the eigenvalues of the associated adjoint problem can be related to the direct problem as follows

$$k_{mn}^{*(+)} = \overline{k_{mn}^{(+)}}\,; \quad k_{mn}^{*(-)} = \overline{k_{mn}^{(-)}} \tag{2.55}$$

Also, the axial wavenumbers are given by

$$k_z^{*(+)} = \overline{k_z^{(+)}}\,; \quad k_z^{*(-)} = \overline{k_z^{(-)}} \tag{2.56}$$

Replacing (2.55) and (2.56) into (2.51), the solution of the adjoint Green's function can be expressed as

$$g^{*(+)}\left(\vec{r}\,|\vec{r}_o\right) = \sum_{m=0}^{M}\sum_{n=0}^{N} A_{mn}^{*(+)}\,\overline{\Phi_{mn}^{(+)}} e^{-i\overline{k_z^{(+)}}(z-z_0)} \tag{2.57}$$

$$g^{*(-)}\left(\vec{r}\,|\vec{r}_o\right) = \sum_{m=0}^{M}\sum_{n=0}^{N} A_{mn}^{*(-)}\,\overline{\Phi_{mn}^{(-)}} e^{-i\overline{k_z^{(-)}}(z-z_0)}$$

The modal amplitudes $A_{mn}^{*(+)}$ and $A_{mn}^{*(-)}$ can be found following the same steps presented from equation (2.35) to (2.47). This procedure will also lead to find the modal amplitudes of the adjoint Green's function in terms of the direct solution as

$$A_{mn}^{*(+)} = \overline{A_{mn}^{(+)}}\,; \quad A_{mn}^{*(-)} = \overline{A_{mn}^{(-)}} \tag{2.58}$$

The direction of propagation of the solutions $g^{*(+)}$ and $g^{*(-)}$ can be determined based on the condition that the mode amplitudes must be bounded, i.e. to have decaying propagating modes. The propagating properties of every mode are given by the exponential term of equation (2.57), which in fact depend on the complex conjugate of the axial wavenumber of the direct problem, i.e. $\overline{k_z^{(+)}}$ and $\overline{k_z^{(-)}}$. Consequently, the propagation of the modes in equations (2.57) has to be assigned in the opposite direction to the direct problem as

$$g^{*(+)} \quad \text{for} \quad z < z_o \tag{2.59}$$

$$g^{*(-)} \quad \text{for} \quad z > z_o$$

Figure 2.15 presents a schematic of the propagating direction of the Green's functions. The solid black line represents the Green's function for the direct problem while the dotted red line corresponds to the adjoint solution. Note that there is a symmetry between the positive functions $g^{(+)}$ and $g^{*(+)}$, as well as between the negative solutions $g^{(-)}$ and $g^{*(-)}$. This symmetry will be the responsible of satisfying the Maxwell Reciprocity.

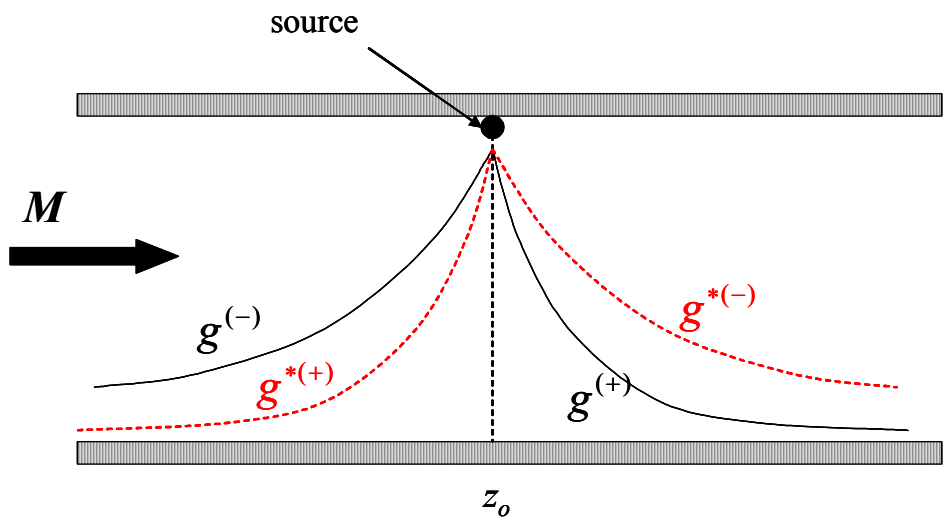

Figure 2.15: Schematic of the adjoint Green's functions propagating direction.

Finally, the associated adjoint Green's function can be expressed as

$$g^{*(+)}\left(\vec{r}\,|\vec{r}_o\right) = \sum_{m=0}^{M}\sum_{n=0}^{N} \overline{A_{mn}^{(+)}}\,\overline{\Phi_{mn}^{(+)}} e^{-i\overline{k_z^{(+)}}(z-z_0)} \qquad z < z_o \tag{2.60}$$

$$g^{*(-)}\left(\vec{r}\,|\vec{r}_o\right) = \sum_{m=0}^{M}\sum_{n=0}^{N} \overline{A_{mn}^{(-)}}\,\overline{\Phi_{mn}^{(-)}} e^{-i\overline{k_z^{(-)}}(z-z_0)} \qquad z > z_o$$

The solution found in equation (2.60) satisfies the Maxwell reciprocity [53, 54]. If the associated adjoint Green's function is expressed for the complete domain in terms of the Heaviside function as

$$g^*\left(\vec{r}\middle|\vec{r_0}\right) = g^{*(+)}\left(\vec{r}\middle|\vec{r}_o\right)\left[1 - H\left(z - z_0\right)\right] + g^{*(-)}\left(\vec{r}\middle|\vec{r}_o\right)H\left(z - z_0\right) \tag{2.61}$$

then, the reciprocity principle is satisfied in the following form

$$g\left(\vec{r}\middle|\vec{r}_o\right) = \overline{g^*\left(\vec{r}_o\middle|\vec{r}\right)} \tag{2.62}$$

which will be used in the following section.

2.3 Finite Piston Radiation

The Green's functions can now be used to find the sound field due to a motion of a finite piston source vibrating with a known uniform velocity V_p, i.e. piston source. Figure 2.16 illustrates a sector of the soft wall in the circular duct with the presence of a vibrating piston. For the sake of clarity, this piston source is referred as the radiating surface of the duct. The rest of the duct surface is referred as non-radiating surface. The derivation in this section follows the approach taken by Morse and Ingard [22] for radiation from boundaries of lined duct without flow. However, the formulation is here extended to the case with flow.

It is convenient to first analyze the behavior of the non-radiating surface, i.e. liner. As shown in Figure 2.16, the surface of the liner is covered by a shear layer which separates the flow region from the liner physical surface. Although the non-radiating areas of the duct boundary do not move, this shear layer is allowed to have a radial movement given by the permeability characteristics of the soft wall. Therefore the radial particle velocity v_r at the lined wall does not vanish. The relationship between the particle velocity v_r inside the flow and the pressure at the wall surface was derived in section 2.1 and is presented in equation (2.13). This expression depends on the axial wavenumbers k_z which are certainly a property of every mode. Therefore, the behavior of the particle velocity v_r needs to be investigated in terms of its modal components $v_{r_{mn}}$. The modal particle velocity $v_{r_{mn}}$ in the radial direction is then related to the modal pressure p_{mn} over the liner (non-radiating surface) in the flow as follows [22]

$$v_{r_{mn}} = -\frac{1}{i\rho c\left(k_0 - k_z M\right)} \frac{\partial p_{mn}}{\partial r}\bigg|_{r=a} = \frac{\beta_\omega}{\rho c} \frac{\left(k_0 - k_z M\right)}{k_0} p_{mn}\bigg|_{r=a} \tag{2.63}$$

The first two terms of the equality in (2.63) are related to the equilibrium relation between the pressure gradient and particle velocity, i.e. Euler's equation. The last two terms relate the pressure and its gradient using the definition of the liner specific acoustic admittance. Then, from equation (2.63) the difference between the radial particle velocity and the term $\left(1/\rho c k_0\right)\beta_\omega\left(k_0 - k_z M\right)p_{mn}\big|_{r=a}$ must vanish as follows

$$v_{r_{mn}} - \frac{\beta_\omega}{\rho c} \frac{\left(k_0 - k_z M\right)}{k_0} p_{mn}\bigg|_{r=a} = 0 \tag{2.64}$$

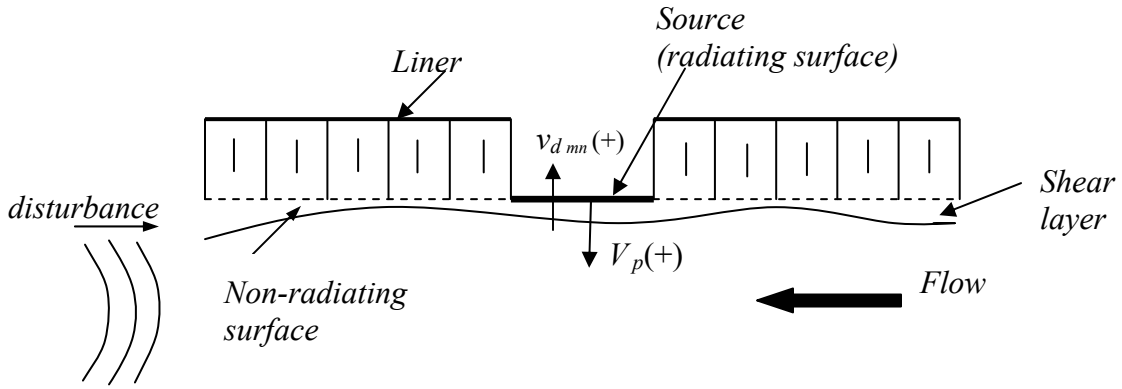

Figure 2.16: Schematic of the shear layer at the lined duct walls
Positive convention of **particle velocity** is outwards.
Positive convention of **piston velocity** is inwards.

In the radiating areas, this difference cannot vanish because of the presence of the piston motion. This difference has to be the perturbation velocity in the flow produced by the piston motion, which is defined as

$$v_{d_{mn}} = -\left(\frac{1}{i\rho c\left(k_0 - k_z M\right)} \frac{\partial p_{mn}}{\partial r} + \frac{\beta_w}{\rho c} \frac{\left(k_0 - k_z M\right)}{k_0} p_{mn} \right)\bigg|_{r=a} \tag{2.65}$$

As shown in Figure 2.16, the modal particle velocity in the flow due to the radiating piston, $v_{d_{mn}}$, needs to be related to the piston velocity at the wall, i.e. outside of shear layer or in the physical surface of the liner. Applying particle displacement continuity [29], the

relation between the piston velocity and the radial particle velocity outside the shear layer (in the flow) is given by

$$v_{d_{mn}} = -\frac{\left(k_0 - k_z M\right)}{k_0} V_p \tag{2.66}$$

where the negative sign is used to change the positive velocity convention to be inwards.

The radiation from the piston source is now obtained by applying the Green's Divergence Theorem with the adjoint solution of the Green's functions [53]. The reason for this is the fact that the linear operator L defining the convected wave equation with soft wall boundary condition is not self-adjoint. Then, although the direct solution is commonly used to solve this problem, the adjoint one must be considered. The pressure anywhere in the duct can be found taking the inner product of p with equation (2.33) and equation (2.3) with g^*. Then subtract the results as follows

$$p = \left\langle p, L\ g^* \right\rangle - \left\langle L\ p, g^* \right\rangle \tag{2.67}$$

where $\langle .,. \rangle$ is the inner product in the Hilbert space as defined in Appendix A. Considering the Green's function that satisfy equation (2.50), the application of the Divergence Theorem on equation (2.67) will lead to integration over the duct surface as

$$\begin{aligned} p_{mn}\left(\vec{r}\right) &= -\int_S \left(\left.\frac{\partial p_{mn}}{\partial r}\right|_{r=a} \overline{g^*_{mn}} - p_{mn} \left.\frac{\overline{\partial g^*_{mn}}}{\partial r}\right|_{r=a} \right) dS = \\ &= -\int_S \left(\left.\frac{\partial p_{mn}}{\partial r}\right|_{r=a} \overline{g^*_{mn}} + i p_{mn} \frac{\beta}{k_0} \left(k_0 - k_z M\right)^2 \overline{g^*_{mn}} \right) dS = \\ &= -i\rho c \left(k_0 - k_z M\right) \int_S \left(\frac{1}{i\rho c \left(k_0 - k_z M\right)} \frac{\partial p_{mn}}{\partial r} + \frac{\beta}{\rho c} \frac{\left(k_0 - k_z M\right)}{k_0} p_{mn} \right) \overline{g^*_{mn}}\, dS \end{aligned} \tag{2.68}$$

As mentioned above, only the radiating surface will be moving with velocity V_p. The integral over the non-radiating surface will then vanish because the Green's functions satisfy the soft wall boundary condition. Thus, only the integral over the radiating

surface, i.e. piston source, needs to be solved. Then, replacing the factor in the integral of equation (2.68) by the perturbation velocity $v_{d_{mn}}$ in equation (2.65) leads to

$$p_{mn}\left(\vec{r}\right) = i\rho c\left(k_0 - k_z M\right) v_{d_{mn}} \int_{S_R} \overline{g^*_{mn}\left(\vec{r_0}\middle|\vec{r}\right)} dS \tag{2.69}$$

Note that in the last expression the integral is over the radiating surface S_R only, and since the piston velocity is uniform, $v_{d_{mn}}$ was taken outside the integral. Finally, using equation (2.66) and the Maxwell reciprocity stated in equation (2.62), the pressure inside the duct due to the motion of a finite source is given by:

$$p^{(+)}\left(\vec{r}\middle|\vec{r_0}\right) = -i\rho c\, V_p \sum_m \sum_n \frac{\left(k_0 - k_z^{(+)} M\right)^2}{k_0} \int_{S_R} g^{(+)}_{mn}\left(\vec{r}\middle|\vec{r_0}\right) dS \tag{2.70a}$$

$$p^{(-)}\left(\vec{r}\middle|\vec{r_0}\right) = -i\rho c\, V_p \sum_m \sum_n \frac{\left(k_0 - k_z^{(-)} M\right)^2}{k_0} \int_{S_R} g^{(-)}_{mn}\left(\vec{r}\middle|\vec{r_0}\right) dS \tag{2.70b}$$

Note that equations (2.70) are given for positive and negative direction of propagation, depending on the relative location between the source and receiver.

2.3.1 Radiation from a rectangular shaped piston

In this section, the radiated pressure from a rectangular shaped piston is derived in closed form. The piston is assumed to be vibrating with a known uniform velocity V_p and it is defined by constant z and θ coordinates, as shown in Figure 2.17. For convenience, the piston position is referred to the center point of the piston $\left(a, \theta_n, z_n\right)$ and its dimensions are given by the distance $\boldsymbol{d}$ and the angle $\boldsymbol{\alpha}$. The formulation presented in this section is based on solving the integrals of equations (2.70) in the previous section. The Green's function for a point source positioned on the lined wall duct at (a, θ_o, z_o) is given by (2.35) as

$$g^{(+)}\left(\vec{r}\middle|\vec{r}_o\right) = \sum_{m=0}^{M_g} \sum_{n=0}^{N_g} A^{(+)}_{mn}(a) \cos\left[m\left(\theta - \theta_o\right)\right] J_m\left(k^{(+)}_{mn} r\right) e^{-ik_z^{(+)}(z - z_o)} \qquad z \geq z_o \tag{2.71}$$

where $k_z^{(+)} = \left\{-Mk_o + \sqrt{k_o^2 - \left(1-M^2\right)k_{mn}^{(+)2}}\right\} / \left(1-M^2\right)$, and

$$g^{(-)}\left(\vec{r}\,|\,\vec{r}_o\right) = \sum_{m=0}^{M_g}\sum_{n=0}^{N_g} A_{mn}^{(-)}(a)\cos\left[m\left(\theta-\theta_o\right)\right]J_m\left(k_{mn}^{(-)}r\right)e^{-ik_z^{(-)}(z-z_o)} \qquad z \geq z_o \tag{2.72}$$

where $k_z^{(-)} = \left\{-Mk_o - \sqrt{k_o^2 - \left(1-M^2\right)k_{mn}^{(-)2}}\right\} / \left(1-M^2\right)$. The eigenfunctions in equations (2.71) and (2.72) are identified as

$$\Phi_{mn}^{(+)}(r,\theta) = \cos\left[m\left(\theta-\theta_o\right)\right]J_m\left(k_{mn}^{(+)}r\right) \tag{2.73a}$$

$$\Phi_{mn}^{(-)}(r,\theta) = \cos\left[m\left(\theta-\theta_o\right)\right]J_m\left(k_{mn}^{(-)}r\right) \tag{2.73b}$$

and M_g and N_g are the number of modes include in the Green's function, and the modal amplitudes $A_{mn}^{(+)}$ and $A_{mn}^{(-)}$ are determined by equation (2.45).

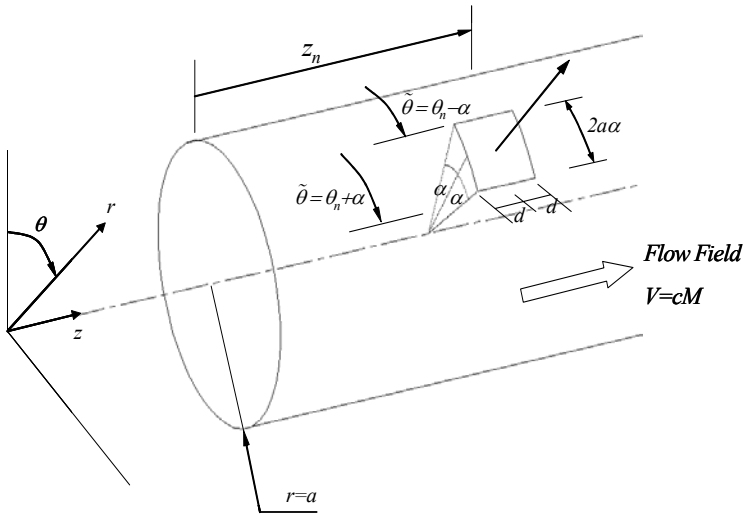

Figure 2.17: Model of the finite sources.

The pressure at $\left(r,\theta,z\right)$ due to a finite rectangular shaped piston with source velocity V_n is then obtained by expression (2.70) as

$$p\left(r,\theta,z\,|\,a,\theta_n,z_n\right) = -i\rho c\sum_{m_g}\sum_{n_g}\frac{\left(k_0-k_zM\right)^2}{k_0}V_n\int_{z_n-d}^{z_n+d}\int_{\theta_n-\alpha}^{\theta_n+\alpha} g_{mn}\left(r,\theta,z\,|\,a,\tilde{\theta},\tilde{z}\right)a\,d\tilde{\theta}\,d\tilde{z} \tag{2.74}$$

where the dimension d and α of the source are given in terms of the source area as $d=\sqrt{S}/2$ and $\alpha=\sqrt{S}/2a$, respectively, and (a,θ_n,z_n) is the location of the source center as defined in the Figure 2.17. Replacing (2.73)a or (2.73)b into (2.74), it is clear that there are two integrals that need to be solved. The first one is with respect to the coordinate θ, which is easily obtained as

$$\int_{\theta_n-\alpha}^{\theta_n+\alpha}\cos m\left(\theta-\tilde{\theta}\right)a\,d\tilde{\theta}=\frac{2a\alpha\sin(m\alpha)}{m\alpha}\cos m\left(\theta-\theta_n\right)=\kappa_\theta(\alpha)\cos m\left(\theta-\theta_n\right) \tag{2.75}$$

where $\kappa_\theta(\alpha)=\dfrac{2a\alpha\sin(m\alpha)}{m\alpha}$.

For the special case of m=0 equation (2.75) gives $2a\alpha$. The second integral is along the *z*-direction and has different wavenumbers $k_z^{(+)}$ and $k_z^{(-)}$ for both propagation directions. The solution of these integrals depends on the position of the observation point *z* relative to the piston source position z_n. Three cases are considered as illustrated in Figure 2. 18.

CASE 1: The observation point is downstream of the source, i.e. $z>z_n+d$. This case is illustrated in Figure 2. 18-a and implies that $z>\tilde{z}$ and the following integral needs to be solved

$$\frac{p\left(r,\theta,z\left|a,\theta_n,z_n\right.\right)}{V_n}=-i\rho c\sum_{m_g}\sum_{n_g}\frac{\left(k_0-k_z^{(+)}M\right)^2}{k_0}\int_{z_n-d}^{z_n+d}\int_{\theta_n-\alpha}^{\theta_n+\alpha}g_{mn}^{(+)}\left(r,\theta,z\left|a,\tilde{\theta},\tilde{z}\right.\right)a\,d\tilde{\theta}\,d\tilde{z} \tag{2.76}$$

For this case the integration along the z-direction is the following

$$\int_{z_n-d}^{z_n+d}e^{-ik_z^{(+)}(z-\tilde{z})}d\tilde{z}=e^{-ik_z^{(+)}(z-z_n)}\frac{\sin(k_z^{(+)}d)}{k_z^{(+)}d}2d \tag{2.77}$$

Using (2.75) and (2.77), equation (2.76) becomes

$$p(r,\theta,z\,|\,a,\theta_n,z_n) = -i\,\rho c\,V_n \sum_{m=0}^{M_g}\sum_{n=0}^{N_g} \frac{\left(k_0 - k_z^{(+)}M\right)^2}{k_0} A_{mn}^{(+)}\,\Phi_{mn}^{(+)}(r,\theta)\times \\ \times \kappa_\theta(\alpha)\; e^{-ik_z^{(+)}(z-z_n)}\,\frac{\sin(k_z^{(+)}d)}{k_z^{(+)}d}\;2d \tag{2.78}$$

CASE 2: The observation point is upstream of the source, i.e. $z < z_n - d$. This case is illustrated in Figure 2. 18-b and implies that $z < \tilde{z}$ and the following integral needs to be solved

$$\frac{p\left(r,\theta,z\left|a,\theta_n,z_n\right.\right)}{V_n} = -i\rho c\sum_{m_g}\sum_{n_g}\frac{\left(k_0 - k_z^{(-)}M\right)^2}{k_0}\int_{z_n-d}^{z_n+d}\int_{\theta_n-\alpha}^{\theta_n+\alpha} g_{mn}^{(-)}\left(r,\theta,z\left|a,\tilde{\theta},\tilde{z}\right.\right) a\,d\tilde{\theta}\,d\tilde{z} \tag{2.79}$$

For this case the integration along the z-direction is the following

$$\int_{z_n-d}^{z_n+d} e^{-ik_z^{(-)}(z-\tilde{z})}d\tilde{z} = e^{-ik_z^{(-)}(z-z_n)}\frac{\sin(k_z^{(-)}d)}{k_z^{(-)}d}2d \tag{2.80}$$

Using (2.75) and (2.80), equation (2.79) becomes

$$p(r,\theta,z\,|\,a,\theta_n,z_n) = -i\,\rho c\,V_n \sum_{m=0}^{M_g}\sum_{n=0}^{N_g} \frac{\left(k_0 - k_z^{(-)}M\right)^2}{k_0} A_{mn}^{(-)}\,\Phi_{mn}^{(-)}(r,\theta)\times \\ \times \kappa_\theta(\alpha)\; e^{-ik_z^{(-)}(z-z_n)}\,\frac{\sin(k_z^{(-)}d)}{k_z^{(-)}d}\;2d \tag{2.81}$$

CASE 3: The observation point is on the surface of the source, i.e. $z_n - d < z < z_n + d$. This case is illustrated in Figure 2. 18-c and requires to separate the integral in two parts as

$$\frac{p\left(r,\theta,z\left|a,\theta_n,z_n\right.\right)}{V_n} = -i\rho c\sum_{m_g}\sum_{n_g}\left\{\frac{\left(k_0 - k_z^{(+)}M\right)^2}{k_0}\int_{z_n-d}^{z}\int_{\theta_n-\alpha}^{\theta_n+\alpha} g_{mn}^{(+)}\left(r,\theta,z\left|a,\tilde{\theta},\tilde{z}\right.\right) a\,d\tilde{\theta}\,d\tilde{z} + \right. \\ \left. + \frac{\left(k_0 - k_z^{(-)}M\right)^2}{k_0}\int_{z}^{z_n+d}\int_{\theta_n-\alpha}^{\theta_n+\alpha} g_{mn}^{(-)}\left(r,\theta,z\left|a,\tilde{\theta},\tilde{z}\right.\right) a\,d\tilde{\theta}\,d\tilde{z}\right\} \tag{2.82}$$

To solve (2.82), it is required to find the following integrals as follows

$$\int_{z_n-d}^{z} e^{-ik_z^{(+)}(z-\tilde{z})}d\tilde{z} = \frac{1-e^{-ik_z^{(+)}(z-z_n+d)}}{ik_z^{(+)}} \tag{2.83)a}$$

$$\int_{z}^{z_n+d} e^{-ik_z^{(-)}(z-\tilde{z})}d\tilde{z} = -\frac{1-e^{-ik_z^{(-)}(z-z_n-d)}}{ik_z^{(-)}} \tag{2.83)b}$$

Thus, replacing (2.83)a and (2.83)b into (2.82) and considering (2.75), the integral results in

$$p(\vec{r}\,|\,\vec{r}_n) = -i\,\rho c\,V_n \sum_{m=0}^{M_g}\sum_{n=0}^{N_g}\left\{\frac{\left(k_0-k_z^{(+)}M\right)^2}{k_0} A_{mn}^{(+)}\,\Phi_{mn}^{(+)}(r,\theta)\;\kappa_\theta(\alpha)\left(\frac{1-e^{-ik_z^{(+)}(z-z_n+d)}}{ik_z^{(+)}}\right)-\right. \tag{2.84}$$
$$\left.\frac{\left(k_0-k_z^{(-)}M\right)^2}{k_0} A_{mn}^{(-)}\,\Phi_{mn}^{(-)}(r,\theta)\;\kappa_\theta(\alpha)\left(\frac{1-e^{-ik_z^{(-)}(z-z_n-d)}}{ik_z^{(-)}}\right)\right\}$$

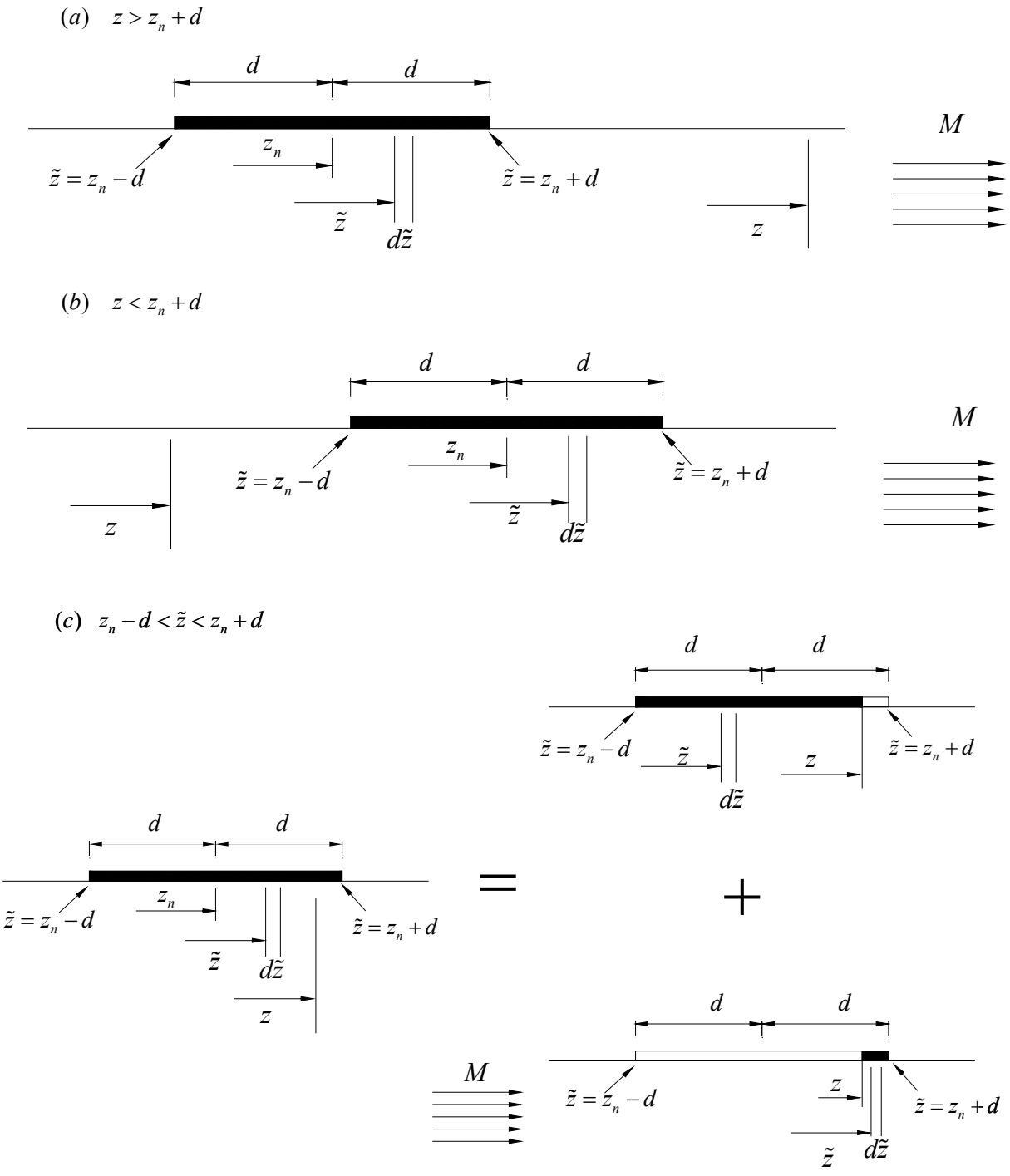

Figure 2. 18: Elements of integration over the source surface (a) case1: observation point is upstream of the source, (b) case 2: observation point is downstream of the source, (c) case 3: observation point is on the surface of the source.

2.4 Acoustic Power Computation

The expression of the acoustic power through a particular duct cross section as shown in Figure 2.19 is derived. The formulation presented in this section is different from the computation of the acoustic power in a hard wall circular duct. The difference is introduced by the fact that the modes in a lined duct with flow are not orthogonal. The computation of the acoustic power is developed by first assuming the pressure and axial particle velocity field inside the duct. As indicated in section 2.1, the duct pressure field is the superposition of the modes inside the duct. If only positive propagating modes are assumed present, the pressure field is given in terms of spinning modes as

$$\begin{aligned} p &= \sum_{m=0}^{M_s}\sum_{n=0}^{N_s}\left(A_{mn}^{(+)}\right)^{pos} J_m\left(k_{mn}^{(+)}r\right)e^{-im\theta}e^{-ik_z^{(+)}z} + \sum_{m=0}^{M_s}\sum_{n=0}^{N_s}\left(A_{mn}^{(+)}\right)^{neg} J_m\left(k_{mn}^{(+)}r\right)e^{im\theta}e^{-ik_z^{(+)}z} \\ p &= \sum_{m=0}^{M_s}\sum_{n=0}^{N_s} p_{mn}^{(+)} \end{aligned} \tag{2.85}$$

where $\left(A_{mn}^{(+)}\right)^{pos}$ and $\left(A_{mn}^{(+)}\right)^{neg}$ are the modal amplitudes of the positive and negative spinning modes (propagating in the positive z-direction), respectively.

The transmitted acoustic power is obtained by integrating the axial component of the acoustic intensity, $I_z^{(+)}(r,\theta,z_n)$, over the duct cross section at z_n as shown in Figure 2.19. That is

$$W(z_n) = \int_0^a \int_0^{2\pi} I_z^{(+)}(r,\theta,z_n)\, r\, dr d\theta \tag{2.86}$$

The acoustic intensity in the positive z-direction is given by [50]:

$$I_z = \frac{1}{2}\mathrm{Re}\left[pv_z^* + \rho c\left|v_z\right|^2 M + \frac{\left|p\right|^2}{\rho c}M + v_z p^* M^2 \right] \tag{2.87}$$

The axial particle velocity $v_z\left(a,\theta,z\right)$ can be found in terms of the pressure using the axial component of the equilibrium equation (See equation (2.4)):

$$-\frac{\partial p}{\partial z} = i\omega\rho v_z + \rho c M \frac{\partial v_z}{\partial z} \tag{2.88}$$

Considering the expression for the pressure in (2.85), equation (2.88) reduces to

$$v_z = \sum_{m=0}^{M_s}\sum_{n=0}^{N_s} \frac{k_z^{(+)}}{\rho c\left(k_0 - k_z^{(+)}M\right)} p_{mn}^{(+)} \tag{2.89}$$

where $p_{mn}^{(+)}$ are the modal components of the pressure (z-direction positive propagating). Expanding the pressure, equation (2.89) can be written as

$$\begin{aligned} v_z = &\sum_{m=0}^{M_s}\sum_{n=0}^{N_s}\left(A_{mn}^{(+)}\right)^{pos} \frac{k_z^{(+)}}{\rho c\left(k_0 - k_z^{(+)}M\right)} J_m\left(k_{mn}^{(+)}r\right)e^{-im\theta}e^{-ik_z^{(+)}z} + \\ &+\sum_{m=0}^{M_s}\sum_{n=0}^{N_s}\left(A_{mn}^{(+)}\right)^{neg} \frac{k_z^{(+)}}{\rho c\left(k_0 - k_z^{(+)}M\right)} J_m\left(k_{mn}^{(+)}r\right)e^{im\theta}e^{-ik_z^{(+)}z} \end{aligned} \tag{2.90}$$

Then, replacing the transmitted pressure from (2.85) and the velocity from (2.90) into the intensity (2.87), the acoustic power is given as follows

$$\begin{aligned} W(z_n) = &\frac{1}{2}\mathrm{Re}\left[\frac{2\pi a^2}{\rho c}\cdot\right. \\ &\sum_{m=0}^{M}\sum_{n=0}^{N}\sum_{r=0}^{N}\left\{\left(\left(A_{mn}^{(+)}\right)^{pos}\left(A_{mr}^{*(+)}\right)^{pos} + \left(A_{mn}^{(+)}\right)^{neg}\left(A_{mr}^{*(+)}\right)^{neg}\right)\frac{e^{-i\left(k_z^{(+)}\right)_{mn}z}.e^{-i\left(k_z^{*(+)}\right)_{mr}z}\left(k_z^{*(+)}\right)_{mr}}{\left(k_0-\left(k_z^{*(+)}\right)_{mr}M\right)}\hat{\Lambda}_{m,nr}\right\} + \\ &M\left\{\left(\left(A_{mn}^{(+)}\right)^{pos}\left(A_{mr}^{*(+)}\right)^{pos} + \left(A_{mn}^{(+)}\right)^{neg}\left(A_{mr}^{*(+)}\right)^{neg}\right)e^{-i\left(k_z^{(+)}\right)_{mn}z}\,e^{-i\left(k_z^{*(+)}\right)_{mr}z}\times\right. \\ &\left.\times\frac{\left(k_z^{(+)}\right)_{mn}\left(k_z^{*(+)}\right)_{mr}}{\left(k_0-\left(k_z^{(+)}\right)_{mn}M\right)\left(k_0-\left(k_z^{*(+)}\right)_{mr}M\right)}\hat{\Lambda}_{m,nr}\right\} + \\ &M\left\{\left(\left(A_{mn}^{(+)}\right)^{pos}\left(A_{mr}^{*(+)}\right)^{pos} + \left(A_{mn}^{(+)}\right)^{neg}\left(A_{mr}^{*(+)}\right)^{neg}\right)e^{-i\left(k_z^{(+)}\right)_{mn}z}\,e^{-i\left(k_z^{*(+)}\right)_{mr}z}\hat{\Lambda}_{m,nr}\right\} + \\ &\left.M^2\left\{\left(\left(A_{mn}^{(+)}\right)^{pos}\left(A_{mr}^{*(+)}\right)^{pos} + \left(A_{mn}^{(+)}\right)^{neg}\left(A_{mr}^{*(+)}\right)^{neg}\right)e^{-i\left(k_z^{(+)}\right)_{mn}z}e^{-i\left(k_z^{*(+)}\right)_{mr}z}\frac{\left(k_z^{(+)}\right)_{mn}}{\left(k_0-\left(k_z^{(+)}\right)_{mn}M\right)}\hat{\Lambda}_{m,nr}\right\}\right] \end{aligned} \tag{2.91}$$

where the factor $\hat{\Lambda}_{m,nr}$ is defined as

$$\hat{\Lambda}_{m,nr} = \frac{1}{a^2}\int_0^a J_m\left(k_{mn}^{(+)}r\right)J_m\left(k_{mr}^{*(+)}r\right)r\,dr \tag{2.92}$$

These integrals have closed form solution. Also note that the double summation in n and r has to be done because of the fact that the modes in the lined duct with flow are not orthogonal. Then, the cross terms $\hat{\Lambda}_{m,nr}$ for $n \neq r$ do not vanish. The power computation of a negative propagating sound field is derived in Appendix E.

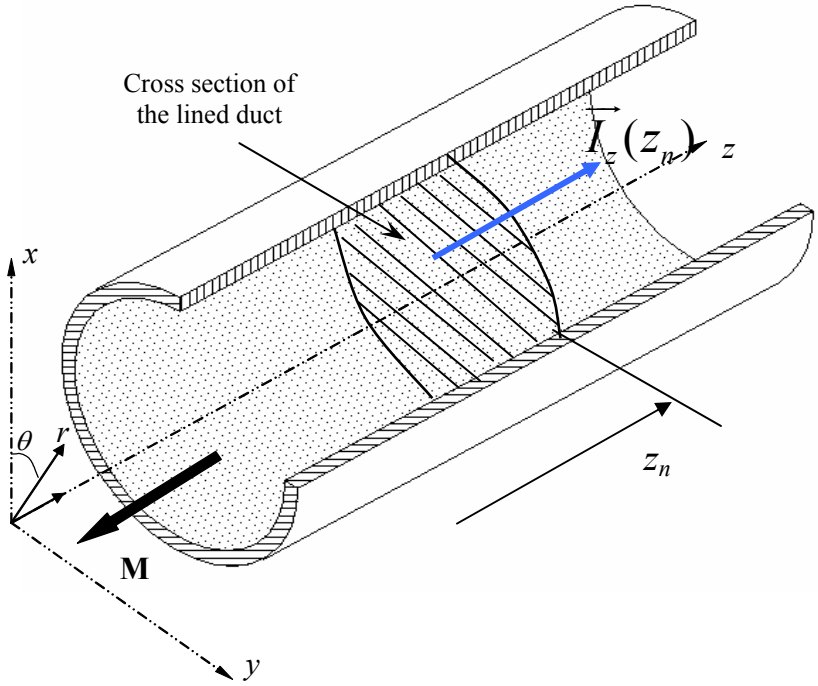

Figure 2.19: Acoustic axial intensity at a fixed duct cross section.

2.5 Potential Applications of the Sound Radiation Model

The mathematical model for sound radiation developed in this dissertation can be used to investigate many problems of practical significance in turbofan engine noise. These potential applications are concerned with the discontinuities in liners such as due to active noise control actuators, Helmholtz or HQ resonators, the scattering effects of liner splices, the effect of non-uniform wall impedance distributions and so forth. Therefore, the considered discontinuity can be replaced by a sector moving boundary that radiates sound into the lined circular duct with certain intensity. In fact, the main difference from one case to another is given by the intensity of the sound radiated by such device. In other words, each application will require a different way of computing the source velocity or strength required by the model.

The case of the effect of liner splices with no penetration properties is a typical example that can show the potential use of this formulation, i.e. hard wall splices in the liner surface. These discontinuities can be produced in turbofan inlet liners by the presence of flow sensors or the structural strips separating adjacent liner panels. As a consequence, this will always lead to reflection of acoustic energy back towards the fan and scatter of energy among both circumferential and radial propagating modes. The case of a single rigid patch can be modeled as a piston source vibrating with a certain velocity V_p, which needs to be determined. The fact that the patch is rigid implies that the radial particle velocity must vanish at its surface. For this case, the piston velocity V_p must be the strength of a fictitious source required to cancel the existing particle velocity due to the disturbance on the surface of the patch. This condition implies satisfying the following condition

$$v_{r_{dist}}\left(\vec{r}_n\right) + v_{r_{piston}}\left(\vec{r}_n\right) + V_p = 0 \tag{2.93}$$

where $v_{r_{piston}}$ is the particle velocity induced by the piston and $\vec{r}_n$ is the location of the patch. In addition, the formulation of a single squared shaped piston can be extended to the case of complex shapes by breaking the patch into smaller basic pistons. The analysis for a single patch can then be extended for the case of several rigid wall patches. Since the problem is linear, the effect of the rigid patches is superposed to obtain the resulting sound field. An example consisting of a circumferential array of rigid patches mounted on the wall of the lined duct is illustrated in Figure 2.20. The application of this model to the combination HQ-Liner will be presented in the next chapter.

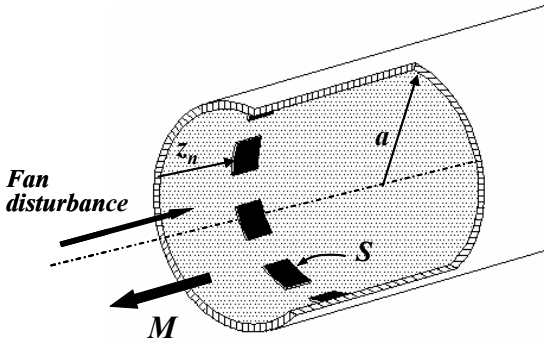

Figure 2.20: Lined duct with a single circumferential array of rigid patches.

Chapter 3 HQ-Liner Model

This chapter presents the development of a model to predict the HQ-Liner performance. This model is based on the mathematical formulation of Chapter 2. The technique consists in first separating the HQ tubes from the liner and solving for the sound field in both systems separately, i.e. in the HQ tubes and duct systems. The interface of the HQ tubes with the duct is modeled as piston sources with unknown velocity radiating sound into the duct. Then, the systems are coupled together by matching the acoustic impedance at the interfaces to find the motion of the piston sources. The resultant sound field in the duct can then be determined. This modeling approach is described in more details in section 3.1.

The sound field in the duct is presented first in section 3.2, including the effect of the fan sound disturbance plus the sound generated by several arrays of circumferential vibrating pistons located at the duct walls. The sound field inside the HQ tubes is assumed to be composed of plane waves. The relationship between the acoustic variables at the two ports of the HQ tube is referred as the dynamics of the HQ tube. The dynamics of the HQ tube are derived using a theoretical model in section 3.3. The model of the HQ tubes and the duct are later coupled in section 3.4.

The performance of the HQ-Liner can be studied by superposing the effects of the fan sound disturbance with the sound generated by the HQ tubes at a certain plane in the duct. The formulation of the transmitted sound is presented in section 3.5. In order to obtain a more realistic model for the sound field inside HQ tubes, the dynamics of the tube are investigated experimentally. The **experimental determination of the HQ tube dynamics is an original contribution of this dissertation** and is presented in Section

3.6. In addition, a simplification of the HQ-Liner model to a two-dimensional formulation is derived in Section 3.7. This formulation is intended to reduce the computation time of the piston source velocities.

3.1 Modeling Approach

The modeling approach for the HQ-Liner system mounted on the inlet liner of a turbofan engine is presented in this section. Figure 3.1a is a depiction of the combined HQ-Liner system installed on a real fan casing. The noise generated by the fan propagates upstream and it will be partially reflected back towards the fan due to the discontinuity introduced by the HQ system. Some of the sound will continue propagating upstream towards the inlet opening. In the model presented here, the sound reflections at the open end of the inlet and at the fan are neglected. Therefore, the inlet of the turbofan engine is modeled as an infinite lined-wall circular duct with flow as shown in Figure 3.1b.

Thus, the problem to solve is that of the propagation of acoustic modes in a circular lined duct with flow and circumferential arrays of HQ waveguides mounted at the wall. The duct has radius "*a*" and the flow is assumed to be uniform. Also, the aerodynamic interactions between the fan blades and the tube-duct interfaces will be neglected. Figure 3.1b shows a schematic of the model in conjunction with the cylindrical coordinate system $\vec{r} = (r, \theta, z)$. Note that the positive *z*-coordinate is assumed to be pointing out of the fan face. Consequently, the flow direction is considered to be opposite to the positive sound propagation, i.e. incoming into the inlet.

a) HQ system mounted on a <u>real</u> inlet liner of the turbofan engine

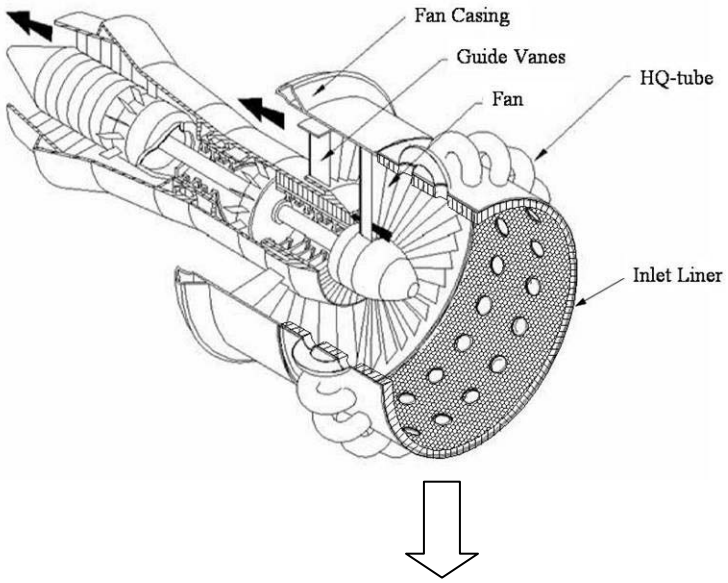

b) <u>Model:</u> Infinite lined-wall duct with HQ system

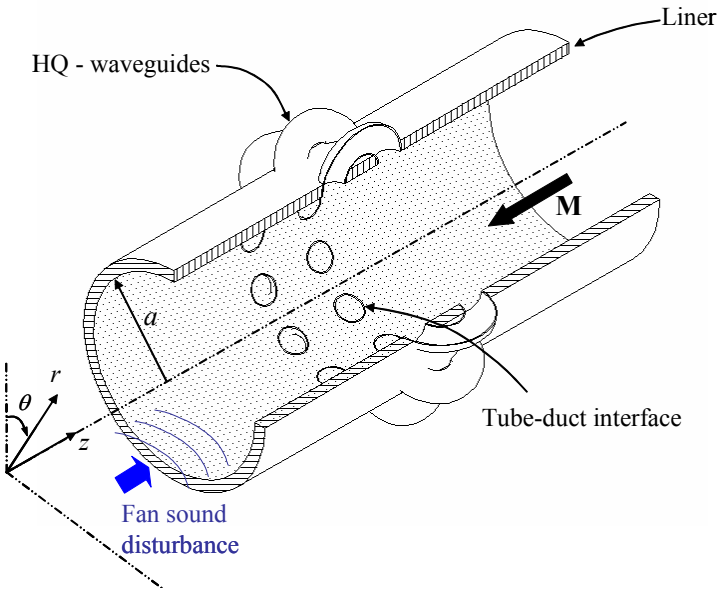

Figure 3.1: HQ-Liner System Model. a) HQ system mounted on the inlet liner of the turbofan engine and b) Infinite lined-wall duct with HQ system.

The technique used in the modeling approach is illustrated in Figure 3.2. The HQ waveguides or tubes are separated from the duct at the interface, i.e. tube-duct interfaces, yielding two dynamic systems as indicated in Figure 3.2b,c. The effect of the HQ-waveguides on the duct sound field is modeled as piston sources with unknown

velocities. This assumption limits the model capabilities to frequencies below the first transversal resonance, i.e. lowest mode cut-off frequency of the tube. The equations of motion for the duct (including the pistons) and the tubes are then derived independently. The duct and HQ-waveguide models are subsequently coupled by matching the acoustic variables at the interfaces. This coupling yields a complex, non-symmetric linear system of equations that are solved for the piston source motion which in turn are used to solve for the sound fields in the system. This modeling process involves several steps and they are described in more detail in the following sections.

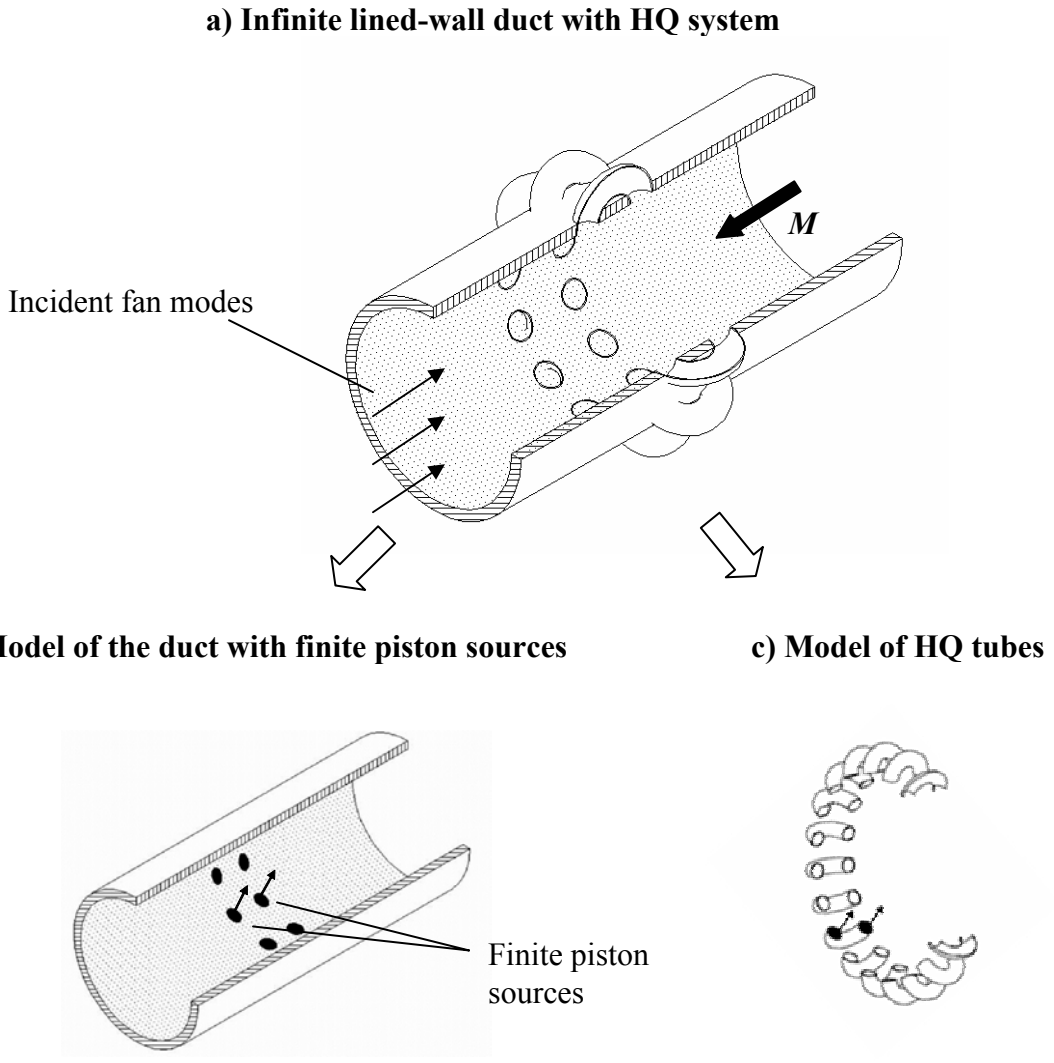

Figure 3.2: Modeling approach. a) infinite lined-wall duct. Model of sound fields b) inside the duct and c) inside the HQ tubes are developed individually.

3.2 Duct Sound Field: Disturbance and Piston Sources

The sound field in the lined duct due to the fan disturbance and circumferential arrays of piston sources, which account for the effect of the HQ tubes, is presented in this section. The pressure field inside the duct is expressed using the mathematical formulation developed in Chapter 2. This formulation is based on solving the linear acoustic wave equation inside a lined circular duct with constant mean flow. As a consequence, the sound field in the duct can be expressed as a linear superposition of the disturbance, i.e. upstream propagating noise generated by the fan, and the sound generated by the arrays of pistons that propagates in both upstream and downstream directions. That is, the pressure in the duct is given as

$$p(\vec{r}) = p_{dist}(\vec{r}) + \sum_{\ell}^{N_{pist}} p_{piston}^{\ell}(\vec{r}) \tag{3.1}$$

where $p_{dist}(\vec{r})$ is the pressure due to the disturbance, $p_{piston}^{\ell}(\vec{r})$ is the pressure due to the ℓ^{th} piston source, and $N_{pist.}$ is the number of pistons, i.e. twice the number of HQ tubes. The expressions for these two components are presented in the following sub-sections.

3.2.1 Disturbance Sound Field

In general, the sound field in a lined duct with flow is expressed as a linear combination of the acoustic modes present in the duct as follows

$$p(\vec{r}) = \sum_{m}\sum_{n} A_{mn}^{(+)}\Phi_{mn}^{(+)}(r,\theta)e^{-ik_z^{(+)}z}e^{i\omega t} + \sum_{m}\sum_{n} A_{mn}^{(-)}\Phi_{mn}^{(-)}(r,\theta)e^{-ik_z^{(-)}z}e^{i\omega t} \tag{3.2}$$

where the superscripts (+) and (-) indicate variables associated to positive and negative z-direction propagation, respectively. Thus, $A_{mn}^{(+)}$ and $A_{mn}^{(-)}$ are the complex modal amplitudes, $k_z^{(+)}$ and $k_z^{(-)}$ are the mode axial wavenumbers, and $\Phi_{mn}^{(+)}$ and $\Phi_{mn}^{(-)}$ are the acoustic modes corresponding the mn^{th} mode propagating in the positive and negative z-direction, respectively. The subscripts m and n refer to the circumferential and radial mode order, respectively. The fan disturbance is considered to be composed of only

positive z-direction spinning propagating modes. Then, it can be expressed by the first term in equation (3.2) as follows:

$$p_{dist}\left(\vec{r}\right)=\sum_{m=0}^{M_d}\sum_{n=0}^{N_d}\left(A_{mn}^{(+)}\right)_{dist}\Phi_{mn}^{(+)}\left(r,\theta\right)e^{-ik_z^{(+)}z}e^{i\omega t} \tag{3.3}$$

where the complex amplitude of the disturbance modes $\left(A_{mn}^{(+)}\right)_{dist}$ are assumed to be known. It is also assumed that there are disturbance modes spinning in both azimuthal directions. Thus, the disturbance modes take the form of $\Phi_{mn}^{(+)}\left(r,\theta\right)=J_m\left(k_{mn}^{(+)}r\right)e^{-im\theta}$ or $\Phi_{mn}^{(+)}\left(r,\theta\right)=J_m\left(k_{mn}^{(+)}r\right)e^{im\theta}$ for the (+) and (–) spinning θ-directions, respectively.

3.2.2 Piston Source Sound Field

As mentioned in section 3.1, the interfaces of the HQ-waveguides and the duct are modeled as piston sources radiating sound into the duct. As described in Chapter 2, the pistons are assumed to have a rectangular shape defined by constant values of the cylindrical coordinates, as shown in Figure 3.3.

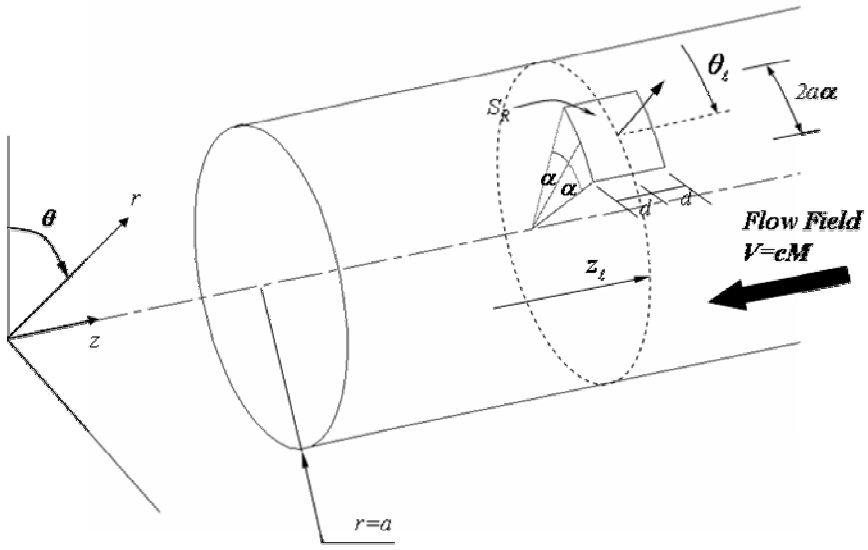

Figure 3.3: Modeling HQ-duct interfaces as rectangular shaped piston source.

The sound field generated by a piston source located at $\vec{r}_\ell = (a, \theta_\ell, z_\ell)$ vibrating with a known velocity V_p^ℓ was derived in Chapter 2. From section 2.3.1, the pressure field due to the piston source, depending on the relative location between the piston and the observer, is given as

$$p_{piston}^{\ell(+)}\left(\vec{r}\,\middle|\,\vec{r}_\ell\right) = Z^{(+)}\left(\vec{r}\,\middle|\,\vec{r}_\ell\right)\cdot V_p^\ell = -i\rho c\, V_p^\ell \sum_m^M \sum_n^N \frac{\left(k_0 - k_z^{(+)} M\right)^2}{k_0} \int_{z_\ell - d}^{z_\ell + d} \int_{\theta_\ell - \alpha}^{\theta_\ell + \alpha} g_{mn}^{(+)}\left(\vec{r}\,\middle|\,\vec{r}_\ell\right) a\, d\theta\, dz \tag{3.4)a}$$

for $z \geq z_\ell + d$, and

$$p_{piston}^{\ell(-)}\left(\vec{r}\,\middle|\,\vec{r}_\ell\right) = Z^{(-)}\left(\vec{r}\,\middle|\,\vec{r}_\ell\right)\cdot V_p^\ell = -i\rho c\, V_p^\ell \sum_m^M \sum_n^N \frac{\left(k_0 - k_z^{(-)} M\right)^2}{k_0} \int_{z_\ell - d}^{z_\ell + d} \int_{\theta_\ell - \alpha}^{\theta_\ell + \alpha} g_{mn}^{(-)}\left(\vec{r}\,\middle|\,\vec{r}_\ell\right) a\, d\theta\, dz \tag{3.4)b}$$

for $z \leq z_\ell - d$. Note that these expressions are valid when the observation point $\vec{r}$ is upstream or downstream of the source. One more case has to be considered for the observer axially located at the same position as the piston, i.e. $z_\ell - d \leq z \leq z_\ell + d$. The expression for this condition is

$$p_{piston}^{\ell}\left(\vec{r}\,\middle|\,\vec{r}_\ell\right) = Z\left(\vec{r}\,\middle|\,\vec{r}_\ell\right)\cdot V_p^\ell = -i\rho c\, V_p^\ell \sum_m^M \sum_n^N \left\{ \frac{\left(k_0 - k_z^{(+)} M\right)^2}{k_0} \int_{z_\ell - d}^{z} \int_{\theta_\ell - \alpha}^{\theta_\ell + \alpha} g_{mn}^{(+)}\left(\vec{r}\,\middle|\,\vec{r}_\ell\right) a\, d\theta\, dz + \right.$$
$$\left. + \frac{\left(k_0 - k_z^{(-)} M\right)^2}{k_0} \int_{z}^{z_\ell + d} \int_{\theta_\ell - \alpha}^{\theta_\ell + \alpha} g_{mn}^{(-)}\left(\vec{r}\,\middle|\,\vec{r}_\ell\right) a\, d\theta\, dz \right\} \tag{3.4)c}$$

where *M* and *N* are the maximum number of terms to be included in the series expansion and the modal components $g_{mn}^{(+)}$ and $g_{mn}^{(-)}$ of the Green's functions were explicitly derived in Chapter 2. As seen in these expressions, the pressure radiated by a piston can be expressed in a compact form in terms of a transfer function $Z\left(\vec{r}\,\middle|\,\vec{r}_\ell\right)$, which certainly has units of acoustic impedance. This function is similarly chosen according to the relative location between the piston and the observer. In addition, the integrals in

equations (3.4) have the closed form expressions in (2.78), (2.81) and (2.84) also derived in Chapter 2.

The pressure due to an array of pistons will then be the linear combination of the effect of every single piston as

$$p_{piston}(\vec{r}) = \sum_{\ell}^{N_{pist.}} Z\left(\vec{r}\,\middle|\,\vec{r}_{\ell}\right) \cdot V_p^{\ell} \tag{3.5}$$

in terms of the impedance functions $Z\left(\vec{r}\,\middle|\,\vec{r}_{\ell}\right)$. As shown in the next section, the pressure due to the array of pistons can be computed, in particular, at the face of every piston in the array. To this end, the **average pressure** is computed over a source due to another piston source with unit velocity, i.e. to obtain impedance functions between piston sources. The average pressure over a piston source ("output or observer") due to another source ("input or source") with unit velocity is obtained by appropriately integrating the expressions in equations (2.78), (2.81) and (2.84) over the observer piston. The resultant impedance functions are denoted as $Z_{os}\left(\vec{r}_o\,\middle|\,\vec{r}_s\right)$.

3.2.3 Combination of Disturbance and Piston Source Sound Fields

This section combines the pressure fields due to the disturbance and piston sources at the face of all the vibrating pistons in a circumferential array. As sketched in Figure 3.2b, the array of pistons represents the interfaces between the duct and the HQ tubes. In order to appropriately formulate a model for the HQ-Liner, the unknown piston velocities V_p^{ℓ} have to be found. As mentioned before, this formulation requires computing the average pressure due to the array of piston sources on each piston face in the array and express it in matrix form. The matrix of this "average" impedance coefficients Z_{os} will be found in closed form in Section 3.4.1. Also, the average pressure due to the disturbance on the piston faces has to be considered in the formulation. Then, the total average pressure over each piston, i.e. due to both the fan disturbance and piston interaction, is given by

$$\begin{Bmatrix} \langle p \rangle_{1i} \\ \langle p \rangle_{1o} \\ \vdots \\ \langle p \rangle_{Ni} \\ \langle p \rangle_{No} \end{Bmatrix}_{2N\times 1} = \begin{bmatrix} & & \\ & Z_{os} & \\ & & \end{bmatrix}_{2N\times 2N} \begin{Bmatrix} V_{p_{1i}} \\ V_{p_{1o}} \\ \vdots \\ V_{p_{Ni}} \\ V_{p_{No}} \end{Bmatrix}_{2N\times 1} + \begin{Bmatrix} \langle p \rangle_{1i}^{dist} \\ \langle p \rangle_{1o}^{dist} \\ \vdots \\ \langle p \rangle_{Ni}^{dist} \\ \langle p \rangle_{No}^{dist} \end{Bmatrix}_{2N\times 1} \tag{3.6}$$

In this equation, the elements of matrix $[Z_{os}]$ represents the average pressure over piston source "o" due to piston source "s" as described in section 3.2.2. Thus, the dimension of this matrix is *2N*x*2N* since there are N HQ tubes each having two interfaces with the duct. The sub-indices *i/o* inside the average pressure vectors is used to identify the two interfaces of a tube with the duct, i.e. input and output.

3.3 HQ Tube Model

In this section, the model of the acoustic field inside the HQ tubes is derived independently from the duct as illustrated in Figure 3.2c. The HQ tubes can be considered as a two-port resonating acoustic device. Similarly to the previous section, the HQ model requires to relate the two ports of this dynamic system in order to solve for the motion of the piston sources. To this end, the acoustic variables, i.e. pressure and particle velocity, must be considered at the two open ends of the HQ tubes. The relation between these variables can be expressed in terms of a 2×2 matrix as

$$\begin{Bmatrix} p_{\ell i}^t \\ p_{\ell o}^t \end{Bmatrix} = \left[Z_\ell^t \right] \begin{Bmatrix} v_{\ell i}^t \\ v_{\ell o}^t \end{Bmatrix} \tag{3.7}$$

where the sub-indices *i/o* are used to identify the input and output of the HQ tube. In the case of an array of HQ tubes, a single matrix equation can be arranged as

$$\begin{Bmatrix} p_{1i}^t \\ p_{1o}^t \\ \vdots \\ p_{Ni}^t \\ p_{No}^t \end{Bmatrix}_{2N\times 1} = \begin{bmatrix} [Z_1^t] & 0 & 0 & 0 & 0 \\ 0 & [Z_2^t] & \ddots & \ddots & 0 \\ 0 & \ddots & \ddots & \ddots & 0 \\ 0 & \ddots & \ddots & \ddots & 0 \\ 0 & 0 & 0 & 0 & [Z_N^t] \end{bmatrix}_{2N\times 2N} \begin{Bmatrix} v_{1i}^t \\ v_{1o}^t \\ \vdots \\ v_{Ni}^t \\ v_{No}^t \end{Bmatrix}_{2N\times 1} \tag{3.8}$$

Note that the 2×2 elements $\left[Z_\ell^t\right]$ of the matrix in (3.8) correspond to the different HQ tubes in the array. The crossed terms of the assembled matrix are zero because the sound field inside one HQ tube is independent from the rest, i.e. they are related only through the duct sound field.

In order to obtain an expression for the matrix $\left[Z_\ell^t\right]$, the HQ tubes are assumed to be straight tubes with uniform cross section and no flow. This model was previously investigated by Hallez *et al.* [56]. The sound field that propagates inside the HQ tubes is considered to be composed only by plane waves. This assumption leads to obtain a simple relation for the pressure and particle velocity at the tube ends. In addition, impedance layers are included at both ends of the tube to account for the effect of the screen used at the tube-duct interfaces to prevent vortex shedding. The acoustic property of these layers is defined by the screen impedance $\boldsymbol{Z}_{ps}$ which includes the non-linear effect of the duct flow and the noise level. Figure 3.4 shows a schematic of the straight tube model with two plane waves defined in terms of the local coordinate system ξ. It is important to remark that the plane wave assumption is only valid below the first cut-off frequency of the tube.

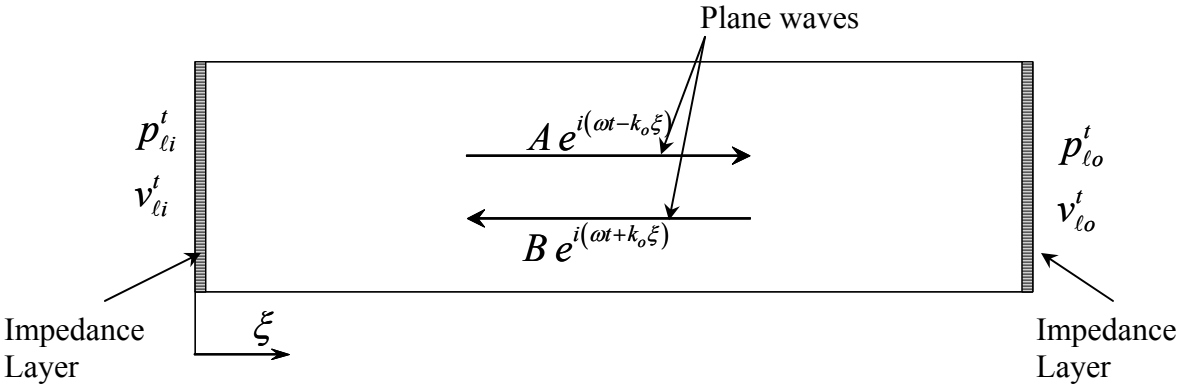

Figure 3.4: HQ **t**ube model as a straight tube with plane waves.

The acoustic variables, i.e. pressure $p_{\ell i}^t$ and $p_{\ell o}^t$ and particle velocity $v_{\ell i}^t$ and $v_{\ell o}^t$, at the ends of the ℓ^{th} tube can then be related using a transfer matrix as [56]

$$\begin{Bmatrix} p_{\ell i}^t \\ \rho c v_{\ell i}^t \end{Bmatrix} = \left[T_{io}^t \right] \begin{Bmatrix} p_{\ell o}^t \\ \rho c v_{\ell o}^t \end{Bmatrix} = \begin{bmatrix} 1 & \dfrac{Z_{ps}}{\rho c} \\ 0 & 1 \end{bmatrix} \begin{bmatrix} \cos(k_o L) & i\sin(k_o L) \\ i\sin(k_o L) & \cos(k_o L) \end{bmatrix} \begin{bmatrix} 1 & \dfrac{Z_{ps}}{\rho c} \\ 0 & 1 \end{bmatrix} \begin{Bmatrix} p_{\ell o}^t \\ \rho c v_{\ell o}^t \end{Bmatrix} \tag{3.9}$$

which includes the presence of the perforated screens. Equation (3.9) can be rearranged to relate the pressure on one side of the equation and particle velocity on the other as in (3.7). Then, the matrix $\left[Z_\ell^t \right]$ for a single HQ tube is obtained as

$$\left[Z_\ell^t \right] = \rho c \begin{bmatrix} \dfrac{T_{11}^t}{T_{21}^t} & \dfrac{T_{12}^t T_{21}^t - T_{11}^t T_{22}^t}{T_{21}^t} \\ \dfrac{1}{T_{21}^t} & -\dfrac{T_{22}^t}{T_{21}^t} \end{bmatrix} \tag{3.10}$$

where T_{io}^t are the coefficients from the transfer matrix in (3.9). This impedance matrix can also be obtained by using other alternative approaches. For instance, a more realistic model may be developed by including the effect of the bends of the HQ tubes. However, a formulation of this kind would be of great mathematical complexity. Instead, the experimental measurement of the acoustic variables at the HQ tube ends provides a practical method to accurately obtain the matrix $\left[Z_\ell^t \right]$. This experimental procedure will be developed in this dissertation and presented in section 3.6.

3.4 Tube-Duct Coupling

The sound fields inside the duct due to both the disturbance and the piston sources (see section 3.2 and Figure 3.2-b) and inside the HQ tubes (see section 3.3 and Figure 3.2-c) were developed separately. In this section, these models are combined to find an expression for the particle velocity of the piston sources, i.e. coupled tube-duct system. The model for the coupled tube-duct system is obtained by matching:

(i) the average pressure on the surface of the source to the pressure in the tube, i.e. $\langle p \rangle_{\ell i} = p_{\ell i}^t$ and $\langle p \rangle_{\ell o} = p_{\ell o}^t$, and

(ii) the average particle velocity on the surface of the source to the particle velocity in the tube, $\langle v \rangle_{\ell i} = v_{\ell i}^t$ and $\langle v \rangle_{\ell o} = v_{\ell o}^t$.

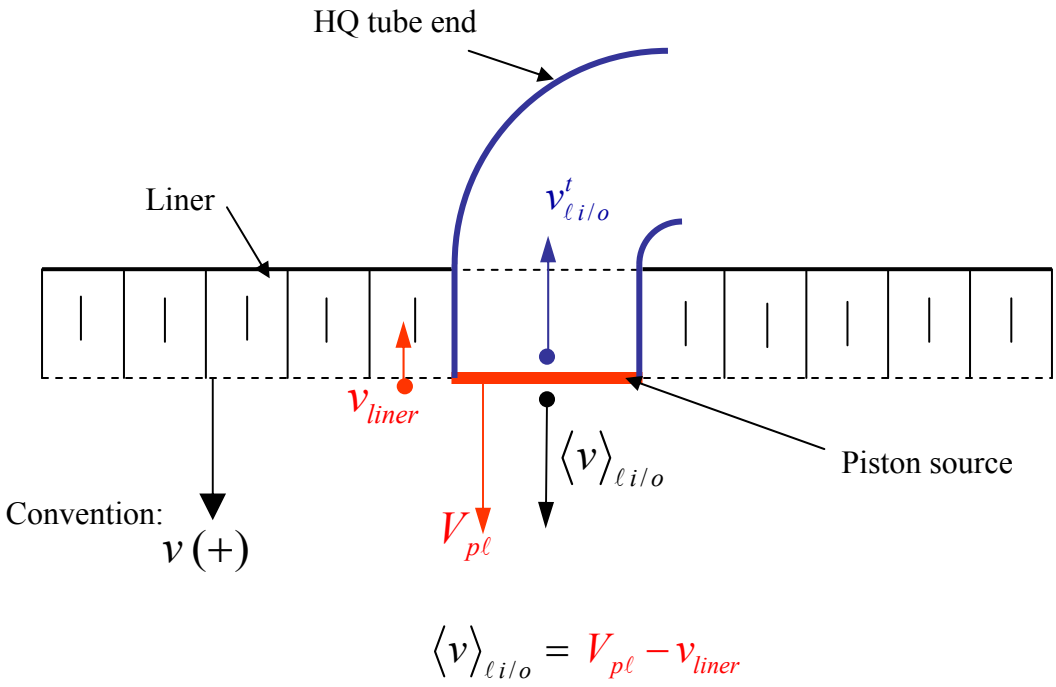

Figure 3.5: Particle and piston velocity relations and positive sign conventions.

It is important to note that in the process of matching the piston source velocity $V_{p\ell}$ to the corresponding tube particle velocity $v^t_{\ell i/o}$, a consistent convention for the positive direction must be kept as shown in Figure 3.5, i.e. pointing towards inside the duct. To this end, the positive particle velocity in the entrance end of the HQ tube at $\xi = 0$ (see Figure 3.4), which is opposite to the positive source velocity, must be reversed by changing the sign of the first column of the matrix in equation in (3.10). If the dynamics of the HQ tubes are experimentally obtained, this correction is not needed since, as it will be shown, the positive velocity convention is towards outside of both HQ tube ends.

In addition, the average particle velocity at the surface of the source has two components that must be differentiated in order to couple correctly the duct with the tube. In the case of the hard wall, it is clear that the average particle velocity $\langle v \rangle_{\ell i}$ at the piston face is the same as the piston velocity $V_{p\ell}$. On the contrary, for the soft wall case, the average particle velocity is composed by the induced particle velocity v_{liner} due to the

soft wall boundary condition and the piston source velocity $V_{p\ell}$. Then, according to the sign conventions adopted in Figure 3.5, the average particle velocity is given by

$$\langle v \rangle_{\ell i/o} = V_{p\ell} - \langle v \rangle_{liner} \tag{3.11}$$

where the particle velocity induced by the soft wall condition is obtained using equation (2.12) as

$$\langle v \rangle_{liner} = \frac{\beta_w}{\rho c} \langle p \rangle \Big|_{\substack{piston \\ face}} \tag{3.12}$$

The first pressure matching condition is imposed by replacing equation (3.8) into the left-hand side of equation (3.6). The second velocity matching conditon is then imposed by setting the tube's particle velocity vector on the left hand side equal to the average particle velocity vector on the right hand side. Then,

$$\begin{aligned} \begin{bmatrix} & Z_{ij}^t & \end{bmatrix}_{2N\times 2N} \left\{ \begin{Bmatrix} V_{p_{1i}} \\ V_{p_{1o}} \\ \vdots \\ V_{p_{Ni}} \\ V_{p_{No}} \end{Bmatrix} - \frac{\beta_w}{\rho c} \begin{Bmatrix} \langle p \rangle_{1i} \\ \langle p \rangle_{1o} \\ \vdots \\ \langle p \rangle_{Ni} \\ \langle p \rangle_{No} \end{Bmatrix} \right\}_{2N\times 1} &= \\ = \begin{bmatrix} & Z_{os} & \end{bmatrix}_{2N\times 2N} \begin{Bmatrix} V_{p_{1i}} \\ V_{p_{1o}} \\ \vdots \\ V_{p_{Ni}} \\ V_{p_{No}} \end{Bmatrix}_{2N\times 1} &+ \begin{Bmatrix} \langle p \rangle_{1i}^{dist} \\ \langle p \rangle_{1o}^{dist} \\ \vdots \\ \langle p \rangle_{Ni}^{dist} \\ \langle p \rangle_{No}^{dist} \end{Bmatrix}_{2N\times 1} \end{aligned} \tag{3.13}$$

The average pressure $\langle p \rangle_{\ell i/o}$ on the left hand side of equation (3.13) must be replaced again in terms of the piston velocities using equation (3.6). Then, reordering (3.13), the following linear system of equations yields to find the unknown piston source velocities as

$$\left(\begin{bmatrix} \\ Z_{io}^{t} \\ \\ \end{bmatrix} - \frac{\beta_w}{\rho c}\begin{bmatrix} \\ Z_{io}^{t} \\ \\ \end{bmatrix}\begin{bmatrix} \\ Z_{os} \\ \\ \end{bmatrix} - \begin{bmatrix} \\ Z_{os} \\ \\ \end{bmatrix}\right)_{2N\times 2N} \begin{Bmatrix} V_{p_{1i}} \\ V_{p_{1o}} \\ \vdots \\ V_{p_{Ni}} \\ V_{p_{No}} \end{Bmatrix}_{2N\times 1} = \begin{Bmatrix} \langle p\rangle_{1i}^{dist} \\ \langle p\rangle_{1o}^{dist} \\ \vdots \\ \langle p\rangle_{Ni}^{dist} \\ \langle p\rangle_{No}^{dist} \end{Bmatrix} + \frac{\beta_w}{\rho c}\begin{bmatrix} \\ Z_{io}^{t} \\ \\ \end{bmatrix}\begin{Bmatrix} \langle p\rangle_{1i}^{dist} \\ \langle p\rangle_{1o}^{dist} \\ \vdots \\ \langle p\rangle_{Ni}^{dist} \\ \langle p\rangle_{No}^{dist} \end{Bmatrix} \tag{3.14}$$

The piston velocities found from the above linear system of equations can then be replaced in equations (3.4) to find the complete sound field along the duct.

3.4.1 Computation of the matrix Z_{os}

This section presents the derivation of closed form expressions of the piston interaction coefficients $Z_{os}\left(\vec{r}_o\,|\vec{r}_s\right)$. To this end, it is required to compute the average pressure over a source due to another piston source with unit velocity, i.e. impedance functions. This average is obtained by integrating the expressions in (3.4) over the surface of a piston as in Figure 3.3. Thus, the average pressure over a piston source "*o*" due to another source "*s*" with unit velocity is simply given by [56]

$$Z_{os} = \frac{1}{S_o}\int_{z_o-d_o}^{z_o+d_o}\int_{\theta_o-\alpha_o}^{\theta_o+\alpha_o}\left[-i\rho c\sum_m\sum_n \frac{\left(k_0 - k_z M\right)^2}{k_0}\int_{S_s} g_{mn}\left(\vec{r_o}\,|\vec{r_s}\right)dS_s\right] a\, d\theta\, dz \tag{3.15}$$

In order to find the closed form expressions for (3.15), equations (2.78), (2.81) and (2.84) are going to be considered. The piston shapes are considered rectangular as shown in Figure 3.3. The solution of (3.15) requires to solve two integrals. The first integral is in the θ-coordinate as

$$\begin{aligned}\int_{\theta_o-\alpha_o}^{\theta_o+\alpha_o}\cos m\left(\theta_o-\theta_s\right) a\, d\tilde{\theta} &= \frac{2a\alpha_o \sin\left(m\alpha_o\right)}{m\alpha_o}\cos m\left(\theta_o-\theta_n\right) \\ &= \kappa_\theta(\alpha_o)\cos m\left(\theta_o-\theta_n\right)\end{aligned} \tag{3.16}$$

while the second integral is with respect to the *z*-coordinate which depends on the location of the observation source "*o*" relative to the "*s*" source. Three cases are possible as illustrated in Figure 3.6a-c.

CASE 1: The observation source "*o*" is downstream of source "*s*", i.e. $z_o - d_o > z_s + d_s$. In this case, equation (2.78) is replaced into (3.15) and the following integral needs to be solved

$$\int_{z_o-d_o}^{z_o+d_o} e^{-ik_z^{(+)}(z-z_s)} \frac{\sin(k_z^{(+)}d_s)}{k_z^{(+)}d_s} 2d_s \, dz = e^{-ik_z^{(+)}(z_o-z_s)} \frac{\sin(k_z^{(+)}d_o)}{k_z^{(+)}d_o} 2d_o \frac{\sin(k_z^{(+)}d_s)}{k_z^{(+)}d_s} 2d_s \tag{3.17}$$

Consequently, the transfer function for this case become

$$\begin{aligned} Z_{os} = -i\frac{\rho c}{S_o} \sum_{m=0}^{M_g}\sum_{n=0}^{N_g} \frac{\left(k_0 - k_z^{(+)}M\right)^2}{k_0} A_{mn}^{(+)} \cos m(\theta_o - \theta_s) J_m\left(k_{mn}^{(+)}a\right) \times \\ \times \kappa_\theta(\alpha_o)\,\kappa_\theta(\alpha_s)\, e^{-ik_z^{(+)}(z_o-z_s)} \frac{\sin(k_z^{(+)}d_o)}{k_z^{(+)}d_o} \, 2d_o \frac{\sin(k_z^{(+)}d_s)}{k_z^{(+)}d_s} \, 2d_s \end{aligned} \tag{3.18}$$

CASE 2: The observation source "*o*" is upstream of source "*s*", i.e. $z_o + d_r < z_o - d_s$. In this case, equation (2.81) is replaced into (3.15) and the following integral needs to be solved

$$\int_{z_o-d_o}^{z_o+d_o} e^{-ik_z^{(-)}(z-z_s)} \frac{\sin(k_z^{(-)}d_s)}{k_z^{(-)}d_s} 2d_s \, dz = e^{-ik_z^{(-)}(z_o-z_s)} \frac{\sin(k_z^{(-)}d_o)}{k_z^{(-)}d_o} 2d_o \frac{\sin(k_z^{(-)}d_s)}{k_z^{(-)}d_s} 2d_s \tag{3.19}$$

Consequently, the transfer function for this case become

$$\begin{aligned} Z_{os} = -i\frac{\rho c}{S_o} \sum_{m=0}^{M_g}\sum_{n=0}^{N_g} \frac{\left(k_0 - k_z^{(-)}M\right)^2}{k_0} A_{mn}^{(-)} \cos m(\theta_o - \theta_s) J_m\left(k_{mn}^{(-)}a\right) \times \\ \times \kappa_\theta(\alpha_o)\,\kappa_\theta(\alpha_s)\, e^{-ik_z^{(-)}(z_o-z_s)} \frac{\sin(k_z^{(-)}d_o)}{k_z^{(-)}d_o} \, 2d_o \frac{\sin(k_z^{(-)}d_s)}{k_z^{(-)}d_s} \, 2d_s \end{aligned} \tag{3.20}$$

CASE 3: The observation source "*o*" is at the same location as source "*s*". In addition, we assume they have same dimensions, i.e. $d_o = d_s$. In this case, eq. (2.84) is replaced into (3.15) and solving the following integrals

$$\int_{z_o-d_o}^{z_o+d_o} \frac{1-e^{-ik_z^{(+)}(z-z_s+d_s)}}{ik_z^{(+)}} dz = \frac{2d_o}{ik_z^{(+)}} + \frac{1-e^{-ik_z^{(+)}2d_o}}{\left(k_z^{(+)}\right)^2} \tag{3.21}$$

$$\int_{z_r-d_r}^{z_r+d_r} -\frac{1-e^{-ik_z^{(-)}(z-z_s-d_s)}}{ik_z^{(-)}} dz = -\frac{2d_r}{ik_z^{(-)}} + \frac{1-e^{-ik_z^{(-)}2d_r}}{\left(k_z^{(-)}\right)^2} \tag{3.22}$$

Thus, the transfer function Z_{os} is

$$\begin{aligned} Z_{os} = -i\,\rho c \sum_{m=0}^{M_g}\sum_{n=0}^{N_g} \Bigg\{ & \frac{\left(k_0 - k_z^{(+)}M\right)^2}{k_0} A_{mn}^{(+)} \cos m\left(\theta_o-\theta_s\right) J_m\left(k_{mn}^{(+)}\right) \times \\ & \times \kappa_\theta(\alpha_o)\kappa_\theta(\alpha_s)\left(\frac{2d_o}{ik_z^{(+)}} + \frac{1-e^{-ik_z^{(+)}2d_o}}{\left(k_z^{(+)}\right)^2}\right) + \\ & + \frac{\left(k_0 - k_z^{(-)}M\right)^2}{k_0} A_{mn}^{(-)} \cos m\left(\theta_o-\theta_s\right) J_m\left(k_{mn}^{(-)}\right) \times \\ & \times \kappa_\theta(\alpha_o)\kappa_\theta(\alpha_s)\left(-\frac{2d_o}{ik_z^{(-)}} + \frac{1-e^{-ik_z^{(-)}2d_o}}{\left(k_z^{(-)}\right)^2}\right) \Bigg\} \end{aligned} \tag{3.23}$$

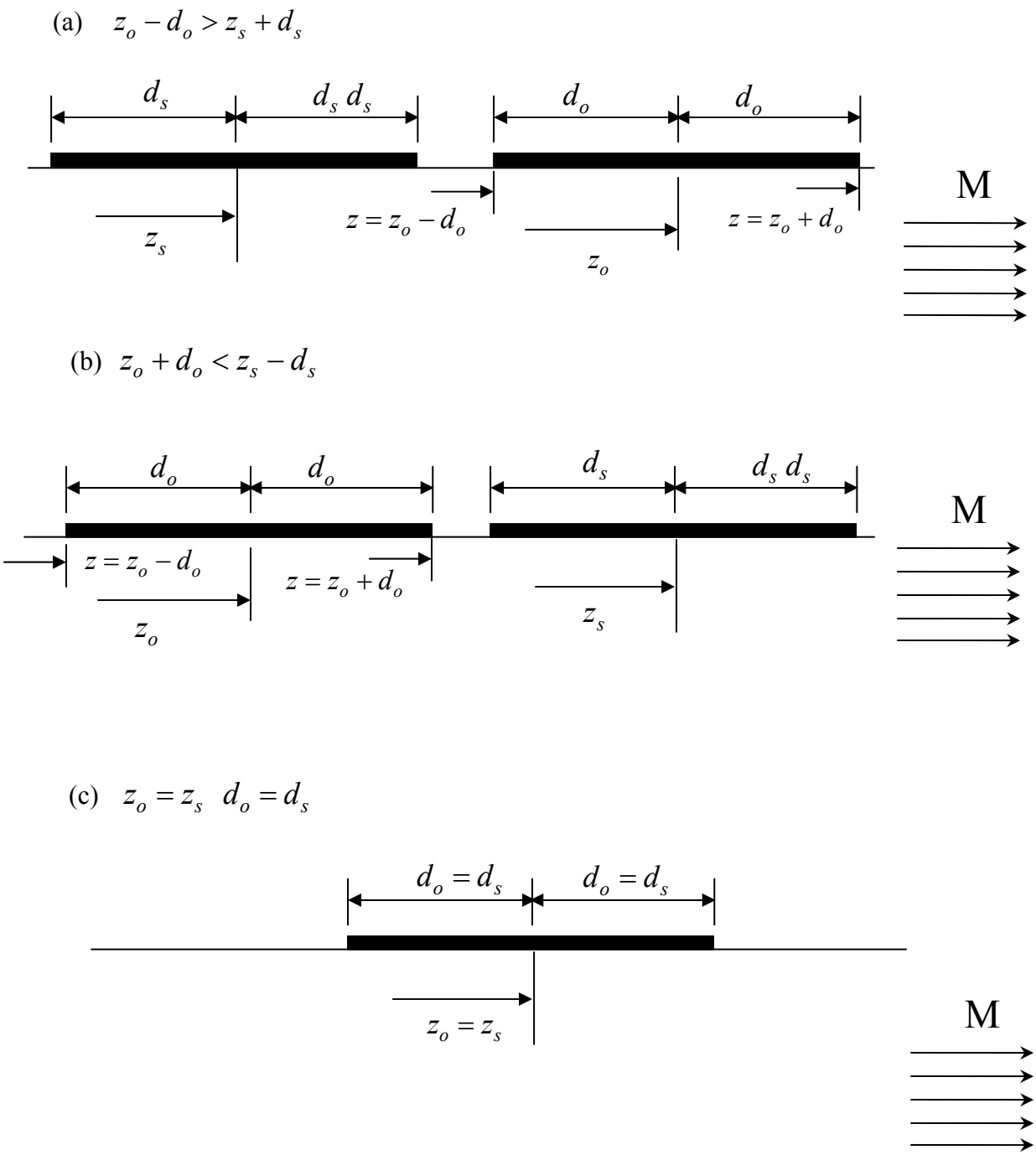

Figure 3.6: (a) case 1: observation source *"o"* is downstream of the source *"s"*
(b) case 2: observation source *"o"* is upstream of the source *"s"*
(c) case 3: observation source *"o"* and source *"s"* at same axial location.

3.5 Performance of the HQ-Liner

In this section, the performance of the HQ-liner system is determined in terms of the total transmitted sound through a particular duct cross section. As indicated in section 3.2, the duct pressure field is due to the superposition of the fan disturbance and the piston sources. The transmitted pressure field can be written in terms of positive and negative spinning modes as follows

$$p_{trans} = \sum_{m=0}^{M_s}\sum_{n=0}^{N_s}\left(A_{mn}^{(+)}\right)_{hq}^{pos} J_m\left(k_{mn}^{(+)}r\right)e^{-im\theta}e^{-ik_z^{(+)}z} + \sum_{m=0}^{M_s}\sum_{n=0}^{N_s}\left(A_{mn}^{(+)}\right)_{hq}^{neg} J_m\left(k_{mn}^{(+)}r\right)e^{im\theta}e^{-ik_z^{(+)}z} \quad (3.24)$$

where $\left(A_{mn}^{(+)}\right)_{hq}^{pos}$ and $\left(A_{mn}^{(+)}\right)_{hq}^{neg}$ are the modal amplitudes of the positive and negative spinning modes (propagating in the positive z-direction), respectively. These amplitudes account for the effects of both the liner and HQ tubes and can be expressed as

$$\left(A_{mn}^{(+)}\right)_{hq}^{pos} = \left(A_{mn}^{(+)}\right)_{d}^{pos} + \sum_{r=1}^{N_s}\left(A_{mn}^{(+)}\right)_{r}^{pos} V_{p_r} \quad (3.25)a$$

$$\left(A_{mn}^{(+)}\right)_{hq}^{neg} = \left(A_{mn}^{(+)}\right)_{d}^{neg} + \sum_{r=1}^{N_s}\left(A_{mn}^{(+)}\right)_{r}^{neg} V_{p_r} \quad (3.25)b$$

The modal amplitudes $\left(A_{mn}^{(+)}\right)_{d}^{pos}$ and $\left(A_{mn}^{(+)}\right)_{d}^{neg}$ are the known amplitudes of the spinning modes included in the disturbance. The source velocities V_{p_r} are obtained from the solution of the system of equations in (3.14). The objective of this section is to derive an expression for $\left(A_{mn}^{(+)}\right)_{r}^{pos}$ and $\left(A_{mn}^{(+)}\right)_{r}^{neg}$. The first step is to write the expression of the transmitted pressure as the linear superposition in (3.1)

$$p_{trans}(r,\theta,z) = p_d(r,\theta,z) + \sum_{r=1}^{N_s} p\ (r,\theta,z\,|\,r_r,\theta_r,z_r) \quad (3.1)$$

As mentioned before, the modal amplitudes of the pressure p_d due to the disturbance are assumed to be known as $\left(A_{mn}^{(+)}\right)_{d}^{pos}$ and $\left(A_{mn}^{(+)}\right)_{d}^{neg}$. The pressure produced by the r^{th} source with a unit velocity at the transmitted location, i.e. downstream of the source, is obtained from the finite piston radiation formula in equation (2.78) as

$$p(r,\theta,z\,|\,a,\theta_r,z_r) = -i\,\rho c \sum_{m=0}^{M_g}\sum_{n=0}^{N_g} \frac{\left(k_0 - k_z^{(+)}M\right)^2}{k_0} A_{mn}^{(+)}\ \cos m\left(\theta-\theta_r\right) J_m\left(k_{mn}^{(+)} r\right) \times \\ \times \kappa_\theta(\alpha)\ e^{-ik_z^{(+)}(z-z_r)}\ \frac{\sin(k_z^{(+)}d_r)}{k_z^{(+)}d_r}\ 2d_r \tag{3.26}$$

The Green's functions modal amplitudes $A_{mn}^{(+)}$ in equation (3.26) are determined from the linear system of equations in (2.45). The sound field created by the r^{th} piston source is non-spinning and symmetric with respect to $\theta=\theta_r$. However, it can be written as a set of positive and negative spinning modes by using the following trigonometric relationship

$$\cos m\left(\theta-\theta_r\right) = e^{-im\theta}\left(\frac{e^{im\theta_r}}{2}\right) + e^{im\theta}\left(\frac{e^{-im\theta_r}}{2}\right) \tag{3.27}$$

Thus, equation (3.26) can be written as

$$p\ (r,\theta,z\big|r_r,\theta_r,z_r) = \sum_{m=0}^{M_g}\sum_{n=0}^{N_g} (A_{mn}^{(+)})_r^{pos} J_m\left(k_{mn}^{(+)} r\right) e^{-im\theta} e^{-ik_z^{(+)}z} \\ + \sum_{m=0}^{M_g}\sum_{n=0}^{N_g} (A_{mn}^{(+)})_r^{neg} J_m\left(k_{mn}^{(+)} r\right) e^{+im\theta} e^{-ik_z^{(+)}z} \tag{3.28}$$

where $\left(A_{mn}^{(+)}\right)_r^{pos}$ and $\left(A_{mn}^{(+)}\right)_r^{neg}$ are the complex amplitude of transmitted modes spinning in the positive and negative direction, respectively, due to source "*r*". These amplitudes are given from (3.26) and (3.27) as

$$\left(A_{mn}^{(+)}\right)_r^{pos} = -i\,\rho c \frac{\left(k_0 - k_z^{(+)}M\right)^2}{k_0} A_{mn}^{(+)} \frac{2a\alpha_r \sin\left(m\alpha_r\right)}{m\alpha_r}\ e^{ik_z^{(+)}z_r}\ \frac{\sin(k_z^{(+)}d_r)}{k_z^{(+)}d_r}\ 2d_r\ \frac{e^{+im\theta_r}}{2} \tag{3.29a}$$

$$\left(A_{mn}^{(+)}\right)_r^{neg} = -i\,\rho c \frac{\left(k_0 - k_z^{(+)}M\right)^2}{k_0} A_{mn}^{(+)} \frac{2a\alpha_r \sin\left(m\alpha_r\right)}{m\alpha_r}\ e^{ik_z^{(+)}z_r}\ \frac{\sin(k_z^{(+)}d_r)}{k_z^{(+)}d_r}\ 2d_r\ \frac{e^{-im\theta_r}}{2} \tag{3.29b}$$

The mode of circumferential order *m=0* is not spinning; therefore, there is no use of defining positive and negative spinning amplitudes for this mode. However, in order to stay consistent with the previous notations and avoid presenting too many equations, it can simply be assumed that, for mode *m=0*, $(A_{0n}^{(+)})_r^{neg}$ is equal to zero and $(A_{0n}^{(+)})_r^{pos}$ is given by the equation

$$\left(A_{0n}^{(+)}\right)_r^{pos} = -i\,\rho c\,\frac{\left(k_0 - k_z^{(+)}M\right)^2}{k_0} A_{0n}^{(+)}\;2a\alpha_r\;e^{ik_z^{(+)}z_r}\,\frac{\sin(k_z^{(+)}d_r)}{k_z^{(+)}d_r}\;2d_r \qquad (3.30)$$

A similar formulation is presented in Appendix E to investigate the reflected sound field produced by the HQ tubes.

3.6 Experimental HQ Tube Dynamics

This section presents the experimental determination of the dynamics of the HQ tubes. The investigation is intended to capture the effects of the HQ tube bends, the honeycomb core and any other irregularity not considered by the theoretical straight tube model. The technique to be applied is similar to the two-microphone method to measure liner impedance [57]. The two-microphone method is shown schematically in Figure 3.7(a).

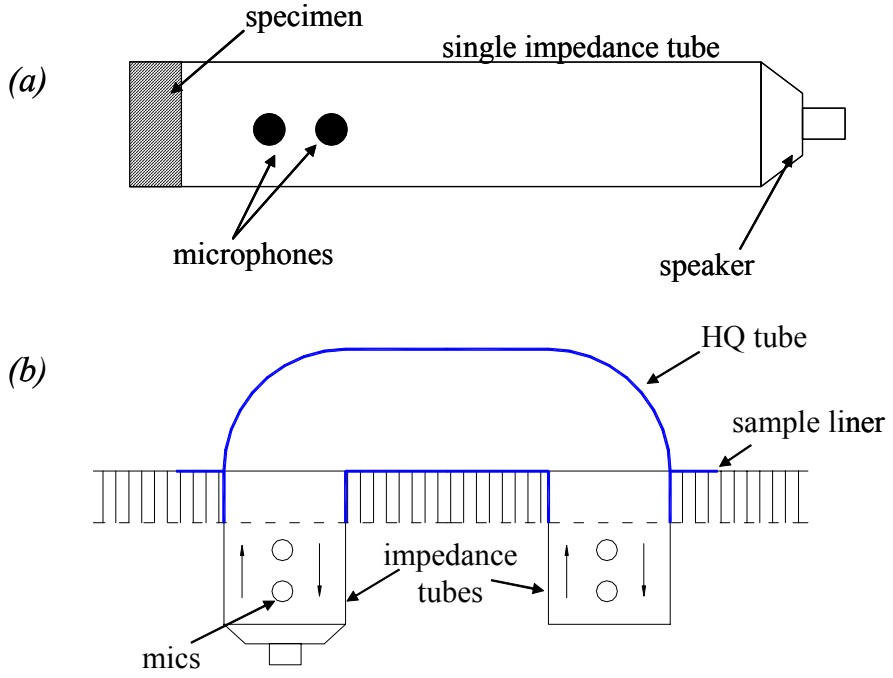

Figure 3.7: Two microphone method for testing the impedance of (a) a single material and (b) two HQ tube ends.

A sample of the material to be tested is placed in a sample holder and mounted to one end of a straight tube. A rigid plunger with an adjustable depth is placed behind the sample to provide a reflecting surface. A sound source, typically a high-output acoustic driver, is connected at the opposite end of the tube to generate plane waves. The decomposition of the standing wave pattern into forward- and backward- traveling plane waves is obtained by simultaneously measuring the pressure at two points. To this end, a pair of microphones is mounted flush with the inner wall of the tube near the sample end of the tube. Then, the material impedance can be determined using the measured transfer function between microphones.

An extension of the two-microphone technique can be applied to determine the dynamics of the HQ tubes without the effect of the grazing flow. This method consists of mounting two impedance tubes at both ends of the HQ-Liner tube as shown in Figure 3.7b. One impedance tube is excited with an acoustic driver, and the other is closed with a hard wall end or any other boundary condition. Plane waves are generated by the acoustic driver into the impedance tubes at both sides of the HQ-Liner cell as shown in Figure 3.8. In this way, the pressure field inside the tubes can be expressed as

$$P_L(\omega) = A(\omega)e^{-ik_o x} + B(\omega)e^{ik_o x} \tag{3.31a}$$

$$P_R(\omega) = C(\omega)e^{-ik_o x} + D(\omega)e^{ik_o x} \tag{3.31b}$$

and, using Euler's equation, the particle velocity as

$$V_L(\omega) = \frac{A(\omega)}{\rho c}e^{-ik_o x} - \frac{B(\omega)}{\rho c}e^{ik_o x} \tag{3.32a}$$

$$V_R(\omega) = \frac{C(\omega)}{\rho c}e^{-ik_o x} - \frac{D(\omega)}{\rho c}e^{ik_o x} \tag{3.32b}$$

where ω is the frequency in radians per second, k_o is the free wavenumber, and $A(\omega)$, $B(\omega)$, $C(\omega)$ and $D(\omega)$ are the unknown modal amplitudes of the plane waves inside the impedance tubes. The sub-indices L and R refer to the each impedance tube.

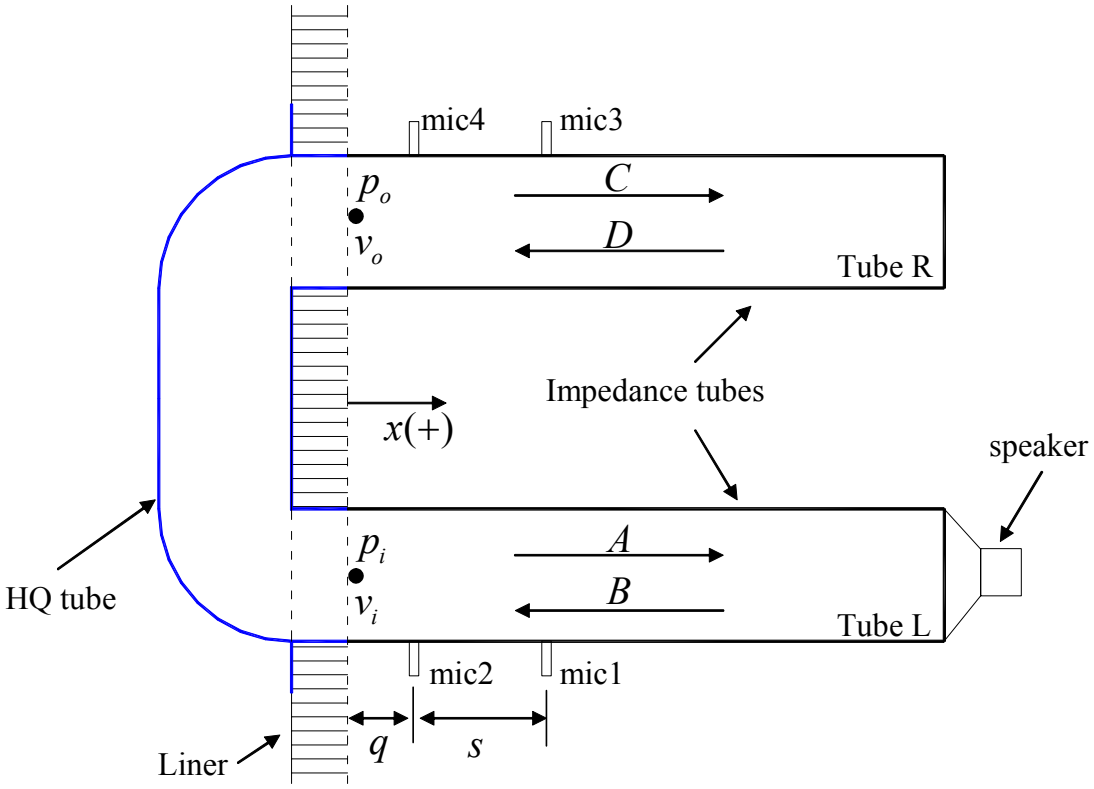

Figure 3.8: Schematic of the HQ-Liner dynamics experimental setup.

The forward- and backward-traveling components, i.e. the amplitudes A, B, C and D, can be computed by measuring the pressure at two points in each impedance tube. Therefore, a pair of microphones is mounted in each impedance tube near the HQ tube ends as shown in Figure 3.8. The position of the microphones is defined by the parameters q and s shown in the figure. The pressure at the four microphones can be expressed as

$$\begin{aligned} P_1 &= A\,e^{-ik_o(q+s)} + B\,e^{ik_o(q+s)} \\ P_2 &= A\,e^{-ik_o(q)} + B\,e^{ik_o(q)} \\ P_3 &= C\,e^{-ik_o(q+s)} + D\,e^{ik_o(q+s)} \\ P_4 &= C\,e^{-ik_o(q)} + D\,e^{ik_o(q)} \end{aligned} \tag{3.33}$$

The pressures at the four microphones are then obtained in terms of the measured transfer function of all the microphones relative to microphone #1. Thus, P_1 is conventionally set

to 1 in equation (3.33) and the rest of the pressures take the measured transfer function values as

$$\begin{aligned} H_{12} &= \frac{P_2}{P_1} \\ H_{13} &= \frac{P_3}{P_1} \\ H_{14} &= \frac{P_4}{P_1} \end{aligned} \tag{3.34}$$

where H_{12}, H_{13} and H_{14} are the transfer functions between microphones, i.e. note that $H_{11}=1$. Replacing (3.34) into (3.33), the following system of equations yields to solve for the amplitudes *A(ω)*, *B(ω)*, *C(ω)* and *D(ω)*

$$\begin{aligned} 1 &= \left(e^{-ik_o(q+s)}\right) A + \left(e^{ik_o(q+s)}\right) B \\ H_{12} &= \left(e^{-ik_o(q)}\right) A + \left(e^{ik_o(q)}\right) B \\ H_{13} &= \left(e^{-ik_o(q+s)}\right) C + \left(e^{ik_o(q+s)}\right) D \\ H_{14} &= \left(e^{-ik_o(q)}\right) C + \left(e^{ik_o(q)}\right) D \end{aligned} \tag{3.35}$$

Once the amplitudes are found from equation (3.35), the pressure and particle velocity anywhere inside the impedance tubes can be computed using the equations (3.31) and (3.32). In particular, the point of calculation can be selected at the HQ tube ends, i.e. *x=0*. Then,

$$\begin{aligned} P_i(\omega) &= A(\omega) + B(\omega); \quad P_o(\omega) = C(\omega) + D(\omega) \\ V_i(\omega) &= \frac{A(\omega)}{\rho c} - \frac{B(\omega)}{\rho c}; \quad V_o(\omega) = \frac{C(\omega)}{\rho c} - \frac{D(\omega)}{\rho c} \end{aligned} \tag{3.36}$$

In this way, it is possible to find the coefficients of the impedance matrix given in equation (3.10) as

$$\begin{Bmatrix} P_i \\ P_o \end{Bmatrix} = \rho c \begin{bmatrix} Z_1^{\exp} & Z_2^{\exp} \\ Z_3^{\exp} & Z_4^{\exp} \end{bmatrix} \begin{Bmatrix} V_i \\ V_o \end{Bmatrix} \tag{3.37}$$

Note that for a constant cross sectional area HQ tube, the existing geometrical symmetry of the system simplifies the problem as $Z_1^{\exp} = Z_4^{\exp}$ and $Z_2^{\exp} = Z_3^{\exp}$. Then the experimental dynamics of the HQ-Liner cell can be determined from solving the following system of equations

$$\begin{Bmatrix} P_i \\ P_o \end{Bmatrix} = \rho c \begin{bmatrix} V_i & V_o \\ V_o & V_i \end{bmatrix} \begin{Bmatrix} Z_1^{\exp} \\ Z_2^{\exp} \end{Bmatrix} \tag{3.38}$$

Figure 3.9 presents the schematic of an experimental setup of the impedance tubes for a HQ-Liner. The transfer functions between microphones are obtained using a dynamic signal analyzer. As shown in the figure, the noise signal is generated by the spectrum analyzer, and input into a power amplifier. Then, the amplified signal is connected to the speaker. In order to obtain the transfer functions, each microphone is connected to an individual channel of the dynamic spectrum analyzer.

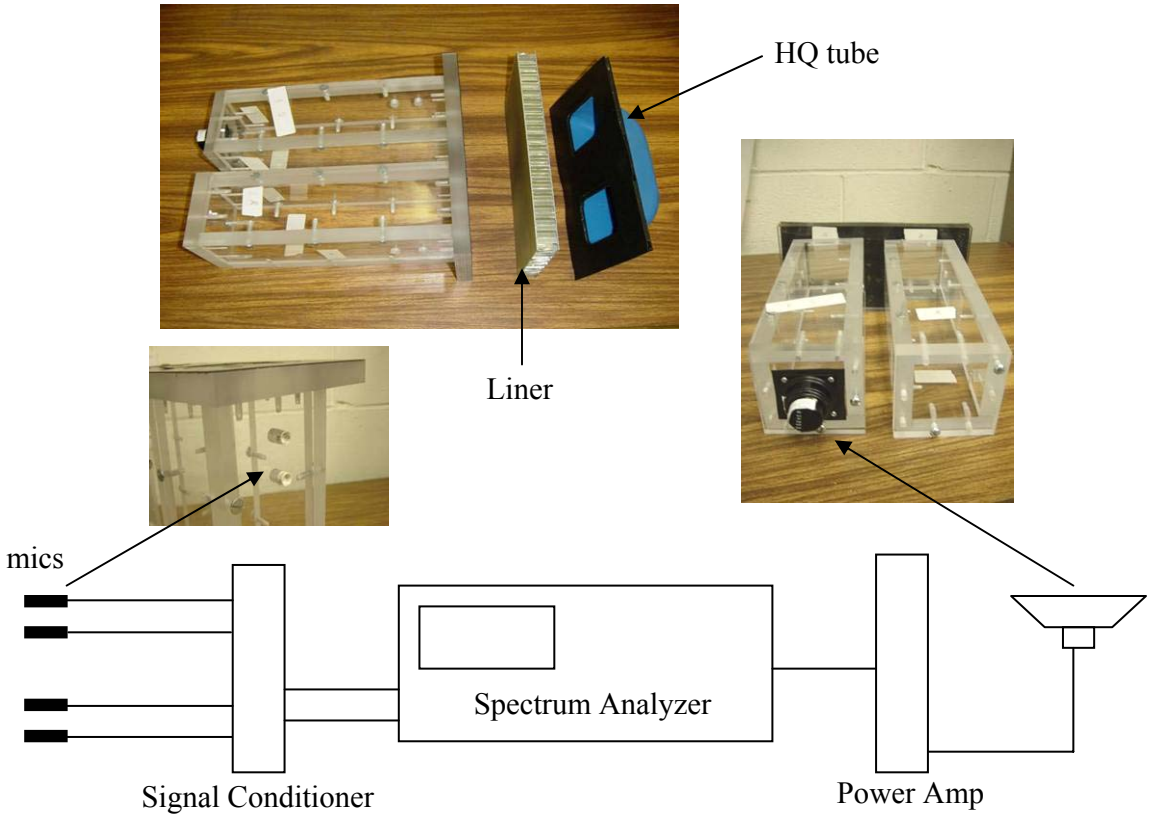

Figure 3.9: Schematic of experiments setup.

The experimental dynamics were investigated for a real HQ-Liner cell and presented next. This HQ-Liner was designed to investigate its capabilities for noise reduction on a scale simulated turbofan engine. This system was the first attempt to combine the Liner and HQ concept as a noise control device. A description of this HQ-Liner system is presented in Chapter 4. The obtained experimental dynamics of a sample HQ-Liner cell of this system is presented in Figures 3.10 and 3.11. These figures present the magnitude of the normalized impedance coefficients Z_1 and Z_2 as a function of frequency. The experiment was undertaken using a random noise input signal in the range of 0-6400 Hz, and the OASPL generated by the speaker was approximately 145.0 dB. The estimated length of the HQ tube was 5.0 inches (centerline) and the facing screen of the liner sample was a PU film with $1.65\rho c$ resistance level. The core depth of the liner sample is 0.5 inches. In addition, the experimental coefficients are compared to the theoretical model developed for a straight tube. Although the theoretical model does not include the presence of the HQ tube bends or the liner honeycomb core, it is expected to find similar trends. The theoretical coefficients Z_1 and Z_2 are obtained from equations (3.9) and (3.10) as

$$\begin{aligned} Z_1 &= \frac{i}{\sin\left(k_o L\right)}\left[\cos\left(k_o L\right) + i\frac{Z_{ps}}{\rho c}\sin\left(k_o L\right)\right] \\ Z_2 &= \frac{i}{\sin\left(k_o L\right)} \end{aligned} \tag{3.39}$$

The results show that the trend of the experimental HQ dynamics matches very well the theoretical model. However, there are some differences that need to be investigated. First, it is observed that the theoretical curves present sharp peaks at several discrete frequencies, which are not well reproduced by the experiments. Also, it is observed that the experimental impedance coefficient magnitudes are lower than the theoretical curves. Although some of these differences can be attributed to the parameters that were ignored in the model, it is still expected to improve the experimental procedure in order to obtain more accurate results. However, the improvement of the experimental procedure will not be included in this dissertation and will be left for future work.

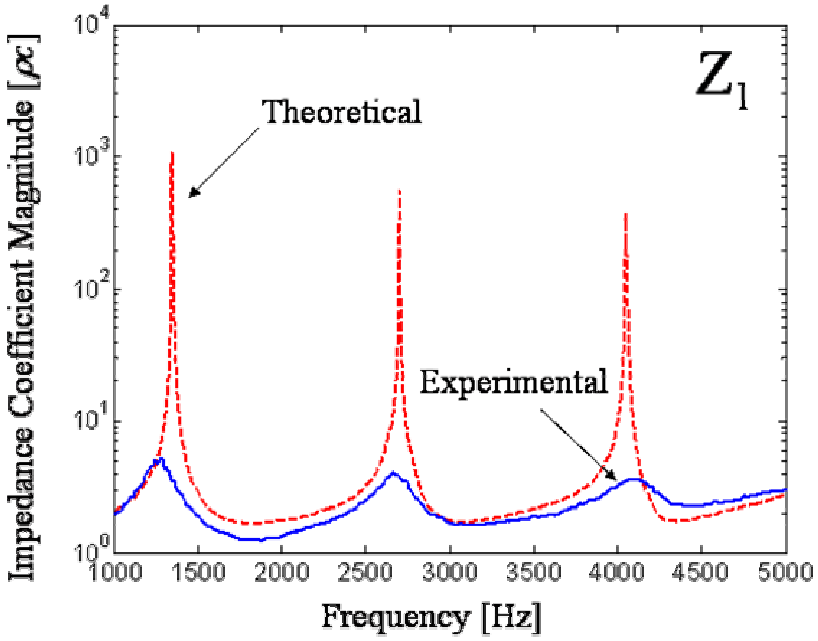

Figure 3.10: Comparison between theoretical and experimental coefficient Z_1.

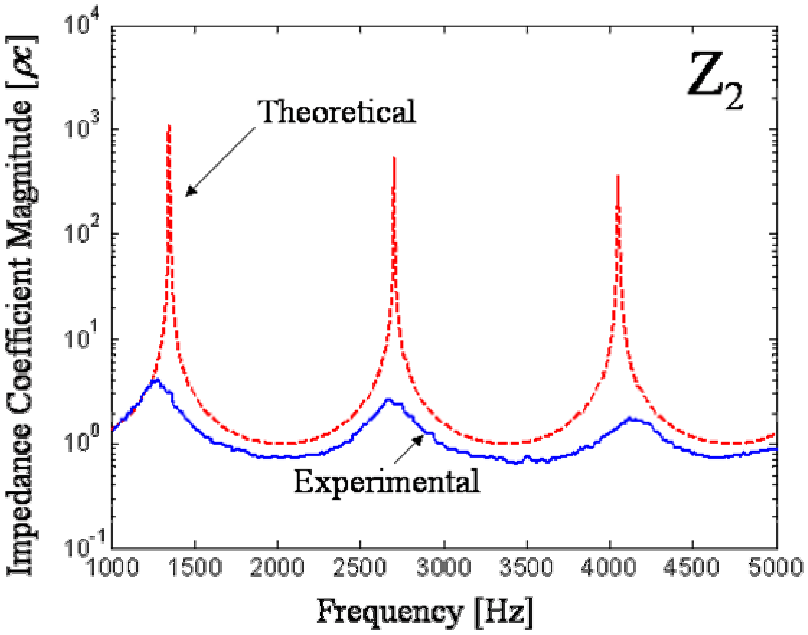

Figure 3.11: Comparison between theoretical and experimental coefficient Z_2.

3.6.1 Correction of Experimental Data to the Case with Flow

This section describes an approach to extend the experimental data of the HQ tubes to the case with flow. The approach consists of correcting the coefficients Z_1 and Z_2 based on the variation in the impedance of the liner screen due to the grazing flow.

The impedance of the screen can be divided into two components. The first component corresponds to the impedance with no grazing flow, while the second part is the variation of the impedance due to the presence of the flow. Thus, the impedance of the screen can be expressed as

$$Z_{ps}^{flow} = Z_{ps}^{no\ flow} + \Delta Z_{ps}^{flow} \tag{3.40}$$

The correction due to the presence of the flow can be obtained by replacing this impedance in the theoretical coefficients Z_1 and Z_2 of equations (3.39) as

$$\begin{aligned} Z_1^{flow} &= \frac{i}{\sin(k_o L)}\left[\cos(k_o L) + i\frac{\left(Z_{ps}^{no\ flow} + \Delta Z_{ps}^{flow}\right)}{\rho c}\sin(k_o L)\right] \\ Z_2^{flow} &= \frac{i}{\sin(k_o L)} \end{aligned} \tag{3.41}$$

The first equation of (3.41) can be rearranged in order to recover the coefficient without flow plus a correction factor. This can be done as follows

$$\begin{aligned} Z_1^{flow} &= \frac{i}{\sin(k_o L)}\left\{\cos(k_o L) + i\frac{\left(Z_{ps}^{no\ flow} + \Delta Z_{ps}^{flow}\right)}{\rho c}\sin(k_o L)\right\} = \\ &= \underbrace{\frac{i}{\sin(k_o L)}\left\{\cos(k_o L) + i\frac{Z_{ps}^{no\ flow}}{\rho c}\sin(k_o L)\right\}}_{Z_1^{no\ flow}} + \frac{i}{\cancel{\sin(k_o L)}}\left(i\frac{\Delta Z_{ps}^{flow}}{\rho c}\cancel{\sin(k_o L)}\right) \end{aligned}$$

Thus, the corrected coefficient becomes

$$Z_1^{flow} = Z_1^{\exp} - \frac{\Delta Z_{ps}^{flow}}{\rho c} \tag{3.42}$$

On the other hand, the second expression in (3.41) shows that the coefficient Z_2 does not depend on the flow. Therefore,

$$Z_2^{flow} = Z_2^{no\ flow} = Z_2^{\exp} \tag{3.43}$$

3.7 Simplification to 2D Model

A simplification to a 2D HQ-Liner model is presented in this section. The objective of developing this model is to have a faster prediction tool for a HQ-Liner system optimization. The simplification consists in including only one circumferential order in the modal decomposition of the propagating sound inside the lined duct. As a consequence, the acoustic problem to solve lays only in the radial and axial direction, while the circumferential variation of the modes becomes a known solution.

The main assumption to create a 2D model of propagation of modes in a lined circular duct with HQ tubes is to ignore the circumferential scattering effects. This assumption is valid when the number of HQ tubes in a circumferential array is greater than $2 \times m_{dist}$, e.g. the circumferential mode order of the disturbance sound field is denoted as m_{dist} (*see Figure 3.12a*). A high number of HQ tubes is selected in order not to scatter energy into low order modes. The scattering rule with such circumferential discontinuities created by the HQ tubes is given by $m_{HQ} = m_{dist} \pm k \cdot N_T$ [1]. If a large number of tubes is selected, the scattering will be into higher order modes, which are cut-off and decay quickly. The limit case will be the one shown in Figure 3.12b, where the tubes are one next to the other. This arrangement consists of a single waveguide divided into separate cavities by thin spacers. Therefore, the tube-duct interfaces can be thought of a continuous slot that will not produce any circumferential scattering whatsoever.

Under this assumption, the effect of the HQ tubes can then be modeled in 2D, where the plane will represent only the slice of the circumference shown in Figure 3.12b. The model simplification of the piston radiation and tube-duct coupling is presented in the following sections.

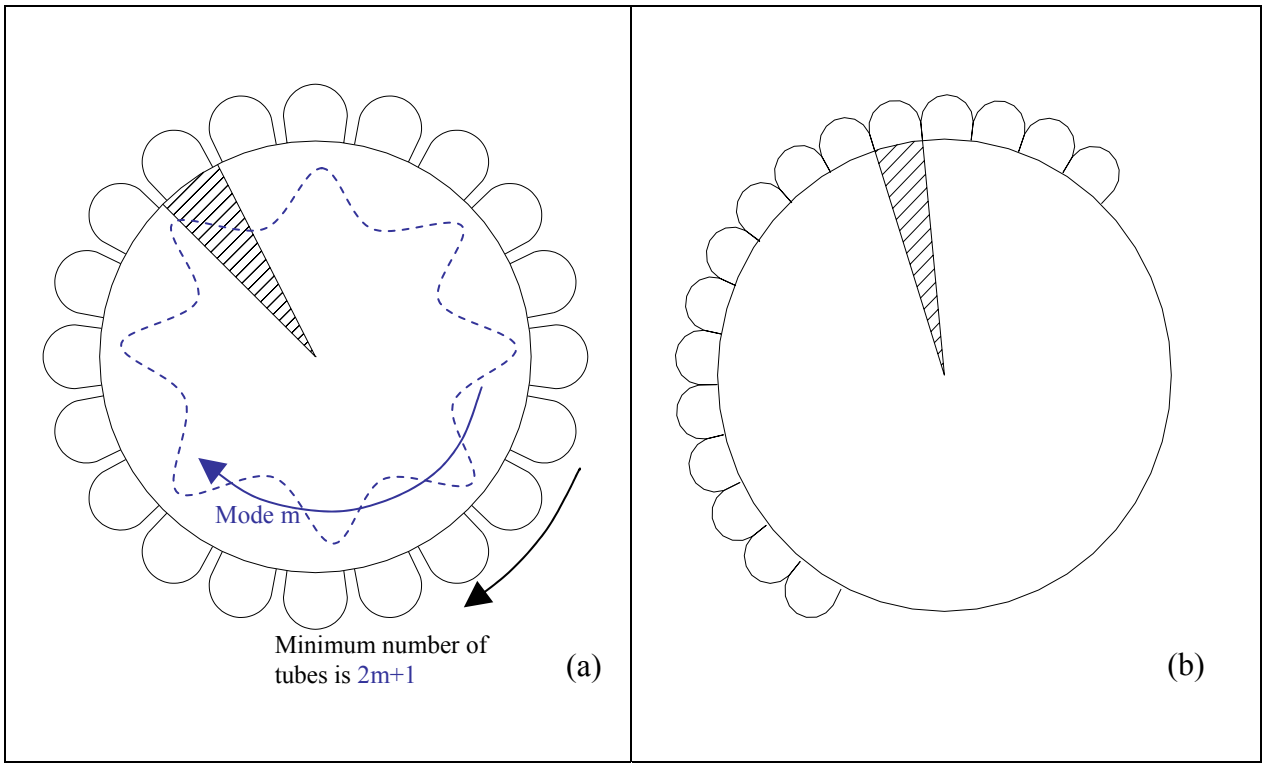

Figure 3.12: Schematic of a circumferential array of HQ tubes (a) when the scattering effects can be neglected and, (b) when scattering effects do not happen.

3.7.1 Piston radiation in the 2D Duct

This section presents a simplified formulation of the piston sound radiation in a 2D duct. As mentioned before, this model consists of ignoring all the circumferential scattering effects produced by the HQ tubes. Then, the problem can be treated as 2D with only one tube present, as shown in Figure 3.13. This 2D plane will represent a slice of cross section of the circular duct as shown in Figure 3.14a. The tube-duct interfaces of the single HQ tube are modeled as vibrating pistons making use of the Green's functions. To this end, the Green's functions found in Chapter 2 are simplified to the case with no circumferential variation. Given the fact that the circumferential variation of the motion of the pistons in the array is known, the solution can easily be extended to the whole array of pistons as shown in Figure 3.14b. Since the problem has been reduced to find only the motion of one HQ tube in the array, the computation time will be much faster than the 3D case. However, the HQ-Liner predictions for simple systems are expected to be identical as shown in Appendix B, e.g. only one array of HQ tubes.

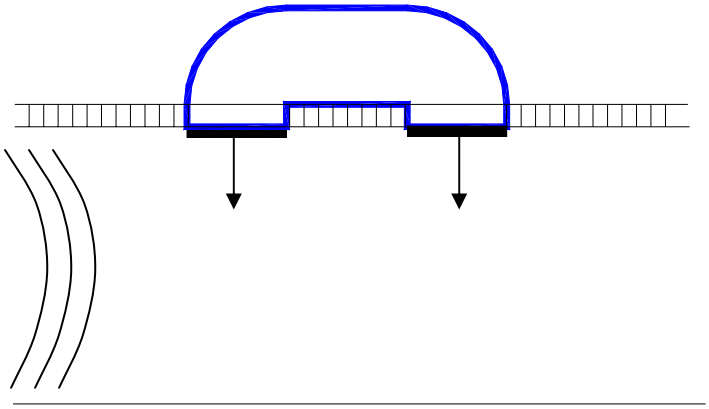

Figure 3.13: Schematic of 2D HQ-Liner System Model. HQ tube interfaces are modeled as vibrating pistons.

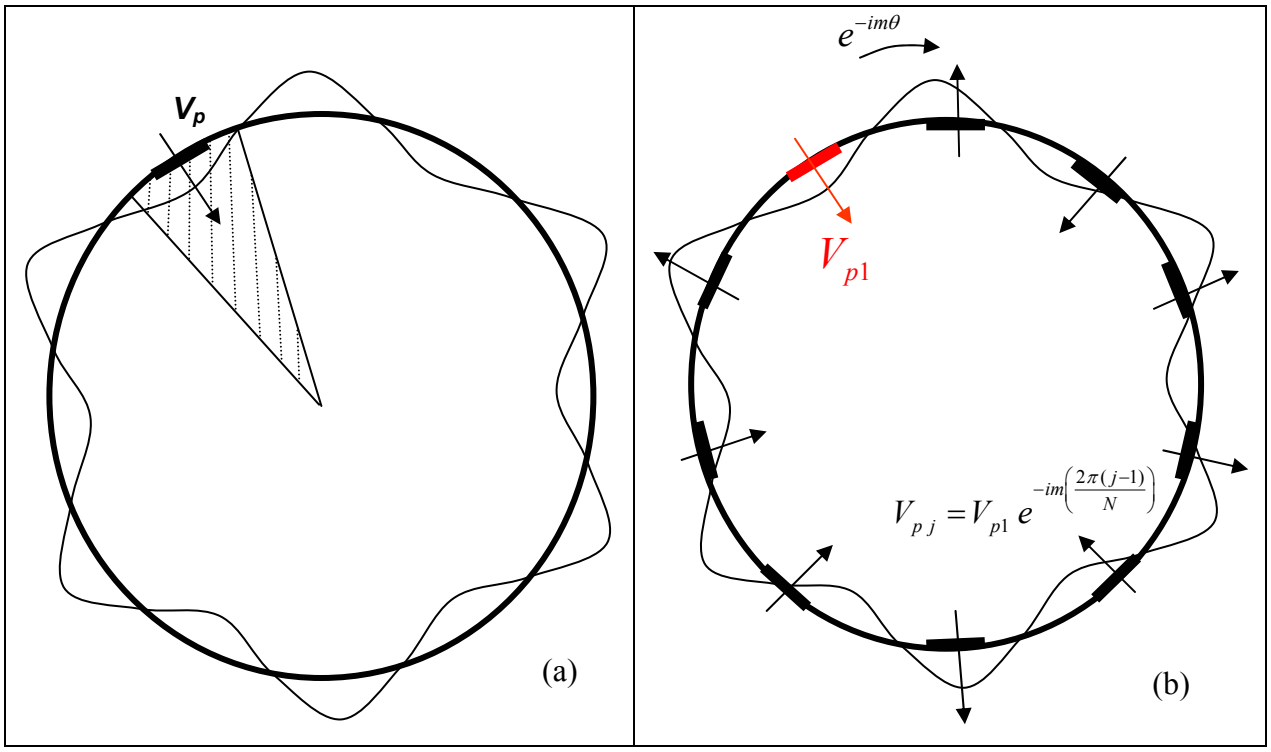

Figure 3.14: Motion of the array of pistons. (a) Modeled slice to compute Vp. (b) Computation of the motion of the pistons in the array using the calculated Vp.

The problem to solve consists of a lined wall 2D duct of height ***a*** and mean flow ***M***. The disturbance sound field inside the duct is assumed to be a combination of positive propagating radial modes of the same circumferential order as follows

$$p_d\left(\vec{r}\right) = e^{-im\theta}\sum_n \left(A_{mn}^{(+)}\right)_d J_m\left(k_{mn}^{(+)}r\right)e^{-k_z^{(+)}z} \tag{3.44}$$

where $\vec{r} = \left(r,\theta,z\right)$ is the position vector, *m* is the fixed circumferential order, *n* is the radial order, $k_z^{(+)}$ is the positive propagating mode axial wavenumber, and $k_{mn}^{(+)}$ is the positive mode eigenvalue found from the soft-wall boundary condition problem. Note that θ is a fixed value according to the section considered in the model.

The lined duct is assumed to have arrays of HQ tubes. The number of HQ tubes in the array is assumed to be greater than $2\times m_{dist}$ as shown in Figure 3.12a. Assuming that the first tube is given at $\theta = 0$, the azimuth coordinate of the j^{th} tube is given as

$$\theta_j = \frac{2\pi(j-1)}{N} \qquad\qquad j = 1,\ldots..,\mathrm{N} \tag{3.45}$$

The effect of the HQ tubes in the duct is modeled by considering the tube-duct interfaces as finite pistons radiating sound. As shown in Figure 3.14, the motion of only one of the pistons has to be found (under the no scattering assumption), and then extended to the rest of the pistons in the array using (3.45). The motion of the rest of the pistons in the array will have the same azimuth variation as the sound in the disturbance as follows

$$V_{ij} = V_{i1}\,e^{-im\left(\frac{2\pi(j-1)}{N}\right)} \qquad \text{and} \qquad V_{oj} = V_{o1}\,e^{-im\left(\frac{2\pi(j-1)}{N}\right)} \tag{3.46}$$

where *i* and *o* correspond to the entrance and exit source arrays. Then, the problem is reduced to solve only for the motion $V_{1i/o}$ of the first piston. In order to solve this problem, the Green's functions for piston radiation developed in Chapter 2 have to be simplified. The simplification consists on expanding the Green's functions as a linear combination of radial modes, but only considering a fixed m order. The expression for both propagating directions will be found as

$$g^{(+)}\left(\vec{r}\,|\vec{r}_o\right)=\sum_{n=0}^{N}A_{mn}^{(+)}\,J_m(k_{mn}^{(+)}r)\cos[m(\theta-\theta_o)]\,e^{-ik_z^{(+)}(z-z_0)} \qquad z>z_0 \qquad (3.47)\text{a}$$

$$g^{(-)}\left(\vec{r}\,|\vec{r}_o\right)=\sum_{n=0}^{N}A_{mn}^{(-)}\,J_m(k_{mn}^{(-)}r)\cos[m(\theta-\theta_o)]\,e^{-ik_z^{(-)}(z-z_0)} \qquad z<z_0 \qquad (3.47)\text{b}$$

where m is a fixed order, and $\theta_o=0$ for simplicity. The modal amplitudes $A_{mn}^{(+)}$ and $A_{mn}^{(-)}$ are found by solving the system of equations (2.45) for the fixed m order only. The radiated pressure due to a finite piston with uniform velocity V_p is found by integrating the 2D Green's function over the surface of the vibrating piston. In this way, the sound field at a point $\vec{r}$ produced by a source at $\vec{r}_0$ is given as

$$p^{(+)}\left(\vec{r}\,|\vec{r}_0\right)=-i\rho c\,V_p\sum_n\frac{\left(k_0-k_z^{(+)}M\right)^2}{k_0}\int_{S_R}g_{mn}^{(+)}\left(\vec{r}\,|\vec{r}_0\right)dS \qquad z\geq z_o \qquad (3.48)\text{a}$$

$$p^{(-)}\left(\vec{r}\,|\vec{r}_0\right)=-i\rho c\,V_p\sum_n\frac{\left(k_0-k_z^{(-)}M\right)^2}{k_0}\int_{S_R}g_{mn}^{(-)}\left(\vec{r}\,|\vec{r}_0\right)dS \qquad z\leq z_o \qquad (3.48)\text{b}$$

for both directions of propagation, i.e. depending on the relative location between the source and the receiver.

Equations (3.48) can be extended to the pressure radiated by a circumferential array of pistons. The pressure at any point in the fluid can be obtained by a summation of the pressure due to all the pistons in the array. The velocity of each piston will be given by expression (3.46) in terms of the reference piston, e.g. piston 1:

$$V_{i\,j}=V_{i1}\,e^{-im\left(\frac{2\pi(j-1)}{N}\right)} \quad \text{and} \quad V_{o\,j}=V_{o1}\,e^{-im\left(\frac{2\pi(j-1)}{N}\right)} \qquad (3.46)$$

Then, equations (3.48) can be rewritten as follows for the whole array of pistons

$$p^{(+)}\left(\vec{r}\,|array\right)=-i\rho c\,V_{p1}\sum_j e^{-im\left(\frac{2\pi(j-1)}{N}\right)}\sum_n\frac{\left(k_0-k_z^{(+)}M\right)^2}{k_0}\int_{S_R}g_{mn}^{(+)}\left(\vec{r}\,|\vec{r}_j\right)dS \qquad z\geq z_o \quad (3.49)\text{a}$$

$$p^{(-)}\left(\vec{r}\,|array\right)=-i\rho c\,V_{p1}\sum_j e^{-im\left(\frac{2\pi(j-1)}{N}\right)}\sum_n\frac{\left(k_0-k_z^{(-)}M\right)^2}{k_0}\int_{S_R}g_{mn}^{(-)}\left(\vec{r}\,|\vec{r}_j\right)dS \qquad z\geq z_o \quad (3.49)\text{b}$$

The acoustic field inside the duct is obtained from the superposition of the sound disturbance from the fan and the radiated pressure due to the arrays of pistons. In particular, it is of interest to compute the average pressure over the piston surfaces. This pressure can be written in matrix form as follows

$$\begin{Bmatrix} \langle p \rangle_i \\ \langle p \rangle_o \end{Bmatrix} = \begin{bmatrix} Z_{ii} & Z_{io} \\ Z_{oi} & Z_{oo} \end{bmatrix} \begin{Bmatrix} V_{1i} \\ V_{1o} \end{Bmatrix} + \begin{Bmatrix} \langle p \rangle_{di} \\ \langle p \rangle_{do} \end{Bmatrix} \tag{3.50}$$

where the elements Z_{io} of the 2×2 matrix are computed as the average pressure over a source due to another array of sources with unit velocity, i.e. impedance function (see Figure 3.15). To compute the impedance functions, the average pressure over a piston sources "*i*" due to an array of sources "*o*" with unit velocity is simply given by

$$Z_{oi} = \frac{1}{S_o} \int_{z_o-d_o}^{z_o+d_o} \int_{\theta_o-\alpha_o}^{\theta_o+\alpha_o} \left[-i\rho c \sum_j e^{-im\left(\frac{2\pi(j-1)}{N}\right)} \sum_n \frac{\left(k_0 - k_z M\right)^2}{k_0} \int_{S_s} g_{mn}\left(\vec{r}_o \middle| \vec{r}_j\right) dS_s \right] a\, d\theta\, dz \tag{3.51}$$

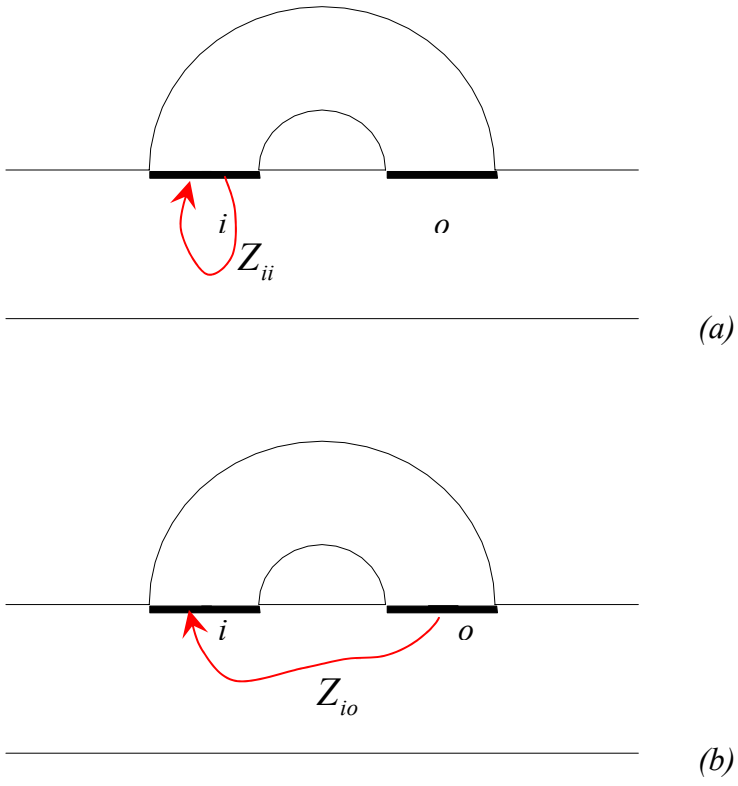

Figure 3.15: Schematic of impedance functions. (a) Influence of a piston on itself, and (b) Influence of a piston on another piston.

3.7.2 HQ tube model

The acoustic variables, i.e. pressure p_i^t and p_o^t and particle velocity v_i^t and v_o^t, at the i^{th} and o^{th} end of the tubes can be related using the transfer matrix developed in section 3.3. The relation between the acoustic variables for a single tube is rewritten here as

$$\begin{Bmatrix} p_i^t \\ p_o^t \end{Bmatrix} = \begin{bmatrix} Z_{ii}^t & Z_{io}^t \\ Z_{oi}^t & Z_{oo}^t \end{bmatrix} \begin{Bmatrix} v_i^t \\ v_o^t \end{Bmatrix} \tag{3.52}$$

3.7.3 Tube-Duct Coupling

The sound fields inside the duct due to both the disturbance and the piston sources and inside the HQ tubes were developed separately. In this section, these models are combined to find an expression for the particle velocity of the piston sources, i.e. coupled tube-duct system. The model for the coupled tube-duct system is obtained with a similar procedure as in section 3.4 for the 3D system. The conditions to satisfy are

(i) the average pressure on the surface of the source to the pressure in the tube, i.e. $\langle p \rangle_{\ell i} = p_{\ell i}^t$ and $\langle p \rangle_{\ell o} = p_{\ell o}^t$, and

(ii) the average particle velocity on the surface of the source to the particle velocity in the tube, $\langle v \rangle_{\ell i} = v_{\ell i}^t$ and $\langle v \rangle_{\ell o} = v_{\ell o}^t$.

Once this conditions are imposed in the same fashion as in section 3.4, the unknown piston source velocities are then obtained by solving the following 2×2 linear system of equations

$$\left(\begin{bmatrix} Z_{ii}^t & Z_{io}^t \\ Z_{oi}^t & Z_{oo}^t \end{bmatrix} - \frac{\beta_w}{\rho c} \begin{bmatrix} Z_{ii}^t & Z_{io}^t \\ Z_{oi}^t & Z_{oo}^t \end{bmatrix} \begin{bmatrix} Z_{ii} & Z_{io} \\ Z_{oi} & Z_{oo} \end{bmatrix} - \begin{bmatrix} Z_{ii} & Z_{io} \\ Z_{oi} & Z_{oo} \end{bmatrix} \right) \begin{Bmatrix} V_{1i} \\ V_{1o} \end{Bmatrix} = \\ = \begin{Bmatrix} \langle p \rangle_{di} \\ \langle p \rangle_{do} \end{Bmatrix} + \frac{\beta_w}{\rho c} \begin{bmatrix} Z_{ii}^t & Z_{io}^t \\ Z_{oi}^t & Z_{oo}^t \end{bmatrix} \begin{Bmatrix} \langle p \rangle_{di} \\ \langle p \rangle_{do} \end{Bmatrix} \tag{3.53}$$

The computation time to find the piston velocities V_{1i} and V_{1o} is now insignificant compare to the 3D case. The piston velocities found from the above linear system of equations are then replaced in (3.49) to find the complete sound field along the duct.

Chapter 4 Model Validation

The theoretical formulations presented in the previous chapters are intended to give a mathematical foundation for the propagation of sound in the **lined inlet** of a Turbofan Engine **with arrays of HQ tubes**. This Chapter presents a validation of this formulation using experimental results obtained on a real HQ-Liner system. Certainly, the application of this model as a prediction tool in future HQ-Liner designs depends on the outcome of a validation of this kind.

The first part of the chapter is concentrated on describing the tested system as well as some of the experimental results. The experiments were performed by **Goodrich Corporation** on a scale engine rig at the Rolls-Royce Ansty facility. The rig configuration consisted on a scale simulated Turbofan Engine with a HQ-Liner system mounted on the inlet. The corresponding liner and HQ tubes were designed independently and then integrated together. A description of the HQ-Liner parameters is presented in section 4.1. The obtained experimental data was kindly provided by Goodrich in order to perform the validation of the model. Only the cases needed to undertake the model validation were considered in this dissertation. A summary of this experimental data is presented in section 4.2.

Once the experimental cases to be simulated are identified, the model validation is performed in Section 4.3. The first step of the numerical simulations is the analysis of the eigenvalues, which give the propagation characteristics of the acoustic modes inside the circular lined duct, i.e. axial wavenumbers. Then, the theoretical predictions are presented in comparison with the experiments for configurations of 2 and 4 arrays of HQ tubes and two different power settings.

4.1 Description of Tested HQ-Liner System

This section presents a description of the HQ-Liner system that was tested on the scale engine rig at the Rolls-Royce Ansty facility. The experiments were carried out to evaluate the attenuation of a system designed with the goal that it could potentially be implemented on the inlet of a real Turbofan Engine. This system was the first attempt to combine the HQ and Liner technologies in order to obtain an improved noise control device. For these first experiments, the corresponding liner and HQ tubes were designed independently and then integrated together. Figure 4.1 presents a picture of the ANCTF Rig at the Rolls-Royce Ansty testing facility.

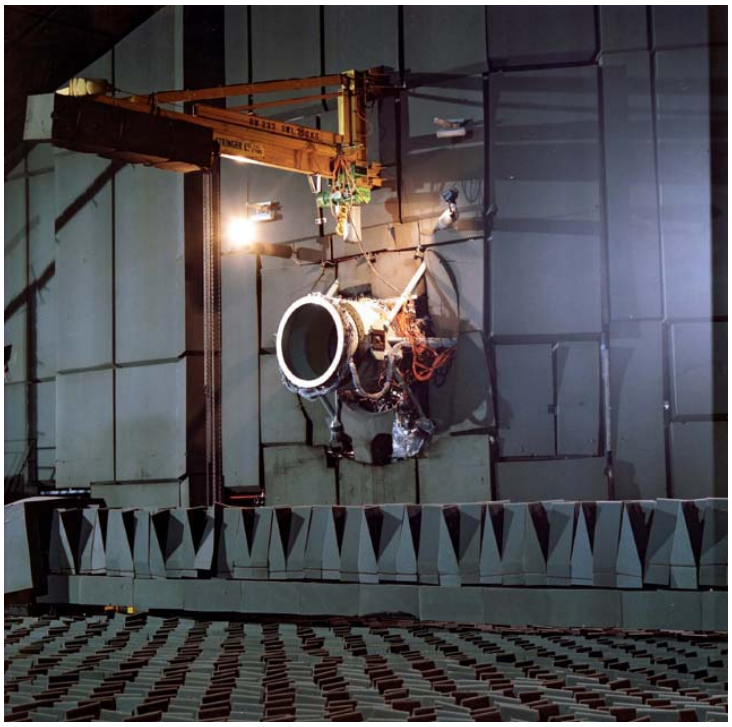

Figure 4.1: Picture of Rolls-Royce Ansty Testing Facility[†].

The rig was configured to simulate a real Turbofan Engine for which the noise parameters had been clearly identified. These parameters are important to determine the main requirements and objectives of the design as well as to calculate the dimensions of a preliminary system. The feasibility and construction of the HQ-Liner can be analyzed

[†] Picture is courtesy of Goodrich Corporation.

from this initial design. The main engine parameters to be considered in the preliminary stages of the HQ-Liner design for turbofan inlets are described in this section. As shown in Figure 4.2, many of these parameters are related to the geometry of the turbofan. The rest of the required information is related to operation parameters of the different engine regimes.

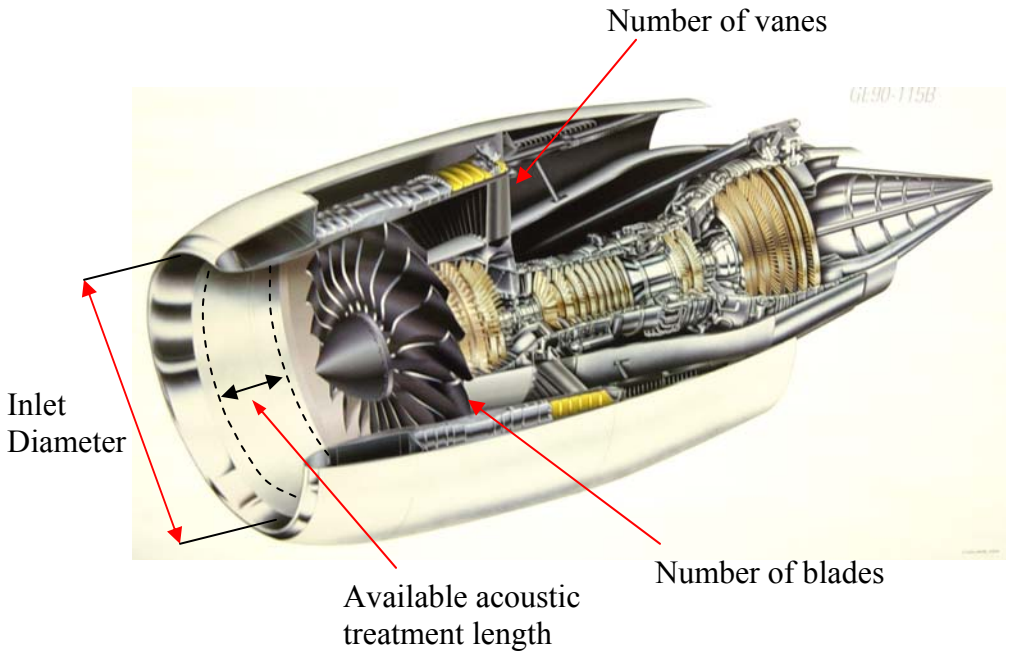

Figure 4.2: Picture of a high-bypass turbofan engine[†] with geometric parameters that are relevant for noise generation.

The geometry of the turbofan engine inlet is firstly characterized by its size. The engine inlet diameter determines the type of turbofan engine to be considered, i.e. small, medium or large engine. The engine diameter will determine the order of magnitude of the size of the required HQ system, as well as the frequency range of the BPF tone. In order to determine the available space to locate the HQ tubes in combination with the liner, it is required to specify the acoustic treatment length. Also, the acoustic patterns generated by the fan, i.e. propagating modes, will depend on the number of blades, vanes and struts of the particular engine. Next section presents a summary of the Rig configuration used for the experiments.

[†] GE90-115B – Picture available at www.volvo.com

4.1.1 Scale Engine Rig

The experiments were performed on the Rig 649, which is a scale model of the Trent 500 engine. Due to limitations of the testing facility, the experiments could only reproduce the sound radiation to the front of the fan without including the presence of the engine core. Then, the objective of this experimental investigation was to evaluate the capabilities of an HQ-Liner system designed only for the inlet of this rig. A picture of the Rig 649 is presented in Figure 4.3.

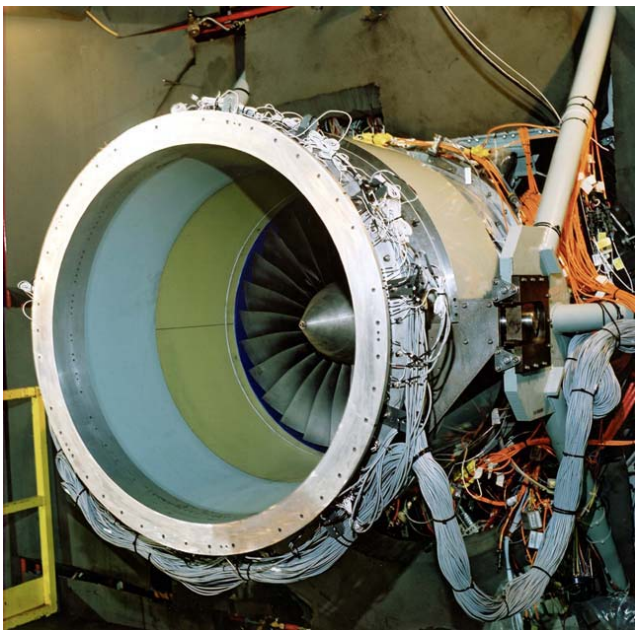

Figure 4.3: Picture of tested scale engine Rig 649[†].

The engine conditions required by the regulations for noise certification are usually reproduced during these experiments. Noise regulations require the manufacturer to keep the noise levels of the engine at different power settings below a well-defined limit. As a consequence, it is necessary to identify the noise source for these different engine conditions, and determine the most critical requirements to be satisfied. Figure 4.4 presents a schematic of the principal engine conditions stated in the aircraft noise regulations for turbofan engines [58]. As shown in the figure, these conditions are approach (during the final landing), sideline and cutback (during the take-off). The power

[†] Picture is courtesy of Goodrich Corporation.

settings for these conditions are ~60%RPM_{max} at approach, ~85%RPM_{max} at cutback, and ~95%RPM_{max} at take-off.

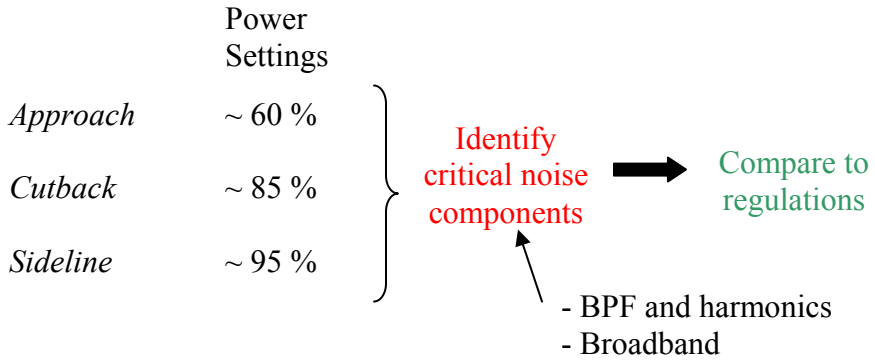

Figure 4.4: Identification of turbofan noise sources at early design stages.

Each of the stated power setting is dominated by a different noise pattern that has to be effectively controlled. The noise pattern for each condition depends on the particular engine, i.e. depends on size, number of blades, geometry, etc. The knowledge of this information is vital for the design of the proper acoustic treatment that leads to satisfy the noise certification levels. The geometric specifications of the Rig 649 are presented in Table 4.1.

Table 4.1: RR Rig 649 Description.

Inlet Diameter, D_{inlet}	0.87 m (34'')
Number of Blades	26
Number of Vanes	58
Number of Struts	10
Intake Liner Length	0.47 D_{inlet}
RPM 100%	10197

In addition, the information about the flow Mach number in the inlet sector for each condition is required to estimate the correct propagation properties of the modes

generated by the fan. In the case of the Rig 649, the flow speed was estimated as follows: *M=0.27* for approach, *M=0.44* for cutback, and *M=0.56* for sideline.

Based on previous experiments, it was determined that the noise produced by the Rig 649 was critical for the higher power setting configurations. At these high power settings, the blade tips start to reach sonic speeds that lead to the generation of shock waves that increase dramatically the noise levels. Also, the non-uniform generation of the shock waves by the different fan blades produces the noise component known as "buzz saw". Since there is a main concern to meet the certification requirements mainly on the flyover maneuver, the cutback condition was adopted as the design target for the HQ-Liner system. The objective of the HQ tubes was defined to control the BPF tone and the liner was designed for attenuating the broadband noise on the frequency range from the 1st BPF to the 3rd BPF. Figure 4.5 presents the HQ-Liner objectives on the noise spectrum of the Rig 649 at the simulated cutback condition. It was also expected that the HQ tubes could improve the broadband noise attenuation of the liner.

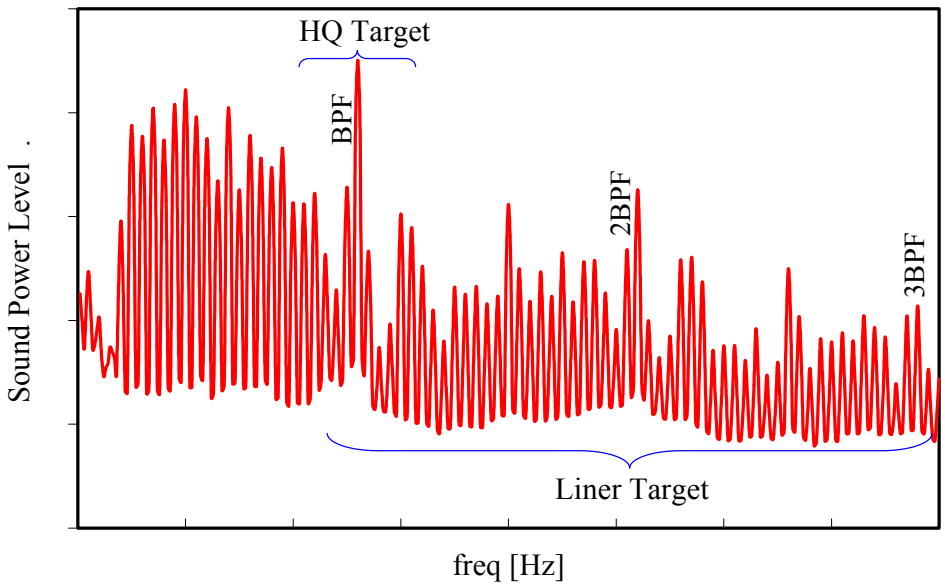

Figure 4.5: Fan noise spectrum at the cutback condition – Definition of system target.

The noise structure of the BPF tone at cutback (and sideline) condition is dominated by the rotor alone modes, also known as rotor-rotor modes. The reason is that the noise generated by the highly compressed air at the blade tips is dominant over the noise

contribution from the other aerodynamic interactions, i.e. rotor-strut, rotor-vanes, etc. Consequently, it is necessary to investigate at what frequency the rotor-rotor modes start to propagate, i.e. identify the cut-off frequency of rotor-rotor modes. Additionally, the cut-off frequencies of the rotor-strut interaction modes will be determined.

The circumferential modes generated by the fan (rotor) at the BPF and harmonics are given by the Tyler and Sofrin [1] relation as

$$m = nB \pm kV \tag{4.1}$$

where V is the number of vanes or struts , B is the number of blades, and k is a positive integer constant. The integer constant n defines the harmonic order, e.g. n=2 corresponds to 2BPF. The information about the radial orders for each generated circumferential mode is generally unknown. As a consequence it is considered that the present modes will consist of all the cut-on radial modes (*for hard wall*). The cut-off (hard wall) frequencies of the propagating modes are obtained from the positive propagating axial wavenumber of the (m,n) mode as

$$k_z^{(+)} = \frac{-k_0 M + \sqrt{k_0^2 - \left(1-M^2\right)\left(k_{mn}\right)^2}}{\left(1-M^2\right)} \tag{4.2}$$

The cut-off frequency is obtained when the square-root term vanishes as

$$k_{0-cut-off}^2 - \left(1-M^2\right)\left(k_{mn}\right)^2 = 0 \quad \rightarrow \quad f_{cut-off} = \frac{c}{2\pi}\sqrt{\left(1-M^2\right)}\, k_{mn} \tag{4.3}$$

where k_{mn} is the (m,n) hard wall mode eigenvalue which is independent of the flow speed. A list of the normalized eigenvalues is given in Appendix A. For the Rig 649, the generated modes from the interaction of the 26 blades and 10 struts are presented in Table 4.2. The table includes all the possible circumferential order modes generated by the rotor (rotor-rotor) and by the interaction between rotor and strut (rotor-strut) at the BPF and 2BPF for the cutback condition. The BPF frequency for this case is approximately 3500 Hz and flow Mach number is M=-0.44. The modes highlighted in green are the cut-on modes. Note that the rotor-vane modes (not presented) for the Rig 649 are all cut off at the BPF tone. **Since the rotor-rotor mode is cut on at the cutback**

condition, it will be dominant over the modes generated by the rotor-strut interaction.

Table 4.2: Generated modes by a fan of 26 blades and 10 vanes.
BPF at 3500Hz – M = -0.44 – Modes in green are cut-on.

	Harmonic Component	
Index *k*	***n=1 BPF***	***n=2 BPF***
1	36	62
0	26	52
-1	16	42
-2	6	32
-3	-4	22
-4	-14	12
-5	-24	2
-6	-34	-8
-7	-44	-18
-8	-54	-28
-9	-64	-38

4.1.2 Liner Parameters

The intake liner was designed to attenuate the broadband noise on the frequency range from the 1st BPF to the 3rd BPF, including the BPF tone and harmonics. A common technique to obtain the desired system consists in tuning the liner to a frequency higher than the BPF. As a result, the liner is able to control the broadband noise and harmonics, and also creates the effect of delaying the cut-off frequencies of the rotor-rotor mode for the BPF at the engine cutback and take-off operating range. Table 4.3 presents the properties of the liner used in the RR Rig 649. A polyurethane film was bonded on the perforate plate face sheet in order to achieve the high resistance required for the liner. The wall impedance, including the effect of the grazing flow, was computed by Goodrich Corporation and presented for two engine conditions in Figure 4.6, i.e. at approach and cutback conditions. As shown in this figure, the real part of the normalized impedance is higher for the cutback condition. This is a consequence of the higher flow speed and sound pressure levels at the cutback condition. In addition, the imaginary part at both conditions is slightly shifted, producing a change of 1000 Hz in the resonant frequencies of the liner core cavities.

Table 4.3: Properties of the PU liner used on the Rig 649 (Goodrich Proprietary).

POA	4.5 %
hole diameter (PU)	0.006”
Plate thickness	0.015”
Core Depth	0.5”
Average Resistance (M=0.27-approach)	1.23 ρc
Average Resistance (M=0.44-cutback)	1.9 ρc

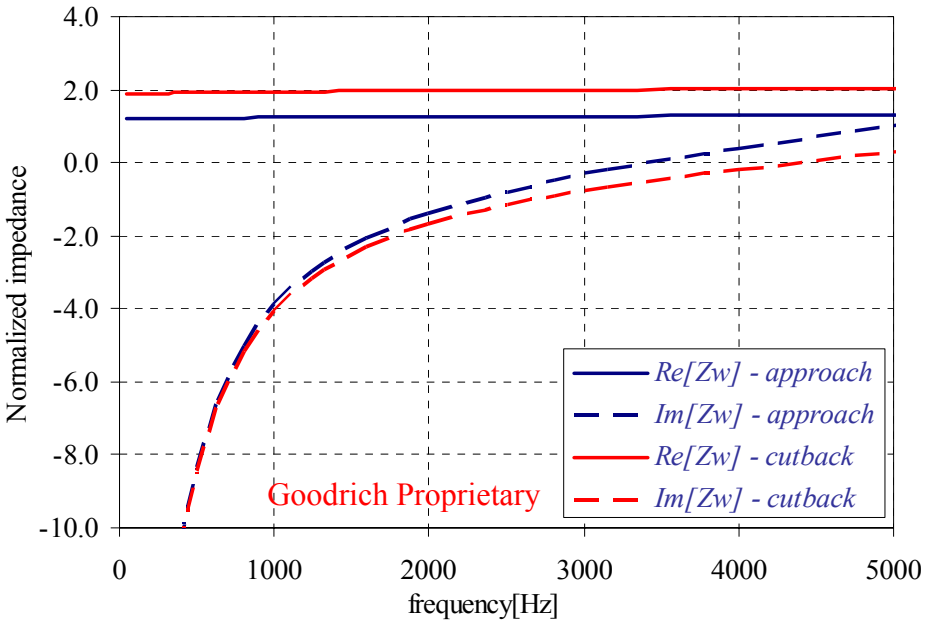

Figure 4.6: Normalized impedance of Rig649 liner for 55% and 82% RPM conditions.

Since the liner has to be integrated with the HQ tubes, it is first needed to investigate the effect of the liner impedance on the sound attenuation. In particular, the high liner resistance, obtained with the PU film, is intended to increase the dissipation properties of the wall. On the other hand, it is well known that a high resistance in the facing sheet introduces a considerable amount of damping in the HQ tube and decreases its performance. For this reason, the effect of the liner impedance is investigated on the frequency range around the BPF for different screen resistances. The cases of BPF tone and broadband attenuation will be considered. The first case consists in identifying the effect of the impedance on the propagation properties of the rotor-rotor mode, i.e. mode (26,0). The second case is concentrated on the broadband attenuation for different liner resistance in a small range of frequencies around the BPF.

Effect of Liner Impedance on Rotor-Rotor Mode

This section describes the investigation of the effect of the liner impedance on the rotor-rotor mode at cutback condition. The flow Mach number for this condition is M=0.44 in the opposite direction of sound propagation, the BPF tone is approximately at 3500 Hz, and the dominant BPF rotor-rotor mode is the (26,0). Also, the liner impedance for the cutback condition was presented in Figure 4.6. According to this figure, the liner is tuned to a frequency of 4500 Hz, which is higher than the BPF (*see where the reactance (dashed red curve) goes to zero*). In addition, the liner resistance was selected to have two additional values in order to investigate its effect on the mode propagation, i.e. 0.8, 1.9 (original) and 3.0 ρc. Figure 4.7 presents the axial wavenumber $k_z^{(+)}$ of the mode (26,0) for these different liner configurations. The solid lines correspond to the real part of the wavenumber and the dashed lines correspond to the imaginary part. The attenuation of the rotor-rotor mode is measured in terms of the magnitude of the imaginary part of the wavenumber $k_z^{(+)}$. The hard wall case is compared with liners of difference resistances. The hard wall cut-off frequency is identified when the imaginary part of the wavenumber becomes zero. The figure shows that, since the liner is tuned to a frequency higher than the BPF, it creates the effect of shifting the cut-off frequency to higher values.

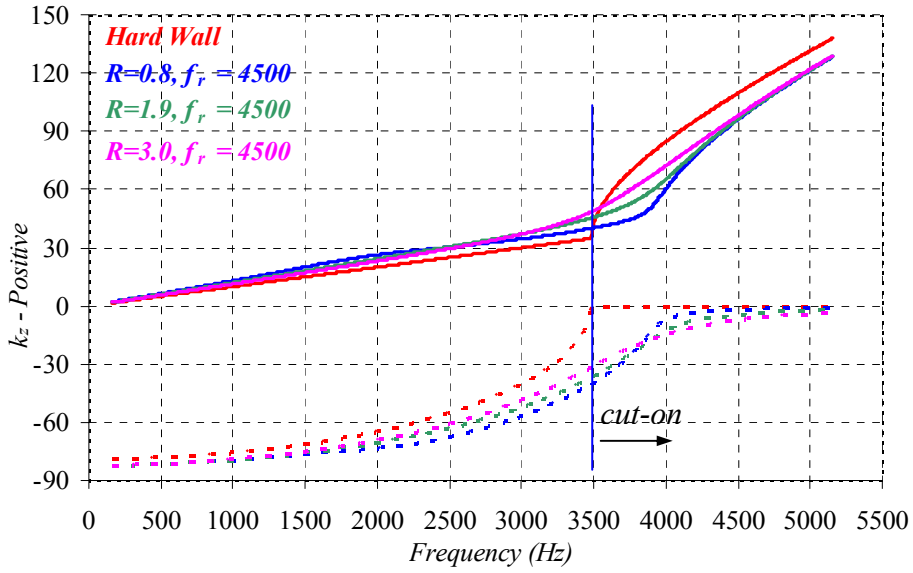

Figure 4.7: Axial wavenumber of (26,0) mode for various liners. M=-0.44 Liner Tuned to ~4500 Hz.

In addition, it is observed that when the mode is well cut-on in the hard wall condition, the cut-off frequency of the mode is shifted to even higher values for the cases with higher resistance. As a result, an increase in the mode attenuation is achieved. This same result is shown in Figure 4.8 in terms of the sound power attenuation of the liner for the mode (26,0) over the range of frequencies close to the BPF at cutback. This figure shows more in detail the effect of the liner resistance on the mode attenuation, which has two opposite effects. These two effects occur in two different regions separated by a transition interval at 3900 Hz. The two effects can be summarized as

- For frequencies higher than 3900 Hz, the mode attenuation increases for higher resistance
- For frequencies lower than 3900 Hz, the attenuation decreases also for higher resistance. Note that in this range the mode is essentially cut-off and does not represent an acoustic problem.

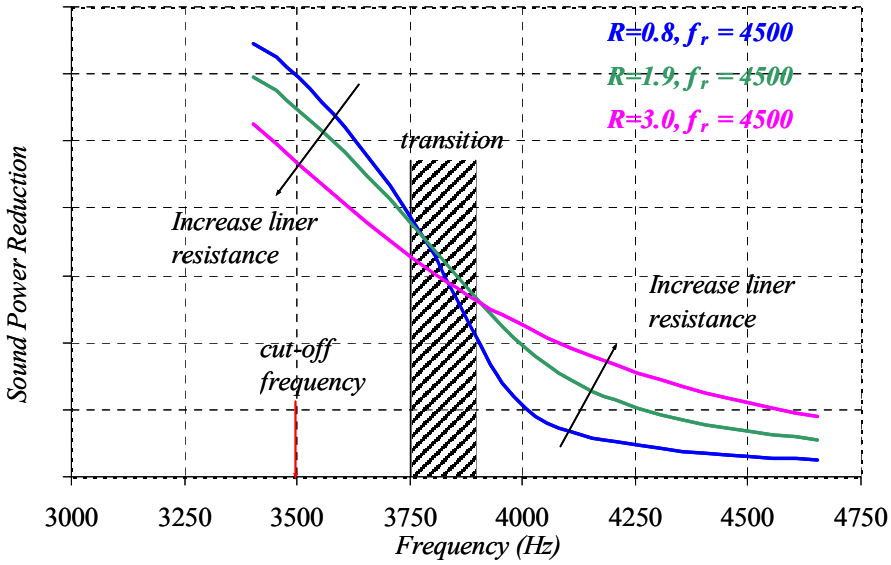

Figure 4.8: Liner BPF mode (26,0) attenuation predictions for different liners.

Effect of Liner Resistance on the Broadband Attenuation

This section presents the effect of the liner resistance on the broadband noise attenuation. Similarly to the previous case, the cutback condition was selected and three different values were assigned to the liner resistance, i.e. 0.8, 1.9 (original) and 3.0 ρc . In addition, the investigated frequencies are only in a range close to the BPF, which is the range of interest for the HQ tubes. The noise disturbance produced by the fan was assumed to be the broadband component. To simulate this case, all the cut-on modes (in the hard wall condition) are assumed present with an equal power approach. The noise attenuation predictions for different liner resistance are presented in Figure 4.9. As observed in the figure, the broadband attenuation of the liner is fairly constant over the presented small range of frequencies. Also, it is clear that the effect of a higher resistance is to increase the liner broadband attenuation. An improvement of about 2 dB can be achieved over the investigated range of frequencies by changing the liner resistance from 0.8 to 3.0 ρc . However, it is proven that the HQ tubes, which will be targeted to the BPF tone at cutback, lose performance when the resistance of the screen is high. As mentioned before, the liner was designed independently from the HQ tubes and then integrated.

Nevertheless, in order to obtain an optimized design for the combination HQ-Liner, it is recommended to investigate these effects also with the presence of the HQ tubes and find a compromise solution. The next section presents the HQ tube system that was implemented with the liner.

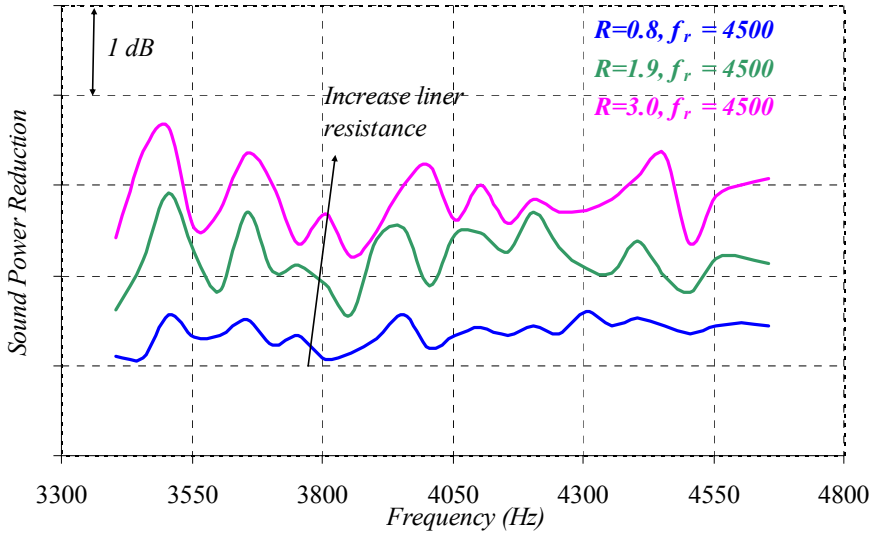

Figure 4.9: Liner broadband attenuation predictions for different liners.

4.1.3 HQ System Parameters

This section describes the HQ-system that was used in conjunction with the liner on the Rig 649. The technique used to obtain the HQ dimensions was previously developed and applied to HQ systems implemented in two small size turbofan engines without liners [17, 19, 56]. This technique consists in using simple acoustic calculations to determine the dimensions of a configuration of HQ tubes that meets the main requirements and constraints. Also, it gives a fast idea of the feasibility of implementation of the system. Figure 4.10 describes the design procedure. For the case of the system tested on the Rig 649, a description of the main HQ parameters presented in this figure will be presented.

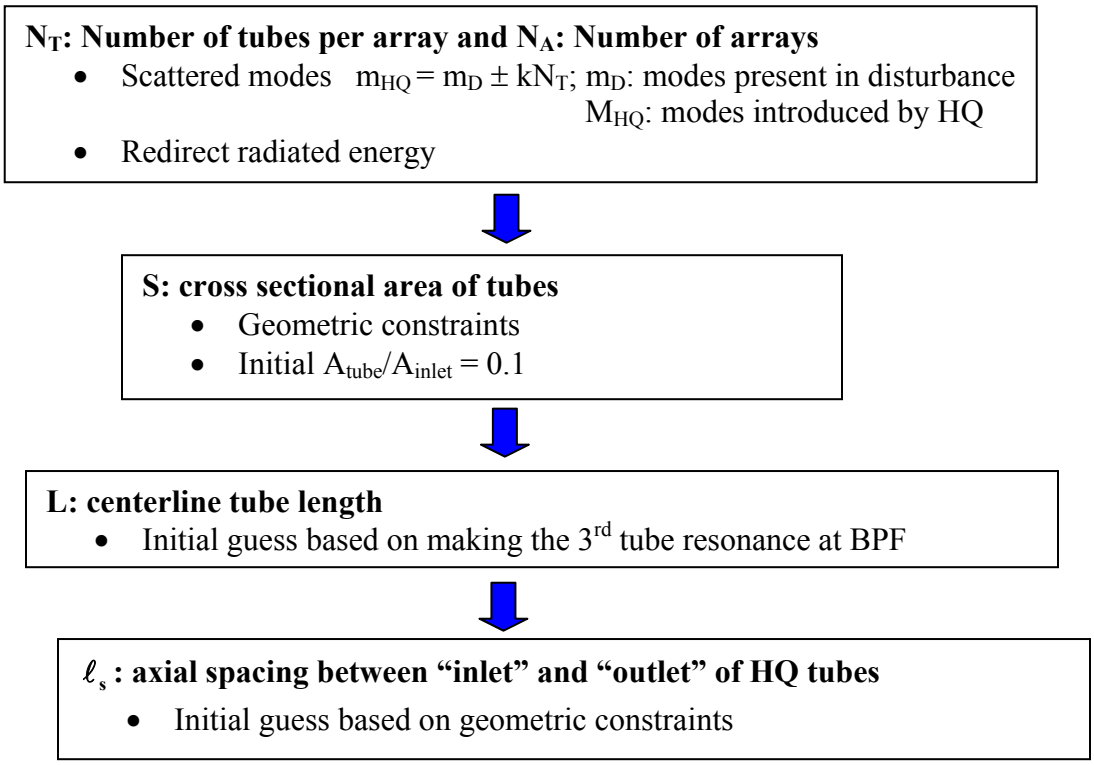

Figure 4.10: HQ-Tube initial design procedure.

Number of HQ tubes per array: N_T

Analytical and experimental studies have demonstrated that circumferential scattering of the fan modes take place in the presence of an array of HQ-tubes. This effect is very important for the determination of the number of tubes in the array. The modes excited by the HQ are given by the following expression [1, 17, 56]:

$$m_{HQ} = m_{dist} \pm kN_T \tag{4.4}$$

where

m_{HQ} = circumferential mode order excited by the HQ system

m_{dist} = circumferential mode order present in the disturbance,

N_T = number of HQ tubes in the array,

k = integer number.

In general, the number of HQ tubes in one array N_T should be selected in order to scatter energy into modes that are well attenuated by the liner, i.e. higher order modes. For the case of the Rig 649, the minimum number of tubes required is 52, which is certainly a large number. Since there was no previous experience with this high amount of HQ tubes per array, an alternative approach was considered based on the sound radiation pattern. For the BPF at cutback condition, the rotor-rotor mode m=26 is just cut on and thus, radiates sound to the sidelines where the regulations are concerned. On the contrary, a well cut on mode (very low order) would radiate sound to the front of the engine, which is of less important for certification. Therefore, the number of tubes N_T can be selected to scatter energy into the very low order modes that radiate energy to the front of the inlet. This concept is illustrated in Figure 4.11. Finally, the number of tubes was selected to be $N_T = 27$ in order to scatter energy into the circumferential mode m = -1.

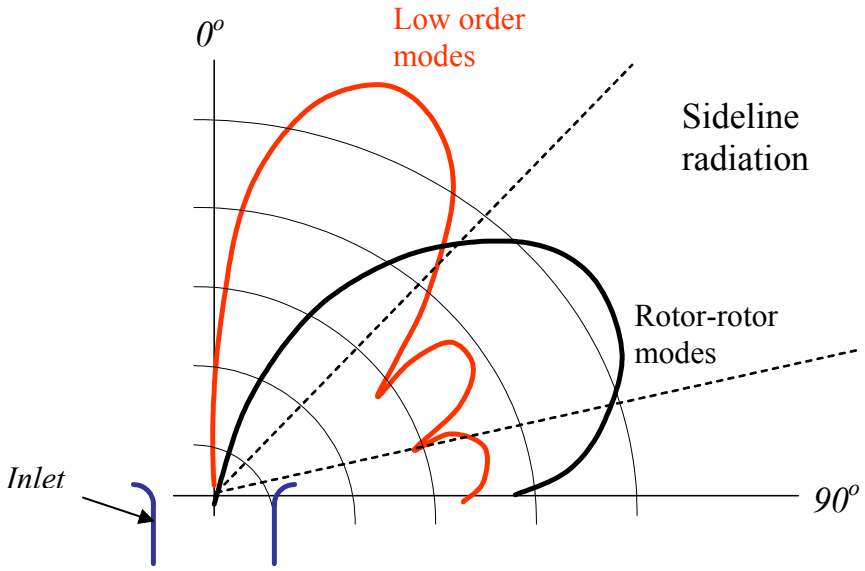

Figure 4.11: Modal Sound Radiation Directivity comparison between high and low order circumferential modes at high power settings.

Number of arrays: N_A

The number of arrays of HQ tubes is limited by the available acoustic treatment length. The adopted configuration for the Rig 649 system consisted on placing 4 arrays of

HQ tubes, which were staggered in pairs as shown in Figure 4.12. The angle defined by two adjacent tubes was optimized for a better control of the rotor-rotor mode (26,0). The rotation (spin) of the mode (26,0) combined with its axial propagation describe a wave front that has a certain angle with the duct axis. Based on previous experience, the attenuation of the HQ system tends to improve when the angle of two adjacent arrays matches the wave front [17]. Therefore, this angle was adjusted to match the rotation of the mode (26,0) for BPF at cutback condition. In order to achieve this configuration, the HQ tube cross sectional area was selected to be $S_{HQ} = 1$ inch^2.

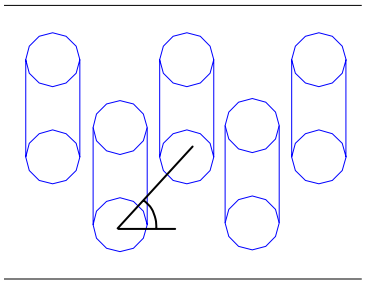

Figure 4.12: Layout of a pair of arrays of HQ tubes in a staggered configuration.

Tube Length *L* and Spacing between HQ tube openings

The tube length is mainly determined by the frequency of the tone to be attenuated and the tube acoustic resonance to be used, i.e. 1st, 2nd, etc. The HQ design goal is to reduce the BPF tone at cutback condition. In addition, based on experience, the 3rd resonance of the HQ tube will be chosen to control this frequency. The resonances of the open-open HQ tube are obtained by considering the pressure release boundary condition. These resonances including the mass-like reactance of the facing screen are the solutions of the transcendental relation obtained from equating to zero the term T_{12} of equation (3.9) as

$$2\frac{X_{ps}}{\rho c}\cos(k_o L) - \left(\left(\frac{X_{ps}}{\rho c}\right)^2 - 1\right)\sin(k_o L) = 0 \qquad (4.5)$$

where X_{ps} is the reactance of the screen, ρc is the characteristic impedance of air, k_o is the free wavenumber corresponding to the design frequency and L is the tube length. Equation (4.5) is solved for several values of the length L, corresponding to the different tube resonances. The obtained preliminary values can then be optimized using predictions for the HQ system performance in a hard wall [17]. For this case, the length of the tube was adjusted to $L = 4.8$ inches.

In order to illustrate the obtained geometry, Figure 4.13 presents a schematic of the combined HQ-Liner cell. Since the tubes are installed on the back plate of the liner, the liner depth has to be accounted for as part of the tube length. Therefore, the actual physical length of the tube mounted on the back of the liner is shorter than the estimated value. The interface distance for this system was defined according to the schematic of Figure 4.13 as $\ell = 3$ inches. Figures 4.14 and 4.15 present pictures of the tested HQ-Liner system.

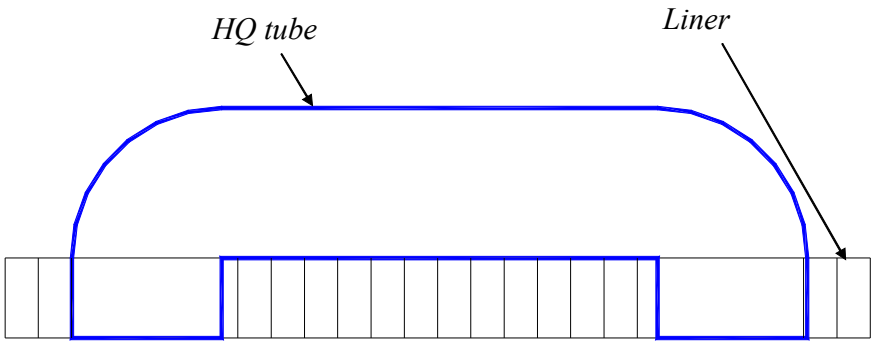

Figure 4.13: Schematic of designed HQ-Liner cell.

Figure 4.14: Tested HQ-Liner system[†].

Figure 4.15: HQ-Liner system mounted on the Rig 649 inlet[†].

[†] Pictures are courtesy of Goodrich Corporation.

4.2 Experimental Results Summary

This section presents a small part of the experimental results of the HQ-Liner system tested on the Rig649 at the ANCTF Rolls-Royce facility (Ansty, England). The small amount of data selected here will be used to perform an initial validation of the HQ-Liner computer code developed in Appendix C. To this end, the code was used to run broadband noise simulations of the tested HQ-Liner system for two conditions, i.e. 55% and 70% RPM. The comparison of these results with the experimental data is presented in the next section. The first case (*55% RPM*) corresponds to the engine power setting at the approach condition. The second case (*70% RPM*) is the condition at which the rotor blades of the fan start to generate shock waves. Below this condition, the acoustic field in the fan inlet is free of the presence of shock waves and thus, the problem can be analyzed using linear acoustics theory.

4.2.1 Results for 55% RPM (approach)

Experimental data at the approach condition (*55%*) is presented in this section. The sound power spectrum for four tested configurations is presented in Figure 4.16 as a function of the engine order, i.e. order 26 corresponds to the BPF tone. The hard wall (HW) case configuration (*red curve*) shows a broadband component with a fairly constant sound power level. Furthermore, the BPF tone and harmonics present "peaks" of about 6-8 dB above the broadband level. The lined wall configuration (*blue curve*) clearly presents an attenuation of 4-6 dB for the broadband component and 3 dB for the BPF tone. Also, it is shown that the HQ-Liner configuration (*green curve*) improves the broadband attenuation of the liner over all the range of frequencies and gives an extra 1 dB reduction for the BPF tone. The BPF for this condition is 2426 Hz.

The performance of the liner can be more clearly seen in Figure 4.17. The experimental attenuation of the liner is shown in light blue curve, while the dark blue curve is obtained by a 10% moving average process. Although it is mathematically incorrect, this plot is shown to make a better comparison with the predictions. These results show that the liner yielded a broadband attenuation of about 4-6 dB centered at the 44 order (~4100 Hz) and a 3 dB of the BPF tone. The improvement due to the HQ on the

attenuation on the liner is presented in the same fashion in Figures 4.18 and 4.19, for 2 and 4 arrays of HQ tubes, respectively. It is observed that the HQ system results in additional attenuation over the liner performance. The 2-array HQ system (*Figure 4.18*) yielded an improvement of about 0.5-0.8 dB over the full frequency range. Also, this 2-array HQ configuration resulted in an additional 2 dB of the BPF tone. The same trends are shown for the 4-array configuration (*Figure 4.19*) with an improvement of 0.5 dB over the broadband component and of 1 dB on the BPF tone. In addition, for this case there is a broad "peak" of attenuation around order 8 (low frequency ~ 780 Hz).

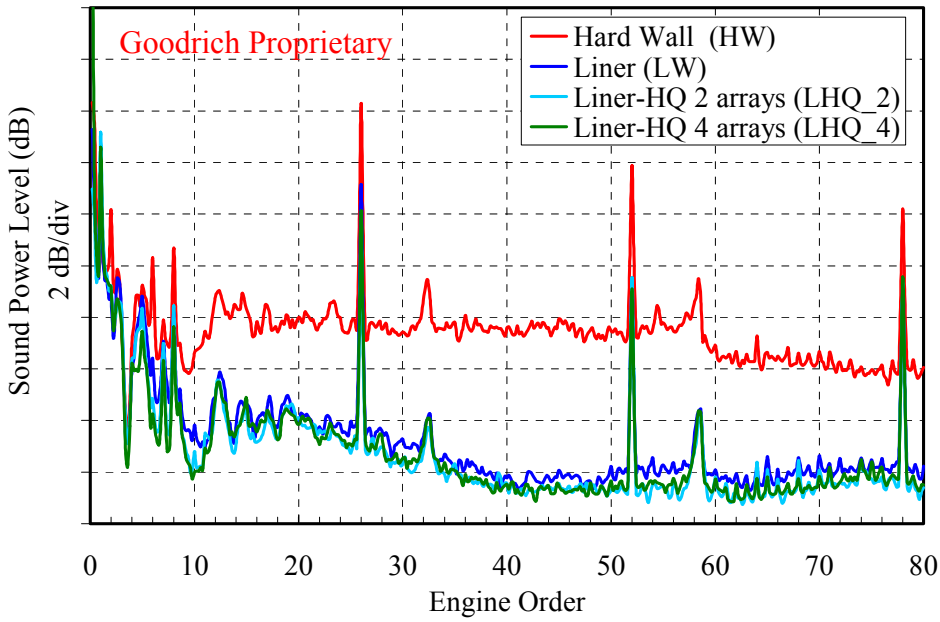

Figure 4.16: Sound Power Spectrum at 55% Power Setting (BPF = 2426 Hz (26 order)).

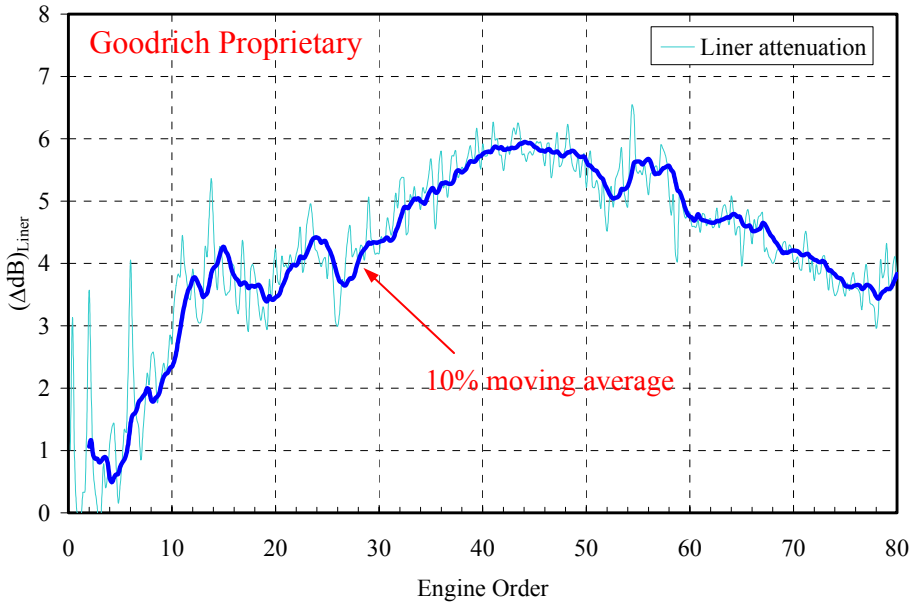

Figure 4.17: Sound Power Reduction due to Liner at 55% Power Setting.

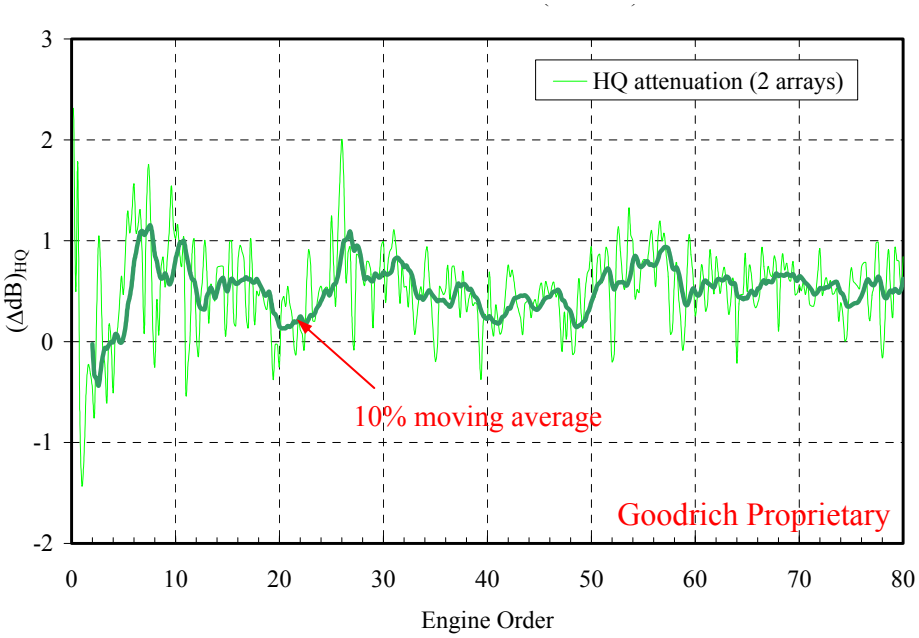

Figure 4.18: Sound Power Reduction due to 2 arrays of HQ tubes at 55% Power Setting.

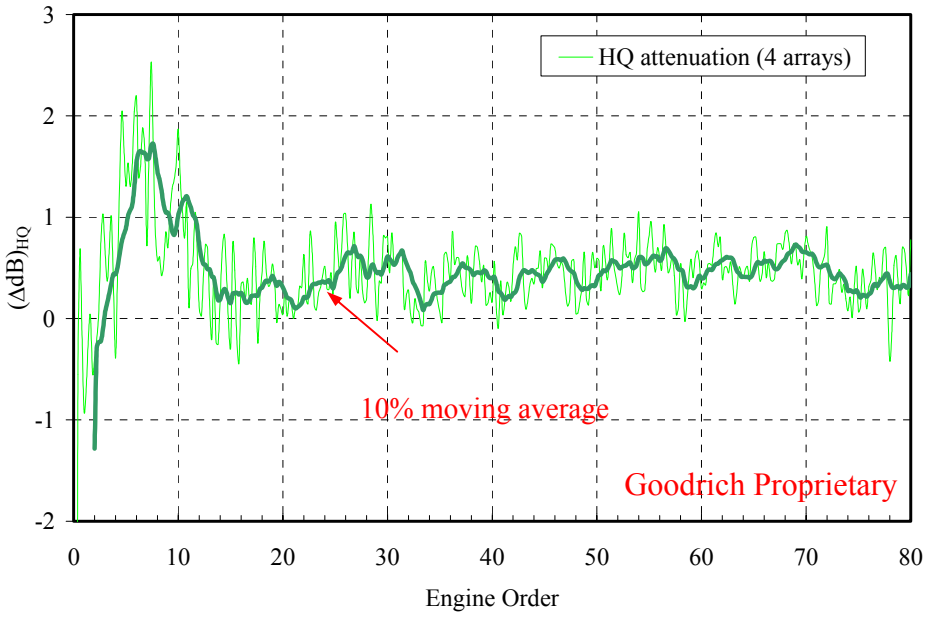

Figure 4.19: Sound Power Reduction due to 4 arrays of HQ tubes at 55% Power Setting.

4.2.2 Results for 70% RPM

This section presents experimental results for the condition at 70% RPM, which is the limit at which the fan starts to generate a sound field with the presence of shock waves. Below this point, the sound field is free of this high compressibility effect and it can be modeled with a linear formulation. On the other hand, the structure of the noise for higher power settings is a set of combination tones produced by the shock waves, which are known as the "buzz saw" noise. The model of the sound field at these conditions is arguably non-linear and it is not included in this dissertation. The experimental results are shown in the same fashion as in the past section. The sound power spectrum for the four tested configurations is presented in Figure 4.20 as a function of the engine order, i.e. order 26 corresponds to the BPF tone. The hard wall (HW) case configuration (*red curve*) shows a broadband component with a constant sound power level, while the BPF tone and harmonics present "peaks" of about 6-8 dB above the broadband level. The lined wall configuration (*blue curve*) presents an attenuation of 4-5 dB for the broadband component and 7 dB for the BPF tone. The reason of the increase in the BPF attenuation

can be explained from the point of view of the eigenvalue problem analyzed in section 4.3.1. At the high power settings, the modal structure of the BPF tone starts to be dominated by the mode *m=26*. But as it was previously analyzed, the effect of the liner on the propagation properties of this mode is to push the cut-off frequency to a higher value. Thus, the mode *m=26*, which was able to propagate in the hard wall condition, will now decay fast and produce an increase of the observed liner BPF tone attenuation. It is shown in Figure 4.20 that the HQ-Liner configuration (*green curve*) improves the broadband attenuation of the liner over all the range of frequencies and gives an extra 1.2 dB reduction for the BPF tone. The BPF for this condition is 3033 Hz.

The performance of the liner can be more clearly seen in Figure 4.21. As in the previous section, the experimental attenuation of the liner is shown in light blue curve, while the dark blue curve is obtained by a 10% moving average process. These results show that the liner yielded a broadband attenuation of about 4-5 dB centered at the 35 order (~4100 Hz) and a 6.8 dB of the BPF tone. The improvement due to the HQ on the attenuation on the liner is presented in the same fashion in Figures 4.22 and 4.23, for 2 and 4 arrays of HQ tubes, respectively. For this power setting, it is again observed that the HQ system results in additional attenuation over the liner performance. The 2-array HQ system (*Figure 4.22*) yielded an improvement of about 0.5-0.8 dB over the frequency range below the engine order 40 and also 1 dB for the frequency range above this point. The HQ system also resulted in an additional attenuation of 1 dB on the BPF tone. In addition, there is a broad “peak” of attenuation around order 5 (low frequency ~ 500 Hz). The 4-array configuration (*Figure 4.23*) shows the same trend with an improvement of 0.5 dB over the broadband component. For this case, this broadband improvement is constant over the full range of frequencies. Also, the HQ system improves by 1.3 dB the attenuation of the BPF tone.

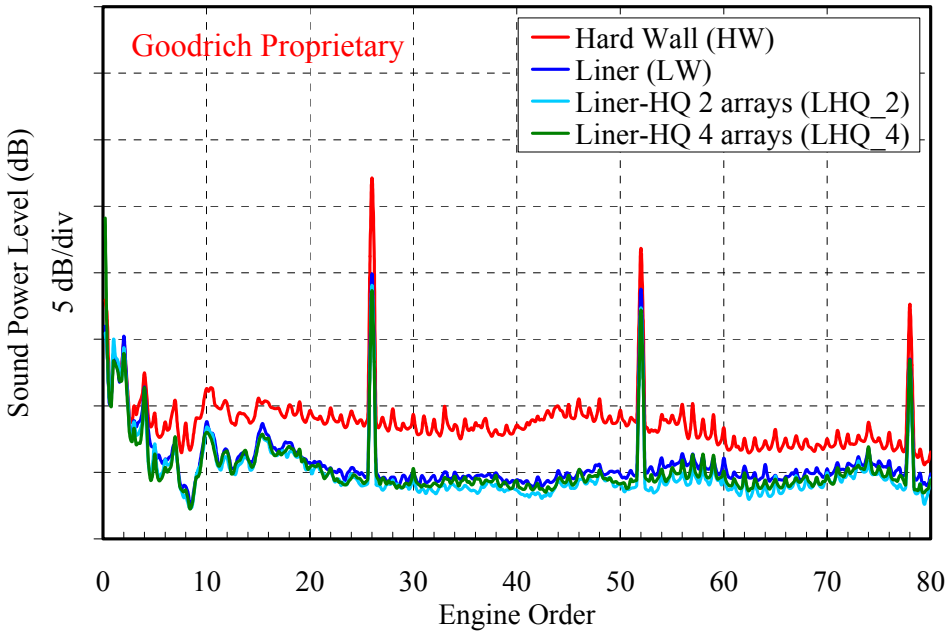

Figure 4.20: Sound Power Spectrum at 70% Power Setting (BPF = 3033 Hz (26 order)).

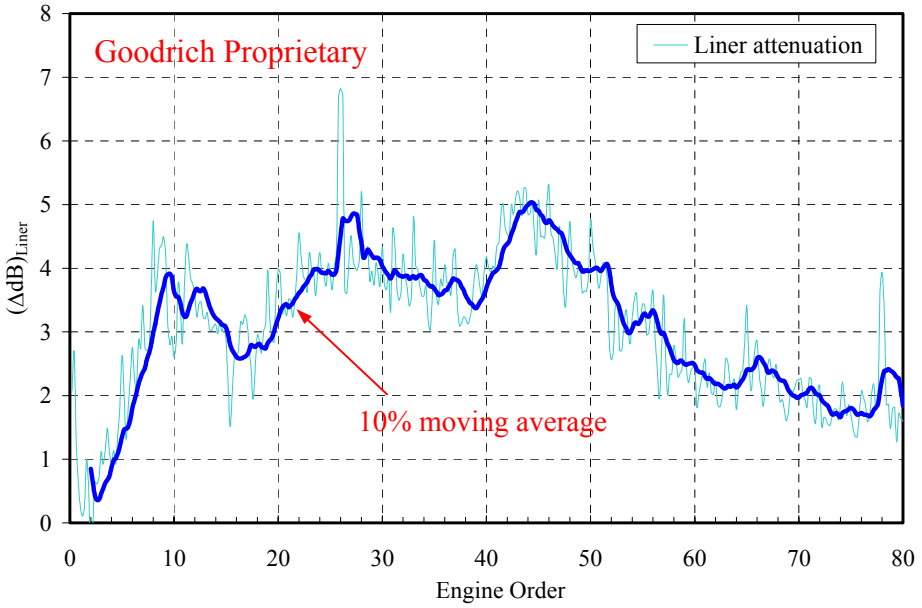

Figure 4.21: Sound Power Reduction due to Liner at 70% Power Setting.

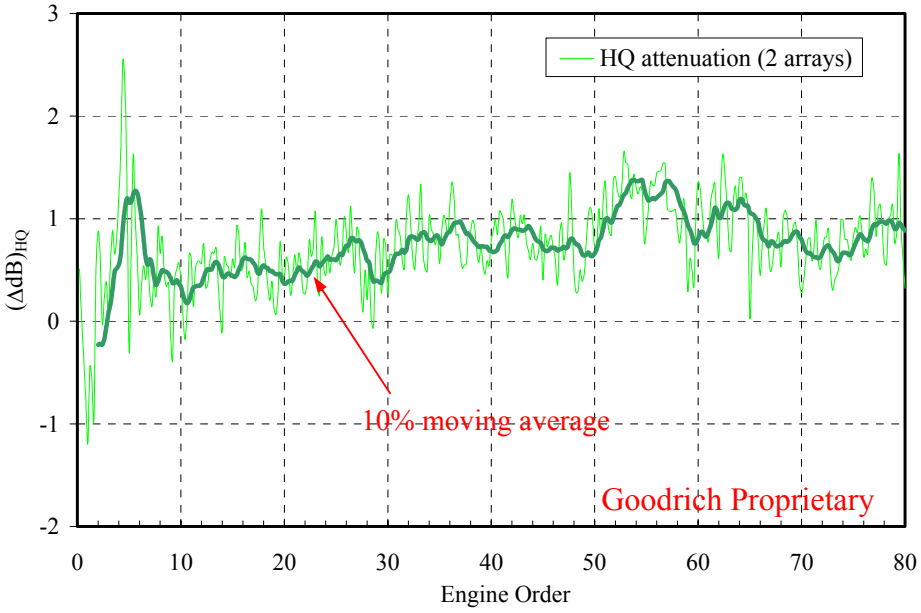

Figure 4.22: Sound Power Reduction due to 2 arrays of HQ tubes at 70% Power Setting.

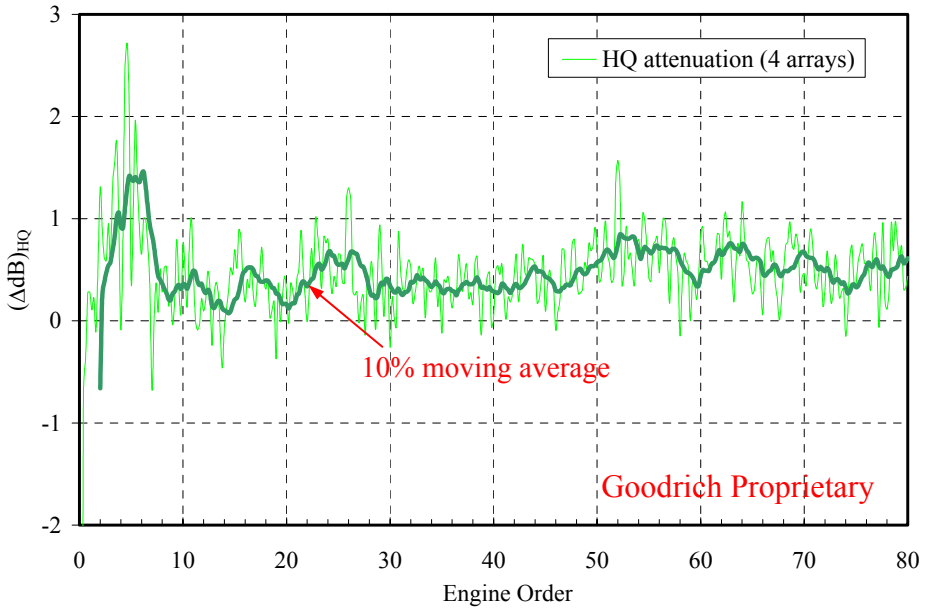

Figure 4.23: Sound Power Reduction due to 4 arrays of HQ tubes at 70% Power Setting.

4.3 Numerical Results

The analytical predictions of the performance of the HQ-Liner applied to the inlet of a turbofan inlet are compared to the experimental results in this section. The turbofan operation conditions are considered to be the same as for the experimental results presented in this Chapter, i.e. 55% and 70% power setting. The noise component to be predicted is mainly broadband. The analyzed configurations are for lined wall, combination of liner with 2 arrays of HQ tubes and combination of liner with 4 arrays of HQ tubes. The dimensions and location of each array of HQ tubes is presented in Table 4.4. In addition, the performance of 4 arrays of HQ tubes on the BPF tone for a range of subsonic rotational speeds is briefly investigated. The higher power settings will not be investigated since the sound field at these conditions is arguably non-linear, i.e. due to shock waves.

The numerical predictions were obtained using the FORTRAN code developed in Appendix C and based in the theoretical model in Chapter 3. The code predicts the attenuation of the liner as well as the performance of the combined HQ-Liner system. As a consequence, the performance of the HQ system will be presented as the difference between the attenuation of the HQ-Liner and the Liner alone, i.e. improvement of the attenuation as $(\Delta dB)_{HQ} = (\Delta dB)_{HQ-Liner} - (\Delta dB)_{Liner}$. The results presented in this manner will give a clear idea of the effect of the HQ tubes at different frequencies.

Table 4.4: HQ Arrays configurations.

Array #	N [-]	Tube Length [m]	Tube Cross Section Area [m^2]	Interface distance I/O [m]	Axial location [m]	Azimuth angle of 1st first tube
1	27	0.1223	0.0007	0.08	0.1377	5.423
2	27	0.1223	0.0007	0.08	0.1841	0
3	27	0.1223	0.0007	0.08	0.2941	5.423
4	27	0.1223	0.0007	0.08	0.3405	0

It is important to remark that the code requires knowledge of the modal structure in both magnitude and phase in order to compute the system performance. However, the generation of broadband noise by a turbofan engine is still an open topic for future research. Thus, since it is proven to be a good approximation [20], a conventional assumption will be made in the numerical simulations. This conventional approach consists in modeling the broadband noise in the turbofan inlet using an "equal energy" distribution into the cut-on modes inside the duct. Since it is not possible to define the cut-off frequency in a soft wall duct, all the modes should be included in the fan disturbance. However, this will lead to obtain incorrect results because the liner attenuation predictions will reflect very good performance on modes that are basically cut-off, and therefore were likely never generated by the fan. Then, an alternative approach was used to select the modes present in the duct. This method consists in including in the disturbance only the modes that satisfy the following rules

- The mode must be cut-on in the hard wall case, and
- The absolute value of the imaginary part of the lined wall complex mode axial wavenumber $k_z^{(+)}$ (*see Figure 4.24*) must be less than 5 in order to be included. Thus, modes that are basically cut-off in the soft wall are eliminated.

The "equal energy/random phase" approach was then applied to these modes as an attempt to simulate the broadband component.

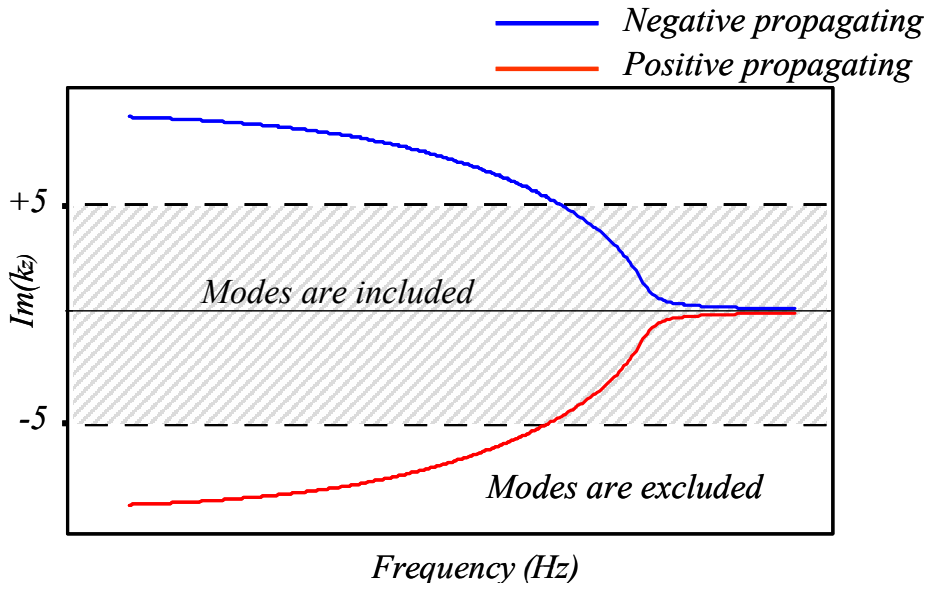

Figure 4.24: Analysis of the imaginary part of k_z to include modes in the fan disturbance.

The next sections will present the broadband noise attenuation predictions of the Liner and HQ-Liner configurations. Due to the plane wave limitation in the HQ tube modeling, these predictions are only performed on the range of frequencies 0-3500 Hz. These frequencies cover the range of engine orders 0-40 for 55% RPM and 0-30 for 70% RPM. As described in Chapter 3, the sound field inside the HQ is only described by plane wave modes. Thus, when the disturbance starts to be of the same order of magnitude as the dimensions of the HQ tubes, i.e. higher frequencies, the excitation of these HQ plane waves will decrease to the point that stops producing any effect on the incoming duct modes. Consequently, the predictions are limited to the specified frequency range. It is important to mention that the objective of the HQ tubes is to produce an improvement in the attenuation of the liner for frequencies up to the BPF. For this reason, it is required that the theoretical model can predict the HQ noise attenuation for a range of frequencies that can capture this BPF. Fortunately for this case, the BPF is always below the specified limit of 3500 Hz for all fan conditions and the model can be safely applied.

4.3.1 Eigenvalue Problem

This section presents the numerical results of the eigenvalue problem derived in section 2.1. The found eigenvalues contain the information about the propagation characteristics of the acoustic modes inside the lined circular duct. These characteristics correspond to the behavior of the modal axial wavenumbers $k_z^{(+)}$ and $k_z^{(-)}$, which are obtained using equations (2.27) in terms of the eigenvalues $k_{mn}^{(+)}$ and $k_{mn}^{(-)}$. The eigenvalues are the roots of the characteristic equations in (2.28). As described in section 2.1.1, these equations are solved iteratively starting from very low frequencies, where the roots are close to the hard wall eigenvalues. For the hard wall case, the roots k_{mn} are simply obtained from the zeros of the derivative first kind Bessel functions which are generally tabulated [1]. Then, for higher frequencies, these eigenvalues are displaced into the complex plane, describing a path-line that is parametric with frequency and starts from the real axis at the hard wall values. Calculations were performed for several modes in the inlet of the Rig 649 and a flow Mach number $M=-0.27$ opposite to the direction of

positive propagation. Both hard and lined wall cases were analyzed and compared. The wall impedance considered for these calculations correspond to the liner used on the Rig649 experiments and was presented in Figure 4.6 (for *M=0.27*).

The positive and negative propagating eigenvalues and wavenumbers are presented in the following figures for two different circumferential orders *m=6* and *26*. The eigenvalues for the two circumferential mode orders and their seven first radials, i.e. from *n = 0* to *6*, are presented in Figure 4.25. The figure clearly shows the behavior of the eigenvalues for a low order mode (*m=6*) compared to the case of a high order mode (*m=26*). For the positive propagating *m=6* modes, the first radial mode (*n=0*) describes a considerably large trajectory compared to the rest of the modes. Also, this trajectory describes a lobe that surrounds up to the 5th radial mode (*n=4*). On the contrary, for higher order positive propagating modes (*m=26*), the trajectory of the first radial order mode is similar to the rest of the modes. For the negative propagating, both the low (*m=6*) and high order (*m=26*) modes present the same behavior. The first radial mode (*n=0*) describes a considerably large trajectory compared to the rest of the modes, describing a lobe that surrounds up to the 2nd radial mode (*n=1*).

It is clearly observed in Figure 4.25 that the exact location of the eigenvalues of every mode as a function of frequency can be identified from the described trajectories in the complex plane. Thus, the order of the eigenvalues has to be assigned based on the initial location at low frequency, which corresponds to the hard wall case. In addition, their displacement in the complex plane as a function of frequency will give an idea on how the mode is distorted by the presence of the liner. This shows that the common technique to order the eigenvalues [32], which is based in the magnitude of their real part, may lead to incorrect results.

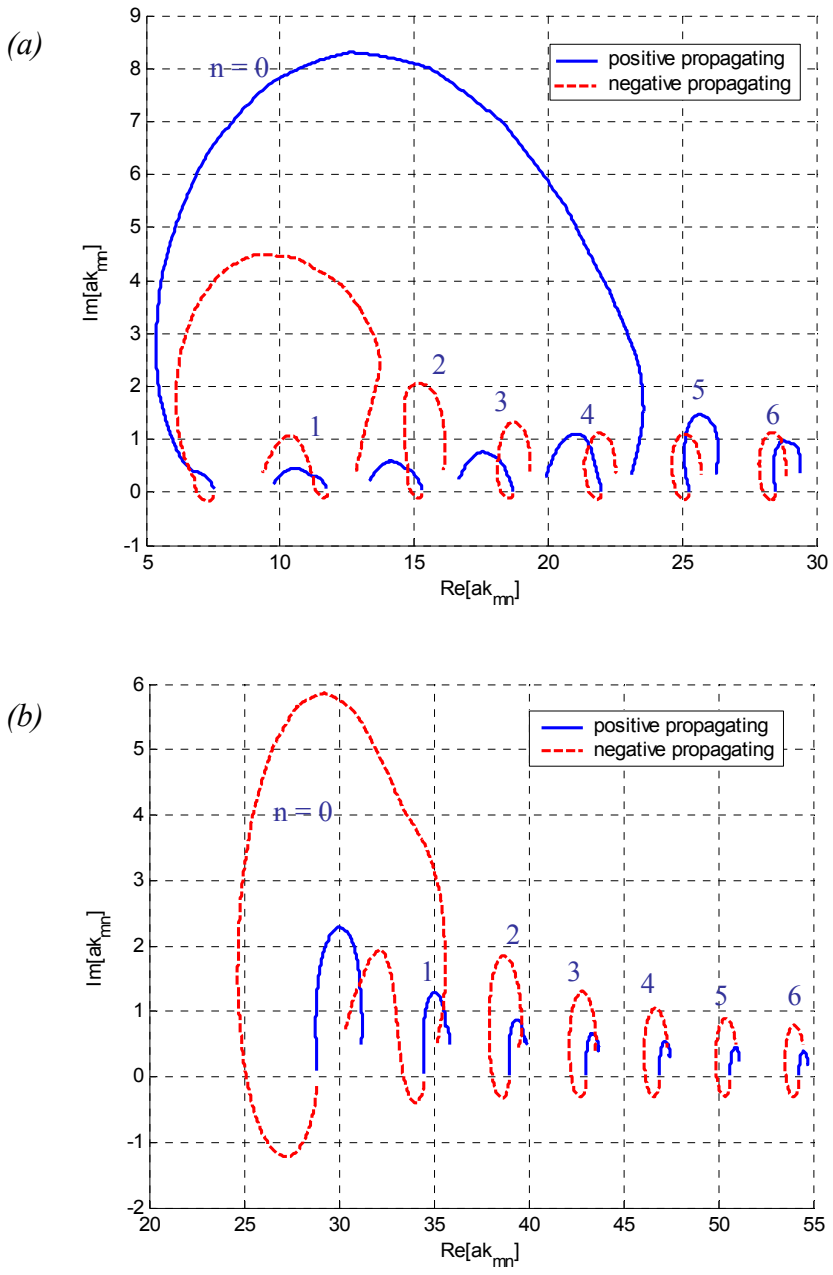

Figure 4.25: Positive and Negative propagating eigenvalues for the modes (a) m = 6 and (b) m = 26.

The behavior of the eigenvalues shown in Figure 4.25 suggests that the influence of the liner appears mainly on the first radial order of each circumferential mode, and it decreases for the higher radial orders. This effect will be more clearly identified on the propagation characteristics given by the axial wavenumbers $k_z^{(+)}$ and $k_z^{(-)}$, which are

plotted in Figures 4.26 through 4.29. Each figure shows: *(a)* the real and imaginary axial wavenumber $k_z^{(\pm)}$ components for the *n=0* radial mode, and *(b*) the real and imaginary axial wavenumber $k_z^{(\pm)}$ components for the *n=1* radial mode. Plots for both hard and lined wall cases are presented in the same figures for comparison purposes and to clearly see the influence of the liner on the propagation of the modes.

For the analyzed modes, the optimum attenuation of the liner is observed to take place on the *2000* to *4000* Hz frequency range. Note that the liner is tuned to approximately *3400* Hz (*see Figure 4.6)*. In this range, it can be seen that for the first radial order mode, i.e. *n=0*, both the real and imaginary part of the axial wavenumber are distorted from the hard wall case. The distortion of the imaginary part of the wavenumber has a direct effect on the mode attenuation, which results in exponential decay even if the mode is well cut-on. As mentioned before, this effect is produced by the behavior of the first radial order eigenvalues as shown in Figure 4.25. On the other hand, the influence of the wall impedance on the second radial mode, i.e. *n=1*, does not affect the axial wavenumber significantly compared to the previous case. Since the eigenvalues of the higher order modes get less distorted, their axial wavenumbers are even closer to the hard wall case. Also, the same trend is shown by the higher order radial modes, and therefore their plots are not presented.

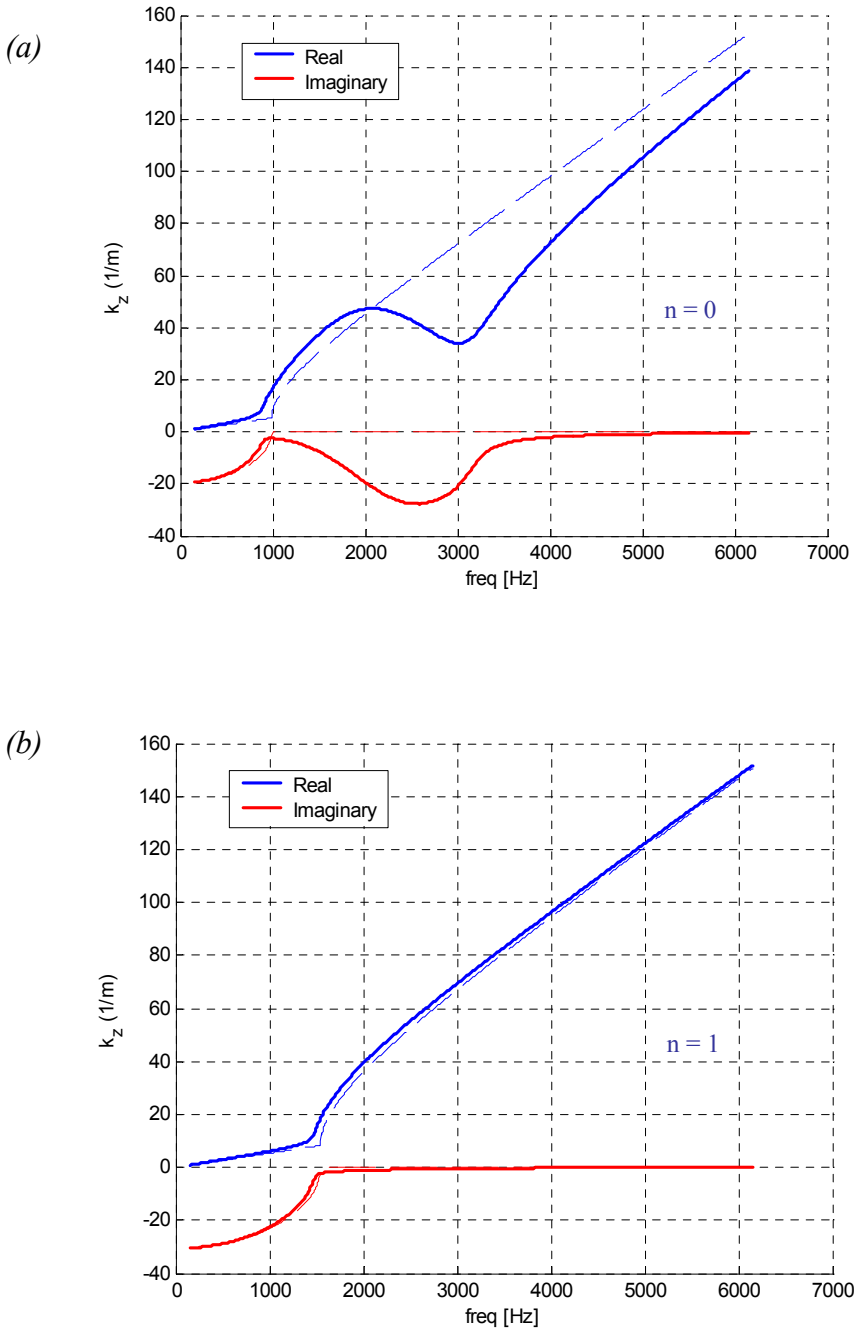

Figure 4.26: Positive propagating axial Wavenumbers $k_z^{(+)}$ for the mode ***m=6***. (a) n=0, (b) n=1. The solid and dashed lines represent the lined and hard wall case, respectively.

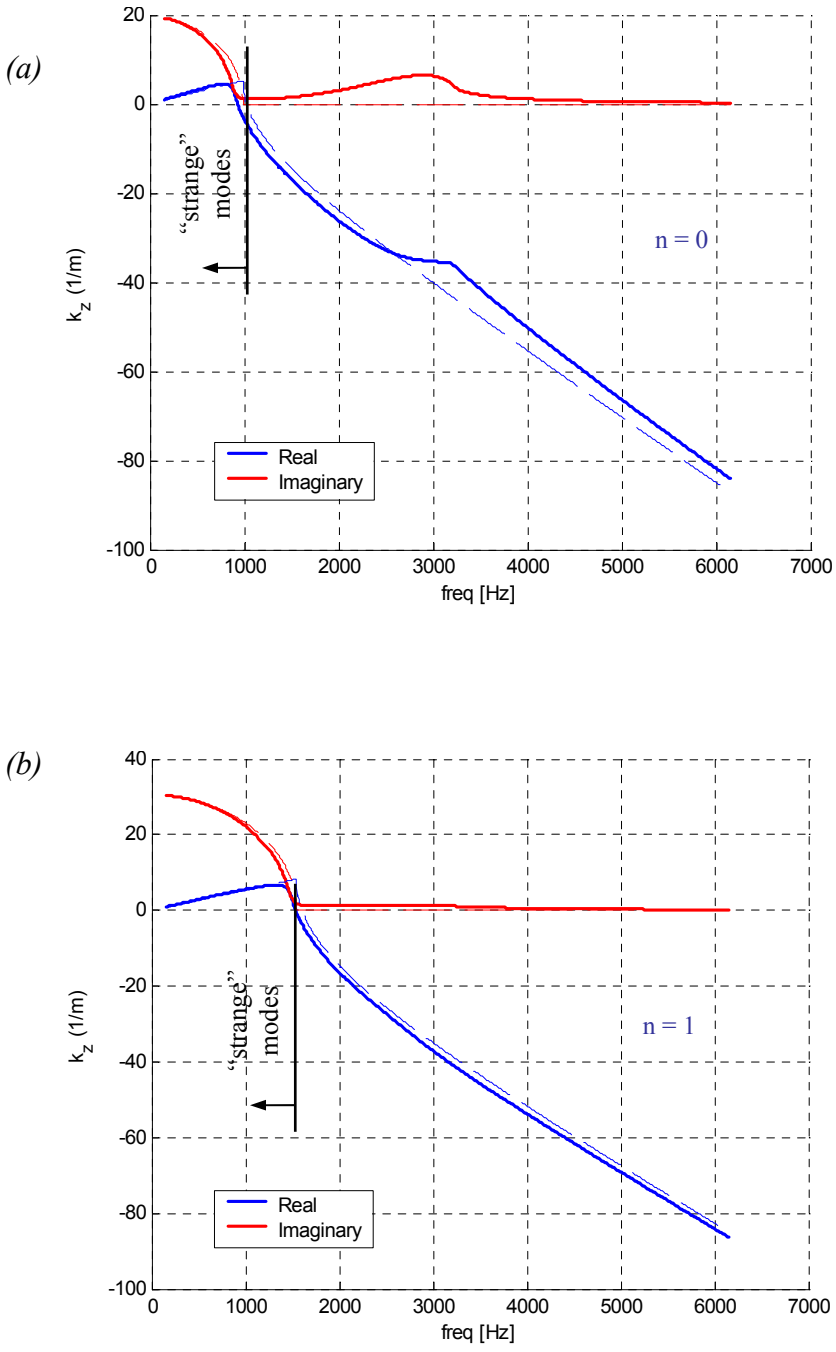

Figure 4.27: Negative propagating axial Wavenumbers $k_z^{(-)}$ for the mode ***m=6***. (a) n=0, (b) n=1. The solid and dashed lines represent the lined and hard wall case, respectively.

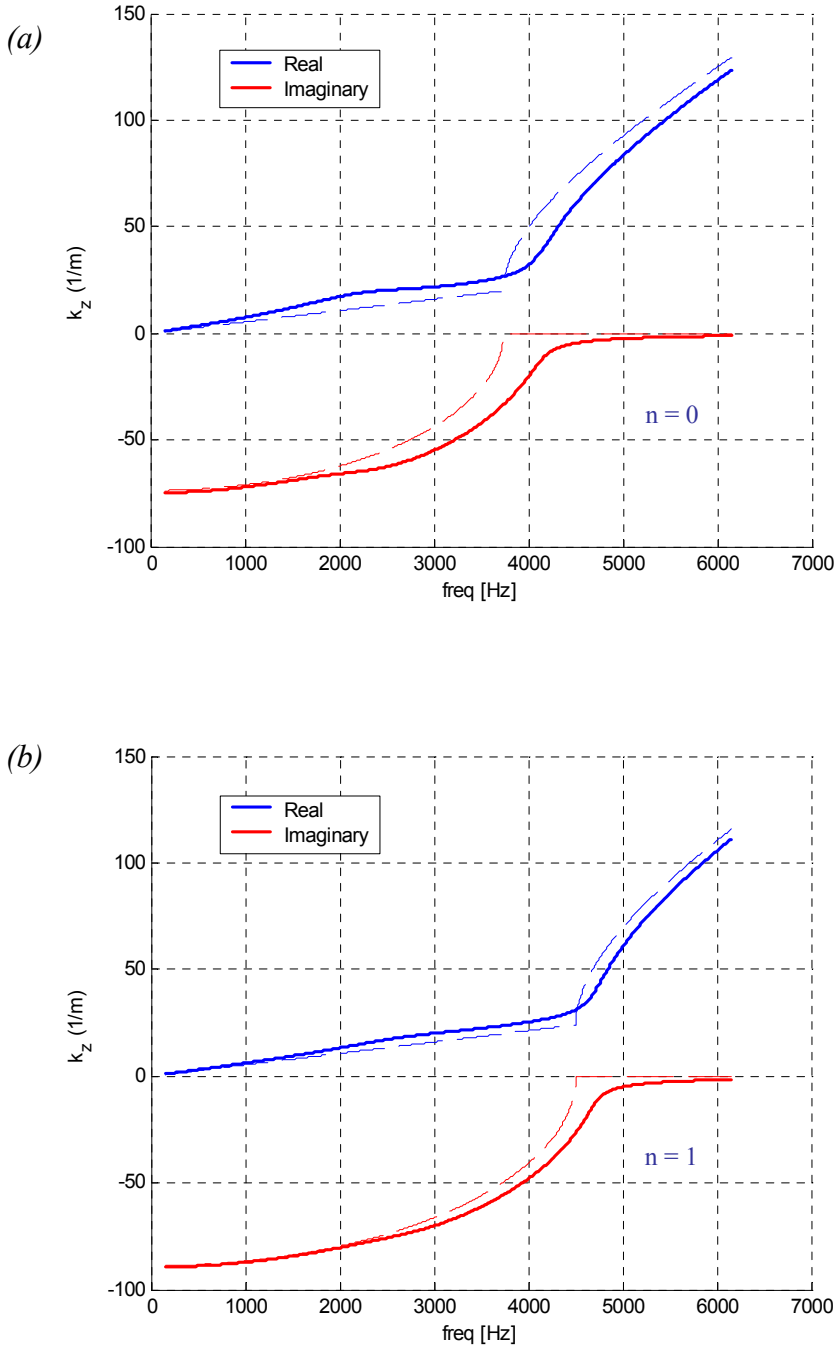

Figure 4.28: Positive propagating axial Wavenumbers $k_z^{(+)}$ for the mode ***m=26***. (a) n=0, (b) n=1. The solid and dashed lines represent the lined and hard wall case, respectively.

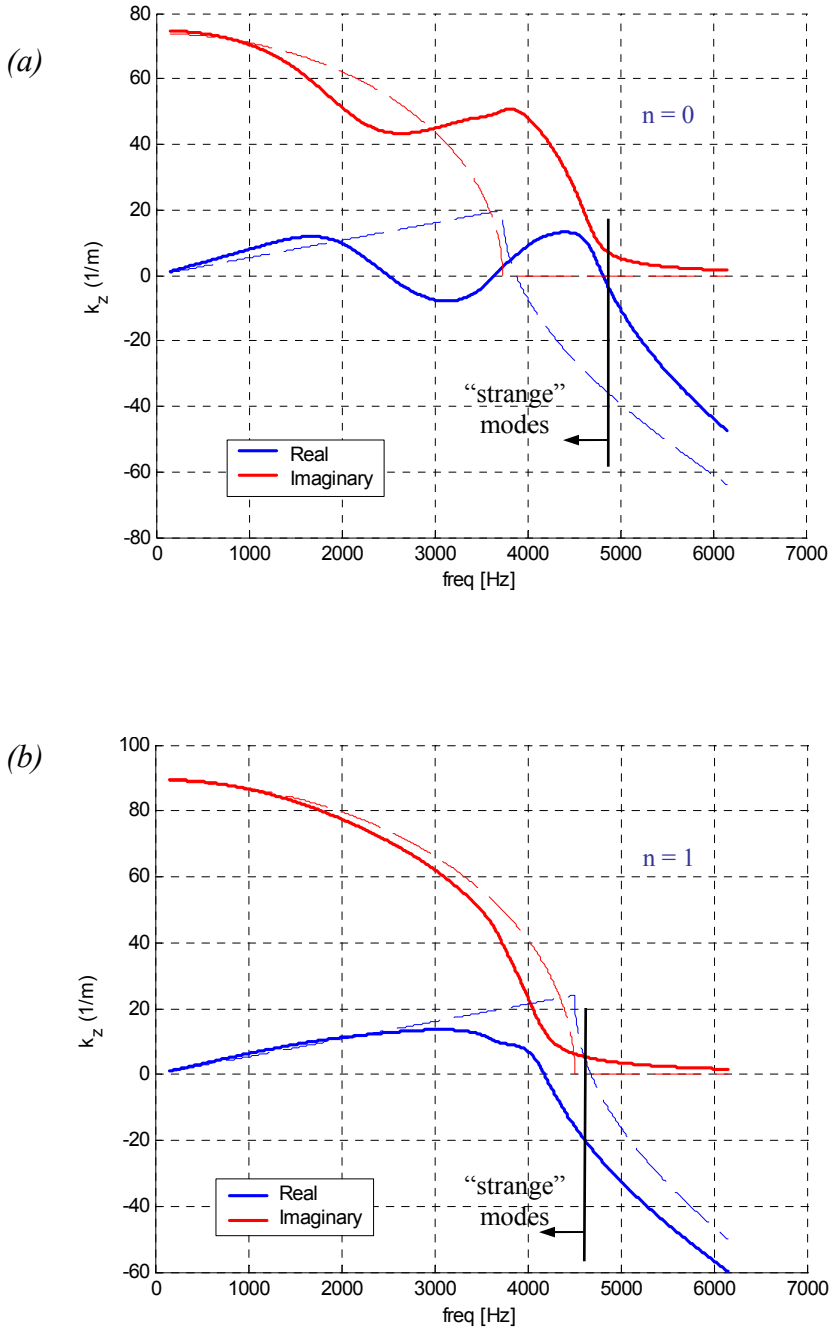

Figure 4.29: Negative propagating axial Wavenumbers $k_z^{(-)}$ for the mode ***m=26***. (a) n=0, (b) n=1. The solid and dashed lines represent the lined and hard wall case, respectively.

At this point it is important to remark the effect of the liner on the imaginary part of the axial wavenumbers $k_z^{(+)}$ of the mode *m = 26*, which are presented in Figure 4.28. It is observed in the figure, that the imaginary part of the axial wavenumbers is shifted from the hard wall case to higher frequencies. It can also be seen that the hard wall cut-off frequency of the mode (26,0), i.e. ~3800 Hz, is exactly in the range of effectiveness of the liner. Consequently, the distortion of the imaginary part of the axial wavenumber $k_z^{(+)}$ has the effect of producing a shift in the cut-on frequency of that mode towards higher frequencies.

Finally, the figures presenting the axial wavenumbers for the **negative** propagating modes, i.e. Figures 4.27 and 4.29, show that these modes have "strange" behavior for low frequencies. These modes were identified previously by Tester [30] since they have a phase velocity opposite to the direction of attenuation. In his work, Tester used these modes to represent instabilities produced by noise sources located in a lined duct with flow. However, for the investigation purposes of this dissertation, these instabilities are not allowed to exist and the "strange" modes are included only to satisfy the problem boundary conditions.

4.3.2 HQ-Liner Predictions at 55% RPM – 2 arrays of HQ tubes

This section presents the comparison between the predicted and experimental HQ-Liner broadband attenuation for the approach condition at 55% RPM. The flow Mach number for this case is *M=-0.27* (in the direction opposite to the positive mode propagation). In addition, the corresponding liner impedance was supplied by Goodrich Corporation and it was presented in Figure 4.6. The sound power broadband attenuation of this liner without the HQ tubes is presented first in Figure 4.30. As mentioned before, the predictions are shown for the range of 0-40 engine orders (the BPF is order 26) and are compared to the experimental data using a curve obtained by a moving average process.

The results in Figure 4.30 show a good agreement between the predicted and observed liner attenuation, i.e. predicted error is ~1.0 dB over the entire frequency range. In addition, it is observed that the comparison of both the predicted and experimental

attenuation shows that the model is under predicting the liner performance. This under prediction can be an indication that it might be necessary to include more modes in the disturbance, which implies to readjust the parameter shown in Figure 4.24, i.e. imaginary part of k_z limit. However, this study will be left for future work.

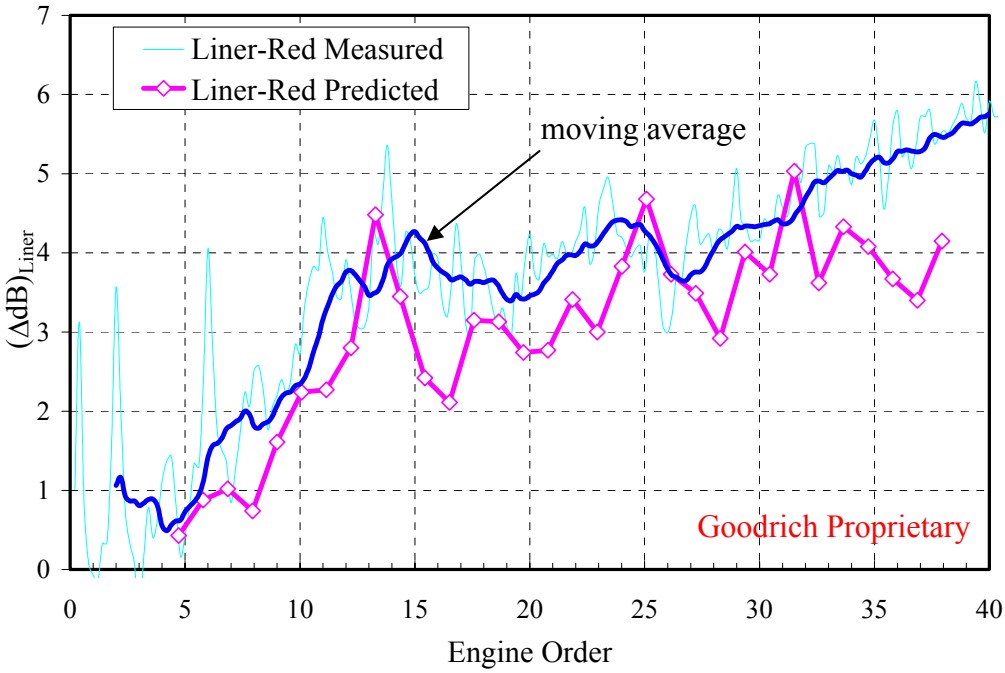

Figure 4.30: Predicted liner sound power reduction – 55% RPM – M = -0.27.

The predicted attenuation improvement due to the presence of 2 arrays of HQ tubes in conjunction with the liner is presented next in Figure 4.31. The results are shown in terms of the difference of the noise reduction due to the HQ-Liner and the Liner, i.e. $(\Delta dB)_{HQ} = (\Delta dB)_{HQ-Liner} - (\Delta dB)_{Liner}$. The dimensions and location of the HQ tubes are specified in Table 4.4 for arrays **3** and **4**. Similarly to the previous case, the predictions are compared to the experimental data using a curve obtained by a moving average process.

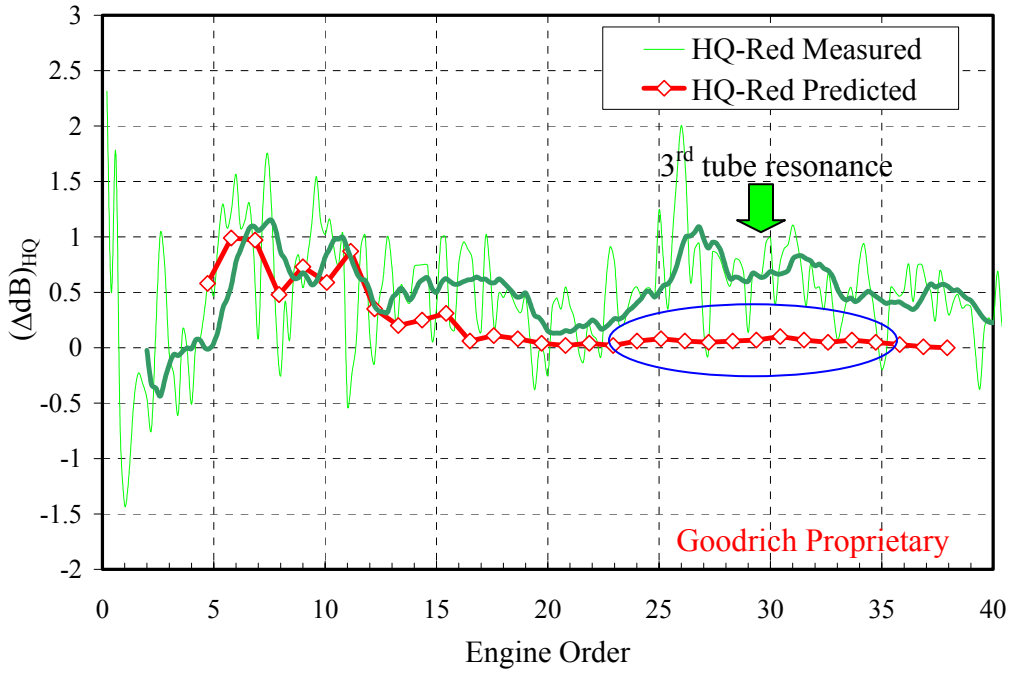

Figure 4.31: Predicted HQ sound power reduction – 2 HQ arrays – 55% RPM – M = -0.27

The predictions shown in the figure are very accurate at low frequencies (order ≤ 15 ~ 1400 Hz), and it deteriorates for higher orders: for orders in the 16-35 range it predicted an attenuation of about 0.1 dB as compared to the 0.4-0.5 dB experimentally observed. For order > 35 (~3250 Hz), the attenuation remains at around 0.5 while the numerical results show no additional reduction, i.e. after order 35 the predicted attenuation rolls off to zero. The predicted behavior at higher order, i.e. frequencies, is not unexpected since the modeling assumes that the sound field inside the HQ is only described by plane wave modes. Thus, as mentioned at the beginning of this section, the predicted attenuation for high frequencies will show little influence by the HQ tubes. For the case shown in Figure 4.31, the predicted sound power attenuation of the HQ tubes starts to be very low at order 20 and higher, compared to the experimental data. Nevertheless, it is still observed in the range of 25-35 orders that the attenuation effect due to the 3rd resonance of the tube is still captured. As a consequence, although the attenuation is very low at these higher frequencies, the prediction tool can be still very useful in order to study the region of optimum performance of the HQ tubes.

4.3.3 HQ-Liner Predictions at 55% RPM – 4 arrays of HQ tubes

The predicted attenuation improvement due to the presence of 4 arrays of HQ tubes in conjunction with the liner is presented in this section. Similarly to the previous case, the predictions correspond to the approach condition (55%RPM) and are compared to the experimental results as shown in Figure 4.32. The results are shown in terms of the difference of the noise reduction due to the HQ-Liner and the Liner only, i.e. $(\Delta dB)_{HQ} = (\Delta dB)_{HQ-Liner} - (\Delta dB)_{Liner}$. The dimensions and location of the 4 arrays of HQ tubes are specified in Table 4.4. The comparison of the predicted and experimental data is one more time performed making use of a moving average curve to represent the experimental noise reduction.

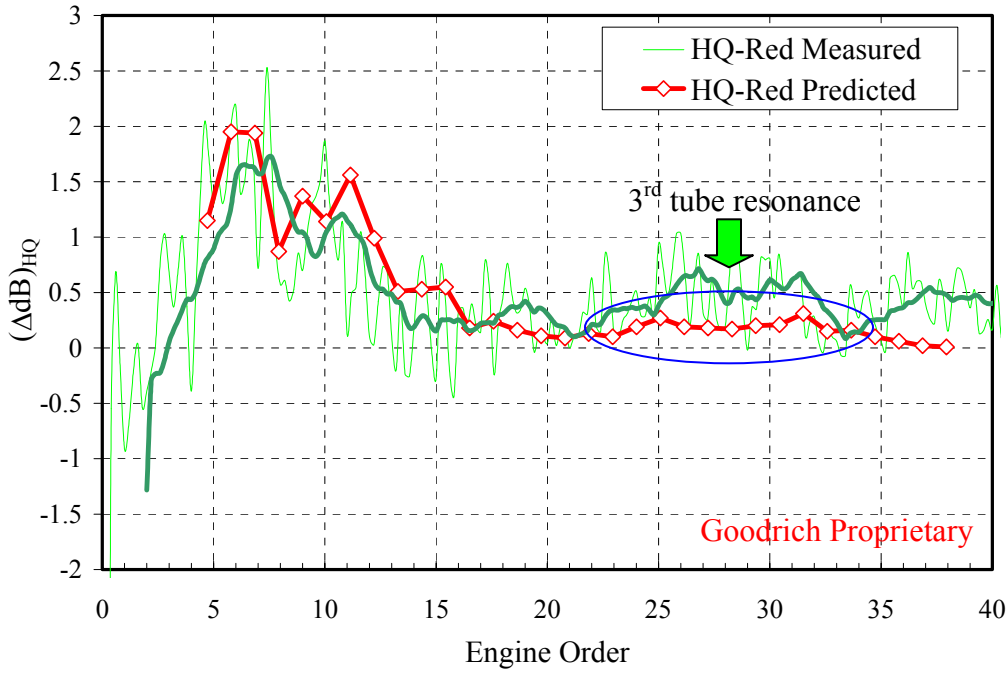

Figure 4.32: Predicted HQ sound power reduction – 4 HQ arrays – 55% RPM – M = -0.27

It is important to first note that the predicted sound power attenuation due to the presence of the HQ tubes is higher than the previous 2-array configuration. This predicted increase is produced because of the HQ system now consists of 2 more arrays of tubes, i.e. the system has twice as many tubes as before. The predictions shown in Figure 4.32

are very accurate at low frequencies (order ≤ 15 ~ 1400 Hz), and it predicts fairly well the experimental data for higher orders: for orders in the 16-35 range it predicted an attenuation of about 0.25-0.3 dB as compared to the 0.4-0.5 dB experimentally observed. As in the previous case, the predicted sound power attenuation of the HQ tubes in the 25-35 order range remarkably captures the effect of the 3rd resonance of the HQ tubes. For order > 35 (~3250 Hz), the attenuation remains at around 0.5 while the numerical results show no additional reduction, i.e. after order 35 the predicted attenuation again rolls off to zero.

4.3.4 HQ-Liner Predictions at 70% RPM – 2 arrays of HQ tubes

This section presents the comparison between the predicted and experimental HQ-Liner attenuation for the condition at 70% RPM. The flow Mach number for this case is *M=-0.37* and the corresponding liner impedance was obtained by linear interpolation of the data presented in Figure 4.6. The predictions are shown for the range of 0-30 engine orders (the BPF is order 26) and are compared to the experimental data using a curve obtained by a moving average process. The results for the liner without the HQ tubes are shown first in Figure 4.33. The results in this figure show a good agreement between the predicted and observed liner attenuation, i.e. predicted error is ~0.5 dB over most of the frequency range. However, it is observed that the comparison also shows that the model clearly over predicts by ~1 dB the liner performance on the range 15-20 orders.

The predicted improvement produced by 2 arrays of HQ tubes for this operating condition is shown in Figure 4.34. The dimensions and location of the HQ tubes are specified in Table 4.4 for arrays **3** and **4.**

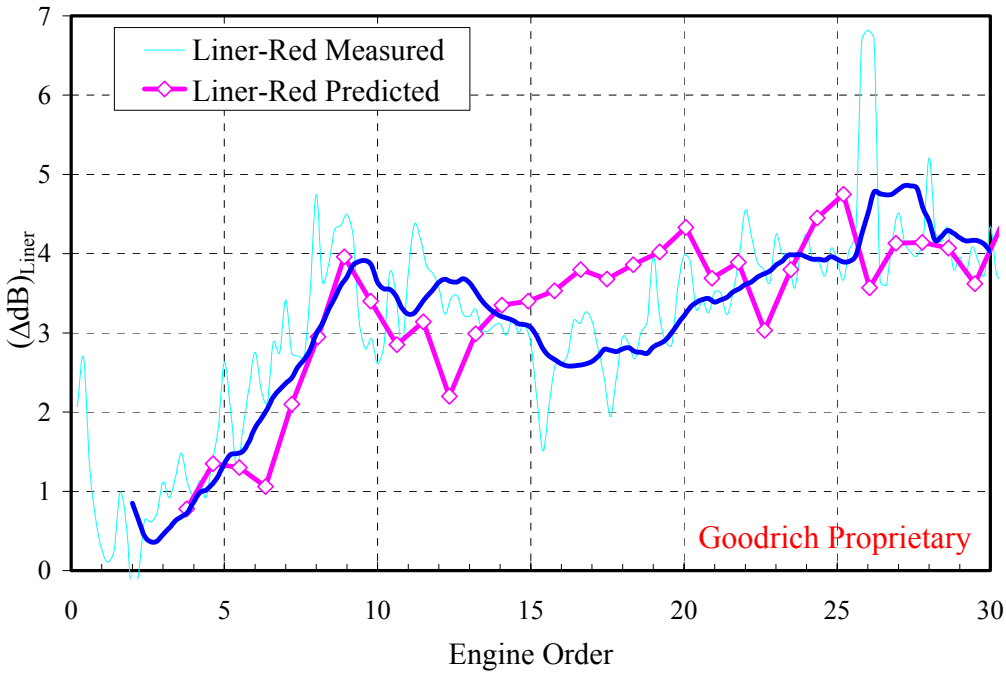

Figure 4.33: Predicted liner sound power reduction – 70% RPM – M = -0.37.

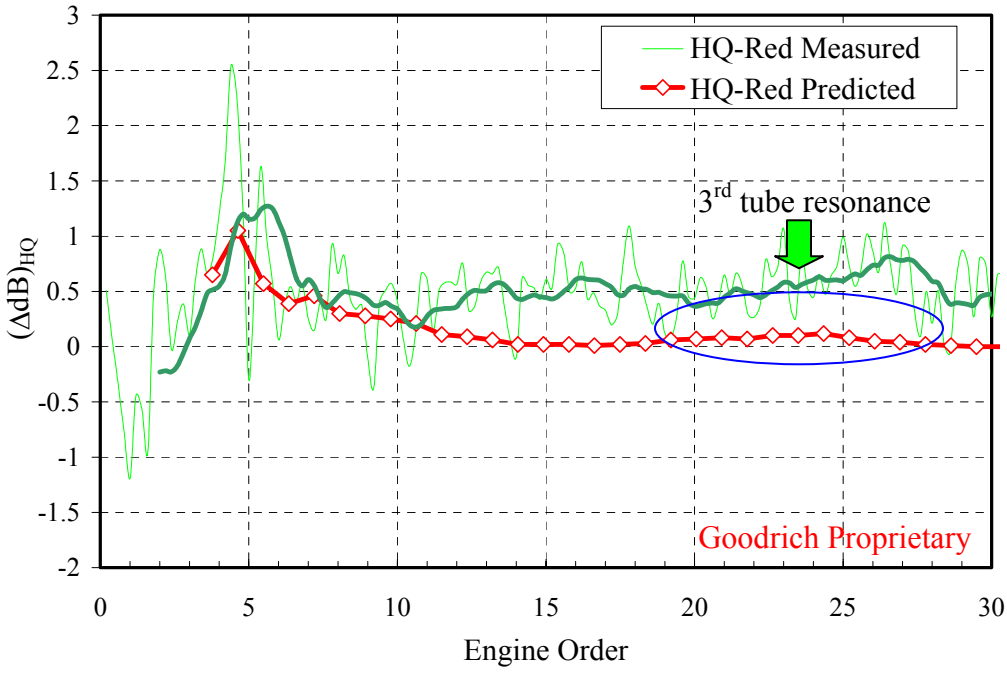

Figure 4.34: Predicted HQ sound power reduction – 2 HQ arrays – 70% RPM – M = -0.37

The predictions shown in Figure 4.34 are fairly accurate at low frequencies (order ≤ 15 ~ 1750 Hz) and it deteriorates for higher orders, following the same trend as the case for the approach condition. For engine orders higher than 15 the predicted attenuation remains under 0.1 dB while the experimental results show a constant attenuation of about 0.5 dB. This predicted behavior was already discussed in section 4.3.2 as caused by the model limitation of considering that the sound field inside the HQ tubes is only composed by plane waves. Nevertheless, it is still observed in the range of 20-30 orders that the attenuation effect due to the 3rd resonance of the tube is still captured.

4.3.5 HQ-Liner Predictions at 70% RPM – 4 arrays of HQ tubes

This section presents the attenuation improvement for the case of 4 arrays of HQ tubes for the operating condition at 70% RPM. The theoretical results are shown in terms of the difference of the noise reduction due to the HQ-Liner and the Liner only, i.e. $(\Delta dB)_{HQ}$ and are compared to the experimental data as shown in Figure 4.35. The dimensions and location of the 4 arrays of HQ tubes are specified in Table 4.4.

Similarly to the case at approach condition, the predicted sound power attenuation due to the presence of the HQ tubes is higher than the 2-array configuration. This predicted increase was produced because the system now has twice as many tubes as before. The predictions shown in Figure 4.35 are very accurate at low frequencies (order ≤ 15 ~ 1750 Hz), and it predicts well the experimental data for higher orders: for orders in the 16-30 range it predicted an attenuation of about 0.25-0.3 dB as compared to the 0.4-0.5 dB experimentally observed. As in the previous case, the predicted sound power attenuation of the HQ tubes in the 20-30 order range remarkably captures the effect of the 3rd resonance of the HQ tubes. For order > 30 (~3500), the attenuation remains at around 0.5 while the numerical results show no additional reduction, i.e. after order 30 the predicted attenuation again rolls off to zero.

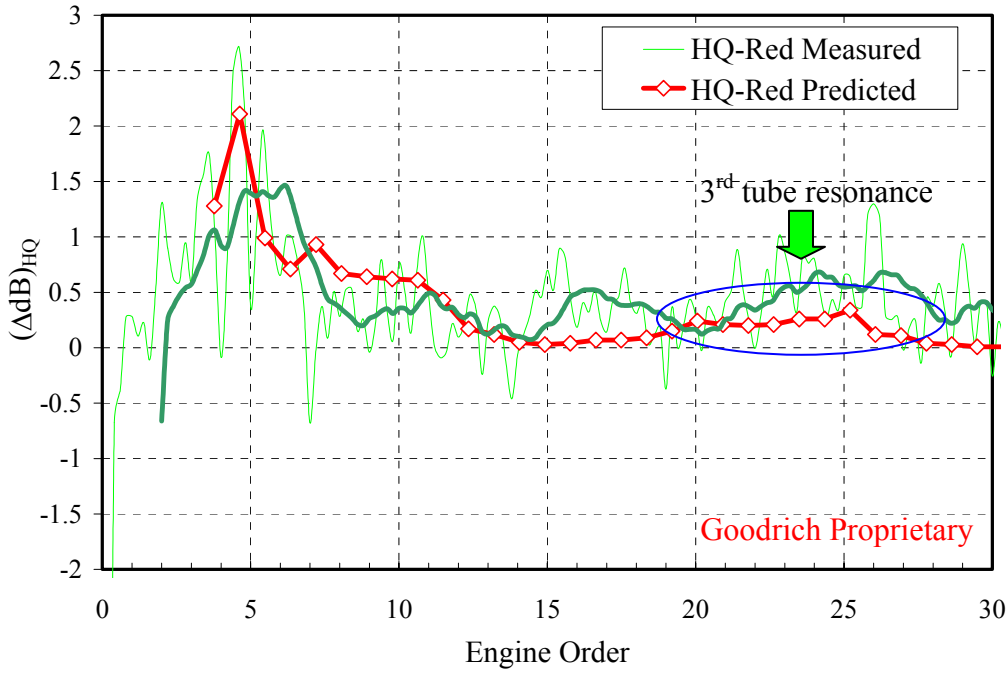

Figure 4.35: Predicted HQ sound power reduction – 4 HQ arrays – 70% RPM – M = -0.37

From these studies, it can be concluded that the broadband noise attenuation predictions are an important tool for the investigation of the performance of the Liner and HQ-Liner. The comparison between experimental and predicted data for 55% RPM and 70% RPM show a fairly good agreement and also the effects of the HQ tubes are remarkably captured. In addition, the presented predictions are dependent upon the modal structure of the broadband noise disturbance. In order to be able to get more accurate results, it is suggested to improve the "equal energy" approach to simulate structure of the broadband noise.

4.3.6 HQ-Liner Predictions for BPF tone – 4 arrays of HQ tubes

As the last results, this section presents preliminary predictions of the HQ-Liner performance at the BPF tone for subsonic conditions, i.e. the blade tips do not reach supersonic speed. The investigated configuration is for 4 arrays of HQ tubes (see Table 4.4). Due to limited accuracy in the modal data, only the engine regimes in the range 65-75 %RPM are considered. The flow Mach number for these regimes is assumed to be

constant at *M=-0.37*. As mentioned before, the code requires accurate knowledge of the modal structure in both magnitude and phase in order to compute the system performance. This information is required especially in the case of the BPF tone, which is usually dominated by a few modes. For the case of the Rig 649, the modal analysis of the experimental data was developed by Rolls Royce [61]. This technique allows identifying the pressure levels of the present circumferential modes, but the radial orders are unknown. The information about the phase is also unavailable. For this reason, a simple analysis on the available modal data at subsonic condition was performed. This analysis showed that the dominant modes in the range 65-70 %RPM was dominated by the circumferential order m=-4, and in the 70-75% was dominated by m=8. The information for other RPM ranges was uncertain. Under this consideration, the BPF tone predictions were undertaken using these modes, including all the radial cut-on modes for each m order, i.e. using the same modified "equal energy" approach of section 4.3. The predictions are shown in Figure 4.36. This figure shows that the trend is captured fairly well by the predictions, but the results are under predicted. The figure shows the individual influence of both m orders, i.e. m=-4 and m=8. It is observed that some of the experimental results can be explained by the influence of these modes. However, in order to improve these predictions, it is necessary to have better information. A detailed study is left for future work.

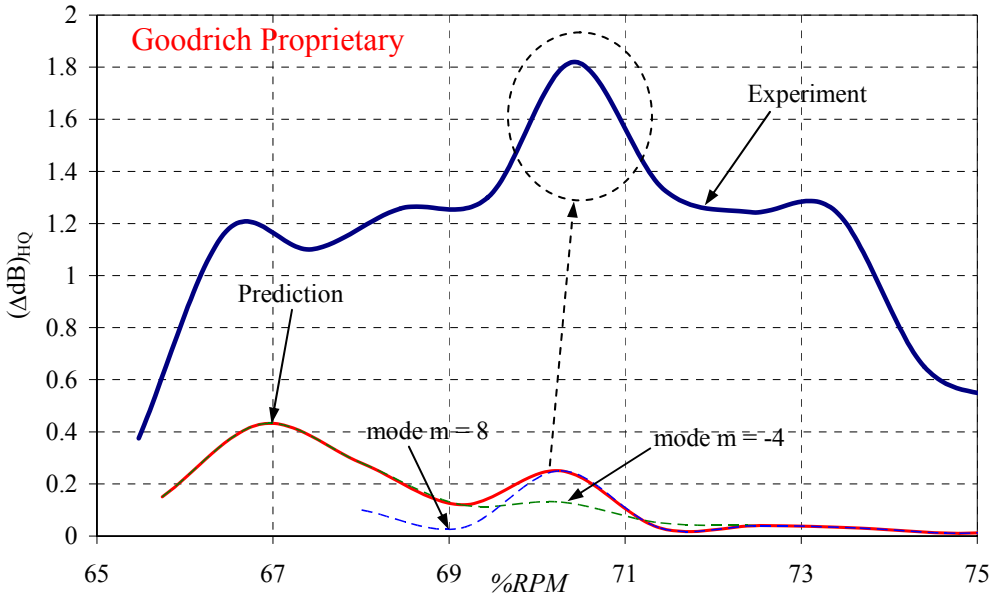

Figure 4.36: Predicted HQ sound power reduction for BPF tone (subsonic condition).

Chapter 5 Conclusions and Recommendations

This dissertation describes the modeling approach of the HQ waveguides used in conjunction with locally reacting liners for cylindrical ducts with flow. The development of this model required the analytical formulation of the Green's function for a infinitly long, soft walled circular duct in the presence of uniform flow. The model has been applied to the sound attenuation of turbofan inlet noise. An initial study to validate the model was undertaken by comparing the predicted results with experimental data, including insight into the procedure for the HQ tube design. The main conclusions of this effort are presented in this Chapter together with the recommendations and future work suggestions.

5.1 Conclusions

The most important conclusions of the work presented in this thesis are explained in this section. In order to have a clear statement for each developed task, the conclusions are itemized as follows:

i. The theoretical formulation of the HQ-Liner system has been completed. The predictions have been compared to experimental data obtained from a realistic test rig and good correlations were found.

ii. The analytical solution of the sound generation and propagation in a lined duct with flow was found in order to have the mathematical foundation for the HQ-Liner

model. This solution required to find the Green's functions that represent the sound radiation in a lined duct with flow, which is a new contribution of this dissertation. In addition, this solution was extended to the case of piston radiation using the divergence theorem in a general form for non-self adjoint operators.

iii. A experimental techinque was developed in order to replace the one dimensional model of sound propagation inside the HQ tube. The experimental setup was built and the dynamics of the HQ tubes were obtained. The results show fairly the same trends as the simple model.

iv. A preliminary design methodology for the HQ-Liner has been presented and can potentitally be used to obtain a system that can be further optimized.

v. The design approach was constructed for a SDOF liner, which is commonly used in the inlet of turbofan engines. Nevertheless, the trend of noise control of new generation ultra high by-pass engines is the use of DDOF liners. Thus, the design technique has to be reviewd for this case in order to obtain an optimum DDOF Liner – HQ system.

vi. Though not the main goal of the code development, the **Liner** prediction part of the model is shown to perform very well. For the broadband noise component at subsonic condition, the model predicts the attenuation within ~1dB.

vii. The model generally underpredicts the experimentally observed performance of the HQ system. This performance was analyzed in terms of the attenuation improvement produced by the HQ tubes when implemented in conjuction with the liner, i.e. $(\Delta dB)_{HQ} = (\Delta dB)_{HQ-Liner} - (\Delta dB)_{Liner}$. The specific results can be summarized as follows:

   - For the broadband noise component at subsonic condition (e.g. approach), the model predicts very accurately the HQ attenuation at low frequencies, e.g. approaximately below the BPF tone. At frequencies around and above the BPF tone, the code underpredicts the attenuation.

- Altough the preformance of the HQ tubes at the higher frequencies is under predicted, the effect of the 3rd resonance of the HQ tubes, i.e. the target resonance, was captured very well.

v. Several assumptions were taken to compute the fan disturbance modal amplitudes (required by the code) for the investigated broadband noise component. It was observed that the predicted performance of both the liner and HQ system was sensitive to the modal content of the disturbance. In order to improve the predictions it is needed to refine these models.

5.2 Recommendations

The following is a list of recommendations for further development of the HQ technology integrated with conventional liners.

i. To refine model of the fan disturbance: The HQ-Liner prediction code requires to know the fan disturbance modal amplitudes in both magnitude and phase. The predictions presented in this report were performed by using a modified "equal energy" approach to define the broadband disturbance. Thus, it is important to refine the definition of the fan disturbance for the broadband component in order to improve the predictions in this work.

ii. To validate the model for mode attenuation: The model of the HQ-Liner has to be experimentally validated for the case where the disturbance mode is basically well attenuated, i.e. cut-off. This situation occurs at cutback condition where the liner delays the propagation of the rotor-rotor mode. Although modal data was available for a validation of this kind, the process could not be completed due to some difficulties found in the data. Consequently, it was not possible to find any correlation between the predictions and experiments or to draw any conclusion.

iii. To use the experimental HQ-dynamics to run predictions: The predictions presented in this thesis were obtained using the theoretical dynamics of the HQ tubes. As

another attempt to improve the predictions, it is suggested to replace the model by the measured HQ dynamics and repeat the simulations.

iv. To extend the design procedure to HQ-Liner systems for high bypass turbofans: The design technique has to be readjusted in order to design systems for new engines with DDOF Liners.

v. To extend the frequency range capability of the model: One of the key assumptions in the model is that the sound field inside the HQ-waveguide is described in terms of plane waves. This in turn implies that the effect of the tube on the duct can be described as piston sources with uniform velocity. At high frequencies where the wavelength is of similar magnitude as the size of the HQ cross section, this plane wave/piston source assumtion is not valid and it should be relaxed.

5.3 Future Work

This section summarizes the different research topics that can arise from the work in this dissertation. Based on these work conclusions and the suggested recommendations given in the previous section, the following future tasks are proposed:

i. To perform simple experiments to validate the modal attenuation: In order to be able to have clear information about the propagation of a single mode in the lined duct, it is proposed to run simple experiments with a few modes present. The resutls from these experiments can be used to validate the HQ-Liner model for modes that are essentially cut-off or attenuate rapidly.

ii. To extend model and design procedure of HQ-Liner systems for Aft-Fan radiation: In order to also address the problem of aft-fan radiation, the model has to be modified for annular geometry. Also, it is necessary to analytically and experimentally investigate the combination of Liners and HQ tubes in this sector of the engine in order to obtain an improved noise abatement device.

iii. Study the HQ-Liner concept as an adaptive device: Adapting the tube parameters with a control system could potentially target the performance of the HQ tubes to different engine conditions. For instance, the adaptation of the tube parameters can be virtually achieved by changing the plane wave propagation inside the tube.

iv. Investigate the HQ-Fan interaction: the model presented in this thesis does not account for the reflection of energy on the fan. It will be challenging to investigate the effect of the sound radiation from the inlet of a turbofan by considering the whole HQ-Fan system as the sound source.

v. Implement the HQ-Liner system on a real high bypass turbofan engine: It is finally proposed to test the performance of the HQ-Liner system on a real commercial turbofan engine at real flight conditions. This experiment would give an insight in the potential of the HQ-Liner technology for improving the noise reduction in airport areas.

Bibliography

[1] – Tyler, J.M. and Sofrin, T.G., "Axial Flow Compressor Noise Studies", *SAE Transactions*, 1961, Vol. 70. pp. 123-149.

[2] – Kantola, R.A., and Gliebe, P.R., "Effects of Vane/Blade Ratio and Spacing on Fan Noise", AIAA Paper no. 81-2033, Oct. (1981).

[3] – Dittmar, J. H. and Woodward, R. P., "An Evaluation of some Alternative Approaches for Reducing Fan Tone Noise", NASA Technical Memorandum 105356, February (1992).

[4] – Mangiarotty, R. A., "The Reduction of Aircraft Engine Fan-Compressor Noise Using Acoustic Linings", *Journal of Sound and Vibration*, 18 (4), 565-576, (1971).

[5] – Walker, B. E., and Hersh, A. S., "Application of active Helmholz resonator technology to plane wave duct acoustics", CEAS/AIAA-95-163, presented at the 1st Joint CEAS/AIAA Aeroacoustics Conference, Munich, Germany, vol. 2, June 1995, pp. 1115-1120.

[6] – Smith, J. P. and Burdisso, R. A., "Active Control of Inlet Noise From a Turbofan Engine Using Inlet Wavenumber Sensors", CEAS/AIAA-99-1808, presented at the 5th CEAS/AIAA Aeroacoustics Conference, Seattle, WA, May 1999.

[7] – Burdisso, R.A., Fuller, C.R., Smith, J.P., "Experiments on the Active Control of a Turbofan Inlet Noise using Compact, Lightweight Inlet Control and Error Transducers", CEAS/AIAA-95-028, 1995, pp. 177-185.

[8] – Smith, J.P., Burdisso, R.A., and Fuller, C.R., "Experiments on the Active Control of Inlet Noise From Turbofan Jet Engine Using Multiple Circumferential Control Arrays", AIAA 96-1792, 1996.

[9] – Joseph, P., Nelson, P.A., and Fisher, M.J., "Active Control of Turbofan Radiation Using an In-Duct Error Sensor Array", *Proceedings of Active 97,* pp. 273-286, August 21-23, Budapest, Hungary 1997.

[10] – Kraft, R. E., Janardan, B. A., Kontos, G. C., and Gliebe, P. R., "Active Control of Fan Noise – Feasibility Study. Volume 1: Flyover System Noise Studies", NASA CR 195392, October, 1994.

[11] – Kraft, R. E., Janardan, B. A., Gliebe, P. R., and Kontos, G. C., "Active Control of Fan Noise – Feasibility Study. Volume 4: Flyover System Noise Studies, Part 2", NASA CR 198512, September 1996.

[12] – Herschel, J. F. W. ,"On the absorption of light by coloured media, viewed in connexion with the undulatory theory", *Philosophical Magazine and Journal of Science*, **3**, 401-412, (1833).

[13] – Quincke, G., "Ueber interferenzapparate fur schallwellen", *Annalen der Physik und Chemie*, **128**, 177-192, (1866).

[14] – Stewart, G. W., "The theory of the Herschel-Quincke tube," *Physical Review*, **31**, 696-698, (1928)

[15] – Selamet, A., Dickey, N. S., and Novak, J. M., "The Hershcel-Quincke tube: a theoretical, computational, and experimental investigation," *J. Acoust. Soc. Am.*, **96** (5), 3177-3185, (1994).

[16] – Brady, L.A., "Application of the Herschel-Quincke Tube Concept to Higher-Order Acoustic Modes in Two-Dimensional Ducts", M.S. Thesis, Virginia Tech, March 2002.

[17] – Hallez, R.F. "Investigation of the Herschel-Quincke Tube Concept as a Noise Control Device for Turbofan Engines", M.S. Thesis, Virginia Tech, January 2001.

[18] – Smith, J.P. and Burdisso, R.A., "The Application of the Herschel-Quincke Tube Concept for the Reduction of Tonal and Broadband Noise From Turbofan Engines", VPI report VPI-ENGR.98.167, prepared for NASA under grant # NAG-1-1980 and proposal # 98-0448-10, 1998.

[19] – Smith, J.P., Burdisso, R.A., "Experimental Investigation of the Herschel-Quinke Tube Concept on the Honeywell TFE731-60", Part III, VPI report VPI-ENGR 4-26483 prepared for NASA under grant NAG-1-2137 and proposal # 99-064-909, VAL Lab, Virginia Tech, July 2001.

[20] – Syed, A.A. and Bennett, S.C., "Comparison of Measured Broadband Noise Attenuation Spectra from Circular Flow Ducts and from Lined Engine Intakes with Predictions", *Journal of Sound and Vibration*, 56(4), 531-567, (1978).

[21] – Morse, P.M., Vibration and Sound, McGraw-Hill Book Company, 1948.

[22] – Morse, P.M. and Ingard, K.U., Theoretical Acoustics, McGraw-Hill Book Company, 1968.

[23] – Pridmore-Brown, D.C., "Sound Propagation in Fluid Flowing through an Attenuating Duct", *Journal of Fluid Mechanics*, **4**, 393-406, (1958).

[24] – Kurze, U., "Schallausbreitung im Kanal mit periodischer Wandstruktur unter Berücksichtigung seitlicher Kopplingen in den Feldern hinter der Wand", Doktor-Ingenieur Dissertation, Berlin, 1968.

[25] – Vaidya, P.G., "Some Developments in the Theory of Sound Attenuation", presented at the Symposium of the Acoustics of Flow Ducts, Southampton University, 10-14 January 1972.

[26] – Scott, R.A., "The Propagation of Sound between Walls of Porous Material", *Proceedings of the Physical Society* LVIII, 358-368, 1946.

[27] – Eisenberg, A. and Kao, T.W., "Propagation of Sound Through a Variable-Area Duct with a Steady Compressible Flow", *J. Acoust. Soc. Am.*, **49**, 169-175, (1971).

[28] – Rienstra, S.W., "Sound Transmission in a Slowly Varying Lined Flow Duct", Nieuw Archief voor Wiskunde, 4de serie, deel 6, no. 1-2 maart-juli 1988.

[29] – Ko , S.H., "Sound Attenuation in a Lined Rectangular Duct with Flow and Its Application to the Reduction of Aircraft Engine Noise", *The Journal of the Acoustical Society of America*, **50** (6), 1418-1432, August 1971.

[30] – Tester, B.J., "The Propagation and Attenuation of Sound in Lined Ducts Containing Uniform or 'Plug' Flow", *Journal of Sound and Vibration*, **28**, 151-203, (1973).

[31] – Ko, S.H., "Sound Attenuation in Acoustically Lined Circular Ducts in the Presence of Uniform Flow and Shear Flow", *Journal of Sound and Vibration*, **22**, 193-210, (1972).

[32] – Eversman W., "Theoretical Models for Duct Acoustic Propagation and Radiation", Aeroacoustics of Flight Vehicles: Theory and Practice, Vol. 2, NASA Reference Publication 1258, TR 90-3052, 1991.

[33] – Lord Rayleigh, The Theory of Sound, Volume 2, Dover Publications, 1945 (re-issue)

[34] – Miles, J.W., "On the Disturbed Motion of a Plane Vortex Sheet", *Journal of Fluid Mechanics*, **4**, 538-552, (1958).

[35] – Friedland, A.B. and Pierce, A.D, "Reflection of Acoustic Pulses from Stable and Unstable Interfaces between Moving Fluids", *Physics of Fluids*, **12**, 1148-1159, (1969).

[36] – Tam, K.W., "Directional Acoustic Radiation from a Supersonic Jet Generated by Shear Layer Instability", *Journal of Fluid Mechanics*, **46**, 757-768, (1971).

[37] – Rienstra, S.W., "Hydrodynamic Instabilities and Surface Waves in a Flow over an Impedance Wall", *Proceedings IUTAM Symposium 'Aero- and Hydro- Acoustics' 1985 Lyon*, 483-490, Springer-Verlag, Heidelberg.

[38] – Zorumski, W.E., "Acoustic Theory of Axisymmetric Multisectioned Ducts", NASA TR R-419, May 1974.

[39] – Sawdy, D.T., Beckemeyer, R.J., and Patterson, J.D., "Analytical and Experimental Studies of an Optimum Multisegment Phased Liner Noise Suppression Concept", NASA CR-134960, May 1976.

[40] – Kraft, R.E., "Theory and Measurement of Acoustic Wave Propagation in Multi-Segmented Rectangular Flow-Ducts", Ph.D. Thesis, University of Cincinnati, 1976.

[41] – Koch, W. and Möhring, W., "Eigensolutions for Liners in Uniform Mean Flow Ducts", *AIAA Journal*, **21**(2), 200-212, 1983.

[42] – Tester, B.J., "Some Aspects of 'Sound' Attenuation in Lined Ducts Containing Inviscid Mean Flows With Boundary Layers", *Journal of Sound and Vibration*, **28**(2), 217-245, (1973).

[43] – Eversman, W., "Effect of Boundary Layer on the Transmission and Attenuation of Sound in an Acoustically Treated Circular Duct", *Journal of Fluid Mechanics*, **49**, 1372-1380, (1971).

[44] – Gogate, G.R. and Munjal, M.L., "Analytical Solution of Sound Propagation in Lined Circular Ducts with Laminar Mean Flow", *Journal of Sound and Vibration*, **160**(3), 465-484, (1993).

[45] – Mungur, P. and Plumblee, H.E., "Propagation and Attenuation of Sound in a Soft Walled Annular Duct Containing a Sheared Flow", NASA SP-207, 305-327, 1969.

[46] – Eversman, W., "Representation of 1/N Power Law Boundary Layer in the Sheared Flow Acoustic Transmission Problem", *Journal of Sound and Vibration*, **24**, 459-469, (1972).

[47] – Ko, S.H., "Theoretical Predictions of Sound Attenuation in Acoustically Lined Annular Ducts in the Presence of Uniform Flow and Shear Flow", *J. Acoust. Soc. Am.*, **54**(6), 1592-1606, (1973).

[48] – Mikhail, M.N. and Abdelhamid, A.N., "Transmission and Far Field Radiation of Sound Waves in and from Lined Ducts Containing Shear Flow", AIAA paper No. 73-1013, (1973).

[49] – Drischler, J.A., "Analytic studies of sound pressures inside the duct of ducted propellers", NASA-TN-D-6345, 1971.

[50] – Goldstein, M.E., Aeroacoustics, McGraw Hill Inc., 1976

[51] – Myers, M.K., "On the Acoustic Boundary Condition in the Presence of Flow", *Journal of Sound and Vibration*, **71**(3), 429-434, (1980).

[52] – Stakgold, I., Green's Functions and Boundary Value Problems, Second Edition, John Wiley & Sons Inc., 1998.

[53] – Duffy, D.G., Green's Functions with Applications, Chapman & Hall/CRC, 2001.

[54] – Lamb, G.L., Introductory Applications of Partial Differential Equations, John Wiley & Sons Inc., 1995.

[55] – Griffel, D.H., Applied Functional Analysis, Dover Publications Inc., 1985.

[56] – Hallez, R.F., Smith, J.P. and Burdisso, R.A., "Control of Higher-Order Modes in Ducts using Arrays of Herschel-Quincke Waveguides", presented in the meeting Control of Vibration and Noise – New Millennium, ASME, Nov 5-10, 2000, Orlando, USA.

[57] – ASTM E 1050 – 98 , Standard Test Method for Impedance and Absorption of Acoustical Materials Using a Tube, Two Microphones and a Digital Frequency Analysis System.

[58] – FAR Part 36, Noise Standards: Aircraft Type and Airworthiness Certification, The Federal Aviation Adminstration, 2004.

[59] – Tester, B.J., Baker, N.J., Kempton, A.J. and Wright, M.C., "Validation of an Analytical Model for Scattering by Intake Liner Splices", AIAA-2004-2906, presented at the 10th AIAA/CEAS Aeroacoustics Conference, Manchester, UK, May 2004.

[60] – Alonso, J.S., Molisani, L.R., and Burdisso, R.A., "Spectral and Wavenumber Approaches to Obtain Green's Functions for Convected Wave Equation", AIAA-2004-2943, presented at the 10th AIAA/CEAS Aeroacoustics Conference, Manchester, UK, May 2004.

[61] – Rademaker, E.R., Sijtsma, P., and Tester B.J., "Mode Detection with an Optimized Array in a Model Turbofan Engine Intake at Varying Shaft Speeds", AIAA-2001-2181, presented at the 7th AIAA/CEAS Aeroacoustics Conference, Maastricht, Netherlands, May 2001.

Appendix A. Mathematical Definitions and Functions

This Appendix presents a few mathematical definitions and functions used in this dissertation.

A.1 Definition of Fourier Transform pair

The Fourier (Wavenumber) Transform used in this work is defined as follows

Fourier Transform:
$$F\left(r,\theta,\hat{k}_z,k_o\right)=\int_{-\infty}^{\infty} f\left(r,\theta,z,k_o\right)e^{i\hat{k}_z z}d\hat{k}_z \tag{A.1}$$

Inverse Fourier Transform:
$$f\left(r,\theta,z,k_o\right)=\frac{1}{2\pi}\int_{-\infty}^{\infty} F\left(r,\theta,\hat{k}_z,k_o\right)e^{-i\hat{k}_z z}d\hat{k}_z \tag{A.2}$$

A.2 Normalization Functions for Green's functions in the WT domain

The procedure to find the Green's functions in the wavenumber domain involves solving the following integral as

$$\int_0^{2\pi}\int_0^{a}\cos(m\theta)\cdot\cos(e\theta)\cdot J_m\left(K_{mn}\left(k_o,\hat{k}_z\right)r\right)\cdot J_e\left(K_{es}\left(k_o,\hat{k}_z\right)r\right)rdrd\theta=\delta_{em}\delta_{sn}\ \ \Lambda_{mn}\left(k_o,\hat{k}_z\right) \tag{A.3}$$

where δ_{ij} is the Kronecker delta.

The solution is found using the orthogonality conditions of the eigenfunctions defining the acoustic modes shapes in the wavenumber domain. The normalization factor $\Lambda_{mn}\left(k_o,\hat{k}_z\right)$ is found as

$$\Lambda_{mn}=\begin{cases}\pi a^2\left[J_o^2\left(K_{on}\left(k_o,\hat{k}_z\right)a\right)+J_1^2\left(K_{on}\left(k_o,\hat{k}_z\right)a\right)\right] & \text{for } m=0\\ \dfrac{\pi a^2}{2}\left[J_m^2\left(K_{mn}\left(k_o,\hat{k}_z\right)a\right)-J_{m-1}\left(K_{mn}\left(k_o,\hat{k}_z\right)a\right)J_{m+1}\left(K_{mn}\left(k_o,\hat{k}_z\right)a\right)\right] & \text{for } m\neq 0\end{cases} \tag{A.4}$$

A.3 Definition of Inner Product in the Hilbert space

The inner product $\langle .,. \rangle$ for the Hilbert space used in this work is defined as follows

$$\langle f, g \rangle = \int_{-\infty}^{\infty} \int_{0}^{a} \int_{0}^{2\pi} f(r,\theta,z) \cdot \overline{g(r,\theta,z)}\, d\theta\, r\, dr\, dz \tag{A.5}$$

where the bar $\overline{(.)}$ denotes complex conjugate.

A.4 Zeros of the first derivative Bessel function $J_m(.)$

This section presents a list of the zeros of the first derivative Bessel function $J_m(.)$. These zeros are defined as the arguments of the Bessel function for

$$J'_m(ak_{mn}) = 0 \tag{A.6}$$

where ak_{mn} are the normalized eigenvalues of the hard wall inlet duct and a is the duct radius. The following table is a list of the normalized eigenvalues (zeros of (A.6)) for different mode orders.

Table A.1: Zeros of the first derivative Bessel function of the 1st kind

m \ n	0	1	2	3	4	5	6	7	8	9	10
0	0.00	3.83	7.02	10.17	13.32	16.47	19.62	22.76	25.90	29.05	32.19
1	1.84	5.33	8.54	11.71	14.86	18.02	21.16	24.31	27.46	30.60	33.75
2	3.05	6.71	9.97	13.17	16.35	19.51	22.67	25.83	28.98	32.13	35.28
3	4.20	8.02	11.35	14.59	17.79	20.97	24.14	27.31	30.47	33.63	36.78
4	5.32	9.28	12.68	15.96	19.20	22.40	25.59	28.77	31.94	35.10	38.27
5	6.42	10.52	13.99	17.31	20.58	23.80	27.01	30.20	33.39	36.56	39.73
6	7.50	11.73	15.27	18.64	21.93	25.18	28.41	31.62	34.81	38.00	41.18
7	8.58	12.93	16.53	19.94	23.27	26.55	29.79	33.02	36.22	39.42	42.61
8	9.65	14.12	17.77	21.23	24.59	27.89	31.16	34.40	37.62	40.83	44.03
9	10.71	15.29	19.00	22.50	25.89	29.22	32.51	35.76	39.00	42.22	45.44
10	11.77	16.45	20.22	23.76	27.18	30.53	33.84	37.12	40.37	43.61	46.83
11	12.83	17.60	21.43	25.01	28.46	31.84	35.17	38.46	41.73	44.98	48.21
12	13.88	18.75	22.63	26.25	29.73	33.13	36.48	39.79	43.08	46.34	49.58
13	14.93	19.88	23.82	27.47	30.99	34.41	37.78	41.11	44.41	47.69	50.95
14	15.98	21.02	25.00	28.69	32.24	35.69	39.08	42.43	45.74	49.03	52.30
15	17.02	22.14	26.18	29.91	33.48	36.95	40.37	43.73	47.06	50.36	53.64
16	18.06	23.26	27.35	31.11	34.71	38.21	41.64	45.03	48.37	51.69	54.98
17	19.10	24.38	28.51	32.31	35.94	39.46	42.91	46.31	49.67	53.00	56.31
18	20.14	25.50	29.67	33.50	37.16	40.71	44.18	47.60	50.97	54.32	57.63
19	21.18	26.61	30.82	34.69	38.38	41.94	45.44	48.87	52.26	55.62	58.95
20	22.22	27.71	31.97	35.87	39.58	43.18	46.69	50.14	53.55	56.92	60.26
21	23.25	28.82	33.12	37.05	40.79	44.40	47.93	51.40	54.82	58.21	61.56
22	24.29	29.92	34.26	38.22	41.99	45.62	49.17	52.66	56.10	59.49	62.86
23	25.32	31.01	35.40	39.39	43.18	46.84	50.41	53.91	57.36	60.77	64.15
24	26.36	32.11	36.53	40.56	44.37	48.05	51.64	55.16	58.62	62.05	65.44
25	27.39	33.20	37.66	41.72	45.56	49.26	52.87	56.40	59.88	63.32	66.72
26	28.42	34.29	38.79	42.88	46.74	50.46	54.09	57.64	61.13	64.59	68.00

Appendix B. Comparison of 2D and 3D models

This appendix presents a comparison of the predicted performance of the HQ tubes by the two- and three-dimensional models developed in Chapter 3. The objective of this comparison is to verify that both models generate the same results for simple systems, i.e. single array of tubes, non-staggered arrays, etc. Also, the comparison will be valid only for systems in which the number of tubes per array is significantly large, i.e. bigger than *2m* (*m* is the highest cut-on circumferential mode order), to avoid the presence of scattering effects. The case presented in this section simulates the performance of a single array of *73* tubes mounted on a liner of length *643* mm. The assumed flow Mach number is *M=-0.27* (in the opposite direction of positive propagation) and the corresponding liner impedance for this condition is the same as presented in Figure 4.6. The tube parameters are defined in Table B.1.

Table B.1: HQ parameters for 2/3D simulation.

Tube Length [m]	Cross sectional Area [m^2]	Interface distance I/O [m]	Axial Location [m]
0.636	0.0103	0.447	0.32

Both broadband and single mode attenuation were selected for the comparisons. The single mode case considered was for the (22,0) mode. The results of these predictions are shown in Figures B.1 and B.2 for the broadband and single mode cases, respectively. As shown in these figures, the predicted attenuation is almost identical for both cases using the two- and three-dimensional models. The slight deviation shown in Figure B.1 is attributed to the different summation process of the models to account for the effect of all the tubes in the array.

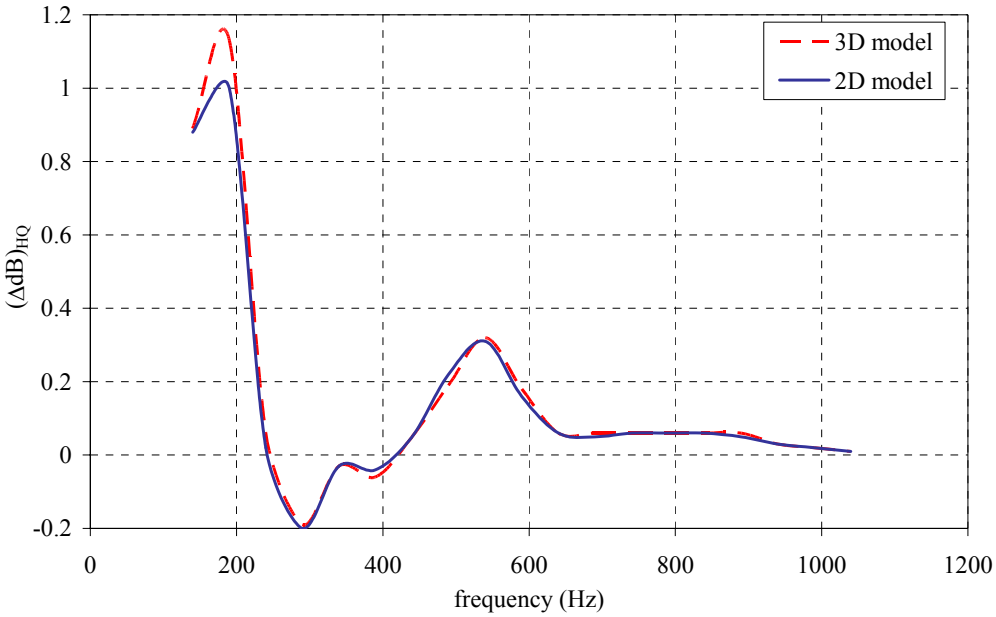

Figure B.1: Comparison of broadband attenuation predictions for 2D and 3D models.

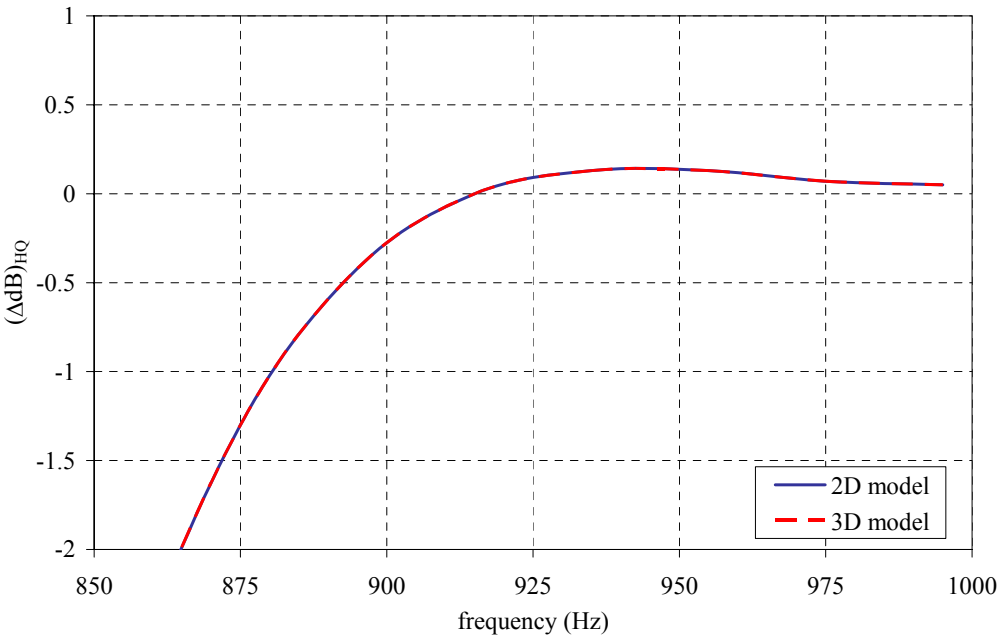

Figure B.2: Comparison of mode (22,0) predictions for 2D and 3D models.

Appendix C. Code Development

A computer code was developed as an analysis tool for the design of the HQ-Liner system and based on the theory of Chapters 2 and 3. A similar code was previously written for the case of a HQ-system installed on a hard wall duct [17, 56]. The new code for the lined wall case follows the same structure but it takes a significant more amount of computational time to run. To improve this issue, a second code for the two-dimensional model was written and the results were presented in Appendix B. Although the computational time was improved, this code can only be applied to simple configurations, e.g. single arrays, non-staggered arrays, etc. Also, the number of tubes in each array has to be significantly large, i.e. larger than $2m$ (m is the largest cut-on circumferential order), to avoid the scattering effects. The full-formulation code was used for the predictions of the RR Rig 649 tests presented in Chapter 4.

Code Flow Chart

The flow chart in Figure C.1 shows the structure of the Liner-HQ code. It can be clearly seen the main difference with the hard wall case [17] are

- the eigenvalue problem needs a subroutine that solves the characteristic equation numerically,
- all the modal properties are divided into positive and negative traveling direction,
- as the modes are not orthogonal, the modal amplitudes of the sources need to be computed solving a large system of equations numerically for each m order.

These factors cause the runtime to increase exponentially with the number of modes.

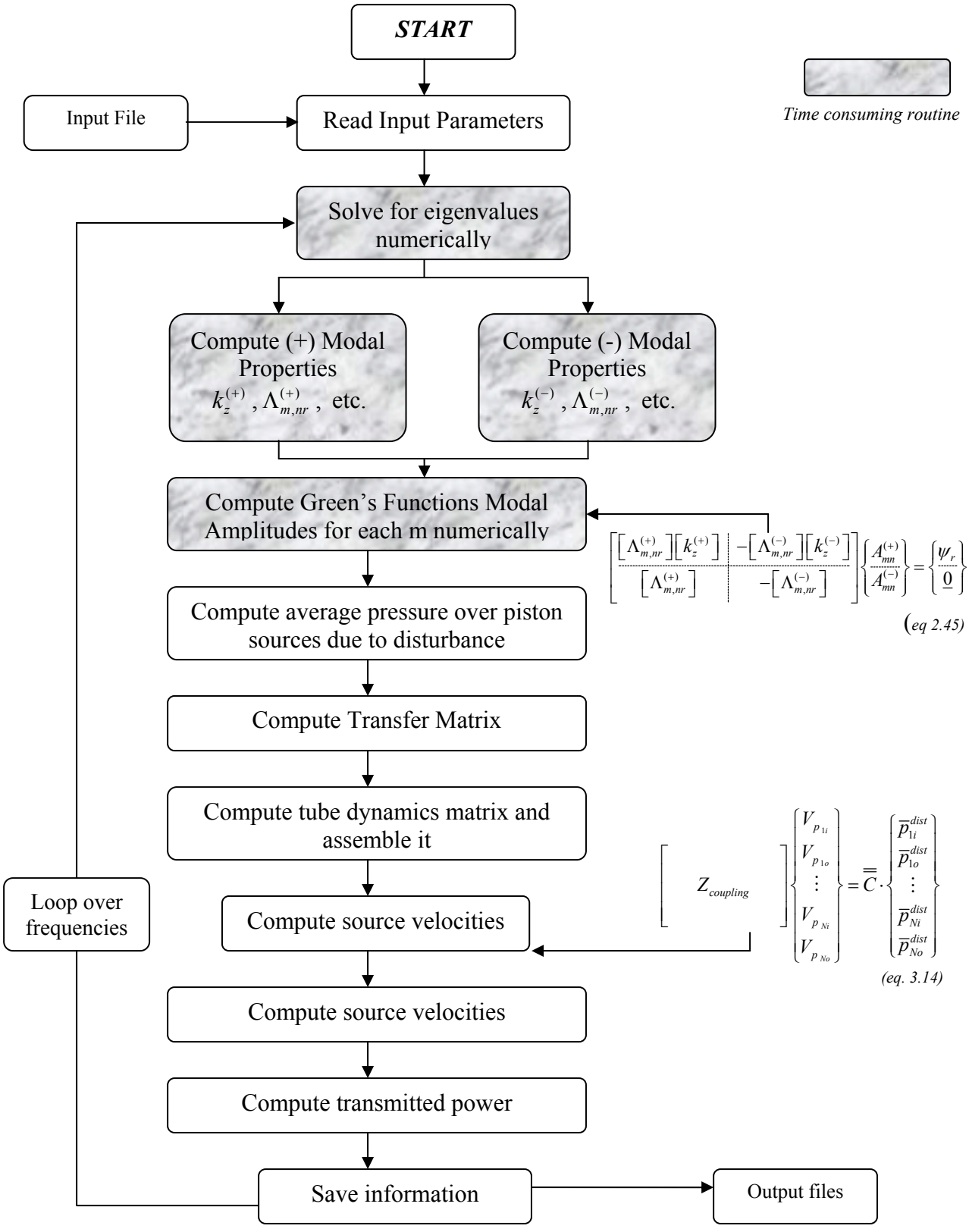

Figure C.1: Code Structure.

Input File

The code is able to solve the acoustic problem for very specific conditions and configurations. Different cases can easily be simulated just by changing parameters in the input file. The following is a description of the data needed to run the code.

Fluid properties and dimensions

- Duct radius.
- Flow speed, fluid density and speed of sound.
- Number of HQ tubes, arrays and dimensions of the tubes.
    - Length
    - I/O distance
    - Cross sectional area
    - Axial location
    - Circumferential rotation of the array
- Axial position to compute the transmitted power.

Wall properties

- Wall normalized admittance.
- Impedance of the screen located at the tubes' openings.

Modal expansion parameters

- Number of modes to include in the Green's Functions expansions
- Number of modes to include in the disturbance
- Number of modes to save propagation properties
- Modal amplitudes for tone noise predictions

Additional data

- Convergence parameters for eigenvalue problem
- Print controllers

Output files

The code prints the information in two output files. One of them, the principal output file, contains all the relevant information that the code uses and computes. Setting the print controllers, this information can be brief or detailed, depending on the level of desired knowledge of the insight of the calculations. The second output file contains fast access information about the acoustic power throughout the duct. This is the most important file in terms of HQ performance.

Appendix D. The Wavenumber Transform Approach

This appendix presents the derivation of the Wavenumber Transform (WT) formulation to find the Green's functions of the wave equation in a lined duct with flow. This theory was previously investigated by Drischler [49] for the hard wall case and then extended to the lined wall case by Zorumski [38]. The WT derivation presented in this appendix is used to verify the validity of the Green's functions developed in this thesis, i.e. modal or spectral expansion approach. Certainly, there is a concern related to the completeness of the eigenfunctions (used to find the Green's functions) that has to be investigated. Since the homogeneous solutions (eigenfunctions) are not guaranteed to be complete, the modal expansion method may not provide all the necessary information to reproduce the sound field originated by a point source. On the other hand, the WT method guarantees the functional completeness of the homogenous solution in the wavenumber domain. Nevertheless, in the process of recovering the spatial axial coordinate by the commonly used Theory of Residues to solve the inverse WT, the solution requires the same eigenproperties as in the modal expansion approach. In addition, solving the inverse WT by the method of residues requires the use of branch cuts that makes the process more involved. To avoid these problems, a straight-forward numerical integration scheme will be used to find the WT solution in the spatial domain.

The first part of this appendix presents the formulation to solve the transformed eigenvalue problem. The second part describes the solution of the Green's functions using the wavenumber transform approach. The comparison of the Green's function using the WT and the spectral (or modal) approaches is presented at the end of the appendix.

D.1 Eigenvalue Problem in the Wavenumber Domain

To obtain the Green's function using the wavenumber transform (WT), the eigenvalue problem in the wavenumber domain needs to be defined first. The solution to this problem is obtained by taking the WT, as defined in Appendix A, in the z-direction

of both the homogeneous equation of motion in eq. (2.1) and boundary condition in eq. (2.19). This yields the following transformed equation of motion

$$\frac{\partial^2 P}{\partial r^2}+\frac{1}{r}\frac{\partial P}{\partial r}+\frac{1}{r^2}\frac{\partial^2 P}{\partial \theta^2}-\hat{k}_z^2(1-M^2)P-2Mk_o\hat{k}_z\,P+k_o^2P=0 \qquad -\infty<\hat{k}_z<\infty \quad \text{(D.1)}$$

where $P=P\left(r,\theta,\hat{k}_z,k_o\right)$ is the WT of $p=p\left(r,\theta,z,k_o\right)$. A parameter $K\left(k_o,\hat{k}_z\right)$ is defined from the previous equation as

$$K^2\left(k_o,\hat{k}_z\right)=\left(k_o^2-\hat{k}_z^2(1-M^2)-2Mk_o\hat{k}_z\;\right) \quad \text{(D.2)}$$

In addition, the WT of the Euler's equation and the boundary condition leads to

$$\left.\frac{\partial P}{\partial r}\right|_{r=a}=-i\beta_w\frac{\left(k_o-\hat{k}_zM\right)^2}{k_o}P\Bigg|_{r=a} \qquad -\infty<\hat{k}_z<\infty \quad \text{(D.3)}$$

Note that $\hat{k}_z$ is now simply a real constant independent of frequency and flow speed *M*. The positive and negative values represent positive and negative propagating waves, respectively.

Using separation of variables, the solution to the transformed system is then given as

$$P\left(r,\theta,\hat{k}_z,k_o\right)=A(k_o,\hat{k}_z)\Phi\left(r,\theta\right) \quad \text{(D.4)}$$

where $A(k_o,\hat{k}_z)$ is the unknown amplitude at the frequency defined by the wavenumber $k_o=\omega/c$, and $\Phi\left(r,\theta\right)$ is

$$\Phi\left(r,\theta\right)=\cos\left(m\theta\right)\,J_m\left(K_{mn}(k_o,\hat{k}_z)\,r\right) \quad \text{(D.5)}$$

Thus, the general solution will be a linear combination of the modes in the transformed space as follows

$$P\left(r,\theta,\hat{k}_z,k_o\right)=\sum_{m=0}^{\infty}\sum_{n=0}^{\infty}A_{mn}(k_o,\hat{k}_z)\,\cos\left(m\theta\right)\,J_m\left(K_{mn}(k_o,\hat{k}_z)\,r\right) \quad \text{(D.6)}$$

Since these equations must satisfy the boundary condition, the solution is replaced in eq. (D.3) which results in the characteristic equation

$$K_{mn}(k_o,\hat{k}_z)\,J_m'\left(K_{mn}(k_o,\hat{k}_z)a\right)+i\beta_w\frac{\left(k_o-\hat{k}_zM\right)^2}{k_o}J_m\left(K_{mn}(k_o,\hat{k}_z)a\right)=0 \quad -\infty<\hat{k}_z<\infty \quad \text{(D.7)}$$

where $J_m'(.)=dJ_m(.)/dr$. Equation (D.7) needs to be numerically solved for the roots of the transformed characteristic equation, i.e. values of $K(k_o,\hat{k}_z)$ that satisfy eq. (D.7). The infinite set of roots of eq. (D.7) is denoted as $K_{mn}(k_o,\hat{k}_z)$ for $m=0,\cdots,\infty$ and $n=0,\cdots,\infty$ and referred as the transformed eigenvalues. Note that $K_{mn}(k_o,\hat{k}_z)$ must be found for each pair $(k_o,\hat{k}_z)$, i.e. solution of an eigenvalue problem at each frequency defined by k_o, and for each wavenumber component defined by $\hat{k}_z$. However, given that $\hat{k}_z$ is a constant at each point of calculation, the solution of the eigenproblem is computationally similar to the case of a lined duct without flow.

It is important to mention at this point that the problem defined by eq. (D.1) and the boundary condition in eq. (D.3) satisfy the requirements of the Sturm-Liouville theory. Therefore, the set of functions that describe the sound field in eq. (D.5) with the roots from eq. (D.7) is complete for each pair $(k_o,\hat{k}_z)$. However, the characteristic equation has to be repeatedly solved in the interval $-\infty<\hat{k}_z<\infty$ for every considered point of calculation.

D.2 Green's Functions obtained using the Wavenumber Transform

The Green's functions are obtained as the solution of the non-homogeneous convected wave equation in cylindrical coordinates given in eq. (2.33). The WT in the z-direction of eq. (2.33) is obtained to find the Green's function in conjunction with the boundary condition defined by eq. (D.3). That is

$$\frac{\partial^2 G}{\partial r^2}+\frac{1}{r}\frac{\partial G}{\partial r}+\frac{1}{r^2}\frac{\partial^2 G}{\partial \theta^2}+K^2\left(k_o,\hat{k}_z\right)=\frac{1}{r}\delta\left(r-r_o\right)\delta\left(\theta-\theta_o\right)e^{i\hat{k}_z z_o} \qquad -\infty<\hat{k}_z<\infty \qquad \text{(D.8)}$$

where $G(r,\theta,\hat{k}_z\big|r_o,\theta_o,z_o;k_0)$ is the WT of $g(r,\theta,z\big|r_o,\theta_o,z_o;k_0)$ and $K^2(k_o,\hat{k}_z)$ is defined in eq. (D.2). The solution of eq. (D.8) can be expressed as a linear combination of the homogeneous solution as follows

$$G(r,\theta,\hat{k}_z\,|\,r_o,\theta_o,z_o;k_0)=\sum_{m=0}^{M}\sum_{n=0}^{N}G_{mn}(r,\theta,\hat{k}_z\,|\,r_o,\theta_o,z_o;k_0)$$
$$=\sum_{m=0}^{M}\sum_{n=0}^{N}A_{mn}\left(\hat{k}_z,k_o\right)\cos\left(m\left(\theta-\theta_o\right)\right)J_m\left(K_{mn}\left(\hat{k}_z,k_o\right)r\right) \tag{D.9}$$

However, from the homogeneous solution it can be written that

$$\frac{\partial^2 G_{mn}}{\partial r^2}+\frac{1}{r}\frac{\partial G_{mn}}{\partial r}+\frac{1}{r^2}\frac{\partial^2 G_{mn}}{\partial \theta^2}+K_{mn}^2\left(k_o,\hat{k}_z\right)G_{mn}=0 \tag{D.10}$$

Thus, replacing eq. (D.9) into (D.8) and considering eq. (D.10) gives

$$\sum_{m}^{M}\sum_{n}^{N}\left[-K_{mn}^2\left(k_o,\hat{k}_z\right)+K^2\left(k_o,\hat{k}_z\right)\right]A_{mn}\left(k_o,\hat{k}_z\right)\cos\left(m\left(\theta-\theta_o\right)\right)J_m\left(K_{mn}\left(k_o,\hat{k}_z\right)r\right)=$$
$$=\frac{1}{r}\delta\left(r-r_o\right)\delta\left(\theta-\theta_o\right)e^{i\hat{k}_z z_o} \tag{D.11}$$

To solve for the unknown amplitudes $A_{mn}\left(k_o,\hat{k}_z\right)$, eq. (D.11) is pre-multiplied by $\cos\left(\mathrm{e}\left(\theta-\theta_o\right)\right)J_e\left(K_{er}(k_o,\hat{k}_z)\,r\right)$ and integrated over the cross section. Using the eigenfunctions orthogonality property in the wavenumber domain, the integration yields

$$\left[K^2(k_o,\hat{k}_z)-K_{mn}^2(k_o,\hat{k}_z)\right]A_{mn}(k_o,\hat{k}_z)\,\Lambda_{mn}(k_o,\hat{k}_z)=J_m\left(K_{mn}(k_o,\hat{k}_z)r_o\right)e^{i\hat{k}_z z_o} \tag{D.12}$$

where the mode normalization factor $\Lambda_{mn}\left(k_o,\hat{k}_z\right)$ is defined in Appendix A. Therefore, the modal amplitude is given as

$$A_{mn}(k_o,\hat{k}_z)=\frac{J_m\left(K_{mn}(k_o,\hat{k}_z)r_o\right)e^{i\hat{k}_z z_o}}{\Lambda_{mn}(k_o,\hat{k}_z)\left[K^2(k_o,\hat{k}_z)-K_{mn}^2(k_o,\hat{k}_z)\right]} \tag{D.13}$$

The wavenumber transformed Green's function becomes

$$G(r,\theta,\hat{k}_z\,|\,r_o,\theta_o,z_o;k_0)=\sum_{m=0}^{M}\sum_{n=0}^{N}\frac{J_m\left(K_{mn}(k_o,\hat{k}_z)r_o\right)e^{i\hat{k}_z z_o}}{\Lambda_{mn}(k_o,\hat{k}_z)\left[K^2(k_o,\hat{k}_z)-K_{mn}^2(k_o,\hat{k}_z)\right]}\cos\left(m\left(\theta-\theta_o\right)\right)J_m\left(K_{mn}(k_o,\hat{k}_z)r\right) \tag{D.14}$$

The Green's function is then obtained by taking the inverse WT as

$$g(r,\theta,z|r_o,\theta_o,z_o;k_o)=\frac{1}{2\pi}\int_{-\infty}^{\infty}G(r,\theta,\hat{k}_z\big|r_o,\theta_o,z_o;k_0)e^{-i\hat{k}_z z}d\hat{k}_z$$

$$g(r,\theta,z|r_o,\theta_o,z_o;k_o)=\frac{1}{2\pi}\sum_{m=0}^{M}\sum_{n=0}^{N}\cos\left(m\left(\theta-\theta_o\right)\right)\int_{-\infty}^{\infty}\frac{J_m\left(K_{mn}(k_o,\hat{k}_z)r_o\right)J_m\left(K_{mn}(k_o,\hat{k}_z)r\right)}{\Lambda_{mn}(k_o,\hat{k}_z)\left[K^2(k_o,\hat{k}_z)-K_{mn}^2(k_o,\hat{k}_z)\right]}e^{-i\hat{k}_z(z-z_o)}d\hat{k}_z \tag{D.15}$$

The evaluation of the integral in eq. (D.15) requires the knowledge of K_{mn} as a function of $\hat{k}_z$. To this end, the eigenvalue problem in eq. (D.7) needs to be solved repeatedly in the interval $-\infty<\hat{k}_z<\infty$ for every point of calculation. In addition, the result is valid only for one location inside the duct because the coordinates *r* and *z* must be fixed in order to solve the integral. For this reason, a solution using a closed form formulation would be of great advantage. This closed form expression is commonly obtained by evaluating the integral in eq. (D.15) using the Theory of Residues, as performed in Refs. [38, 49]. Therefore, it is necessary to investigate the zeros of the denominator of the integrand as in Refs. [49, 55]. These poles are defined as the values of k_z that satisfy the following characteristic equation

$$K^2\left(k_o,\hat{k}_z\right)-K_{mn}^2\left(k_o,\hat{k}_z\right)=0 \tag{D.16}$$

In order to satisfy eq. (D.16), the poles k_z have to be investigated in the complex plane as shown in Figure D.1. Therefore, the integration in the interval $-\infty<\hat{k}_z<\infty$ is replaced by defining a contour enclosing the upper or lower part of the k_z-plane, depending on the direction of propagation that is being considered.

As illustrated in Figure D.1, the positive (+) propagating field is obtained by analyzing the poles located in the lower half of the k_z-plane. Similarly, the negative (–) propagating field is obtained by considering the upper half plane. At this point, it should be recalled that K_{mn} is obtained by solving numerically the following characteristic equation (similar to eq. (D.7) for $\hat{k}_z$ complex)

$$K_{mn}\left(k_o,k_z\right)J_m'\left(K_{mn}\left(k_o,k_z\right)a\right)+i\beta_w\frac{\left(k_o-k_zM\right)^2}{k_o}J_m\left(K_{mn}\left(k_o,k_z\right)a\right)=0 \qquad k_z\in\mathbb{C} \tag{D.17}$$

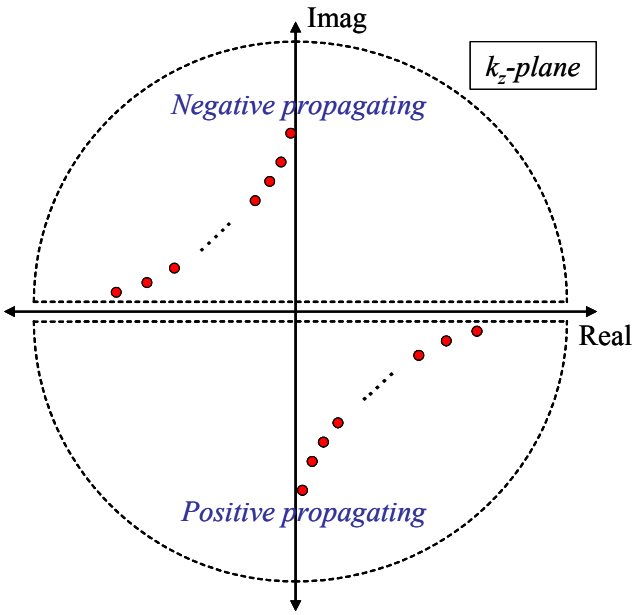

Figure D.1: Location of characteristic equation poles in the complex plane.

Also, as stated in eq. (D.16), the poles k_z are given in terms of K_{mn} by the following condition

$$k_z^2\left(1-M^2\right)+2Mk_ok_z+\left(K_{mn}^2\left(k_o,k_z\right)-k_o^2\right)=0 \tag{D.18}$$

As a result, to solve eqs. (D.17) and (D.18) simultaneously is equivalent to solve eqs. (2.18) and (2.26), which is the original eigenproblem defined for the modal method. Therefore, the obtained Green's function will indeed be expressed in terms of the same eigenfunctions as for the modal expansion approach, which are not guaranteed to be complete. In addition, unlike the hard wall case, the application of this theory to the soft wall duct requires introducing a branch cut for every pole in the $\hat{k}_z$-complex plane in order to avoid the presence of multi-valued functions. The evaluation of the integrals in eq. (D.15) along these branch cuts adds a non-zero component to each modal term obtained by the Residue Theory. Consequently, since it is not possible to find a closed form for these non-zero components, the method becomes impractical to find a safe solution. Instead, a numerical technique will be developed to perform the Fourier inverse integral in eq. (D.15) and presented in the next section.

Hard Wall Case

For the hard wall case, the application of the Theory of Residues leads to a valid closed form solution for the Green's function. The integral in (D.15) can be perfectly evaluated using the poles in the k_z –plane of Figure D.1, leading to express the solution in terms of a complete set of eigenfunctions. Therefore, using these spectral properties, the Green's function for the hard wall case can be expressed as [49]

$$g_{HW}(r,\theta,z|r_o,\theta_o,z_o;k_0)=\begin{cases}\sum_{m=0}^{M}\sum_{n=0}^{N}\dfrac{i\cos\left(m(\theta-\theta_o)\right)J_m\left(k_{mn}r_o\right)J_m\left(k_{mn}r\right)}{2\Lambda_{mn}\sqrt{k_o^2-\left(1-M^2\right)k_{mn}^2}}e^{-ik_z^{(+)}(z-z_o)}, z>z_o\\ \sum_{m=0}^{M}\sum_{n=0}^{N}\dfrac{i\cos\left(m(\theta-\theta_o)\right)J_m\left(k_{mn}r_o\right)J_m\left(k_{mn}r\right)}{2\Lambda_{mn}\sqrt{k_o^2-\left(1-M^2\right)k_{mn}^2}}e^{-ik_z^{(-)}(z-z_o)}, z<z_o\end{cases} \quad \text{(D.19)}$$

Note that eq. (D.19) is given for both directions of propagation in the same fashion as the modal expansion method and it is a function of the "hard wall" propagating modes inside the duct. This formulation will be used to verify the modal expansion method for the limit case of infinite wall impedance, i.e. hard wall.

D.3 Solution of Inverse Fourier Integrals by Numerical Technique

This section presents the development of a simple numerical technique to integrate the inverse of the Fourier Transform. The procedure consists in breaking the improper integral given in eq. (D.15) into a summation over small intervals of width Δk_z as shown in Figure D.2. Therefore the improper integral is solved as

$$\int_{-\infty}^{\infty}\frac{J_m\left(K_{mn}r_o\right)J_m\left(K_{mn}r\right)}{\Lambda_{mn}\left[K^2-K_{mn}^2\right]}e^{-i\hat{k}_z(z-z_o)}d\hat{k}_z\approx\sum_j\frac{J_m\left(K_{mn}^j r_o\right)J_m\left(K_{mn}^j r\right)}{\Lambda_{mn}^j\left[K_j{}^2-\left(K_{mn}^j\right)^2\right]}e^{-i\hat{k}_z^j(z-z_o)}\,\Delta\hat{k}_z=\sum_j\left(F_j\right)_{mn}\Delta\hat{k}_z \quad \text{(D.20)}$$

where the values of *r* and *z* correspond to a fixed point and the integrand *F* is divided into its real and imaginary components, i.e. $\sum F_j\,\Delta\hat{k}_z=\sum\mathrm{Re}[F_j]\Delta\hat{k}_z+i\sum\mathrm{Im}[F_j]\Delta\hat{k}_z$. Note that every point of calculation *j* requires solving the characteristic equation to obtain the corresponding value of K_{mn}^j as follows

$$K_{mn}^{j}\, J_m'\left(K_{mn}^{j}a\right)+i\beta_w \frac{\left(k_o-\hat{k}_z^{j}M\right)^2}{k_o} J_m\left(K_{mn}^{j}a\right)=0 \tag{D.21}$$

As it may be noted, this integration is taken for a single observation point in the duct and it has to be repeated for different locations. Consequently, it is not computationally efficient and again impractical. However, it was developed here to compare the solution to the modal approach developed in this dissertation for a few simple numerical example cases. The fixed values of r and z in eq. (D.20) relative to the source location automatically define the direction of the propagated sound. Thus, it is not necessary to make a distinction between positive and negative propagating eigenfunctions in this numerical case. In addition, the continuity condition at the source plane is naturally obtained by using the numerical integration (see eq. (D.20) for $z \to z_o$).

The Green's functions obtained by this numerical integration will be expressed as

$$g(r,\theta,z\,|r_o,\theta_o,z_o;k_o) \approx \frac{1}{2\pi}\sum_{m=0}^{M}\sum_{n=0}^{N}\cos\left(m\left(\theta-\theta_o\right)\right)\sum_{j}\left(F_j\right)_{mn}\Delta\hat{k}_z \tag{D.22}$$

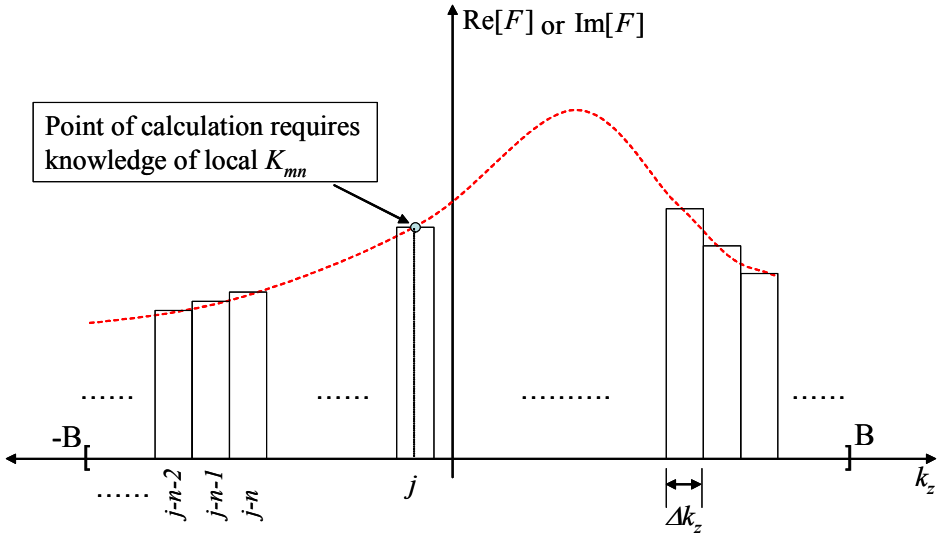

Figure D.2: Schematic of numerical integration structure.

D.4 Numerical Results

This section presents the computation and comparison of the Green's functions for additional cases to the ones presented in Chapter 2. The Green's functions were used to model the presence of a point source at the wall of a circular duct as shown in Figure D.3. As shown in this figure, the cross section plane at the source location defines a propagation interface between the positive and negative propagating sound fields. This interface is a sector of main interest for the computation of the Green's functions since the condition of continuity has to be satisfied. In addition to the computation in this plane, the solution was also evaluated along the coordinate *z* for a fixed radial location *r*.

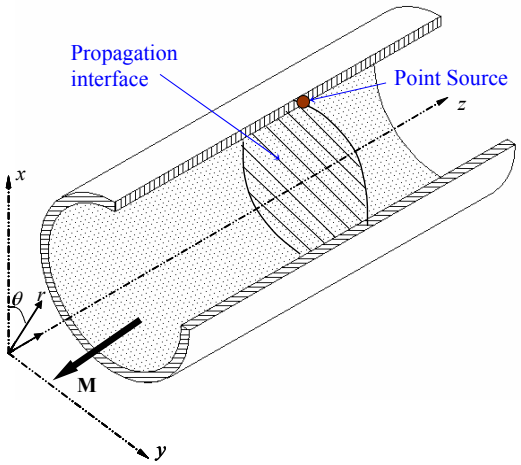

Figure D.3: Schematics of the propagating interface and source position.

The duct is assumed to have a radius $a = 0.43$ m. The uniform flow was assumed to be opposite to the positive direction of propagation. Both the cases of hard and soft wall were considered. Also, different liners and flow conditions were investigated.

D.4.1 Hard Wall Case

The first numerical case considered is the "hard wall" boundary condition, i.e. $\beta_w = 0$, and a flow with Mach number of -0.44 in the z-direction. The Green's function was computed at the propagating interface for a frequency of 1000 Hz using both the Modal Expansion and the WT method using the Residue Theory. Figure D.4 shows the Green's function magnitude at the propagating interface section between positive and

negative traveling waves, i.e. source plane at $z = z_o$. These plots were generated by evaluating only the closed form expressions in (D.19). The number of modes used for both formulations is 1600, i.e. 40 circumferential by 40 radial orders. The source is located at the upper point in the section as indicated in the figure. It is shown in this figure that the Green's functions are identical for both methods. Also, the magnitude contours at the interface are identical for both direction of sound propagation. This implies continuity in the Green function at the propagation interface.

The results presented in this section verify that both approaches to compute the Green's functions collapse in the same formulation when the boundary condition is assumed to be a hard wall.

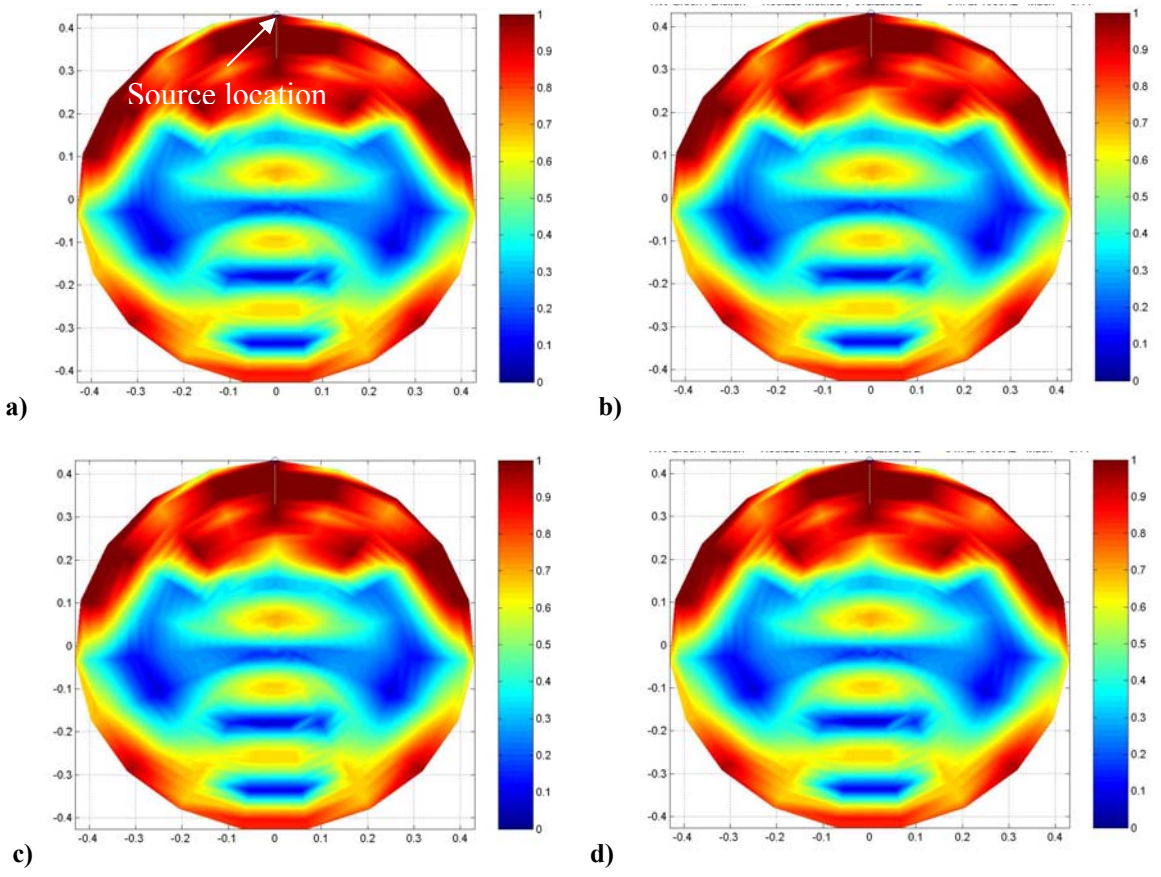

Figure D.4: Comparison of Hard Wall Green's functions magnitude (1/m) at the propagating interface with the Spectral and WT (Residue Theory) methods using (a) Positive Propagating modes (Spectral), (b) Negative Propagating modes (Spectral), (c) Positive Propagating modes (WT), and (d) Negative Propagating modes (WT).

D.4.2 Lined Wall Cases

This section presents the numerical results for the lined wall cases. The cases presented are intended to confirm the results obtained in Chapter 2. Different liners and flow conditions are considered in order to be able to generalize the conclusions on this numerical investigation. Similarly to the hard wall case, the number of modes used in the expansions is 1600, i.e. 40 circumferential by 40 radial mode orders. For all cases, the solution is found by the two approaches: the Spectral Expansion and the WT (numerical integration) methods. The results are presented in Figure D.5 through Figure D.16.

The first case was evaluated for a flow Mach number M=-0.2. Two frequencies of calculation were considered, i.e. 1000 and 3000 Hz. The wall normalized admittance is $\beta_w = 0.121 + i0.155$ for 1000 Hz, and $\beta_w = 0.30 + i0.065$ for 3000 Hz. The results for 1000 Hz are shown in Figures D.5, D.6 and D.7. Figure D.5 shows the obtained Green's function in magnitude and phase at the source plane using the modal expansion approach. The solution for the positive propagating waves is shown in part (a) and for the negative propagating waves in part (b). The results at the source plane using the WT are shown in Figure D.6. Unlike the closed form solution, it is not necessary to make a distinction between positive and negative propagation in this numerical case. The results confirm that the magnitude and phase of Green's function for the WT method present similar trends as the Spectral Expansion approach. The comparison of the Spectral and WT is also undertaken by evaluating the solution of the Green's function in the axial direction of the duct. The fixed radial coordinate is *r=0.2159* m and the azimuth coordinate $\theta=0$. This comparison is presented in Figure D.7 for both magnitude and phase. Similar to the results at the source plane, all approaches show good agreement in terms of the phase. The results for 3000 Hz are presented in the same fashion in Figures D.8 to D.10, and they show the same trends.

The second case was evaluated for a flow Mach number M=-0.44. Similarly to the previous case, the problem was solved for 1000 and 3000 Hz. The wall normalized admittance for this case is $\beta_w = 0.087 + i0.214$ for 1000 Hz, and $\beta_w = 0.50 + i0.228$ for 3000 Hz. The results for 1000 Hz are shown in Figures D.11, D.12 and D.13. Similarly, the results for 3000 Hz are shown in Figures D.14, D.15 and D.16.

Similarly to the investigation in Chapter 2, the comparison between both methods, i.e. Spectral Expansion and WT (numerical integration), confirms that the spectral expansion solution gives a safe formulation to obtain the radiation of sound from a point source in the lined duct. As observed in the results, the continuity condition at the source plane is perfectly achieved by using both methods. Note that this condition is explicitly imposed in the modal expansion approach and naturally satisfied in the WT method (numerical integration). In addition, the results obtained by the WT method require performing a numerical integration that is computationally expensive and thus not practical. On the other hand, **the modal expansion approach not only provides a reliable solution but it is also computationally efficient.**

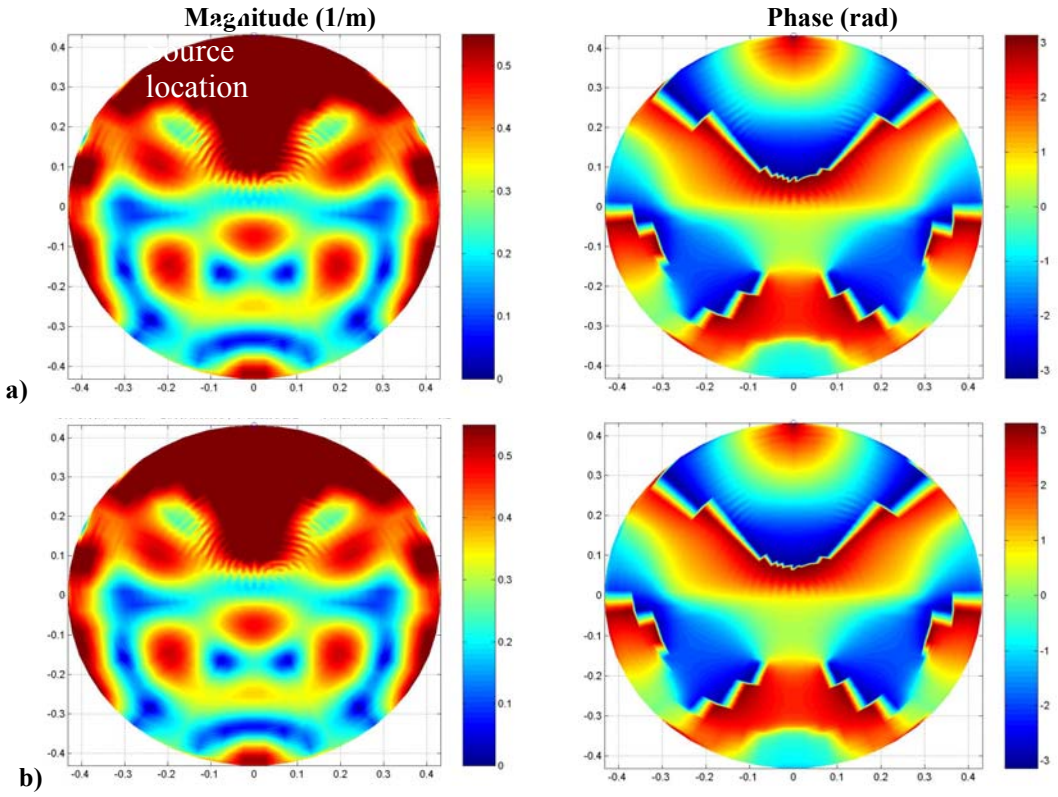

Figure D.5: Magnitude and Phase of the soft wall Green's function at the propagating interface at **1000 Hz** and M=-0.2 for the Spectral Expansion Method a) positive propagating, and b) negative propagating. Wall normalized admittance is $\beta_w = 0.121 + i0.155$

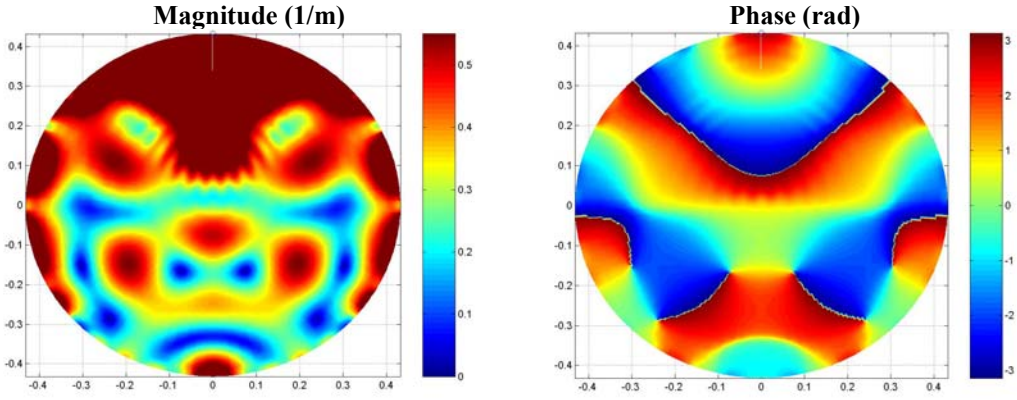

Figure D.6: Magnitude and Phase of the soft wall Green's function at the propagating interface at **1000 Hz** and M=-0.2 for the WT Method using a numerical integration. Wall normalized admittance is $\beta_w = 0.121 + i0.155$

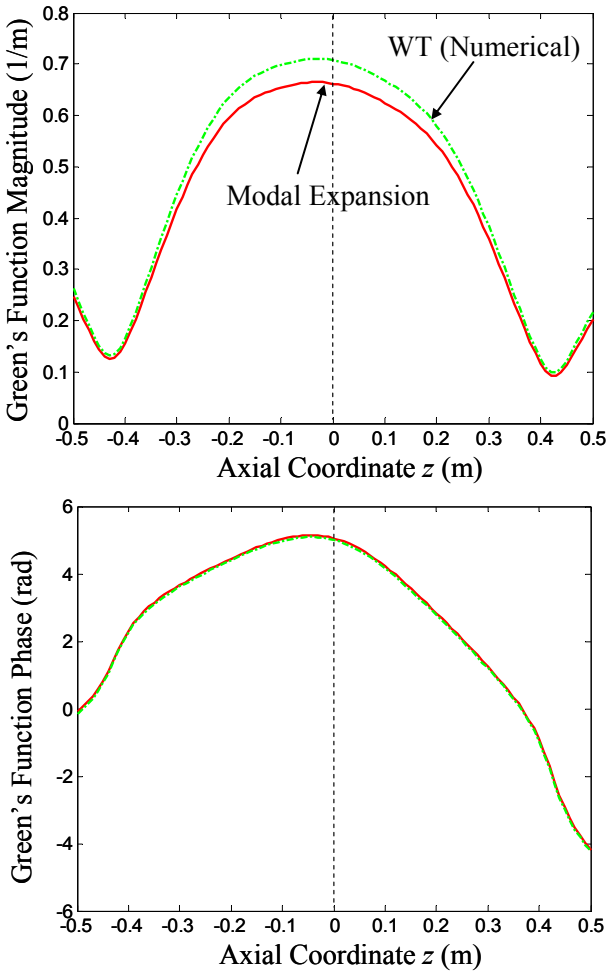

Figure D.7: Magnitude and Phase of the Green's function in the axial direction at **1000 Hz** and M=-0.2. Wall normalized admittance is $\beta_w = 0.121 + i0.155$

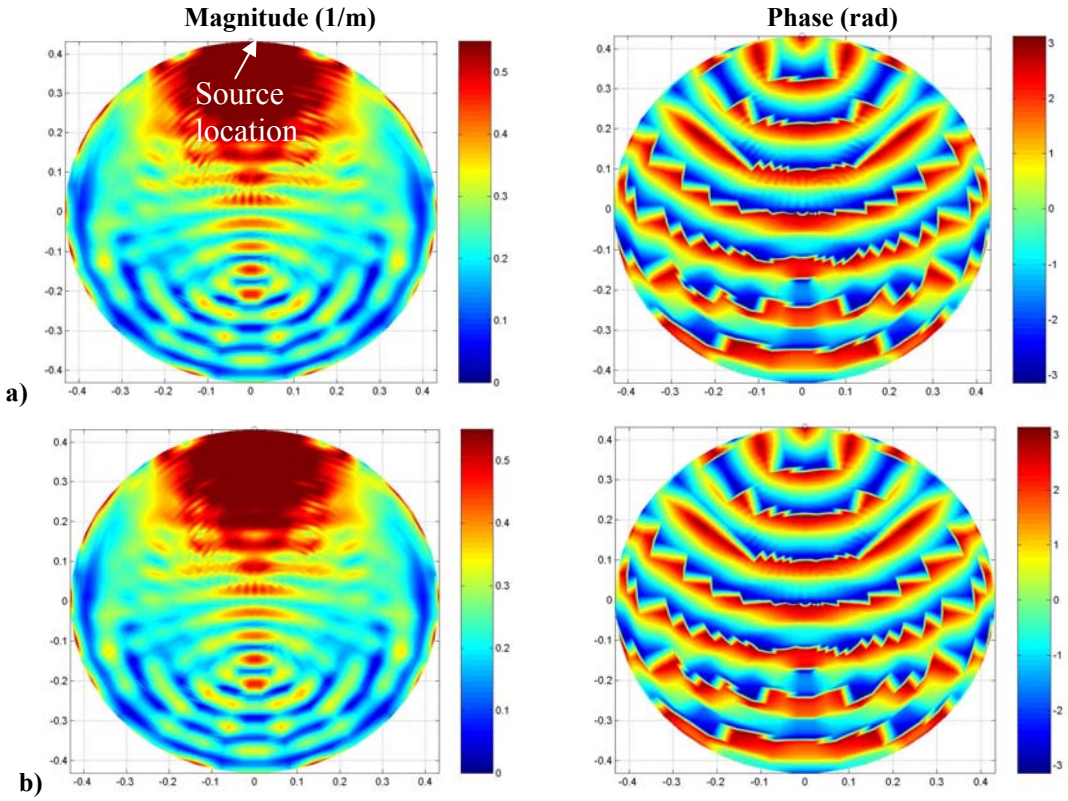

Figure D.8: Magnitude and Phase of the soft wall Green's function at the propagating interface at **3000 Hz** and M=-0.2 for the Spectral Expansion Method a) positive propagating, and b) negative propagating. Wall normalized admittance is $\beta_w = 0.30 + i0.065$

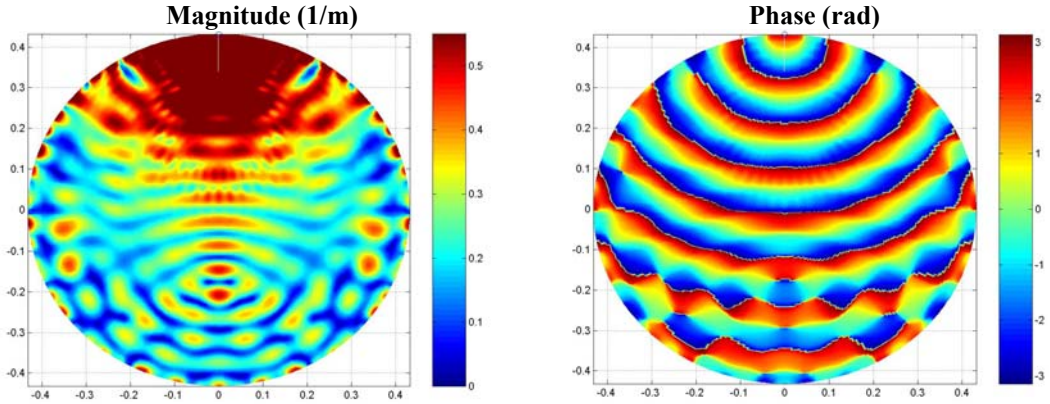

Figure D.9: Magnitude and Phase of the soft wall Green's function at the propagating interface at **3000 Hz** and M=-0.2 for the WT Method using a numerical integration. Wall normalized admittance is $\beta_w = 0.30 + i0.065$

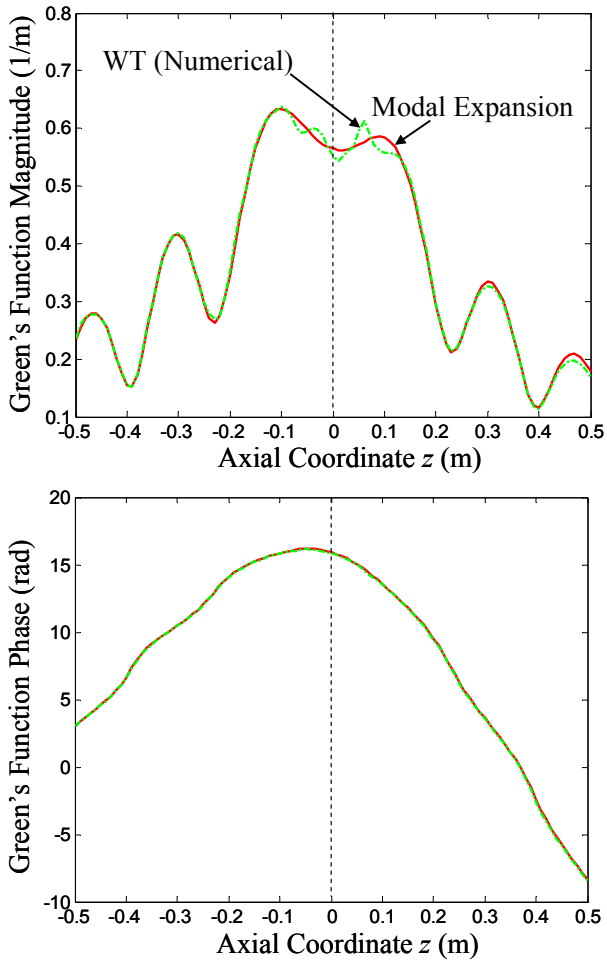

Figure D.10: Magnitude and Phase of the Green's function in the axial direction at **3000 Hz** and M=-0.2. Wall normalized admittance is $\beta_w = 0.30 + i0.065$

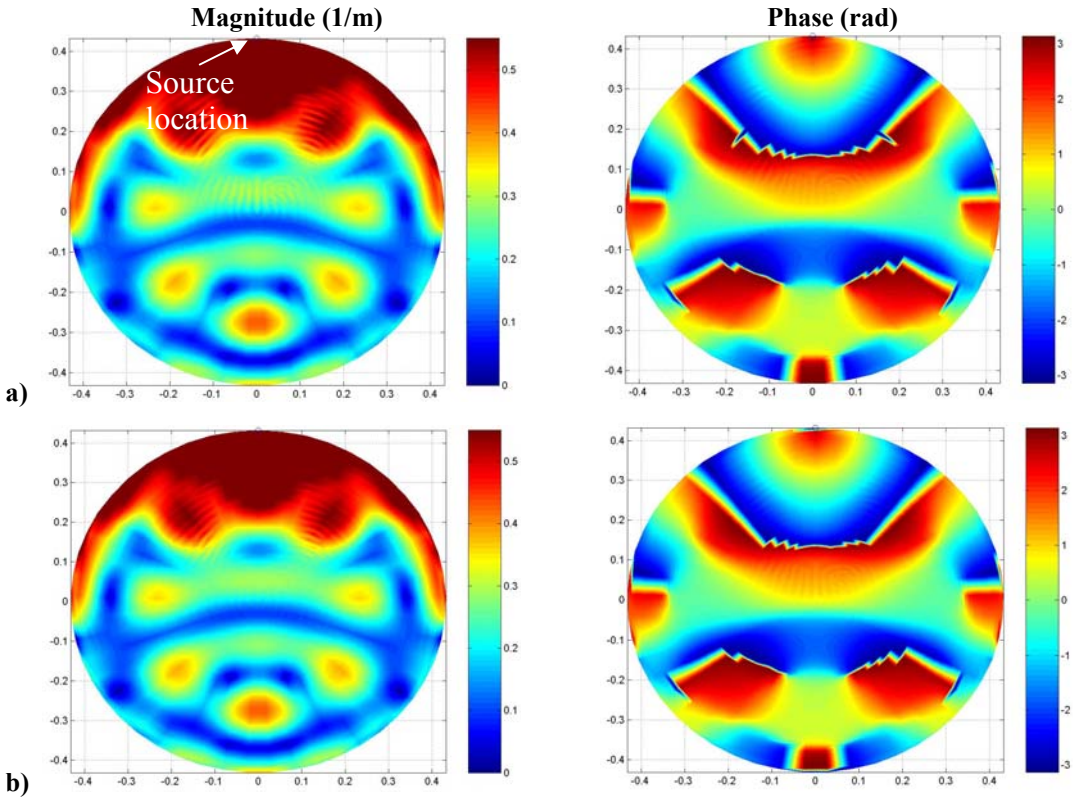

Figure D.11: Magnitude and Phase of the soft wall Green's function at the propagating interface at **1000 Hz** and M=-0.44 for the Spectral Expansion Method a) positive propagating, and b) negative propagating. Wall normalized admittance is $\beta_w = 0.087 + i0.214$

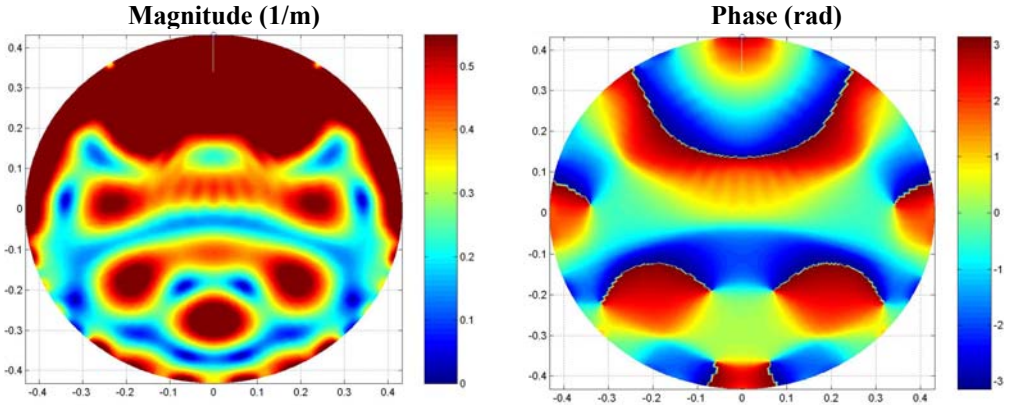

Figure D.12: Magnitude and Phase of the soft wall Green's function at the propagating interface at **1000 Hz** and M=-0.44 for the WT Method using a numerical integration. Wall normalized admittance is $\beta_w = 0.087 + i0.214$

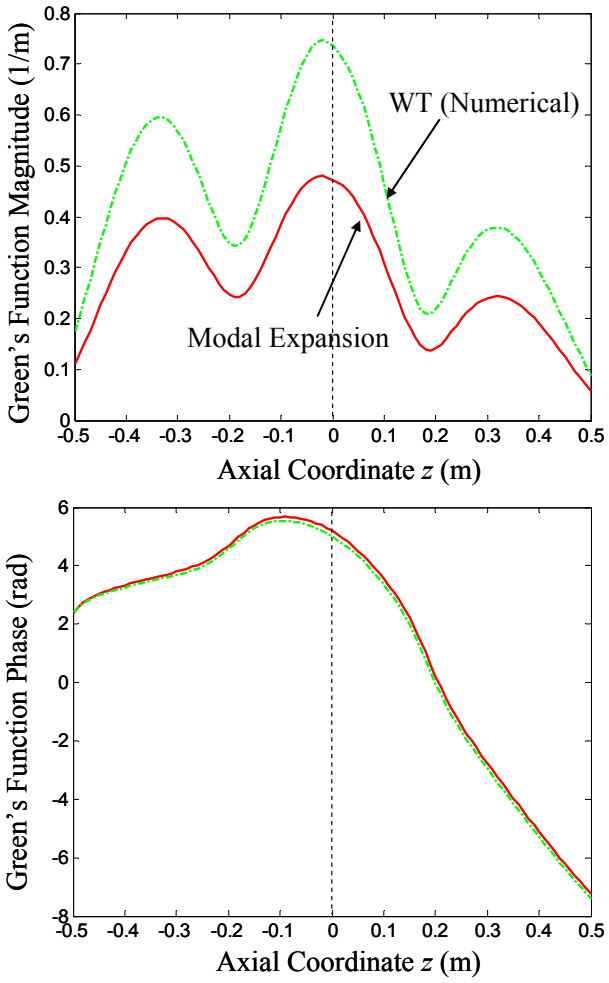

Figure D.13: Magnitude and Phase of the Green's function in the axial direction at **1000 Hz** and M=-0.44. Wall normalized admittance is $\beta_w = 0.087 + i0.214$

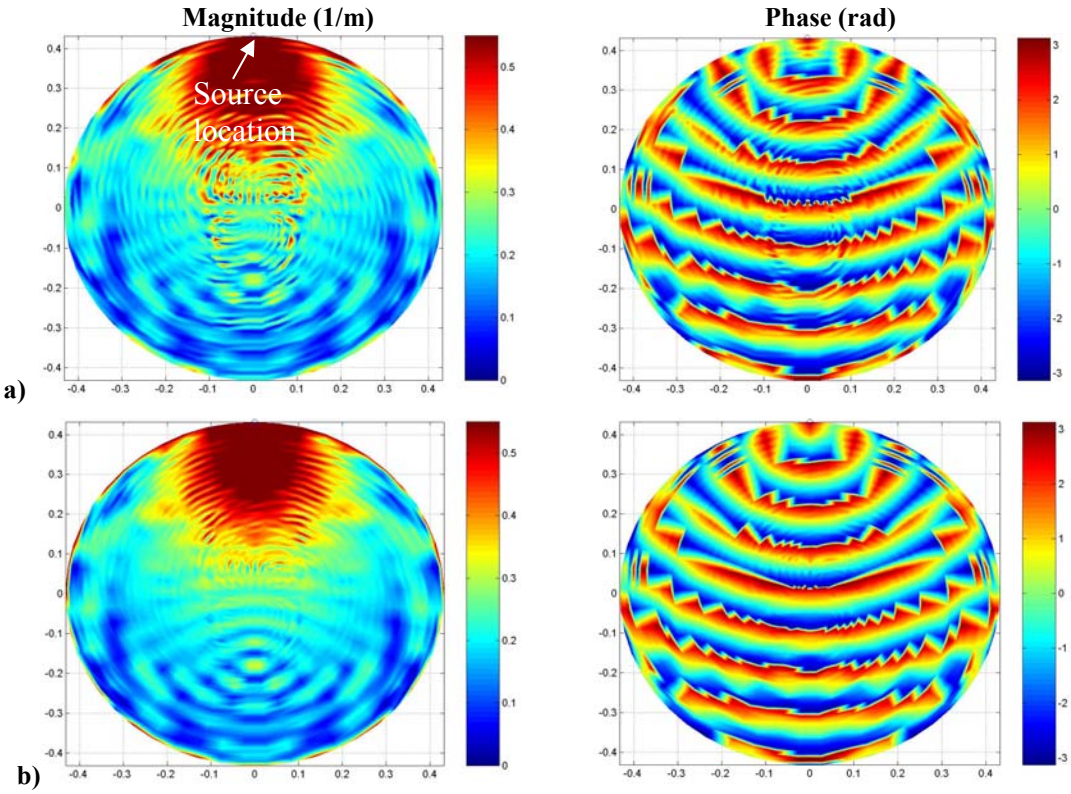

Figure D.14: Magnitude and Phase of the soft wall Green's function at the propagating interface at **3000 Hz** and M=-0.44 for the Spectral Expansion Method a) positive propagating, and b) negative propagating. Wall normalized admittance is $\beta_w = 0.50 + i0.228$

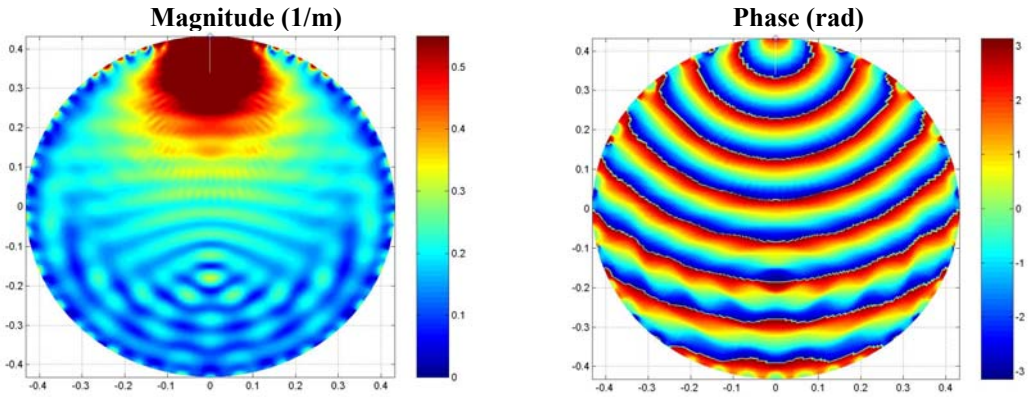

Figure D.15: Magnitude and Phase of the soft wall Green's function at the propagating interface at **3000 Hz** and M=-0.44 for the WT Method using a numerical integration. Wall normalized admittance is $\beta_w = 0.50 + i0.228$

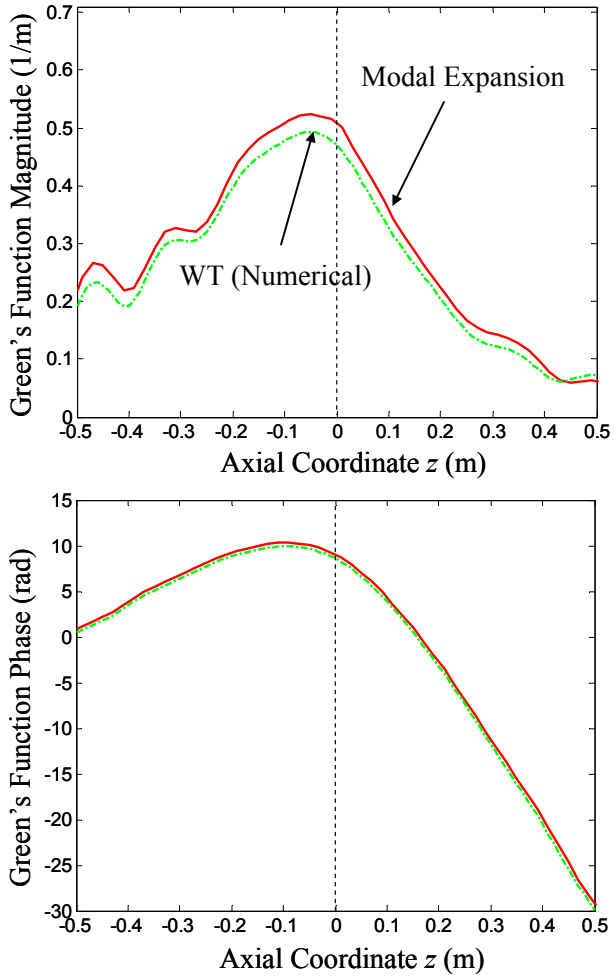

Figure D.16: Magnitude and Phase of the Green's function in the axial direction at **3000 Hz** and M=-0.44. Wall normalized admittance is $\beta_w = 0.50 + i0.228$

Appendix E. Reflected Sound Field

This appendix presents the computation of the reflected sound field generated by the presence of the HQ tubes. The analytical formulation is very similar to the case of the transmitted positive propagating field and it will be developed in detail. The negative propagating modal amplitudes produced by the HQ tubes will be computed first and the acoustic power of this sound field will be computed next.

E.1 Reflected Sound Field due to HQ tubes

In this section, the reflected sound through a particular duct cross section is presented. In this case, the duct negative propagating pressure field is due to the superposition of the piston sources. Therefore, the reflected pressure field can be written in terms of positive and negative spinning modes as follows

$$p_{ref} = \sum_{m=0}^{M_s}\sum_{n=0}^{N_s}\left(A_{mn}^{(-)}\right)_{hq}^{pos} J_m\left(k_{mn}^{(-)}r\right)e^{-im\theta}e^{-ik_z^{(-)}z} + \sum_{m=0}^{M_s}\sum_{n=0}^{N_s}\left(A_{mn}^{(-)}\right)_{hq}^{neg} J_m\left(k_{mn}^{(-)}r\right)e^{im\theta}e^{-ik_z^{(-)}z} \quad \text{(E.1)}$$

where $\left(A_{mn}^{(-)}\right)_{hq}^{pos}$ and $\left(A_{mn}^{(-)}\right)_{hq}^{neg}$ are the modal amplitudes of the positive and negative spinning modes (propagating in the negative z-direction), respectively. These amplitudes account for the effects of the HQ tubes and can be expressed as

$$\left(A_{mn}^{(-)}\right)_{hq}^{pos} = \sum_{r=1}^{N_s}\left(A_{mn}^{(-)}\right)_{r}^{pos} V_{p_r} \quad \text{(E.2)a}$$

$$\left(A_{mn}^{(-)}\right)_{hq}^{neg} = \sum_{r=1}^{N_s}\left(A_{mn}^{(-)}\right)_{r}^{neg} V_{p_r} \quad \text{(E.2)b}$$

Note that, since the fan disturbance is assumed to be propagating in the positive z-direction, the modal amplitudes $\left(A_{mn}^{(-)}\right)_{hq}^{pos}$ and $\left(A_{mn}^{(-)}\right)_{hq}^{neg}$ only include the effect of the piston sources. The source velocities V_{p_r} are obtained from the solution of the system of equations in (3.14). The objective of this section is to derive an expression for

$\left(A_{mn}^{(-)}\right)_r^{pos}$ and $\left(A_{mn}^{(-)}\right)_r^{neg}$. The first step is to write the expression of the reflected pressure as a linear superposition as follows

$$p_{ref}(r,\theta,z) = \sum_{r=1}^{N_s} p^{(-)}(r,\theta,z|\, r_r,\theta_r,z_r) \tag{E.3}$$

As mentioned before, the effect of the disturbance pressure p_d is not included in this analysis. The pressure produced by the r^{th} source with a unit velocity at the transmitted location, i.e. downstream of the source, is obtained from the finite piston radiation formula in equation (2.81) as

$$\begin{aligned} p^{(-)}(r,\theta,z\,|\,a,\theta_r,z_r) = -i\,\rho c \sum_{m=0}^{M_g}\sum_{n=0}^{N_g} \frac{\left(k_0 - k_z^{(-)}M\right)^2}{k_0} A_{mn}^{(-)}\, \cos m\left(\theta-\theta_r\right) J_m\left(k_{mn}^{(-)} r\right) \times \\ \times \kappa_\theta(\alpha)\; e^{-ik_z^{(-)}(z-z_r)}\, \frac{\sin(k_z^{(-)} d_r)}{k_z^{(-)} d_r}\; 2d_r \end{aligned} \tag{E.4}$$

The Green's functions modal amplitudes $A_{mn}^{(-)}$ in equation (E.4) are determined from the linear system of equations in (2.45). The sound field created by the r^{th} piston source is non-spinning and symmetric with respect to $\theta=\theta_r$. However, it can be written as a set of positive and negative spinning modes by using the following trigonometric relationship

$$\cos m\left(\theta-\theta_r\right) = e^{-im\theta}\left(\frac{e^{im\theta_r}}{2}\right) + e^{im\theta}\left(\frac{e^{-im\theta_r}}{2}\right) \tag{E.5}$$

Thus, equation (E.4) can be written as

$$\begin{aligned} p^{(-)}(r,\theta,z|r_r,\theta_r,z_r) = \sum_{m=0}^{M_g}\sum_{n=0}^{N_g} (A_{mn}^{(-)})_r^{pos} J_m\left(k_{mn}^{(-)} r\right) e^{-im\theta} e^{-ik_z^{(-)} z} \\ + \sum_{m=0}^{M_g}\sum_{n=0}^{N_g} (A_{mn}^{(-)})_r^{neg} J_m\left(k_{mn}^{(-)} r\right) e^{+im\theta} e^{-ik_z^{(-)} z} \end{aligned} \tag{E.6}$$

where $\left(A_{mn}^{(-)}\right)_r^{pos}$ and $\left(A_{mn}^{(-)}\right)_r^{neg}$ are the complex amplitude of reflected modes spinning in the positive and negative direction, respectively, due to source "r". These amplitudes are given from (E.4) and (E.5) as

$$\left(A_{mn}^{(-)}\right)_r^{pos} = -i\,\rho c\,\frac{\left(k_0 - k_z^{(-)}M\right)^2}{k_0} A_{mn}^{(-)}\,\frac{2a\alpha_r \sin\left(m\alpha_r\right)}{m\alpha_r}\; e^{ik_z^{(-)}z_r}\,\frac{\sin(k_z^{(-)}d_r)}{k_z^{(-)}d_r}\; 2d_r\,\frac{e^{+im\theta_r}}{2} \quad \text{(E.7)a}$$

$$\left(A_{mn}^{(-)}\right)_r^{neg} = -i\,\rho c\,\frac{\left(k_0 - k_z^{(-)}M\right)^2}{k_0} A_{mn}^{(-)}\,\frac{2a\alpha_r \sin\left(m\alpha_r\right)}{m\alpha_r}\; e^{ik_z^{(-)}z_r}\,\frac{\sin(k_z^{(-)}d_r)}{k_z^{(-)}d_r}\; 2d_r\,\frac{e^{-im\theta_r}}{2} \quad \text{(E.7)b}$$

The mode of circumferential order *m=0* is not spinning; therefore, there is no use of defining positive and negative spinning amplitudes for this mode. However, in order to stay consistent with the previous notations and avoid presenting too many equations, it can simply be assumed that, for mode *m=0*, $(A_{0n}^{(-)})_r^{neg}$ is equal to zero and $(A_{0n}^{(-)})_r^{pos}$ is given by the equation

$$\left(A_{0n}^{(-)}\right)_r^{pos} = -i\,\rho c\,\frac{\left(k_0 - k_z^{(-)}M\right)^2}{k_0} A_{0n}^{(-)}\; 2a\alpha_r\; e^{ik_z^{(-)}z_r}\,\frac{\sin(k_z^{(-)}d_r)}{k_z^{(-)}d_r}\; 2d_r \qquad \text{(E.8)}$$

E.2 Sound Power of the Negative Propagating Field

This section presents the derivation of the expression for the acoustic power of the reflected sound field. The expression is derived for the acoustic intensity through a particular duct cross section as shown in Figure E.1. Recall that, since the modes in a lined duct with flow are not orthogonal, the expression of the acoustic power contains all the cross terms due to the interaction of the modes with each other. In addition, if the fan disturbance is included in the power computation, the expression for the power also contains the cross terms between the positive (*disturbance*) and negative (*piston sources*) propagating modes. In this analysis, the cross terms between the disturbance and piston source modal amplitudes will be assumed to be small and thus disregarded. As a consequence, the power of each component can be computed separately. The computation of the acoustic power is developed by first assuming the pressure and axial particle velocity field inside the duct. As indicated in section 2.1, the duct pressure field is the superposition of the modes inside the duct. If only negative propagating modes are assumed present, the pressure field is given in terms of spinning modes as

$$p = \sum_{m=0}^{M_s}\sum_{n=0}^{N_s}\left(A_{mn}^{(-)}\right)^{pos} J_m\left(k_{mn}^{(-)}r\right)e^{-im\theta}e^{-ik_z^{(-)}z} + \sum_{m=0}^{M_s}\sum_{n=0}^{N_s}\left(A_{mn}^{(-)}\right)^{neg} J_m\left(k_{mn}^{(-)}r\right)e^{im\theta}e^{-ik_z^{(-)}z}$$
$$p = \sum_{m=0}^{M_s}\sum_{n=0}^{N_s} p_{mn}^{(-)} \tag{E.9}$$

where $\left(A_{mn}^{(-)}\right)^{pos}$ and $\left(A_{mn}^{(-)}\right)^{neg}$ are the modal amplitudes of the positive and negative spinning modes (propagating in the positive z-direction), respectively.

The transmitted acoustic power is obtained by integrating the axial component of the acoustic intensity, $I_z^{(-)}(r,\theta,z_n)$, over the duct cross section at z_n as shown in Figure E.1. That is

$$W(z_n) = \int_0^a\int_0^{2\pi} I_z^{(-)}(r,\theta,z_n)\, r\, dr d\theta \tag{E.10}$$

The acoustic intensity in the positive z-direction is given by [50]:

$$I_z = \frac{1}{2}\mathrm{Re}\left[pv_z^* + \rho c\left|v_z\right|^2 M + \frac{\left|p\right|^2}{\rho c}M + v_z p^* M^2 \right] \tag{E.11}$$

The axial particle velocity $v_z\left(a,\theta,z\right)$ can be found in terms of the pressure using the axial component of the equilibrium equation (*See equation (2.4)*):

$$-\frac{\partial p}{\partial z} = i\omega\rho v_z + \rho c M\frac{\partial v_z}{\partial z} \tag{E.12}$$

Considering the expression for the pressure in (E.9), equation (E.12) reduces to

$$v_z = \sum_{m=0}^{M_s}\sum_{n=0}^{N_s}\frac{k_z^{(-)}}{\rho c\left(k_0 - k_z^{(+)}M\right)} p_{mn}^{(-)} \tag{E.13}$$

where $p_{mn}^{(-)}$ are the modal components of the pressure (z-direction positive propagating). Expanding the pressure, equation (E.13) can be written as

$$v_z = \sum_{m=0}^{M_s}\sum_{n=0}^{N_s}\left(A_{mn}^{(-)}\right)^{pos}\frac{k_z^{(-)}}{\rho c\left(k_0 - k_z^{(-)}M\right)} J_m\left(k_{mn}^{(-)}r\right)e^{-im\theta}e^{-ik_z^{(-)}z} +$$
$$+ \sum_{m=0}^{M_s}\sum_{n=0}^{N_s}\left(A_{mn}^{(-)}\right)^{neg}\frac{k_z^{(-)}}{\rho c\left(k_0 - k_z^{(-)}M\right)} J_m\left(k_{mn}^{(-)}r\right)e^{im\theta}e^{-ik_z^{(-)}z} \tag{E.14}$$

Then, replacing the transmitted pressure from (E.9) and the velocity from (E.14) into the intensity (E.11), the acoustic power is given as follows

$$
\begin{aligned}
W(z_n) = \frac{1}{2}\mathrm{Re}\Bigg[& \frac{2\pi a^2}{\rho c}\cdot \\
& \sum_{m=0}^{M}\sum_{n=0}^{N}\sum_{r=0}^{N}\Bigg\{\left(\left(A_{mn}^{(-)}\right)^{pos}\left(A_{mr}^{*(-)}\right)^{pos}+\left(A_{mn}^{(-)}\right)^{neg}\left(A_{mr}^{*(-)}\right)^{neg}\right)\frac{e^{-i\left(k_z^{(-)}\right)_{mn}z}.e^{-i\left(k_z^{*(-)}\right)_{mr}z}\left(k_z^{*(-)}\right)_{mr}}{\left(k_0-\left(k_z^{*(-)}\right)_{mr}M\right)}\hat{\Lambda}_{m,nr}\Bigg\}+ \\
& M\Bigg\{\left(\left(A_{mn}^{(-)}\right)^{pos}\left(A_{mr}^{*(-)}\right)^{pos}+\left(A_{mn}^{(-)}\right)^{neg}\left(A_{mr}^{*(-)}\right)^{neg}\right)e^{-i\left(k_z^{(-)}\right)_{mn}z}\,e^{-i\left(k_z^{*(-)}\right)_{mr}z}\times \\
& \qquad\qquad \times\frac{\left(k_z^{(-)}\right)_{mn}\left(k_z^{*(-)}\right)_{mr}}{\left(k_0-\left(k_z^{(-)}\right)_{mn}M\right)\left(k_0-\left(k_z^{*(-)}\right)_{mr}M\right)}\hat{\Lambda}_{m,nr}\Bigg\}+ \\
& M\Bigg\{\left(\left(A_{mn}^{(-)}\right)^{pos}\left(A_{mr}^{*(-)}\right)^{pos}+\left(A_{mn}^{(-)}\right)^{neg}\left(A_{mr}^{*(-)}\right)^{neg}\right)e^{-i\left(k_z^{(-)}\right)_{mn}z}\,e^{-i\left(k_z^{*(-)}\right)_{mr}z}\hat{\Lambda}_{m,nr}\Bigg\}+ \\
& M^2\Bigg\{\left(\left(A_{mn}^{(-)}\right)^{pos}\left(A_{mr}^{*(-)}\right)^{pos}+\left(A_{mn}^{(-)}\right)^{neg}\left(A_{mr}^{*(-)}\right)^{neg}\right)e^{-i\left(k_z^{(-)}\right)_{mn}z}e^{-i\left(k_z^{*(-)}\right)_{mr}z}\frac{\left(k_z^{(-)}\right)_{mn}}{\left(k_0-\left(k_z^{(-)}\right)_{mn}M\right)}\hat{\Lambda}_{m,nr}\Bigg\}\Bigg]
\end{aligned}
\tag{E.15}
$$

where the factor $\hat{\Lambda}_{m,nr}$ is defined as

$$
\hat{\Lambda}_{m,nr} = \frac{1}{a^2}\int_0^a J_m\left(k_{mn}^{(-)}r\right)J_m\left(k_{mr}^{*(-)}r\right)r\,dr \tag{E.16}
$$

These integrals have closed form solution. Also note that the double summation in *n* and *r* has to be done because of the fact that the modes in the lined duct with flow are not orthogonal. Then, the cross terms $\hat{\Lambda}_{m,nr}$ for $n \neq r$ do not vanish.

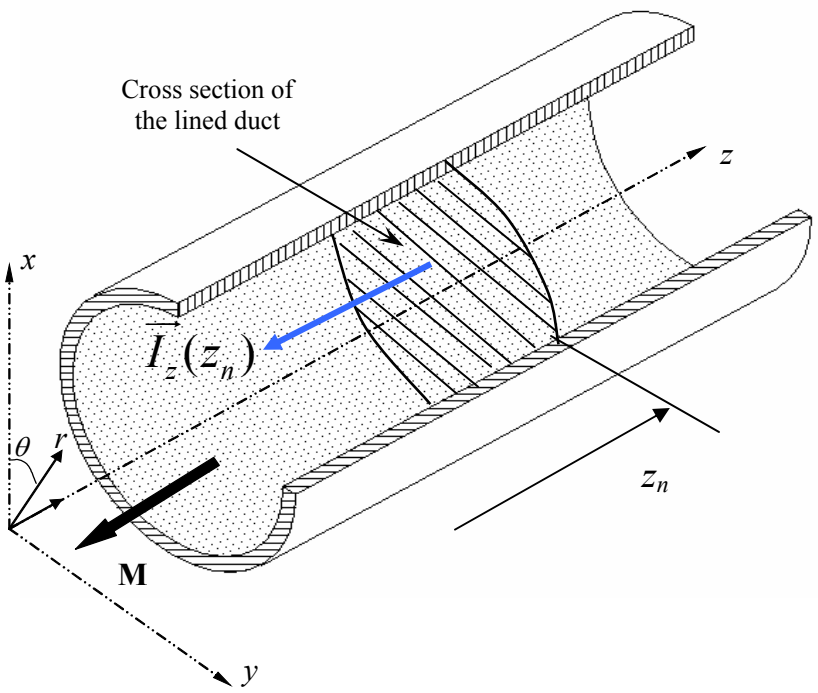

Figure E.1: Acoustic axial intensity at a fixed duct cross section for negative propagating field.

Appendix F. Green's Functions Full Derivation

This appendix presents the full derivation to obtain the modal amplitudes of the Green's functions in equation (2.35). The Green's functions are found as the solution of the non-homogeneous wave equation in cylindrical coordinates as

$$\frac{\partial^2 g}{\partial r^2}+\frac{1}{r}\frac{\partial g}{\partial r}+\frac{1}{r^2}\frac{\partial^2 g}{\partial \theta^2}+\frac{\partial^2 g}{\partial z^2}\left(1-M^2\right)-2iMk_o\frac{\partial g}{\partial z}+k_o^2 g=\frac{1}{r}\delta(\vec{r}\,|\vec{r}_o) \tag{F.1}$$

where $\vec{r}_o$ is the location of the source. As mentioned in Chapter 2, the solution of the Green's functions will be written for the complete domain in terms of the Heaviside function $H\left(z-z_o\right)$ (i.e. $H\left(z\right)=1\ (z>0)$; $H\left(z\right)=0\ (z<0)$ and $H\left(0\right)=1/2$) as follows

$$g\left(\vec{r}\middle|\vec{r}_o\right)=g^{(+)}\left(\vec{r}\,|\vec{r}_o\right)H\left(z-z_o\right)+g^{(-)}\left(\vec{r}\,|\vec{r}_o\right)\left[1-H\left(z-z_o\right)\ \right] \tag{F.2}$$

where the functions $g^{(+)}$ and $g^{(-)}$ correspond to the positive and negative propagating field, respectively. Their expression is given in equation (2.35). For simplicity, a compact notation is used for the linear operator $L(.)=\frac{\partial^2(.)}{\partial r^2}+\frac{1}{r}\frac{\partial(.)}{\partial r}+\frac{1}{r^2}\frac{\partial^2(.)}{\partial\theta^2}$.

The first step to find the Green's functions modal amplitudes is to replace equation (F.2) into (F.1)as

$$\begin{aligned}&\left(k_o^2+L\right)\left[g^{(+)}H\left(z-z_o\right)+g^{(-)}\left[1-H\left(z-z_o\right)\ \right]\right]\\&+\left(1-M^2\right)\frac{\partial^2}{\partial z^2}\left[g^{(+)}H\left(z-z_o\right)+g^{(-)}\left[1-H\left(z-z_o\right)\ \right]\right]\\&-2iMk_o\frac{\partial}{\partial z}\left[g^{(+)}H\left(z-z_o\right)+g^{(-)}\left[1-H\left(z-z_o\right)\ \right]\right]=\frac{1}{r}\delta(\vec{r}\,|\vec{r}_o)\end{aligned} \tag{F.3}$$

Considering that the derivative of the Heaviside function is $H'\left(z-z_0\right)=\delta\left(z-z_0\right)$, equation (F.3) can be rearranged as follows

$$\left(k_o^2+L\right)\left[g^{(+)}H\left(z-z_o\right)+g^{(-)}\left[1-H\left(z-z_o\right)\right]\right]+\left(1-M^2\right)\left[\frac{\partial^2 g^{(+)}}{\partial z^2}H\left(z-z_o\right)+\frac{\partial^2 g^{(-)}}{\partial z^2}\left[1-H\left(z-z_o\right)\right]+\right.$$
$$\left.+2\left(\frac{\partial g^{(+)}}{\partial z}-\frac{\partial g^{(-)}}{\partial z}\right)\delta\left(z-z_o\right)+\left(g^{(+)}-g^{(-)}\right)\delta'\left(z-z_o\right)\right]-$$
$$-2iMk_o\left[\frac{\partial g^{(+)}}{\partial z}H\left(z-z_o\right)+\frac{\partial g^{(-)}}{\partial z}\left[1-H\left(z-z_o\right)\right]+\left(g^{(+)}-g^{(-)}\right)\delta\left(z-z_o\right)\right]=\frac{1}{r}\delta(\vec{r}|\vec{r}_o) \tag{F.4}$$

In order to find the modal amplitudes of $g^{(+)}$ and $g^{(-)}$, equation (F.4) has to be rearranged. For this purpose, the equation has to be pre-multiplied by

$$\Phi_{er}(r,\theta)=\Phi_{er}^{(+)}(r,\theta)H\left(z-z_o\right)+\Phi_{er}^{(-)}(r,\theta)\left[1-H\left(z-z_o\right)\right] \tag{F.5}$$

and integrated over a small volume as

$$\int_0^a\int_0^{2\pi}\lim_{\varepsilon\to 0}\int_{z_o-\varepsilon}^{z_o+\varepsilon}\left\{\Phi_{er}^{(+)}(r,\theta)H\left(z-z_o\right)+\Phi_{er}^{(-)}(r,\theta)\left[1-H\left(z-z_o\right)\right]\right\}\left[Equation\ F.4\right]\,dz\,r\,d\theta\,dr \tag{F.6}$$

Therefore, the objective of this appendix is to fully derive this operation for every single term of equation (F.4).

F.1 Term: $\left(k_o^2+L\right)\left[g^{(+)}H\left(z-z_o\right)+g^{(-)}\left[1-H\left(z-z_o\right)\right]\right]$

The several components of this term can be analyzed in the same fashion. As an illustration of the procedure the following term will be considered

$$\int_0^a\int_0^{2\pi}\lim_{\varepsilon\to 0}\int_{z_o-\varepsilon}^{z_o+\varepsilon}\left\{\Phi_{er}^{(+)}(r,\theta)H\left(z-z_o\right)+\Phi_{er}^{(-)}(r,\theta)\left[1-H\left(z-z_o\right)\right]\right\}\times$$
$$\times\left\{H\left(z-z_o\right)\frac{\partial^2 g^{(+)}\left(\vec{r}\,|\vec{r}_o\right)}{\partial r^2}+\left[1-H\left(z-z_o\right)\right]\frac{\partial^2 g^{(-)}\left(\vec{r}\,|\vec{r}_o\right)}{\partial r^2}\right\}dz\,r\,d\theta\,dr \tag{F.7}$$

Assuming the solution of $g^{(+)}$ and $g^{(-)}$ as in equation (2.35), the derivatives are solved as

$$\frac{\partial^2 g^{(\ell)}}{\partial r^2}=\sum_{m=0}^{M}\sum_{n=0}^{N}A_{mn}^{(\ell)}\frac{\partial^2\Phi_{mn}^{(\ell)}}{\partial r^2}e^{-ik_z^{(\ell)}(z-z_0)}\qquad \ell=+,- \tag{F.8}$$

It is then convenient to group the z-integral as follows

$$\int_0^a\int_0^{2\pi}\sum_{m=0}^{M}\sum_{n=0}^{N}A_{mn}^{(+)}\frac{\partial^2\Phi_{mn}^{(+)}}{\partial r^2}\Bigg\{\Phi_{er}^{(+)}(r,\theta)\lim_{\varepsilon\to0}\int_{z_o-\varepsilon}^{z_o+\varepsilon}H\left(z-z_o\right)H\left(z-z_o\right)e^{-ik_z^{(+)}(z-z_o)}dz+$$
$$+\Phi_{er}^{(-)}(r,\theta)\lim_{\varepsilon\to0}\int_{z_o-\varepsilon}^{z_o+\varepsilon}\left[1-H\left(z-z_o\right)\right]H\left(z-z_o\right)e^{-ik_z^{(+)}(z-z_o)}dz\Bigg\}r\,d\theta\,dr+$$
$$+\int_0^a\int_0^{2\pi}\sum_{m=0}^{M}\sum_{n=0}^{N}A_{mn}^{(-)}\frac{\partial^2\Phi_{mn}^{(-)}}{\partial r^2}\Bigg\{\Phi_{er}^{(+)}(r,\theta)\lim_{\varepsilon\to0}\int_{z_o-\varepsilon}^{z_o+\varepsilon}H\left(z-z_o\right)\left[1-H\left(z-z_o\right)\right]e^{-ik_z^{(-)}(z-z_o)}dz+ \tag{F.9}$$
$$+\Phi_{er}^{(-)}(r,\theta)\lim_{\varepsilon\to0}\int_{z_o-\varepsilon}^{z_o+\varepsilon}\left[1-H\left(z-z_o\right)\right]\left[1-H\left(z-z_o\right)\right]e^{-ik_z^{(-)}(z-z_o)}dz\Bigg\}r\,d\theta\,dr$$

Each of the z-integrals can be solved as

$$\lim_{\varepsilon\to0}\int_{z_o-\varepsilon}^{z_o+\varepsilon}H\left(z-z_o\right)H\left(z-z_o\right)e^{-ik_z^{(+)}(z-z_0)}dz=\lim_{\varepsilon\to0}\left\{\frac{e^{-ik_z^{(+)}(z-z_o)}}{-ik_z^{(+)}}\Bigg|_{z_o}^{z_o+\varepsilon}\right\}=\lim_{\varepsilon\to0}\left\{\frac{e^{-ik_z^{(+)}\varepsilon}}{-ik_z^{(+)}}-\frac{1}{-ik_z^{(+)}}\right\}=0 \tag{F.10}$$

$$\lim_{\varepsilon\to0}\int_{z_o-\varepsilon}^{z_o+\varepsilon}\left[1-H\left(z-z_o\right)\right]H\left(z-z_o\right)e^{-ik_z^{(+)}(z-z_o)}dz=0 \tag{F.11}$$

$$\lim_{\varepsilon\to0}\int_{z_o-\varepsilon}^{z_o+\varepsilon}H\left(z-z_o\right)\left[1-H\left(z-z_o\right)\right]e^{-ik_z^{(-)}(z-z_o)}dz=0 \tag{F.12}$$

$$\lim_{\varepsilon\to0}\int_{z_o-\varepsilon}^{z_o+\varepsilon}\left[1-H\left(z-z_o\right)\right]\left[1-H\left(z-z_o\right)\right]e^{-ik_z^{(-)}(z-z_o)}dz=0 \tag{F.13}$$

Therefore, the integral in (F.7) vanishes. In addition, it can be shown in the same fashion that the rest of the components of the term $\left(k_o^2+L\right)\left[g^{(+)}H\left(z-z_o\right)+g^{(-)}\left[1-H\left(z-z_o\right)\right]\right]$ **vanish** after applying this process.

F.2 Term: $\left(1-M^2\right)\left\{\frac{\partial^2 g^{(+)}\left(\vec{r}\,|\vec{r}_o\right)}{\partial z^2}H\left(z-z_0\right)+\frac{\partial^2 g^{(-)}\left(\vec{r}\,|\vec{r}_o\right)}{\partial z^2}\left[1-H\left(z-z_0\right)\right]\right\}$

The following integral is formed

$$\left(1-M^2\right)\int_0^a\int_0^{2\pi}\lim_{\varepsilon\to0}\int_{z_o-\varepsilon}^{z_o+\varepsilon}\left\{\Phi_{er}^{(+)}(r,\theta)H\left(z-z_o\right)+\Phi_{er}^{(-)}(r,\theta)\left[1-H\left(z-z_o\right)\right]\right\}\times$$
$$\times\left\{H\left(z-z_o\right)\frac{\partial^2 g^{(+)}\left(\vec{r}\,|\vec{r}_o\right)}{\partial z^2}+\left[1-H\left(z-z_o\right)\right]\frac{\partial^2 g^{(-)}\left(\vec{r}\,|\vec{r}_o\right)}{\partial z^2}\right\}dz\,r\,d\theta\,dr \tag{F.14}$$

where the derivatives are given by

$$\frac{\partial^2 g^{(\ell)}}{\partial z^2} = \sum_{m=0}^{M}\sum_{n=0}^{N} A_{mn}^{(\ell)}\Phi_{mn}^{(\ell)}\left(-ik_z^{(\ell)}\right)^2 e^{-ik_z^{(\ell)}(z-z_o)} \qquad \ell = +,- \tag{F.15}$$

Replacing (F.15) into (F.14), the following integral has to be solved

$$\begin{aligned}\left(1-M^2\right)\lim_{\varepsilon\to 0}\int_0^a\int_0^{2\pi}\sum_{m=0}^{M}\sum_{n=0}^{N} A_{mn}^{(+)}\Phi_{mn}^{(+)}\left(-ik_z^{(+)}\right)^2\Bigg\{\Phi_{er}^{(+)}(r,\theta)\int_{z_o-\varepsilon}^{z_o+\varepsilon} H\left(z-z_o\right)H\left(z-z_o\right)e^{-ik_z^{(+)}(z-z_o)}dz + \\ + \Phi_{er}^{(-)}(r,\theta)\int_{z_o-\varepsilon}^{z_o+\varepsilon}\left[1-H\left(z-z_o\right)\right]H\left(z-z_o\right)e^{-ik_z^{(+)}(z-z_o)}dz\Bigg\} r\,d\theta\,dr + \\ + \left(1-M^2\right)\lim_{\varepsilon\to 0}\int_0^a\int_0^{2\pi}\sum_{m=0}^{M}\sum_{n=0}^{N} A_{mn}^{(-)}\Phi_{mn}^{(-)}\left(-ik_z^{(-)}\right)^2\Bigg\{\Phi_{er}^{(+)}(r,\theta)\int_{z_o-\varepsilon}^{z_o+\varepsilon} H\left(z-z_o\right)\left[1-H\left(z-z_o\right)\right]e^{-ik_z^{(-)}(z-z_o)}dz + \\ + \Phi_{er}^{(-)}(r,\theta)\int_{z_o-\varepsilon}^{z_o+\varepsilon}\left[1-H\left(z-z_o\right)\right]\left[1-H\left(z-z_o\right)\right]e^{-ik_z^{(-)}(z-z_o)}dz\Bigg\} r\,d\theta\,dr\end{aligned} \tag{F.16}$$

Equation (F.16) leads to solve the same z-integrals as in the previous case. As a consequence, this term also **vanishes**.

F.3 Term: $2\left(1-M^2\right)\left\{\frac{\partial g^{(+)}}{\partial z}-\frac{\partial g^{(-)}}{\partial z}\right\}\delta\left(z-z_o\right)$

The following integral has to be solved

$$\begin{aligned}\left(1-M^2\right)\int_0^a\int_0^{2\pi}\lim_{\varepsilon\to 0}\int_{z_o-\varepsilon}^{z_o+\varepsilon}\left\{\Phi_{er}^{(+)}(r,\theta)H\left(z-z_o\right)+\Phi_{er}^{(-)}(r,\theta)\left[1-H\left(z-z_o\right)\right]\right\}\times \\ \times 2\left[\frac{\partial g^{(+)}\left(\vec{r}\,|\vec{r}_o\right)}{\partial z}-\frac{\partial g^{(-)}\left(\vec{r}\,|\vec{r}_o\right)}{\partial z}\right]\delta\left(z-z_o\right)dz\,r\,d\theta\,dr\end{aligned} \tag{F.17}$$

where the derivatives are given by

$$\frac{\partial g^{(\ell)}}{\partial z} = \sum_{m=0}^{M}\sum_{n=0}^{N} A_{mn}^{(\ell)}\Phi_{mn}^{(\ell)}\left(-ik_z^{(\ell)}\right)e^{-ik_z^{(\ell)}(z-z_o)} \qquad \ell = +,- \tag{F.18}$$

Replacing (F.18) into (F.17) yields

$$\left(1-M^2\right)\lim_{\varepsilon\to 0}\int_0^a\int_0^{2\pi}\sum_{m=0}^{M}\sum_{n=0}^{N}A_{mn}^{(+)}\Phi_{mn}^{(+)}\left(-ik_z^{(+)}\right)2\left\{\Phi_{er}^{(+)}(r,\theta)\int_{z_o-\varepsilon}^{z_o+\varepsilon}H\left(z-z_o\right)\delta\left(z-z_o\right)e^{-ik_z^{(+)}(z-z_o)}dz+\right.$$
$$\left.+\Phi_{er}^{(-)}(r,\theta)\int_{z_o-\varepsilon}^{z_o+\varepsilon}\left[1-H\left(z-z_o\right)\right]\delta\left(z-z_o\right)e^{-ik_z^{(+)}(z-z_o)}dz\right\}r\,d\theta\,dr-$$
$$-\left(1-M^2\right)\lim_{\varepsilon\to 0}\int_0^a\int_0^{2\pi}\sum_{m=0}^{M}\sum_{n=0}^{N}A_{mn}^{(-)}\Phi_{mn}^{(-)}\left(-ik_z^{(-)}\right)2\left\{\Phi_{er}^{(+)}(r,\theta)\int_{z_o-\varepsilon}^{z_o+\varepsilon}\delta\left(z-z_o\right)H\left(z-z_o\right)e^{-ik_z^{(-)}(z-z_o)}dz+\right.$$
$$\left.+\Phi_{er}^{(-)}(r,\theta)\int_{z_o-\varepsilon}^{z_o+\varepsilon}\delta\left(z-z_o\right)\left[1-H\left(z-z_o\right)\right]e^{-ik_z^{(-)}(z-z_o)}dz\right\}r\,d\theta\,dr \tag{F.19}$$

Therefore, the following z-integrals have to be solved as

$$\lim_{\varepsilon\to 0}\int_{z_o-\varepsilon}^{z_o+\varepsilon}\delta\left(z-z_o\right)H\left(z-z_o\right)e^{-ik_z^{(+)}(z-z_o)}dz=H\left(z_o-z_o\right)e^{-k_z^{(+)}(z_o-z_o)}=\frac{1}{2} \tag{F.20}$$

$$\lim_{\varepsilon\to 0}\int_{z_o-\varepsilon}^{z_o+\varepsilon}\delta\left(z-z_0\right)\left[1-H\left(z-z_o\right)\right]e^{-ik_z^{(+)}(z-z_0)}dz=\frac{1}{2} \tag{F.21}$$

$$\lim_{\varepsilon\to 0}\int_{z_o-\varepsilon}^{z_o+\varepsilon}H\left(z-z_o\right)\delta\left(z-z_o\right)e^{-ik_z^{(-)}(z-z_o)}dz=\frac{1}{2} \tag{F.22}$$

$$\lim_{\varepsilon\to 0}\int_{z_o-\varepsilon}^{z_o+\varepsilon}\left[1-H\left(z-z_o\right)\right]\delta\left(z-z_o\right)e^{-ik_z^{(-)}(z-z_o)}dz=\frac{1}{2} \tag{F.23}$$

Replacing the integral solutions into (F.19), the volume integral can be expressed as

$$\left(1-M^2\right)\sum_{m=0}^{M}\sum_{n=0}^{N}A_{mn}^{(+)}\left(-ik_z^{(+)}\right)\int_0^a\int_0^{2\pi}\Phi_{mn}^{(+)}\left(\Phi_{er}^{(+)}(r,\theta)+\Phi_{er}^{(-)}(r,\theta)\right)r\,d\theta dr-$$
$$-\left(1-M^2\right)\sum_{m=0}^{M}\sum_{n=0}^{N}A_{mn}^{(-)}\left(-ik_z^{(-)}\right)\int_0^a\int_0^{2\pi}\Phi_{mn}^{(-)}\left(\Phi_{er}^{(+)}(r,\theta)+\Phi_{er}^{(-)}(r,\theta)\right)r\,d\theta dr \tag{F.24}$$

F.4 Term: $\left(1-M^2\right)\left\{g^{(+)}-g^{(-)}\right\}\delta'\left(z-z_o\right)$

This term has a complexity given by the presence of the function $\delta'\left(z-z_o\right)$. In order to eliminate this difficulty, integration by parts is used as follows

$$\lim_{\varepsilon\to 0}\int_{z_o-\varepsilon}^{z_o+\varepsilon}\varphi(z)\frac{d\delta(z-z_o)}{dz}dz=\varphi(z)\delta(z-z_o)\Big|_{z_o-\varepsilon}^{z_o+\varepsilon}-\lim_{\varepsilon\to 0}\int_{z_o-\varepsilon}^{z_o+\varepsilon}\frac{d\varphi(z)}{dz}\delta(z-z_o)dz$$
$$=-\lim_{\varepsilon\to 0}\int_{z_o-\varepsilon}^{z_o+\varepsilon}\frac{d\varphi(z)}{dz}\delta(z-z_o)dz \tag{F.25}$$

where the boundary term was vanishes since the function $\varphi(z)$ is assumed to be identically zero at $z=z_0$, i.e. $\varphi(z_o)=0$. Therefore, the integral corresponding to this case can be rewritten as

$$-\left(1-M^2\right)\int_0^a\int_0^{2\pi}\lim_{\varepsilon\to 0}\int_{z_o-\varepsilon}^{z_o+\varepsilon}\left\{\Phi_{er}^{(+)}(r,\theta)H(z-z_o)+\Phi_{er}^{(-)}(r,\theta)\left[1-H(z-z_o)\right]\right\}\times$$
$$\times\left[\frac{\partial g^{(+)}(\vec{r}\,|\vec{r}_o)}{\partial z}-\frac{\partial g^{(-)}(\vec{r}\,|\vec{r}_o)}{\partial z}\right]\delta(z-z_o)dz\,r\,d\theta\,dr-$$
$$-\left(1-M^2\right)\int_0^a\int_0^{2\pi}\lim_{\varepsilon\to 0}\int_{z_o-\varepsilon}^{z_o+\varepsilon}\frac{d\left\{\Phi_{er}^{(+)}(r,\theta)H(z-z_o)+\Phi_{er}^{(-)}(r,\theta)\left[1-H(z-z_o)\right]\right\}}{dz}\times \tag{F.26}$$
$$\times\left[g^{(+)}(\vec{r}\,|\vec{r}_o)-g^{(-)}(\vec{r}\,|\vec{r}_o)\right]\delta(z-z_o)dz\,r\,d\theta\,dr$$

The first integral in (F.26) was already solved in section F.3 and the solution is

$$-\left(1-M^2\right)\int_0^a\int_0^{2\pi}\lim_{\varepsilon\to 0}\int_{z_o-\varepsilon}^{z_o+\varepsilon}\left\{\Phi_{er}^{(+)}(r,\theta)H(z-z_o)+\Phi_{er}^{(-)}(r,\theta)\left[1-H(z-z_o)\right]\right\}\times$$
$$\times\left[\frac{\partial g^{(+)}(\vec{r}\,|\vec{r}_o)}{\partial z}-\frac{\partial g^{(-)}(\vec{r}\,|\vec{r}_o)}{\partial z}\right]\delta(z-z_o)dz\,r\,d\theta\,dr=$$
$$-\left(1-M^2\right)\sum_{m=0}^{M}\sum_{n=0}^{N}\frac{1}{2}A_{mn}^{(+)}\left(-ik_z^{(+)}\right)\int_0^a\int_0^{2\pi}\Phi_{mn}^{(+)}\left(\Phi_{er}^{(+)}(r,\theta)+\Phi_{er}^{(-)}(r,\theta)\right)r\,d\theta dr+ \tag{F.27}$$
$$+\left(1-M^2\right)\sum_{m=0}^{M}\sum_{n=0}^{N}\frac{1}{2}A_{mn}^{(-)}\left(-ik_z^{(-)}\right)\int_0^a\int_0^{2\pi}\Phi_{mn}^{(-)}\left(\Phi_{er}^{(+)}(r,\theta)+\Phi_{er}^{(-)}(r,\theta)\right)r\,d\theta dr$$

The second integral in (F.26) becomes

$$-\left(1-M^2\right)\int_0^a\int_0^{2\pi}\lim_{\varepsilon\to 0}\int_{z_o-\varepsilon}^{z_o+\varepsilon}\left\{\Phi_{er}^{(+)}(r,\theta)-\Phi_{er}^{(-)}(r,\theta)\right\}\delta\left(z-z_o\right)\delta\left(z-z_o\right)\times$$
$$\times\left[g^{(+)}\left(\vec{r}\,|\vec{r}_o\right)-g^{(-)}\left(\vec{r}\,|\vec{r}_o\right)\right]dz\,r\,d\theta\,dr= \qquad \text{(F.28)}$$
$$-\left(1-M^2\right)\int_0^a\int_0^{2\pi}\left(\Phi_{er}^{(+)}(r,\theta)-\Phi_{er}^{(-)}(r,\theta)\right)\left\{\left[g^{(+)}-g^{(-)}\right]\delta\left(z-z_o\right)\right\}_{z=z_o}r\,d\theta\,dr$$

where the term $\left\{\left[g^{(+)}-g^{(-)}\right]\delta\left(z-z_o\right)\right\}_{z=z_o}$ is undetermined $\left(0\times\infty\right)$. The first factor, i.e.$\left[g^{(+)}-g^{(-)}\right]$, vanishes because of the continuity condition of the Green's function at $z=z_0$. In order to eliminate the indetermination, the following representation of the Dirac Delta is used[†]

$$\delta(z-z_0)=\frac{1}{\pi}\lim_{\rho\to 0}\frac{\rho}{\rho^2+(z-z_0)^2} \qquad \text{(F.29)}$$

(Lorentz representation of Dirac Delta function)

Then, the undetermined term can be analyzed as follows

$$\lim_{z\to z_0}\left\{\left[g^{(+)}\left(\vec{r}\,|\vec{r}_o\right)-g^{(-)}\left(\vec{r}\,|\vec{r}_o\right)\right]\frac{1}{\pi}\lim_{\rho\to 0}\frac{\rho}{\rho^2+(z-z_0)^2}\right\}=$$
$$=\frac{1}{\pi}\lim_{\rho\to 0}\lim_{z\to z_0}\frac{\rho\left[g^{(+)}\left(\vec{r}\,|\vec{r}_o\right)-g^{(-)}\left(\vec{r}\,|\vec{r}_o\right)\right]}{\rho^2+(z-z_0)^2}= \qquad \text{(F.30)}$$
$$=\frac{1}{\pi}\lim_{\rho\to 0}\frac{0}{\rho^2}=\frac{1}{\pi}\lim_{\rho\to 0}0=0$$

because $\left[g^{(+)}-g^{(-)}\right]\equiv 0$. Then, the integral **vanishes**.

F.5 Term: $-2iMk_o\left[\frac{\partial g^{(+)}\left(\vec{r}\,|\vec{r}_o\right)}{\partial z}H\left(z-z_0\right)+\frac{\partial g^{(-)}\left(\vec{r}\,|\vec{r}_o\right)}{\partial z}\left[1-H\left(z-z_0\right)\right]\right]$

The derivation of this term is similar to the analysis in section F.1. The integral to be solved can be written as

[†] Obtained from http://www.engr.unl.edu/~glibrary/home/DefineG/node8.html and http://functions.wolfram.com/GeneralizedFunctions/DiracDelta/02/

$$-2iMk_o\int_0^a\int_0^{2\pi}\lim_{\varepsilon\to 0}\int_{z_o-\varepsilon}^{z_o+\varepsilon}\left\{\Phi_{er}^{(+)}(r,\theta)H\left(z-z_o\right)+\Phi_{er}^{(-)}(r,\theta)\left[1-H\left(z-z_o\right)\right]\right\}\times \\ \times\left\{H\left(z-z_o\right)\frac{\partial g^{(+)}\left(\vec{r}\,|\vec{r}_o\right)}{\partial z^2}+\left[1-H\left(z-z_o\right)\right]\frac{\partial g^{(-)}\left(\vec{r}\,|\vec{r}_o\right)}{\partial z^2}\right\}dz\,r\,d\theta\,dr \tag{F.31}$$

Replacing the derivatives in equation (F.18) into (F.31) yields

$$-2iMk_o\lim_{\varepsilon\to 0}\int_0^a\int_0^{2\pi}\sum_{m=0}^{M}\sum_{n=0}^{N}A_{mn}^{(+)}\Phi_{mn}^{(+)}\left(-ik_z^{(+)}\right)\left\{\Phi_{er}^{(+)}(r,\theta)\int_{z_o-\varepsilon}^{z_o+\varepsilon}H\left(z-z_o\right)H\left(z-z_o\right)e^{-ik_z^{(+)}(z-z_o)}dz+\right. \\ \left.+\Phi_{er}^{(-)}(r,\theta)\int_{z_o-\varepsilon}^{z_o+\varepsilon}\left[1-H\left(z-z_o\right)\right]H\left(z-z_o\right)e^{-ik_z^{(+)}(z-z_o)}dz\right\}r\,d\theta\,dr- \\ -2iMk_o\lim_{\varepsilon\to 0}\int_0^a\int_0^{2\pi}\sum_{m=0}^{M}\sum_{n=0}^{N}A_{mn}^{(-)}\Phi_{mn}^{(-)}\left(-ik_z^{(-)}\right)\left\{\Phi_{er}^{(+)}(r,\theta)\int_{z_o-\varepsilon}^{z_o+\varepsilon}H\left(z-z_o\right)\left[1-H\left(z-z_o\right)\right]e^{-ik_z^{(-)}(z-z_o)}dz+\right. \\ \left.+\Phi_{er}^{(-)}(r,\theta)\int_{z_o-\varepsilon}^{z_o+\varepsilon}\left[1-H\left(z-z_o\right)\right]\left[1-H\left(z-z_o\right)\right]e^{-ik_z^{(-)}(z-z_o)}dz\right\}r\,d\theta\,dr \tag{F.32}$$

Equation (F.32) leads to solve the same z-integrals as in (F.10), (F.11), (F.12) and (F.13). As a result, this term also **vanishes**.

F.6 Term: $-2iMk_o\left[g^{(+)}\left(\vec{r}\,|\vec{r}_o\right)-g^{(-)}\left(\vec{r}\,|\vec{r}_o\right)\right]\delta\left(z-z_o\right)$

The following integral needs to be solved

$$-2iMk_o\int_0^a\int_0^{2\pi}\lim_{\varepsilon\to 0}\int_{z_o-\varepsilon}^{z_o+\varepsilon}\left\{\Phi_{er}^{(+)}(r,\theta)H\left(z-z_o\right)+\Phi_{er}^{(-)}(r,\theta)\left[1-H\left(z-z_o\right)\right]\right\}\times \\ \times 2\left[g^{(+)}\left(\vec{r}\,|\vec{r}_o\right)-g^{(-)}\left(\vec{r}\,|\vec{r}_o\right)\right]\delta\left(z-z_o\right)dz\,r\,d\theta\,dr \tag{F.33}$$

Solving the z-integral with the presence of the Dirac Delta yields

$$-2iMk_o\int_0^a\int_0^{2\pi}\left\{\frac{\Phi_{er}^{(+)}(r,\theta)+\Phi_{er}^{(-)}(r,\theta)}{2}\right\}\left[g^{(+)}\left(\vec{r}\,|\vec{r}_o\right)-g^{(-)}\left(\vec{r}\,|\vec{r}_o\right)\right]_{z=z_o}r\,d\theta\,dr\equiv 0 \tag{F.34}$$

The term $\left[g^{(+)}\left(\vec{r}\,|\vec{r}_o\right)-g^{(-)}\left(\vec{r}\,|\vec{r}_o\right)\right]_{z=z_o}$ in the integrand of (F.34) vanishes because of the continuity condition at $z=z_0$. Therefore, the integral in (F.34) **vanishes**.

F.7 Term: $\dfrac{\delta\left(\vec{r}\middle|\vec{r}_o\right)}{r}$

The following integral is formed

$$\int_0^a\int_0^{2\pi}\lim_{\varepsilon\to 0}\int_{z_o-\varepsilon}^{z_o+\varepsilon}\left\{\Phi_{er}^{(+)}(r,\theta)H\left(z-z_o\right)+\Phi_{er}^{(-)}(r,\theta)\left[1-H\left(z-z_o\right)\right]\right\}\times \\ \times\frac{\delta\left(r-r_o\right)}{r}\delta\left(\theta-\theta_o\right)\delta\left(z-z_o\right)dz\,r\,d\theta\,dr \tag{F.35}$$

The integral in the z-direction is solved to yield

$$\int_0^a\int_0^{2\pi}\left\{\frac{\Phi_{er}^{(+)}(r,\theta)+\Phi_{er}^{(-)}(r,\theta)}{2}\right\}\frac{\delta\left(r-r_o\right)}{r}\delta\left(\theta-\theta_o\right)r\,d\theta\,dr= \\ =\frac{\Phi_{er}^{(+)}(r_o,\theta_o)+\Phi_{er}^{(-)}(r_o,\theta_o)}{2} \tag{F.36}$$

F.8 Derivation of final expression

Considering only the terms that do not vanish after applying the integration process, i.e. sections F.3, F.4 and F.7, equation (F.4) becomes

$$\left(1-M^2\right)\int_0^a\int_0^{2\pi}\lim_{\varepsilon\to 0}\int_{z_o-\varepsilon}^{z_o+\varepsilon}\left\{\Phi_{er}^{(+)}(r,\theta)H\left(z-z_o\right)+\Phi_{er}^{(-)}(r,\theta)\left[1-H\left(z-z_o\right)\right]\right\}\times \\ \times\left\{2\left[\frac{\partial g^{(+)}}{\partial z}-\frac{\partial g^{(-)}}{\partial z}\right]\delta\left(z-z_o\right)+\left[g^{(+)}-g^{(-)}\right]\delta'\left(z-z_o\right)\right\}dz\,r\,d\theta\,dr= \\ =\int_0^a\int_0^{2\pi}\lim_{\varepsilon\to 0}\int_{z_o-\varepsilon}^{z_o+\varepsilon}\left\{\Phi_{er}^{(+)}(r,\theta)H\left(z-z_o\right)+\Phi_{er}^{(-)}(r,\theta)\left[1-H\left(z-z_o\right)\right]\right\}\times \\ \times\frac{\delta\left(r-r_o\right)}{r}\delta\left(\theta-\theta_o\right)\delta\left(z-z_o\right)dz\,r\,d\theta\,dr \tag{F.37}$$

Using equation (F.25), rewrite as

$$\begin{aligned}\left(1-M^2\right)\int_0^a\int_0^{2\pi}\lim_{\varepsilon\to 0}\int_{z_o-\varepsilon}^{z_o+\varepsilon}\left\{\Phi_{er}^{(+)}(r,\theta)H\left(z-z_o\right)+\Phi_{er}^{(-)}(r,\theta)\left[1-H\left(z-z_o\right)\right]\right\}\times\\ \times\left\{2\left[\frac{\partial g^{(+)}}{\partial z}-\frac{\partial g^{(-)}}{\partial z}\right]\delta\left(z-z_o\right)-\left[\frac{\partial g^{(+)}}{\partial z}-\frac{\partial g^{(-)}}{\partial z}\right]\delta\left(z-z_o\right)\right\}dz\,r\,d\theta\,dr=\\ =\int_0^a\int_0^{2\pi}\lim_{\varepsilon\to 0}\int_{z_o-\varepsilon}^{z_o+\varepsilon}\left\{\Phi_{er}^{(+)}(r,\theta)H\left(z-z_o\right)+\Phi_{er}^{(-)}(r,\theta)\left[1-H\left(z-z_o\right)\right]\right\}\times\\ \times\frac{\delta\left(r-r_o\right)}{r}\delta\left(\theta-\theta_o\right)\delta\left(z-z_o\right)dz\,r\,d\theta\,dr\end{aligned}\tag{F.38}$$

Then, solving the integrals in the z-direction as shown in sections F.3, F.4 and F.7, equation (F.38) becomes

$$\begin{aligned}\int_0^a\int_0^{2\pi}\frac{1}{2}\left(1-M^2\right)\left[\sum_{m=0}^{M}\sum_{n=0}^{N}A_{mn}^{(+)}\left(-ik_z^{(+)}\right)\left(\Phi_{er}^{(+)}(r,\theta)+\Phi_{er}^{(-)}(r,\theta)\right)\Phi_{mn}^{(+)}-\right.\\ \left.-\sum_{m=0}^{M}\sum_{n=0}^{N}A_{mn}^{(-)}\left(-ik_z^{(-)}\right)\left(\Phi_{er}^{(+)}(r,\theta)+\Phi_{er}^{(-)}(r,\theta)\right)\Phi_{mn}^{(-)}\right]r\,d\theta\,dr=\\ =\frac{\Phi_{er}^{(+)}(r_o,\theta_o)+\Phi_{er}^{(-)}(r_o,\theta_o)}{2}\end{aligned}\tag{F.39}$$

Reordering

$$\begin{aligned}\sum_{m=0}^{M}\sum_{n=0}^{N}A_{mn}^{(+)}k_z^{(+)}\int_0^a\int_0^{2\pi}\left(\frac{\Phi_{er}^{(+)}(r,\theta)+\Phi_{er}^{(-)}(r,\theta)}{2}\right)\Phi_{mn}^{(+)}r\,d\theta\,dr-\\ -\sum_{m=0}^{M}\sum_{n=0}^{N}A_{mn}^{(-)}k_z^{(-)}\int_0^a\int_0^{2\pi}\left(\frac{\Phi_{er}^{(+)}(r,\theta)+\Phi_{er}^{(-)}(r,\theta)}{2}\right)\Phi_{mn}^{(-)}r\,d\theta\,dr=\\ =\frac{i}{\left(1-M^2\right)}\frac{\Phi_{er}^{(+)}(r_o,\theta_o)+\Phi_{er}^{(-)}(r_o,\theta_o)}{2}\end{aligned}\tag{F.40}$$

Note that the mode shape are given by

$$\Phi_{mn}^{(\ell)}\left(r,\theta\right)=\cos\left[m\left(\theta-\theta_o\right)\right]J_m\left(k_{mn}^{(\ell)}r\right)\qquad\ell=+,-\tag{F.41}$$

which satisfy orthogonality in the θ-direction. Therefore, the surface integrals are solved as

$$\int_0^a \int_0^{2\pi} \left(\frac{\Phi_{er}^{(+)} + \Phi_{er}^{(-)}}{2} \right) \Phi_{mn}^{(+)} \, r \, d\theta \, dr = \begin{cases} 0 & if \ m \neq e \\ \int_0^a \int_0^{2\pi} \left(\frac{\Phi_{mr}^{(+)} + \Phi_{mr}^{(-)}}{2} \right) \Phi_{mn}^{(+)} \, r \, d\theta \, dr & if \ m = e \end{cases} \tag{F.42}$$

Therefore, equation (F.40) becomes

$$\sum_{n=0}^{N} \left\{ k_z^{(+)} A_{mn}^{(+)} \int_0^{2\pi} \int_0^a \left(\frac{\Phi_{mr}^{(+)} + \Phi_{mr}^{(-)}}{2} \right) \Phi_{mn}^{(+)} \, r \, d\theta \, dr - k_z^{(-)} A_{mn}^{(-)} \int_0^{2\pi} \int_0^a \left(\frac{\Phi_{mr}^{(+)} + \Phi_{mr}^{(-)}}{2} \right) \Phi_{mn}^{(-)} \, r \, d\theta \, dr \right\} =$$

$$= i \frac{\Phi_{mr}^{(+)}(r_0, \theta_0) + \Phi_{mr}^{(-)}(r_0, \theta_0)}{2\left(1 - M^2\right)} \qquad m = 0, 1, 2, 3, \ldots\ldots \tag{F.43}$$

which is the final equation in (2.42).

Vita

José S. Alonso was born on March 5, 1976 in Bahía Blanca, Argentina. He received his basic and middle education at the Instituto Domingo Savio in Santa Rosa, La Pampa, where he graduated with the degree of Commercial Bachelor in 1993. After graduation he joined the Universidad Nacional del Sur (UNS), Bahía Blanca in 1994, where he completed the first year of the Engineering program, which was concentrated on Advanced Mathematics. In 1995 he transferred to the Universidad Católica de Córdoba (UCC), in Córdoba, where he earned the degree of Diploma Aeronautical Engineer in December 1999. The complete career included three years of studies in the Instituto Universitario Aeronáutico, also in Córdoba, as part of a Cooperation Program between the universities. On July 2000 he moved to the United States and began graduate studies in the Mechanical Engineering Department of Virginia Polytechnic Institute and State University. His main areas of research were Fluid Mechanics, Aeroacoustics, Vibrations and Control. With Professor Ricardo A. Burdisso as his advisor, he completed a Ph.D. Program in September 2004 with his thesis on turbofan engine noise control.